LUDWIG-MAXIMILIANS -UNIVERSITÄT MÜNCHEN

FACULTY OF PHYSICS

INVESTIGATING GENERALIZED KITAEV MAGNETS USING MACHINE LEARNING

NIHAL RAO

München, 2023

INVESTIGATING GENERALIZED KITAEV MAGNETS USING MACHINE LEARNING

Dissertation
an der Fakultät für Physik
der Ludwig-Maximilians-Universität München

vorgelegt von
NIHAL RAO
aus Bengaluru

München, den 30. August 2023

Erstgutachter: Prof. Dr. Lode Pollet
Zweitgutachter : Prof. Dr. Jan von Delft

Datum der mündlichen Prüfung : 17. Oktober 2023

"The universe is full of magical things, patiently waiting for our wits to grow sharper."

Eden Phillpotts

Kurzfassung

INVESTIGATING GENERALIZED KITAEV MAGNETS USING MACHINE LEARNING

Frustration in Kitaev-Materialien führt zu einem sehr reichhaltigen und komplexen Phasendiagramm, einschließlich der klassischen Spinflüssigkeitsphase. Die Suche nach und das Verständnis von Spinflüssigkeiten und weiteren neuartigen komplexen Phasen der Materie stehen im Mittelpunkt der heutigen Forschung zu kondensierter Materie. Mittels analytischer Methoden Ordnungsparameter zur Charakterisierung dieser Phasen zu finden, ist nahezu unmöglich. Bei niedrigen Temperaturen ordnen sich die meisten klassischen Spinsysteme in komplizierte Strukturen, die große magnetische Elementarzellen belegen, was die Komplexität des Problems noch weiter erhöht und außerhalb des Anwendungsbereichs der meisten herkömmlichen Methoden liegt.

In dieser Arbeit untersuchen wir die Hamilton-Operatoren realitätsnaher Kitaev-Materialien mithilfe maschinellen Lernens. Hauptmerkmale des zugrundeliegenden Algorithmus sind *unbeaufsichtigtes Lernen*, welches ermöglicht die Topologie eines Phasendiagramms ohne jegliche Vorkenntnisse erforschen, und *Interpretierbarkeit*, welche zur Analyse der Struktur der klassischen Grundzustände notwendig ist.

In den ersten drei Kapiteln werden wir den Algorithmus des maschinellen Lernens auf verschiedene Hamilton-Operatoren anwenden, die zur Modellierung von Kitaev-Materialien eingesetzt werden, um zu untersuchen inwieweit die Quantenmodelle und die experimentellen Beobachtungen allein durch deren klassischen Grenzfall erklärt werden können. Darüber hinaus erforschen wir weitere Features dieses Algorithmus, die es uns ermöglichen, verborgene Symmetrien, lokale Einschränkungen der klassischen Spinflüssigkeiten, sowie bisher unbekannte Phasen im hochdimensionalen Phasenraum aufzudecken.

In den letzten beiden Kapiteln werden wir uns mit dem Verständnis der Struktur der klassischen Grundzustände befassen, welche durch die Verflechtung mehrerer Helices charakterisiert sind. Wir werden auch versuchen, die Signatur dieser Phasen in Experimenten zu verstehen, indem wir die Dynamik und den Transport durch Kitaev-Magnete untersuchen.

Diese Arbeit beweist die Tauglichkeit von maschinellem Lernen, hochkomplexe Phasendiagramme mit wenig bis gar keinem Vorwissen aufzudecken und hochfrustrierten Magnetismus zu erforschen. Die Kombination aus maschinellem und menschlichem Einsatz ebnet den Weg zu neuen und spannenden physikalischen Erkenntnissen.

Abstract

INVESTIGATING GENERALIZED KITAEV MAGNETS USING MACHINE LEARNING

Bond frustration in Kitaev materials leads to a very rich phase diagram with highly intricate phases including the classical spin liquid phase. The search and understanding of spin liquids and novel complex phases of matter is at the heart pf present day condensed matter research. To search and design order parameters to characterize these phases using analytical approaches is a nearly impossible task. At low temperatures, most of the classical spins order into complicated spin structures occupying large magnetic unit cells which further adds to the complication and is out of the realm of most traditional methods.

In this thesis we investigate realistic Kitaev material Hamiltonians using a machine learning framework whose key features, of *unsupervised learning* which helps us study the topology of the phase diagram without prior knowledge and *interpretability* which helps us analyse the structure of the classical ground states, are exploited.

In the first three chapters, we shall use this framework on different Hamiltonians used to model Kitaev materials and understand to what extent the quantum limit and experimental results could be explained just by the classical limit of these models. We in addition explore other features of this framework which lets us uncover hidden symmetries as well as local constraints for the classical spin liquids and hitherto unreported new phases in the high dimensional phase space.

In the last two chapters we shall dwell on the understanding the structure of the classical ground states which is quite complicated as it hosts a tangle of multiple helices. We shall also try and understand the signature of these phases on experiments by studying the dynamics and transport through Kitaev magnets thus bridging the gap between experiment and theory.

This thesis proves instances of using machine learning to uncover highly complex phase diagrams with little to no previous knowledge and serve as a paradigm to explore highly frustrated magnetism. Through a combination of machine and human effort we are on the way to uncover new and exciting physics.

Acknowledgements

I would begin my acknowledgements by thanking whole heartedly my supervisor **Lode Pollet** for giving me the opportunity to do a PhD as well as work on really interesting Physics as a part of my thesis. Je constante aanmoediging en geduld ondanks andere verplichtingen is lovenswaardig. Je gaf me de vrijheid om in mijn eigen tempo onderzoek te doen en was er altijd om twijfels op te helderen en dingen uit te leggen als ze onduidelijk waren, wat ik op prijs stel. Ook je discussies over andere onderwerpen dan natuurkunde tijdens de Mensa-lunches werkten altijd als een stressbreker en maakten deze werkrelatie een stuk relaxter. Ik zal die ene voetbalwedstrijd die we speelden zeker koesteren en de eindeloze scherts over andere onderwerpen.

A special thanks is also reserved to **Ke Liu** who really played a crucial role in helping me finish the thesis. Nǐ zǒng shì zài chǎng tǎolùn xiǎngfǎ bìng xúnzhǎo xīn de xiàngmù xiǎngfǎ. Zài tǎolùn mǒu xiē huàtí de jìnzhǎn shí, nín de lěngjìng jǔzhǐ huǎnjiěle wǒ de jǐnzhāng, bìng gǔlì wǒ jìnyībù gōngzuò. Wǒ fēicháng gǎnxiè nín bāngzhù tuīdòng hé jīlì wǒ wánchéng xiàngmù, yóuqí shì zài chōngmǎn tiǎozhàn de xīnguān yìqíng shíqí, nín duì wùlǐ xué de guānzhù hé fèngxiàn shì wǒ yǒngyuǎn qīnpèi de.

I would also like to thank **Stefan Wittlinger and Marcel Gievers** who were the first friends I made here and continues to be a good friends. Ich weiß es immer zu schätzen, dass du dich besonders viel Mühe gegeben hast, mir dabei zu helfen, mich an das Leben in München zu gewöhnen, und dass du während des Lockdowns immer für mich da warst. Ich werde auch die Lock down Mittagessen und die endlosen Diskussionen von Physik bis Politik schätzen. Das gemeinsame Wandern, Kochen und Mittagessen sowie das Entdecken neuer Imbissbuden in der Nähe der Uni, insbesondere während der Lock down Zeit, haben eine ansonsten stressige isolierende Zeit wirklich erträglicher gemacht, und für diene Kameradschaft werde ich dir immer zu Dank verpflichtet sein.

A special mention is also reserved to my friends **Nicolas Sadoune, Heloise Albot, Nader Moostan, Gün Günal** who were more than just a work colleague. Les plaisanteries et les discussions sans fin sur tout ce qui se passait sous le soleil étaient une distraction agréable et aidaient à nouer une relation au-delà du travail. Toutes vos hypothèses et exagérations ont toujours fait sourire. Les sports que nous avons pratiqués ensemble et la volonté constante de rivaliser et d'exceller ainsi que de se dire des mots gentils les jours de congé sont quelque chose dont je serai toujours redevable. J'ai aussi beaucoup aimé cuisiner et j'ai appris beaucoup de choses sur la vie autres que la physique grâce à vous tous. Alors merci du fond du cœur d'être des amis si cool.

The administrative help and patience in clarification of formalities of **Cordula Weber** is deeply appreciated. You made sure everything, till the last decimal in the travel reimbursement or time sheet was correct and really made sure the sailing on the administrative front was a smooth one.

This acknowledgement would be incomplete without the mention of my partner **Hajar Häusl mann** who stood like a rock and supported me through thick and thin. Your attitude and persistence in life never ceases to amaze me and I am really fortunate that I get to spend this life with you. You have always been very kind and loving and accepted me for myself despite all the craziness. My life in Munich and in general was a joy thanks to you. I would also like to thank my mother without whom coming this far would have not been possible.

Finally, I would like to thank everyone here at LMU, my office-mates, Mensa mates, people down the corridor who made my time here really special and made an otherwise mundane existence more colorful.

Contents

List of Figures

List of Tables

Dedicated to my love for things that start with the letter "H" - Hockey and Hajar

Chapter 1

Introduction

One of the biggest challenges in present day condensed matter physics is the experimental realisation of spin liquids. The theoretical understanding of this new phase of matter, which is the result of some form of frustration, was to a major extent advanced by the seminal work of Kitaev [119] but the experimental realisation still alludes us till this day and is a hotbed for many debates and discussions in the physics community. In this chapter we shall introduce the reader to the key concepts in spin liquid physics as well as discuss the model which we investigated in this thesis. We shall also provide an overview of the possible realization of spin liquid physics in materials and discuss the most promising candidate materials as well as the experiments done and the discussion and debates surrounding their findings. We shall then proceed to discuss machine learning in general and its applications to condensed matter physics in particular and finally illustrate the motivation behind this thesis.

Phase transitions are the cornerstone of physics and is one of the most ubiquitous phenomena experienced by humans from the melting of ice into water to the vaporization of petroleum pushing our automobiles forward. The theoretical understanding of phase transitions in terms of a spontaneously broken symmetry and the emergence of an order parameter which changes values as we cross the boundary of phase transitions is credited to the seminal work of Landau [129]. The basic idea is that at low enough temperatures interactions between spins results in a magnetically ordered state and this ordered state is preserved upto a critical temperature and upon increasing temperature further we spontaneously lose the order and just have a random thermally fluctuating system of spins. This sudden abrupt change is referred to as a *phase transition*. In the other possible scenario if the transition between the ordered and disordered state is gradual and the order parameters change their values in a continuous manner we refer to such a transition as a *crossover*. This abrupt change is usually accompanied by divergences in thermodynamic quantities which could be first order signalled by the divergence of order parameter or second order signalled by the divergence of susceptibilities followed by a reduction is spin entropy as the system chooses a unique ground state as a result of the symmetry breaking.

Another mechanism of reducing the spin entropy without explicitly breaking any symmetry is to form collective quantum states with long range entanglement known as quantum spin liquids (QSL) conjectured by Anderson [6, 13, 190]. The idea of having these QSLs in more than one dimension was pioneered by Anderson with the conjecture of *resonant valence bond* (RVB) solids.

This was proposed to be the ground state solution of a system of antiferromagnetically interacting Heisenberg spins with $S = 1/2$ on a triangular lattice more commonly shortened as THAFM (Triangluar lattice Heisenberg antiferromagnets). This is an example of geometric frustration and the problem deals with the configuration of the spin on the third vertex of the triangle while the other two vertices are occupied by the AFM configurations. The AFM interaction in conjunction with the geometry results in conflicting interactions between pairs of spins preventing them from finding a new unique ground state. Anderson's solution was that the ground state consists of superpositions of spin singlets formed by a pair of $S = 1/2$ spins which keep on flipping alternately between the three spins in the triangular unit cell resembling a "liquid" of spin singlets than the typical picture of static spins pointing in fixed directions in a magnetically ordered system. This sea of floating spin singlets is the intuitive visualization of a spin liquid. However, it was shown that this RVB ground state idea was not accurate and the ground state does order in a 120° Néel

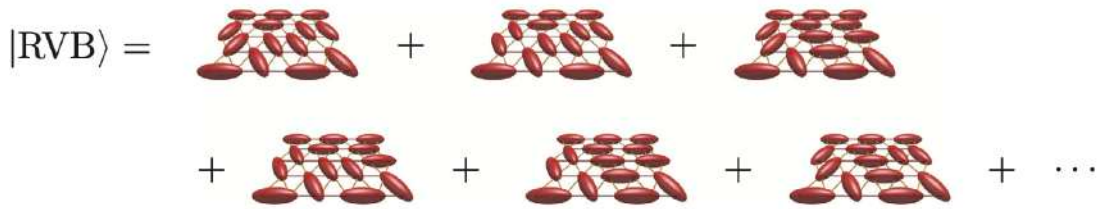

FIGURE 1.1: The (quantum) RVB state depicted as a coherent superposition over different dimer coverings. Each ellipsoid indicates a spin singlet comprising of two $S = 1/2$ spins. The classical manifold is extensively degenerate comprises of these distinct dimer coverings. However the true ground state is not a RVB state rather a 120° Néel state. Figure reproduced from [13]

ground state [90, 33]. In other geometrically frustrated lattices, such as the Kagomé or the triangular lattice with additional interactions, RVB-QSLs are proposed to be the ground state solution. We shall see that these ideas of frustration coupled with interaction form the essential elements for having a spin liquid [237, 157, 250, 87].

The excitations in magnetically ordered materials can be described in the purview of spin wave theory by a magnon dispersion spectrum which is well defined i.e. for a given momentum we have a well defined energy peak. In contrast the key feature of QSLs is the (unusual) fractionalized elementary excitations also known as *spinons*, which give rise to a continuum in energy at any given momentum i.e. we do not have a well defined magnon dispersion spectrum. This fractionalization also has interesting signatures in transport properties giving rise to fractionalized thermal and spin conductances [13].

The major breakthrough from the theoretical front came from the seminal work of Kitaev in 2006 [119] where he was able to obtain a spin liquid ground state as the solution of a realistic Hamiltonian model. Further he showed that the QSL state comprises of spins fractionalized into emergent quasi particles - the Majorana fermions which is an essential ingredient of any spin liquid. Khaliullin and Chaloupka [110] proposed a mechanism comprising of crystal field splitting combined with strong spin orbit coupling resulting in $J = 1/2$ pseudospins in complex Iridates which formed the perfect playground to host Kitaev spin liquids and other exotic physics. This combination of solid state chemistry with advances in theoretical physics has garnered a lot of attention in the recent years and promised to show new, exotic and exciting physics. We shall begin by briefly discussing Kitaev's solution and the emergence of fractionalized excitations.

1.1 Kitaev model and fractionalized excitations

We shall here introduce the Kitaev model [119] and discuss the emergence of fractionalized excitations. The Kitaev model is at its core just a spin $S = 1/2$ model on a hexagonal two dimensional lattice with nearest-neighbour bond-dependent Ising interactions with easy axes parallel to x, y, z axes. On the hexagonal lattice each spin has three nearest neighbours which are indexed to lie along the x,y and z bonds respectively (see figure 1.2). The Hamiltonian of the Kitaev model is then,

$$\mathcal{H} = -\sum_{<ij>\in\gamma} K_\gamma S_i^\gamma S_j^\gamma \tag{1.1}$$

where $\gamma = \{x, y, z\}$ refers to the different bonds to the nearest neighbouring spins on a hexagonal lattice and we sum over all bonds on the hexagon. The coupling constants K_γ may be anistropic which leads to either gapped or gapless excitations but the bond frustration arises from the conflict of each spin with the orthogonal anisotropies of the three nearest neighbour spins.

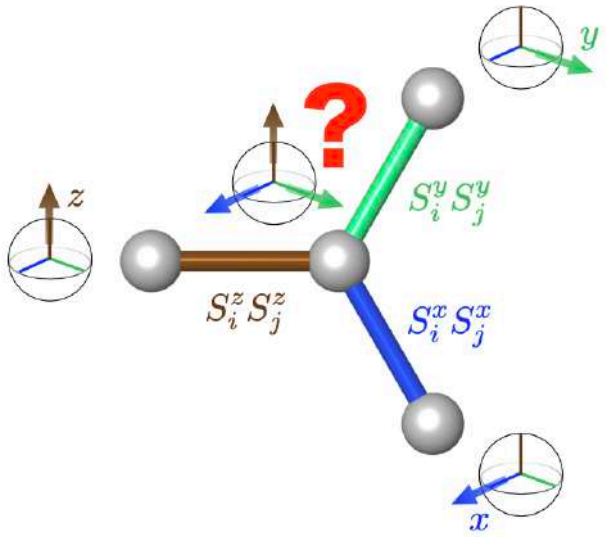

FIGURE 1.2: The Kitaev interaction arising from spin-orbit induced bond directional interactions where spins prefer to remain parallel to the easy axis leading to Ising type interaction. No spin configuration can simultaneously minimize all couplings leading to bond dependent exchange frustration. Figure reproduced from [214]

The solution of the above Hamiltonian can be found by fractionalizing each spin in terms of Majorana Fermions of four different flavours. By definition Majorana Fermions are neutral self-adjoint particles which are also antiparticles of themselves i.e. $f = f^\dagger$ [119]. They are commonly constructed from other fermions by considering the real and imaginary part described by the fermion creation and annihilation operators respectively. Thus every complex fermion with the operators $a, a^\dagger$ can create two Majorana fermion modes as $f_1 = (a + a^\dagger) = f_1^\dagger$ and $f_2 = i(a - a^\dagger) = f_2^\dagger$. We then consider three fixed Majoranas dependent on the bonds (b^x, b^y, b^z) and one free/itinerant Majorana (c) and decompose the spin operator as $S^\gamma = i/2 b^\gamma c$ (see Fig 1.3) and the constraint that $b_j^x b_j^y b_j^z c_j = 1\ ,\ \forall j$ which is imposed by the $SU(2)$ constraint from the $S = 1/2$ operators $[S^i, S^j] = i\epsilon_{ijk} S^k$. This substitution leads to being able to write the Hamiltonian in a free Fermion form as

$$\mathcal{H} = -\sum_{<ij>\in\gamma} K_\gamma S_i^\gamma S_j^\gamma = -\frac{1}{4}\sum_{<ij>\in\gamma} K_\gamma (b_i^\gamma b_j^\gamma) c_i c_j := -\frac{1}{4}\sum_{<ij>\in\gamma} K_\gamma u_{ij}^\gamma c_i c_j \tag{1.2}$$

where the bond operators $u_{ij}^\gamma = \pm i$ and their product around each hexagon determines the flux $W = \pm 1$. The flux operator is just the product of the six spins operators S_i^γ with the bond γ matching the index of the bond, around each hexagon $W_{1-6} = S_1^z S_2^x S_3^y S_4^z S_5^x S_6^y$ and has eigenvalues $W = \pm 1$ and the flux operators not only commute amongst themselves but also with the Hamiltonian i.e. $[W_{lm}, W_{np}] = 0\ ,\ [W_{lm}, \mathcal{H}] = 0$. Thus every many body eigenstate can be labelled by the flux through each hexagon thus block-diagonalizing the Hamiltonian. Since the ground state is flux free we choose every flux operator to have the same eigenvalue $W = 1$ by convention. After choosing $u_{ij}^\gamma = i$ we are just left with a free Hamiltonian for the Majorana Fermions c which can now propagate coherently through the lattice with $\mathcal{H} = i/4 \sum_{<ij>\in\gamma} K_\gamma c_i c_j$. The dispersion relation of this free Hamiltonian is just the Dirac spectrum [66] with all states appearing in pairs (particle-hole picture) with positive and negative energies.

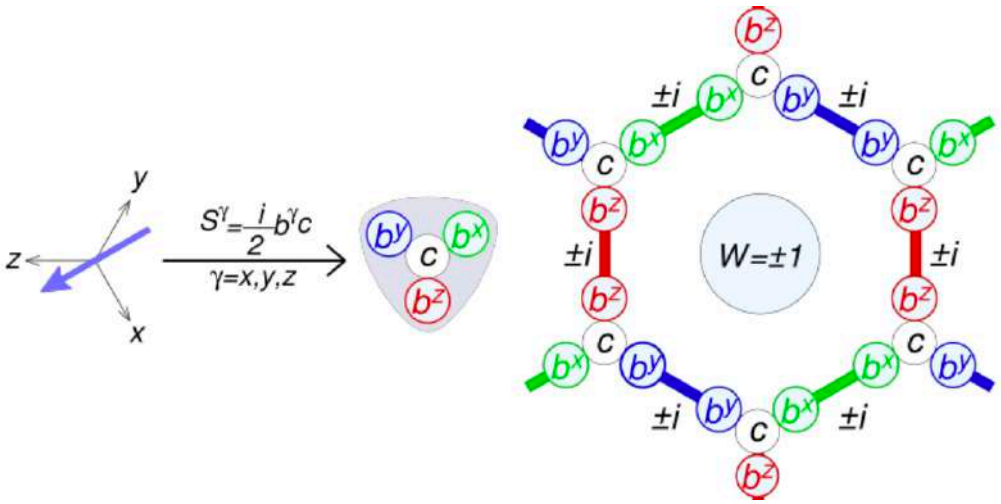

FIGURE 1.3: The fractionalization of spins into two kinds of Majorana fermions depicted here by b^γ for the stationary localized fermions and c for the mobile itinerant fermions. The stationary fermions contribute to the Z_2 flux with their imaginary eigenvalues $\pm i$ through the bond operator $u_{ij}^\gamma = b_i^\gamma b_j^\gamma$ which controls the hopping amplitude of the itinerant Majoranas. Their product around each hexagonal loop measures the Z_2 flux with the eigenvalues ± 1. Figure reproduced from [214]

$$E(\vec{q}) = \pm\sqrt{\epsilon_q^2 + \triangle_q^2}\ ,\ \epsilon_q = 2[K_z - K_x\cos(\vec{q}\cdot\vec{a}) - K_y\cos(\vec{q}\cdot\vec{b})]\ , \tag{1.3}$$

$$\triangle_q = 2[K_x\sin(\vec{q}\cdot\vec{a}) + K_y\sin(\vec{q}\cdot\vec{b})] \tag{1.4}$$

where $\vec{q}$ is the quasi-lattice momentum and $\vec{a} = [0,1]$, $\vec{b} = [3/2, 1/2]$ are the hexagonal lattice primitive vectors. The spectrum is interestingly depends on the values of the coupling constants. For isotropic and weakly anisotropic couplings, where the sum of two couplings is less than the third one, the spectrum is gapless, but for strongly anisotropic couplings where the sum of two couplings is greater than the third one, we get a gapped spectrum. We could get a gapped spectrum in the gapless sector by introducing time reversal symmetry breaking perturbations, such as coupling the spins to an external magnetic field of strength B and the Majorana gap $\Delta \propto B^3/K^2$.

The Majoranas b^γ which form a part of the bond operator u^γ are fixed and immobile and the sign of u determines the direction of hopping of the other free Majorana c. Since $u^\gamma = \pm i$ this is the emergent $\mathbb{Z}_2$ gauge field and this determines the phase of hopping integral for the c Majoranas. In each flux sector we can fix the gauge and just replace u^γ by $\pm i$. The low energy modes correspond to one of the hexagons having an opposite flux to the rest of the other fluxes. The dynamical spin structure factor has an imprint of this fractionalization with a q-independent spin gap [160] which is a result of the localization due to the presence of immobile Fermions in addition to the itinerant ones. The plot of specific heat further confirms this fractionalization with two peaks one at high temperature corresponding to the itinerant Fermions and the other at low temperature corresponding to the flux ordering of the localized Majoranas. Since we have fractionalized charges theoretically a half quantized thermal Hall conductivity $\kappa_{xy} = z/2(T\pi/6)$, $z \in \mathbb{Z}$ [101, 161] is also predicted.

1.2 Realisation of Kitaev Physics

The Kitaev model introduced in the previous section was thought of as a toy model whose ground state hosts a QSL since in general $S = 1/2$ spins do not accommodate strong Ising coupling anisotropies [229]. Khaliullin and Chaloupka in their seminal work [41] showed that it might

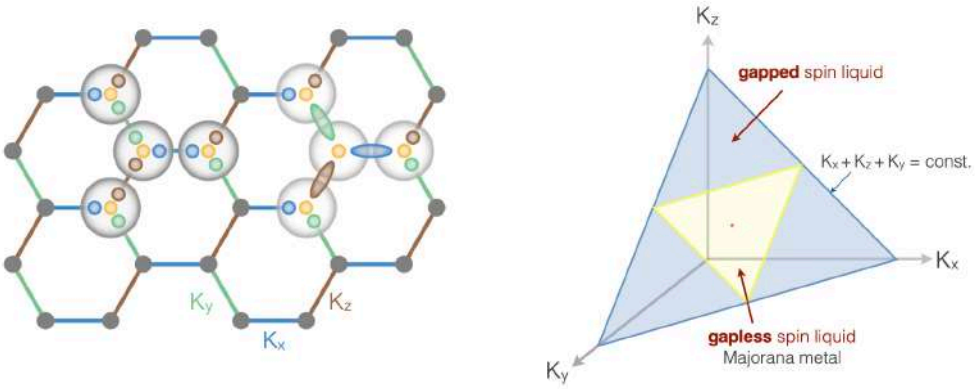

FIGURE 1.4: The honeycomb Kitaev model shown where each circle represents a $S = 1/2$ spin with its fractionalization into fixed and itinerant Majorana fermions. Depending on the chemistry this leads to bond dependent Ising interactions with the couplings K_x, K_y, K_z. The phase diagram of this model dependent on the values of the couplings is shown on the right for $K_x + K_y + K_z = const$. If one of the couplings dominates over the sum of the other two $K_\alpha \geq K_\beta + K_\gamma$ where α, β, γ are mutually exclusive a gapped spin liquid (shaded in blue) is formed. Else around the isotropic point (shown by a red dot) $K_\gamma = K \ \forall \gamma$ a gapless spin liquid is formed which can be gapped by introducing a time reversal symmetry breaking interaction with the Majorana gap $\Delta \propto B^3$. Figure reproduced from [208].

be possible to realise Kitaev physics with effective spin momentum $J_{eff} = 1/2$ in heavy transition metal compounds due to the interplay between electron correlation and strong spin orbit coupling. This opened the door for experimental investigation of Iridium oxides (Iridates) and Ruthenium Chlorides (Ruthenates) as they form the ideal candidates with a d^5 outermost electron shell configuration as required by the mechanism described by Chaloupka et al.

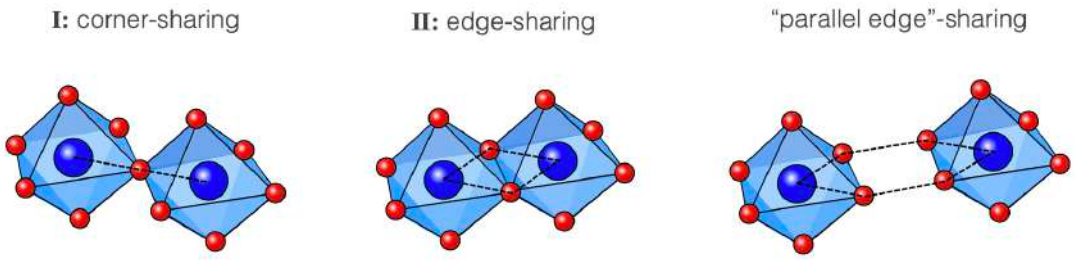

FIGURE 1.5: The different possible orientations of the IrO_6 octahedra lead to different interaction terms between the Iridium ions (shown in dark blue) at the centre of each octahedra. Corner sharing (I) geometry leads to a 180° Ir-O-Ir bond resulting in a ferromagnetic Heisenberg exchange. While edge sharing geometry (II) results in a 90° Ir-O-Ir bond leading to destructive interference between the two pathways and resulting in Kitaev dominated Ising interactions. Figure reproduced from [214]

We shall here discuss the Iridates but a similar story holds for other material candidates too. The essential ingredients are lattice distortions coupled with strong spin orbit coupling that results in $J_{eff} = 1/2$ spin moments. In Iridates the Iridium atoms (Ir^{4+}) are in a $4d^5$ coordination with 5 electrons in its outermost shell. Each Ir^{4+} is in coordination with 6 other oxygen atoms in an octahedral configuration with 4 in plane and 1 above and below each. This oxygen octahedron produces a large crystal field splitting which dominates over the Hunds rule (remember this rule favours individual occupation of orbitals before coupling and hence a high spin state) and we have a low spin state with each of the 5 d electrons occupying the triply degenerate t_{2g} manifold comprising of d_{xy}, d_{yz}, d_{xz} orbitals respectively. The effective orbital momentum of the d orbitals

which is $l = 2$ as a result of the crystal field splitting is reduced to $l = 1$ as the t_{2g} manifold is isomorphic to the p orbitals manifold [145].

Heavy transition metal compounds such as Ir also have a strong spin orbit coupling whose origins lie in relativistic physics which is a few orders of magnitude larger than the crystal field splitting produced by the distortions of the oxygen octahedra. This spin orbit coupling (SOC) additionally splits the t_{2g} manifold into a higher energy $J_{eff} = 1/2$ Kramers doublet and a lower energy $J_{eff} = 3/2$ quartet where the effective momentum is just the sum of the spin and orbital momenta $\vec{J}_{eff} = \vec{L}_{eff} + \vec{S}$ where $|\vec{L}_{eff}| = 1$ and $|\vec{S}| = 1/2$ [113]. In most heavy transition compounds as the spin orbit coupling usually the dominant interaction (over octahedral/trigonal compressions or typical exchange interactions) the low energy physics is dominated by the $J_{eff} = 1/2$ moments and its wave function is just a quantum superposition of the t_{2g} orbitals with equal amplitudes but complex phases to describe orbital motion [114]. Thus the Kramer doublets written in terms of the t_{2g} orbitals are

$$|J_{eff} = 1/2, J^z_{eff} = -1/2\rangle = -\frac{1}{\sqrt{3}}(|d_{xy}, \downarrow\rangle - |d_{yz}, \uparrow\rangle + i|d_{zx}, \uparrow\rangle) \tag{1.5a}$$

$$|J_{eff} = 1/2, J^z_{eff} = +1/2\rangle = \frac{1}{\sqrt{3}}(|d_{xy}, \uparrow\rangle + |d_{yz}, \downarrow\rangle + i|d_{zx}, \downarrow\rangle) \tag{1.5b}$$

Four of the five t_{2g} electrons occupy the quartet state while the remaining one electron or equivalently one hole occupies the Kramer doublet. Thus we end up having a $J_{eff} = 1/2$ spin per octahedra which is one of the two essential ingredients for Kitaev physics. A narrow band of $J_{eff} = 1/2$ doublets is formed as a consequence of nearest neighbour hopping and a moderate onsite Coulomb repulsion opens up a charge gap in this half filled band thus forming a weak Mott insulator with $J_{eff} = 1/2$ moments. Similar physics also applies for the Ruthenates too. The other essential ingredient is the Ising type of bond dependent interactions which is the hallmark of Kitaev physics.

The two neighbouring IrO_6 octahedra could be either edge sharing or corner sharing. When the two octahedra share a corners oxygen atom we get a 180° Ir-O-Ir bond and the two adjacent Ir atoms ($J_{eff} = 1/2$ moments) interact via *super-exchange* which can be describe by the Heisenberg interaction which is the dominant isotropic exchange interaction [93, 113, 63]. We have a pseudospin rotational symmetry ($SU(2)$) as the electron hopping preserves both the spin and orbital index.

The more interesting geometry is when the octahedra share an edge instead of a corner. We now have two 90° Ir-O-Ir bonds and the super-exchange interaction between the two Ir ions have two equivalent paths which results in a destructive interference between the two paths and a complete suppression of the Heisenberg interaction between the two $J_{eff} = 1/2$ moments [93]. We now have an orbital non conserving exchange interaction which manifests as a ferromagnetic Ising interaction $-KJ^z_{eff,i}J^z_{eff,j}$ with the easy axes perpendicular to the Ir-O-Ir plane. This is essentially the Kitaev interaction we are behind and is realised in the edge sharing geometry of the octahedras. In real space the pseudospin $J_{eff} = 1/2$ instead hops to a neighbouring $J_{eff} = 3/2$ quartet orbital and the ferromagnetic pairing of parallel spins between $J_{eff} = 3/2$ and $J_{eff} = 1/2$ is favoured by Hunds coupling. Thus we have all the essential elements as required by Kitaev physics with $J_{eff} = 1/2$ pseudospins and bond-dependent Ising interactions $-K_\gamma J^\gamma_i J^\gamma_j$ where γ is the easy axes perpendicular to the Ir-O-Ir plane. A_2IrO_3 ($A = Na, Li$) and $\alpha - RuCl_3$ were proposed as the earliest candidate materials where the octahedras form a 2D honeycomb layer with edge sharing geometry which spurred the hunt for Kitaev spin liquids but in real materials there are additional interactions which are non-negligible and lead to ordering at low temperatures.

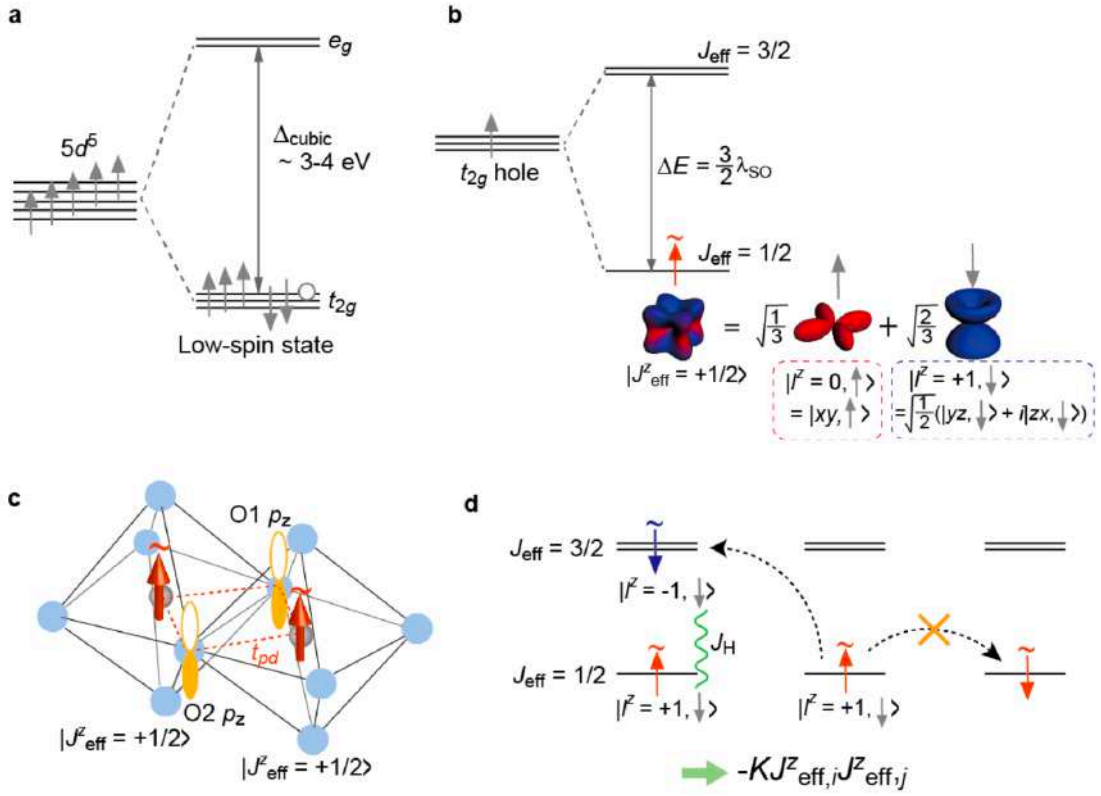

FIGURE 1.6: Figure describing the formation of the effective $J_{eff} = 1/2$ moments essential for Kitaev physics. **a** shows the splitting of the d^5 five fold degenerate orbitals of Ir^{4+}, Ru^{3+} into triply degenerate t_{2g} level and doubly degenerate e_g level due to the cubic crystal field of the octahedra in the low-spin configuration. **b** shows the additional splitting of the t_{2g} orbital with effective $l = 1$ as it is isomorphic to the p orbitals into a Kramer doublet $J_{eff} = 1/2$ and a quartet $J_{eff} = 3/2$ as a result of splitting due to spin orbit coupling. **c** shows the edge sharing geometry that results in a dominant Kitaev interaction mediated via the p orbitals of oxygen and the hopping amplitude is shown by t_{pd}. **d** shows the hopping between the 3/2 and 1/2 neighbouring orbitals followed by a Hund's coupling J_H in real space resulting in an Ising type ferromagnetic Kitaev interaction. Figure reproduced from [214].

1.2.1 Additional interactions and Model

The most general model for the Iridates and Ruthenates $(A_2IrO_3, \alpha - RuCl_3)$ comprise of other exchange interaction terms in addition to the Kitaev interaction. The most generic symmetry allowed Hamiltonian extensively studied in this thesis also known as the $JK\Gamma$ model [94, 41, 180, 236] is,

$$\mathcal{H}_{JK\Gamma} = \sum_{<ij>\in\gamma} J\vec{S}_i \cdot \vec{S}_j - KS_i^\gamma S_j^\gamma + \Gamma[S_i^\alpha S_j^\beta + S_i^\beta S_j^\alpha] \tag{1.6}$$

here $< ij > \in \gamma$ with $\gamma \in \{x, y, z\}$ refer to the three nearest neighbour bonds of every lattice site in each hexagon and α, β, γ are mutually exclusive where α, β refer of the in-plane components and γ refers to the out-of-plane component (perpendicular component) with respect to the Ir-O-Ir plane. In the quantum model the $\vec{S}$ are the $J_{eff} = 1/2$ Kramer doublets but we shall extensively deal with the large-S limit of this Hamiltonian $S \to \infty$ and study the physics at the classical level. We shall over the course of the next few chapters see and understand what our machine (TK-SVM) uncovers as the physics of the above Hamiltonian and later in the last two chapters dwell into the complicated ground state structures as well as the dynamics and currents in this model.

Having declared the model that is investigated in this thesis let us understand how the different terms arise in a realistic material. We already discussed the origin of the Kitaev term. Briefly it originates as a consequence of edge sharing geometry and a combination of super-exchange and Hund's coupling which favours a ferromagnetic parallel alignment of spins. This term is the dominant term and many theoretical methods including those from quantum solid-state chemistry, perturbation theory argue that this term is ferromagnetic in nature $(K > 0)$ [107, 228]. In corner sharing geometries the Heisenberg interaction is the dominant one with $(J < 0)$ favouring a ferromagnetic coupling of spins but in edge sharing the Heisenberg coupling is a sub-dominant term arising from the imperfect destructive interference between the two exchange pathways and originates from a weak $d - d$ hybridization of the two Ir atoms which favours anti-ferromagnetic alignment $(J > 0)$ [180, 99, 70]. The distortion induced lowering of symmetry also could give rise to anisotropic exchanges such as the Dzyaloshinskii-Moriya (DM) interaction [236].

Another significant term is the symmetric off-diagonal Γ [180] interaction which we shall thoroughly examine in the last three chapters of this thesis. In most materials its value is comparable to the Kitaev exchange and leads to some very interesting physics. The origin of this term lies in the combination of the $d - d$ as well as the anion (oxygen) mediated $d - p - d$ exchange.

This is the most widely studied model in Kitaev literature and has been investigated using a host of analytical and numerical techniques. In the JK model with $\Gamma = 0$ [47, 116] four simple magnetic orders are found and in addition the KSL is quite robust to Heisenberg perturbations and extends to a finite window. In the $K\Gamma$ model we get a very rich phase diagram with complicated non-collinear and incommensurate spiral phases.

Experimentally it was found that most of these candidate materials show a magnetic ordering down to low temperatures and in particular zigzag which is one of the phases in the JK model with parameters $J > 0, K < 0$ but other studies have found that these materials have a ferromagnetic K $K > 0$ and therefore one possible resolution is that there are other additional interactions such as Γ' or next-next nearest Heisenberg coupling J_3 which stabilize the zigzag order with a ferromagnetic K. These additional interactions also dramatically change the low energy physics by closing the spin gap or open a spin gap which scales linearly with external field instead of a cubic manner discussed for the pure K model [202].

Having discussed the model in some detail we shall now discuss the candidate materials and the magnetic orderings they enter when we lower the temperature.

1.3 Candidate Kitaev Materials

The list of materials proposed to host Kitaev physics is shown in the table below 1.8. In this section we shall discuss the proposed candidates and their behaviours and experimental results. The most commonly proposed structure is of Iridates with the chemical formula A_2IrO_3 with $A \in \{Na, Li, Cu\}$ [2, 165]. $\alpha - RuCl_3$ [165, 25, 32, 201] is analogous to A_2IrO_3 compounds with the Iridate IrO_6 octahedra replaced with $RuCl_6$ edge-sharing octahedra. $\alpha - Li_2IrO_3$ has an analogous structure to Na_2IrO_3. Other Lithium 2D candidates are synthesised by replacing the inter layer Li ion by another monovalent ion which have the chemical formula $A_3 - LiIrO_6$ with $A \in \{H, Cu, Ag\}$ and these have different stacking pattern from other Lithium 2D candidates. $\beta - Li_2IrO_3$ and $\gamma - Li_2IrO_3$ are 3D analogues of the 2D $\alpha - Li_2IrO_3$ [169, 133]. These 3D structures and be thought of as a stacking of 2D honeycombs. The $\beta - Li_2IrO_3$ structure called the hyper-honeycomb structure has zigzag chains connecting the layers above and below in an alternating fashion about the bridging bond while in $\gamma - Li_2IrO_3$ which has the stripy honeycomb structure stripes of hexagons rotated alternately with respect to the bridging bonds are connected [188] (see the figure 1.7 for a better clarification of the structure). In both these 3D compounds, each Ir ion which participates in the Kitaev physics is chemically and crystallographically equivalent being the center of an oxygen octahedra. This ensures that the local bonds induce Ising type bond frustration and are just a 3D playground for Kitaev physics [148].

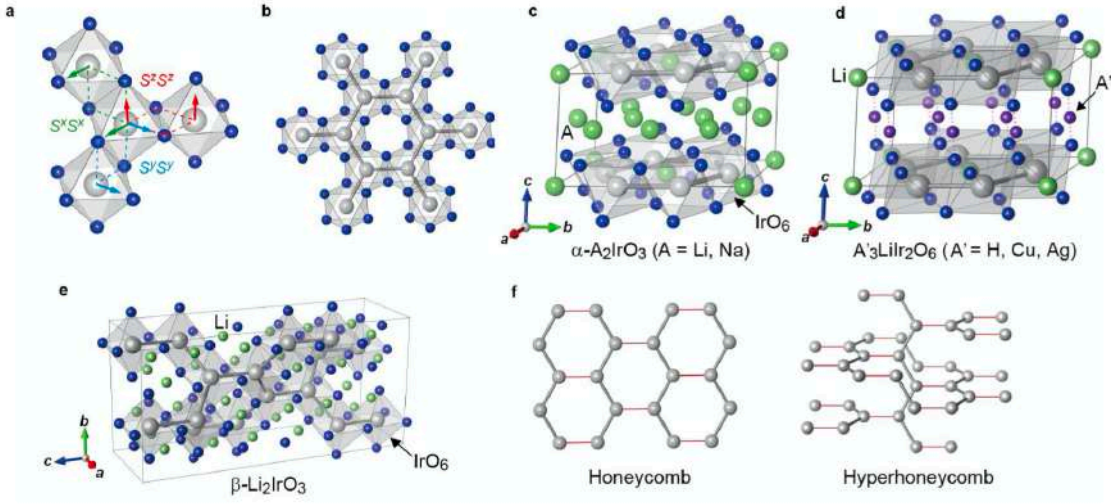

FIGURE 1.7: The structures of different Kitaev candidates are shown above. **a,b** show the general Kitaev interaction and the honeycomb structure of most Kitaev materials that plays a crucial role in realizing Kitaev physics. **c-e** show the crystal structures of the different 2D and 3D materials and **f** shows the relation between the 2D honeycomb and the 3D hyper-honeycomb which are layers of honeycombs attached in an alternating manner along the zigzag chain running along the perpendicular direction. Figures reproduced from [208]

In reality none of these candidates have the perfect geometry to host Kitaev physics and the edge-sharing octahedra are imperfect with small non-cubic distortions that increase or decrease the Ir-O-Ir or Cl-Ru-Cl bond from the ideal 90° required for the edge sharing physics resulting in trigonal compressions or expansions [25, 212]. The result of this trigonal distortion is that we don't have a perfect destructive interference between the two channels and not only the magnitude of Kitaev interaction decreases but also the magnitude of Heisenberg and other non-Kitaev interactions increases. In layered compounds the 2D honeycomb layers are imperfectly stacked resulting in stacking faults evidenced by the broadened X-ray diffraction peaks. $\alpha - RuCl_3$ also suffers from low temperature magnetic ordering and further this was shown to depend on the nature of the sample preparation [32].

Na_2IrO_3 is the most easy to synthesis as single crystals can be grown using the flux method [200]. But single crystals of $\alpha - Li_2IrO_3$ are harder to grow since other polymorphs exist but can be grown by vapour transport method [188, 155]. There are many methods to get single crystals of $\alpha - RuCl_3$ such as Bridgman technique [228], vacuum sublimation [187] or vapour transport method [49] but the ordering and physics seems to be heavily dependent on the technique of growing these single crystals. For $A_3 - LiIrO_6$ candidates only polycrystalline powder is possible which is prepared by soaking $\alpha - Li_2IrO_3$ in molten salt solution containing A ions.

1.3.1 Behaviour of Kitaev Candidates

We shall here discuss the experimental results of various properties such as magnetism and electronic properties. Since this is a brief review we encourage the interested reader to look into various references and the ever growing arxiv list of Kitaev candidates and materials that promise to host spin liquids.

Electronic properties

The Kitaev candidates discussed here are all Mott insulators with $J_{eff} = 1/2$ localized moments. The charge gap in the optical conductivity spectrum ranges from for $300 - 1000$ Mev in the Kitaev candidates [78]. Na_2IrO_3 has a considerable charge gap consistent with an activation energy of

Materials	Crystal structure (Space group)	T_{mag}	anisotropy	p_{eff} (μ_B)	θ_{CW} (K)	Magnetic ground state
Na_2IrO_3	2D (*C*2/*m*)	15 K	$\chi_c > \chi_{ab}$	1.81 (*ab*) 1.94 (*c*)	-176 (θ_{ab}) -40 (θ_c)	zigzag
α-Li_2IrO_3	2D (*C*2/*m*)	15 K	$\chi_{ab} > \chi_c$	1.50 (*ab*) 1.58 (*c*)	+5 (θ_{ab}), -250 (θ_c)	Spiral
$H_3LiIr_2O_6$	2D (*C*2/*m*)	-	$\chi_{ab} > \chi_c$	1.60	-105	Spin-liquid
Cu_2IrO_3	2D (*C*2/*c*)	2.7 K	Not known	1.93(1)	-110	AF order or Spin-glass
$Cu_3LiIr_2O_6$	2D (*C*2/*c*)	15 K	Not known	2.1(1)	-145	AF order
$Ag_3LiIr_2O_6$	2D (*R*-3*m**)	~12 K	Not known	1.77		AF order
α-$RuCl_3$	2D (*C*2/*m* or $P3_112$,or *R*-3) ; *T* and sample dependent	7 K and/or, 14 K See text	$\chi_{ab} > \chi_c$	2.33 (*ab*), 2.71 (*c*)	+39.6(θ_{ab}), -216.4 (θ_c)	zigzag
β-Li_2IrO_3	3D (*Fddd*)	38 K	$\chi_b > \chi_c > \chi_a$	1.87 (*a*) 1.80 (*b*) 1.97 (*c*)	-90.2 (θ_a) +12.9 (θ_b) +21.6 (θ_c)	Spiral
γ-Li_2IrO_3	3D (*Cccm*)	39.5 K	$\chi_b > \chi_c > \chi_a$	~1.6	+40	Spiral

FIGURE 1.8: Table showing the different Kitaev materials and their physical properties as well as the low temperature magnetic states they order to. Table reproduced from [208]

100 meV at room temperature [200, 210]. Other Iridates have a similar activation energy implying a similar charge gap. The charge gap for $\alpha - RuCl_3$ is relatively large due to the narrow 4d Ru bandwidth originating from the strong ionicity of chloride [16].

The resonant inelastic x-ray scattering (RIXS) spectra at the Ir L3 (2p3/2 $\rightarrow$ 5d) edge for the Iridates reveal the presence of low-energy excitations of $\sim$ 0.7 eV [5, 241] corresponding to the spin orbit coupling excitation energy of $E_{SOC} = 3\lambda_{SOC}/2$ between the Kramer doublets and quartets in the t_{2g} manifold indicating a spin-orbit coupling $\lambda_{SOC} \sim 0.4 - 0.5eV$ which originates from the splitting of the t_{2g} manifold due to the trigonal lattice distortion. The small splitting implies that the $J_{eff} = 1/2$ picture would be valid as a first approximation but the effect of trigonal crystal field may not be negligibly small which then changes the physics and introduced non-Kitaev terms as discussed above. For $\alpha - RuCl_3$ a splitting with $\lambda_{SOC} \sim 0.1eV$ [127] is reported by the INS experiments which is much smaller than the iridates. However, despite the small spin-orbit coupling, the $J_{eff} = 1/2$ picture is thought to be a better approximation than for iridates as the $RuCl_6$ octahedra are less trigonally distorted than the IrO_6 octahedra and hence the Kitaev interaction is

assumed to be the dominant interaction [62].

Magnetism

Magnetic susceptibility $\chi(T)$ for the Kitaev model with isotropic couplings $K_\gamma = K$ indicates an isotropic Curie-Weiss behavior with a Curie constant for $S = 1/2$ and a Curie-Weiss temperature of about $\theta_{CW} = K/4$ at high temperatures. Lowering the temperature below $T \sim K$ results in a deviation from the Curie-Weiss behavior and a cross over to almost T-independent behavior around a characteristic temperature of T_H below which all the spin-spin correlations saturate. Thus each curve has two transition temperatures indicating different behaviours of the candidates in their vicinity [144].

From the linear behavior slope of inverse susceptibility $1/\chi(T)$ at high temperatures we get can conclusively infer that the magnetic moments are localized to $J_{eff} = 1/2$. The effective moments which are determined from the slope of the linear behavior show values consistent and expected for the pure $J_{eff} = 1/2$ state and are further material independent. The sizable field-orientation-dependent anisotropy of $\chi(T)$ suggests the presence of bond-dependent anisotropic magnetic couplings and the trigonal field effect. The energy scales of magnetic interactions are around $100 - 200K$ which show up as deviations from the Curie-Weiss behavior [238]. In most materials the Curie-Weiss temperatures are negative and strongly depend on field orientations ranging from -200 K (antiferromagnetic ordering) to almost zero indicating that Kitaev-type ferromagnetic coupling is not the only important interaction and other antiferromagnetic interactions are present and dominate over the ferromagnetic ones. The almost zero CW temperature is further evidence of a cancellation of antiferromagnetic and ferromagnetic interactions [144]. In conclusion the wide range of CW temperatures indicate the sensitivity of the interactions to the local lattice structure and the details of chemical bonding and are very intricately related to the structure and chemistry of the material.

Long range magnetic ordering

All the candidates discussed above, except for $H_3LiIr_2O_6$, clearly order at low temperatures rather than forming a spin liquid state as evidenced by the kink in $\chi(T)$ susceptibility and an anomaly in specific heat C(T) [200, 32, 49]. The ordering temperature T_{mag} being one order of magnitude lower than the energy scale of magnetic interactions around 100 - 200 K is a sign of magnetic frustration, which is consistent with their possible proximity to the frustrated Kitaev SL. However the observed entropy change around T_{mag} is only $10 - 30\% R \ln 2$ [209] of the full entropy of Kramer doublet.

$Na_2IrO_3, \alpha - RuCl_3$ are shown to form a zigzag order from resonant x-ray diffraction and neutron measurements [195, 101]. $\alpha - Li_2IrO_3$ shows a spiral ordering along the zigzag chains [225]. The three-dimensional honeycomb iridates, order with a complex incommensurate spiral order at a very similar ordering temperature $T_{mag} \sim 38K$ which might be due to the identical local connectivity of the three Ir-bonds [26, 132].

The interesting case is of $\alpha - RuCl_3$ whose ordering is actually dependent on how the sample is grown: crystals with minimal stacking faults generally shows a sharp transition at $T_{mag} \approx 7K$ [32] which corresponds to a zigzag order with a three-layer periodicity. However on the other hand for samples with significant stacking faults, there is an additional broad transition near $14K$ corresponding to a two-layer periodicity of the zigzag structure, and powdered samples only show the broad transition at 14 K. However one cannot rule out the existence of other periodic layerings corresponding to different values of T_{mag} [41, 127].

Long-range magnetic ordering rather than a spin liquid state is a consequence of the presence of additional interactions beyond the Kitaev model. While dominant Kitaev interactions are present in some samples the other types of exchange interactions such as Heisenberg exchange

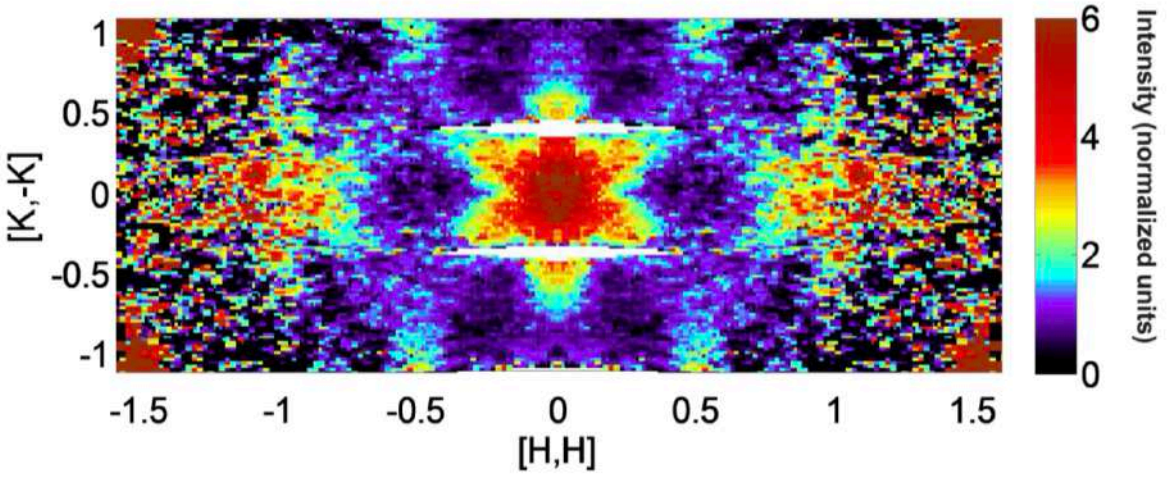

FIGURE 1.9: The INS for $\alpha - RuCl_3$ at $T = 10K$ well above the ordering temperature. The star feature arises from the interplay of spin waves and spin liquid physics which can be explained in the JK model with the proximity of the zigzag and KSL phases. Figure reproduced from [127].

through direct overlap of d-orbitals [180] and off-diagonal exchanges (both symmetric and antisymmetric (DMI)) drive real materials away from the pure Kitaev model regime. Lattice distortions such as the trigonal compression of octahedron perpendicular to the plane may lead to additional exchange paths introducing more non Kitaev terms. Further-neighbor interactions have been shown to be relevant in some compounds.

The Kitaev-Heisenberg (JK) model with additional nearest-neighbor Heisenberg interactions gives a spin liquid in the pure Kitaev limit but in other parameter regimes give the regular magnetic orders such as Néel and stripy [116, 133]. The experimentally observed zigzag and spiral orderings require additional of off-diagonal and further-neighbor interactions to reproduce the zigzag and incommensurate spiral orderings [107, 233].

1.3.2 Possibility of a spin liquid

It is well known that most Kitaev candidates order at low temperatures obfuscating our hunt of the elusive Kitaev spin liquids. There has been a proposal that it is possible to suppress the magnetic ordering by the application of high pressure or a substantial magnetic field [107, 228]. The justification of using external perturbations to tune the magnetic order into a spin liquid state comes from the ab initio and quantum chemistry calculations, for these candidate, which shows a substantial Kitaev interaction term and in most extended models the KSL is quite robust to non Kitaev perturbations extending into a finite region in the JK model as discussed above.

$\alpha - RuCl_3$ is known to form a zigzag-type magnetic ordering for temperatures below the magnetization transition temperature around $T_{mag} \sim 7K$. The cited references found that it was possible to suppress this magnetic order to temperatures as low as $1K$ by applying an in-plane magnetic field with a critical strength of $B_c \sim 7 - 8T$ [196, 12, 70]. It was found that for B values between $7 - 9\ T$ no magnetic ordering appears and a half quantized plateau of transverse Hall conductivity is found. This discovery of unusual excitations and transport properties is what has spurred the physics community to take note of Kitaev materials and the exciting new phases of matter possible. Around the critical field an induced moment of $0.6\mu_B$ [187] indicates that a substantial portion of magnetic entropy is be lifted suggesting the possible existence of spin liquids. In the three-dimensional candidates $\beta, \gamma - Li_2IrO_3$ a similar B-induced suppression of the magnetic order was reported. The magnetic ordering transition was found to disappear by applying a magnetic field along the b-axis, the expected Ising axis of bridging bonds, at a critical field value of around $B_c \sim 3T$ [155, 83] and a reduced magnetic moment suggesting a release of spin entropy of about $0.4\mu_B$ [102, 184].

In the Kitaev candidates $\alpha, \beta - Li_2IrO_3, \alpha - RuCl_3$ under the application of pressure it was found that the zigzag state undergoes a first order transition into a spin singlet dimerized state where a modulation of zigzag chains, i.e. the alternate contraction and extension of Ir-Ir (Ru-Ru) bonds, takes place. The distance of the bonds contracted under pressure is even shorter than that of metallic Ir, which implies the formation of strong Ir_2 dimers rather than a weak spin-Peierls-like transition. Other 3d and 4d transition metal oxides are observed to undergo similar strong dimerization under pressure. In the d5 iridium and ruthenium compounds, the strong dimerization is found to compete with the $J_{eff} = 1/2$ spin-orbital Mott state with isotropic superposition of the three orbital states, as only one of the three are chosen forming the bond that is selected in the dimerized state thus this anisotropy of choice of orbital competes with an isotropic superposition of the orbitals.

Chemical modification which involves replacement of certain ions by others is another approach to control the magnetic interactions. The two-dimensional honeycomb iridates, $A'_3LiIr_2O_6$ $(A' = H, Cu, Ag)$ is the typical playground for such an approach. Recently a QSL ground state was reported in protonated $H_3LiIr_2O_6$ [48, 5]. The honeycomb layers in these chemically modified compounds are more compressed perpendicular to the plane than the other honeycomb iridates and this compression modifies the magnetic interactions appreciably. The absence of magnetic ordering in these compounds is evident in the 7Li- and 1H-NMR spectra which does not show any broadening down to below $1K$ [218]. The Knight shift $K_s(T)$ obtained from the spectra as well as the susceptibility $\xi(T)$ shows a Curie-Weiss behavior with $\theta_{CW} \sim 100K$ at high temperatures analogous to other Iridates. The Knight shift $K_s(T)$ shows a broad peak around 130 K and then saturates to a finite value as the temperature is lowered towards $T = 0$ [117].

Spin defects play a major role in a lot of these measurements and excitation spectra and once these effects are subtracted we still find that the observed values are significantly different from those expected of a “pure" Kitaev spin liquid. These spin defects follow a scaling of B/T in thermodynamic quantities like magnetization or specific heat, while a possible explanation suggested is the formation of random singlets of spin defects embedded in the bulk QSL or from the peculiar band dispersion of Majorana fermions produced by an interlayer coupling, even though no general consensus is reached in the physics community. After subtracting the scaled contribution originating from the defects, it was found that there is only a B-independent T^3 contribution to $C(T)$ below $T = 5K$ [18, 241] most likely originating from the lattice.

The absence of an appreciable magnetic entropy at low temperatures has been thought of as the consequence of a gap in the spin excitations and the observed release of spin entropy behavior is different from that expected for the “pure” Kitaev QSL, which has a specific heat anomaly with entropy of $50\%R \ln 2$ [160] associated with ordering the Z_2 fluxes (localized Majorana fermions). The most common argument explaining the difference is that non Kitaev interactions significantly modifies the nature of the Kitaev spin liquid expected and the positions of chemical elements may play a role in stabilizing the spin liquid state. These claims are yet to be justified and are just theoretical suggestions and to understand the true nature of these purported “spin liquid" states remains a matter of present day research [235, 55].

1.3.3 Fractionalized excitations and half quantized plateaus

Fractionalized excitations as an imprint of the Majorana fermions are a hallmark of spin liquids and to this end the Iridates and Ruthenates are heavily investigated using a variety of spectroscopic techniques including INS, Raman spectroscopy, ESR, NMR and THz spectroscopy [47, 245, 12, 199].

Most of the discussed Kitaev materials, except $H_3LiIr_2O_6$ [120], are found to order magnetically at low temperature, albeit with reduced ordered moments. Magnetically ordered states support conventionally support collective excitations known as the spin wave modes. In collinear magnets without frustrated or competing interactions have well defined magnon peaks with a sharp energy for every momentum. A measurement of single-crystal spin-wave dispersion and

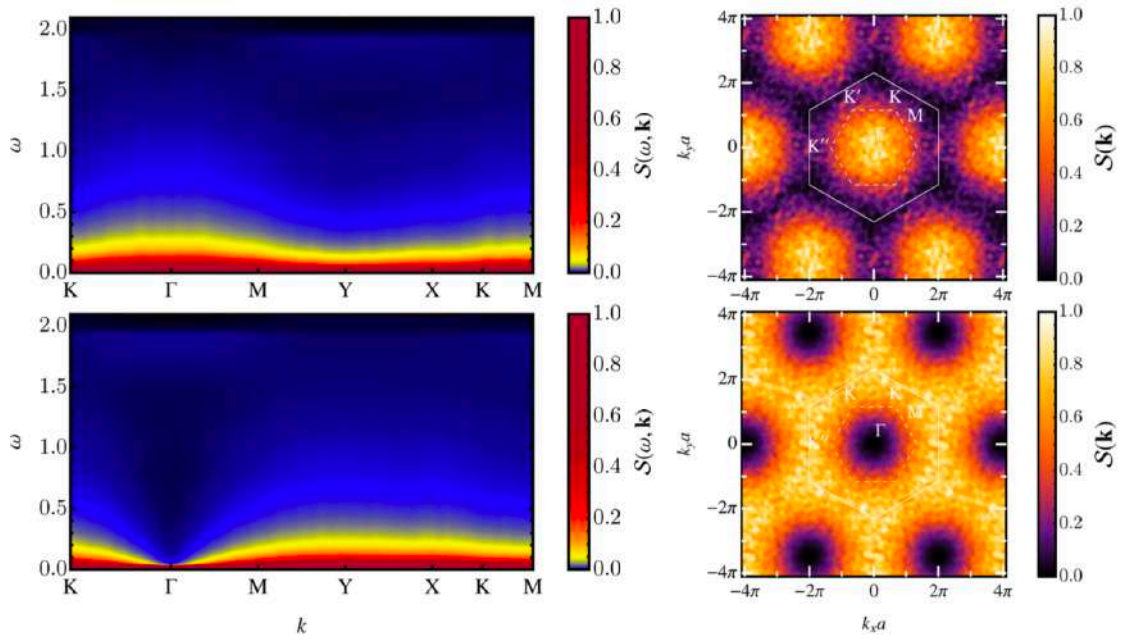

FIGURE 1.10: The dynamic and static structure factors for ferromagnetic (above) and antiferromagnetic (below) KSLs are shown. The prominent features are a continuous band spectrum and most importantly the behaviour at the Γ point that distinguishes the two spin liquids. Figure reproduced from [183]

intensities via inelastic neutron scattering (INS) often enable the direct determination of the effective spin Hamiltonian parameters.

However, the situation in the honeycomb magnets with possible Kitaev interactions is more complicated. The spin-wave spectra for $\alpha - RuCl_3$ [40, 104] is readily calculated theoretically using parameters proposed from experiments. The problem is that, more than one set of parameters that can be fit to reproduce the experimental results which is likely because of strong frustration. For example to describe the zigzag order it is possible to describe it in the JK model or the extended models including the third nearest neighbour coupling or the off-diagonal exchange couplings. The Ir ions are very good neutron absorbers and hence are particularly a challenge for INS which implies that the magnetic form factor appearing in the neutron scattering cross section decays rapidly as the magnitude of the momentum transfer is increased. An additional difficulty in most candidates is that single crystals suitable for INS are not easy to obtain or prepare, forcing measurements to be made using polycrystalline material. Despite these constraints INS measurements on powdered samples provide a valuable source of information. The shape of the scattering threshold alone was sufficient to conclude the magnetic order of Na_2IrO_3 [47] as zigzag and not stripy. In $\alpha - RuCl_3$ powder the shape of the low-energy, low-momentum scattering threshold is well-defined and understood in the confines of spin wave theory but the additional high energy feature which has a temperature dependence is not compatible with simple spin-wave theory [127].

The results of the INS data from single crystals of $\alpha - RuCl_3$ measured using time-of-flight methods are shown below [184, 41]. The responses are measured at Γ point (zone-center) at temperatures above and below the magnetic ordering temperature of $T_{mag} = 7K$. In the magnetically ordered zigzag state the response shows two sharp peaks superposed on a broad continuum that continues to high energies. This disordered state above T_{mag} just shows a single broad continuum which leads to the understanding that the sharp peaks can be explained in the purview of spin wave theory in the ordered state. In addition this continuum of intensities is temperature independent and observed up to well over 100 K. The dispersion plot showing the relation between energy and momentum for the sample at $T = 2K$ shows the spin waves have low-energy features with minima at the Γ point (0,0,0) as well as at the wavevectors $\vec{q} = (\pm 1/2, 0, 0)$. This ordering at

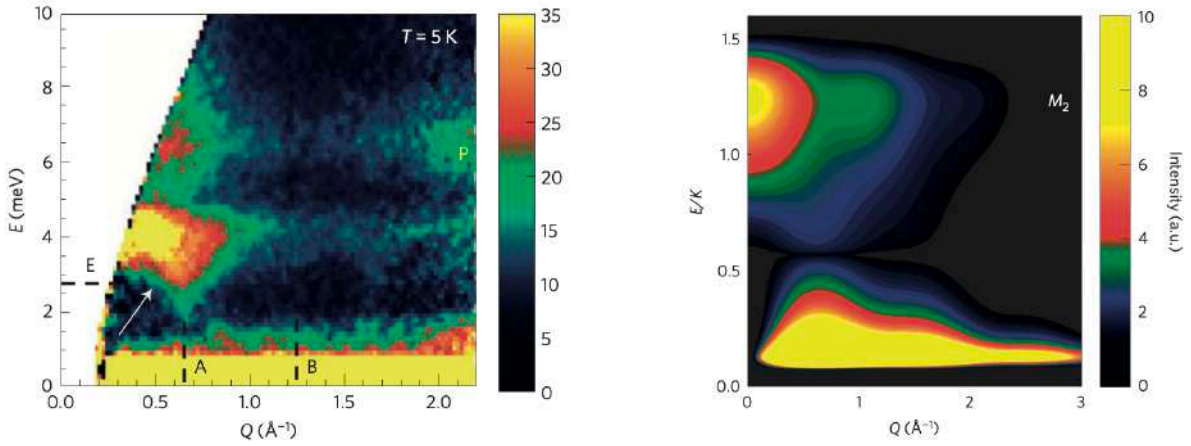

FIGURE 1.11: The INS plot below the ordering temperature for $\alpha - RuCl_3$ shows a low energy band corresponding to the zigzag order followed by a broad high energy non-dispersive band corresponding to a spin liquid. The dispersion and the strength of the peaks lets one infer on the allowed parameters in the Hamiltonian. The right plot is just the numerical simulation of the experimental result and shows the same two band feature. Figures reproduced from [208].

the M points of the first Brillouin zone show at we indeed have a zigzag magnetic ordering and an additional feature is the extended broad continuum at the Γ point. The spin wave spectrum is gapped in the ordered state which might either be a consequence of anisotropic exchange coupling or additional interactions. As discussed above it is possible to suppress the zigzag order by applying an external magnetic field of magnitude $B_c \sim 7.5T$ along the in-plane [110] direction. The resulting disordered state shows no signatures of spin waves as theses are strongly suppressed indicating the absence of any magnetic orders and the continuum gains intensity at low energies. Although the energy gap at the Γ point softens as B_c is approached, it appears that the continuum scattering is gapped above Bc.

This situation of sharp spin-waves coexisting in a broad continuum in the ordered state is reminiscent of weakly coupled $S = 1/2$ Heisenberg antiferromagnets [194] in one dimension. Spinons which are the fractionalized excitations lead to the continuum of the spectrum. At low temperatures the spin wave spectrum at low energies due to the order in the spin chains are found to coexist with the higher energy spinon spectrum while at temperatures above the transition temperature the spin-waves disappear leaving behind only the spinon scattering and this coexistence of spin waves and spinon continuum are readily verified in $KCuF_3$ [126].

In a pure Kitaev magnet the response function shows a sharp peak at low energies corresponding to the static Z_2 gauge flux but a broad continuum at high energies corresponding to the itinerant Majoranas hopping around. Additional perturbations serve to broaden the sharp peaks at low energies. $\alpha - RuCl_3$ forms a regular magnetic structure and hence the low energy spectrum is well defined and completely understood by the propagation of spin waves but the observed high energy spectrum is comparable to the response functions for a pure or perturbed Kitaev model, and it is found that the overall extent and form of the scattering is consistent with the expectations of a system close to a spin liquid. In addition the temperature dependence of the continuum scattering is consistent with expectations for Majorana fermions in the Kitaev QSL. The underlying physics and the Hamiltonian describing $\alpha - RuCl_3$ are far from resolved and there has been a lot of debate and discussions in the community regarding this. Finite size exact diagonalization (ED) suggest that the response functions have broad intensity distributions prompting some to suggest that the scattering is better described by unstable magnons. There is also a debate on the sign of the Kitaev coupling since the response functions for the two different signs are quite indistinguishable. Despite the debates and disagreements there is strong evidence suggesting that the continuum scattering seen in INS is a signature of fractional magnetic excitations.

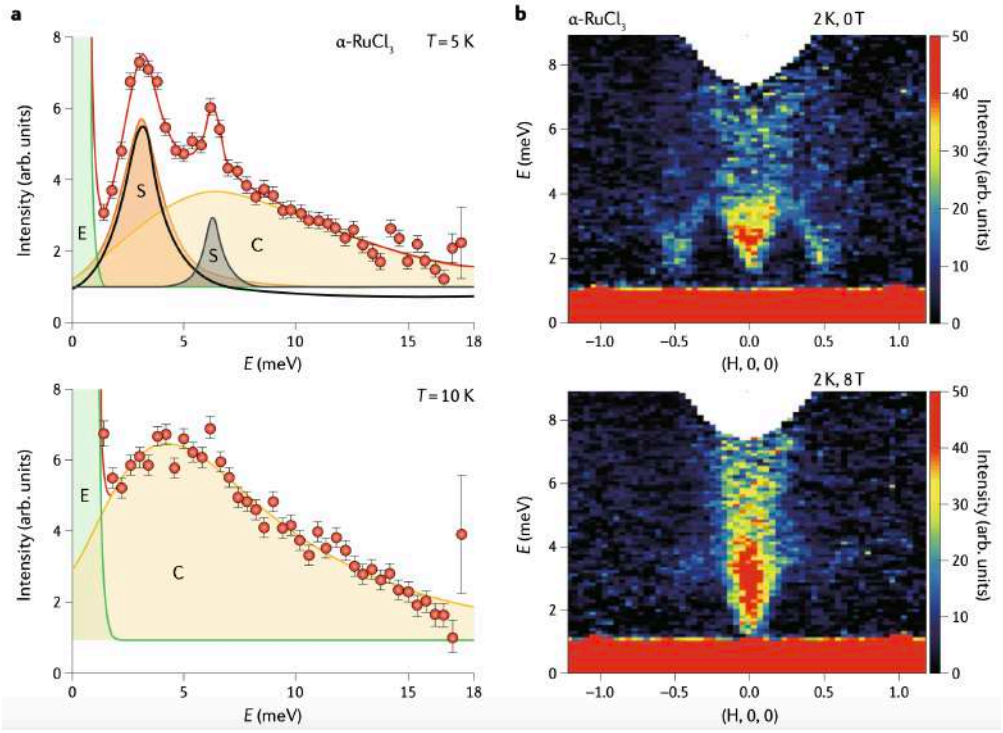

FIGURE 1.12: **a** INS plots shown for $\alpha - RuCl_3$ below $(T = 5K)$ and above $(T = 10K)$ the ordering temperature $T_N = 7K$ around the Γ point at the zone center and shows the different contributions designated as E - elastic, S - spin waves and C - continuum. At low T there are two distinct peaks showing a well defined magnon spectrum corresponding to the zigzag order while at high T there is a continuum corresponding to a potential spin liquid phase where the magnetic order is controlled using temperature. **b** INS plots shown at the same temperature $T = 2K$ but different magnetic fields. The upper plot has the well defined magnon dispersion corresponding to the zigzag order while the lower plot just shows a continuum at the Γ point corresponding to a spin liquid phase (possibly) where the magnetic order is suppressed using an in plane magnetic field. Figures reproduced from [16].

THz (Tetra Hertz) spectroscopy provides a high-resolution measurement of the response function at zero momentum $(Q = 0)$, nicely complementing INS measurements which gives us crucial information about the full Hamiltonian describing $\alpha - RuCl3$ [201, 144, 127]. Although since the weak inter-planar interactions are apparently antiferromagnetic, in the ordered state the lowest gapped excitations at $Q = 0$ may not represent the minimum spin gap associated with the 2D Γ point [228]. The THZ spectra shows sharp spin-wave peaks co-existing with a broad continuum at low fields and the vanishing of the spin-waves above Bc leaving behind just a broad continuum suggests the consistency with the INS measurements. In addition it was also observed that a gapped mode at high fields appears with energy increasing linearly with B which is consistent with a Hamiltonian including non Kitaev terms in a magnetic field. NMR measurements have led to more debate when measuring the field induced spin gap with one group finding gapless excitations, while another group finding the gap growing as B^3 at high fields [184]. The latter has been suggested as the evidence for existence of Majorana fermion. The Raman scattering which involves the interactions between a pair of Majorana fermions shows a continuum resembling the expected scattering for the pure Kitaev model providing further evidence of fractionalied spin excitations.

Half quantized Plateaus

Another signature of fractionalization is in the half quantized thermal transport which is expected since the Majorana fermions carry only half the degrees of freedom of a full/canonical fermion.

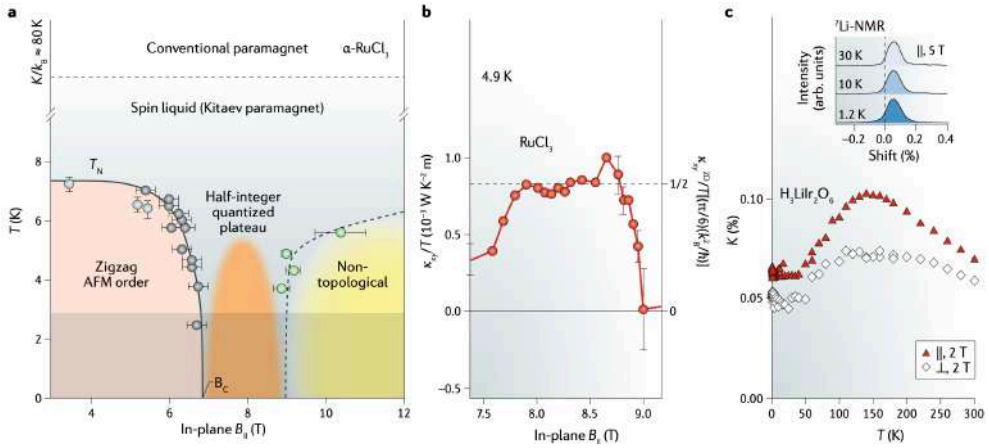

FIGURE 1.13: **a** The phase diagram of $\alpha - RuCl_3$ as a function of temperature and in-plane magnetic field. At about $B_c \sim 7T$ the zigzag magnetic order is suppressed leading to a topological phase with half quantized thermal Hall plateau. **b** The half quantized thermal Hall plateau reported in [103] where the dotted line indicates a half-quantization of $\kappa_{xy}/T = 1/2(\pi/6)(k_B^2/h)$. **c** Temperature dependent Knight shift $K_S(T)$ for in-plane , out-of-plane magnetic fields for $H_3LiIr_2O_6$. There is no broadening down to low temperatures followed by a saturation to a constant value. Figure reproduced from [102].

Kashara et al reported a thermal Hall half quantized value of $\kappa_{xy}/T = 1/2(\pi/6)(k_B^2/h)$ for single crystals of $\alpha - RuCl_3$ in a magnetic field close to the critical in-plane value ($B^{\parallel} \approx B_c$) . In addition earlier studies by the same group found an unusually large thermal Hall effect when the magnetic field was perpendicular ($B^{\perp}$) to the plane above the transition temperature T_N. This was suggested to be a possible signature of half-quantized thermal Hall effect, masked by the long-range ordering below T_N. The long range order can be suppressed by superposing an in plane field $B^{\parallel}$ with the perpendicular field $B^{\perp}$ by titling the field away from the perpendicular direction. The thermal hall conductivity κ_{xy}/T showed a half quantized plateau as a function of the applied (tilted) field and value of the conductivity in the plateau region was independent of the tilting angle as expected implying that the observations concur with the fractionalization of charge. The in-plane component of magnetic field $B^{\parallel} \geq B_c$ in the plateau region suggesting that this phenomenon of half quantization is linked with a phase that results from suppression of the long-range magnetic ordering. However, unfortunately this result has not be reproduced by other groups and has been since contested strongly as a valid claim. However there is still ongoing research both in the theoretical and experimental front to understand this novel state of matter and the exotic physics they promise to host.

1.3.4 Classical spin liquids

The hallmark of classical spin liquids (CSLs) is the absence of long range magnetic order which implies that the low temperature spin-spin correlator decays in an *algebraic or exponential* fashion and a large (extensive) ground state degeneracy which grows exponentially with the system size. It is this precise fluctuations between the different possible ground states that prevents the system from breaking symmetry and finding an unique ground state. In general CSLs are unstable to perturbations at low temperatures lifting the degeneracy upon addition of perturbing terms however owing to their large entropy at low energies they still dominate the finite T phase diagram and are extremely relevant for real frustrated systems. They are usually thought of as intermediate temperature states of a QSL where quantum fluctuations can induce dynamics between the different classical states. QSLs on the other hand have a smaller ground state degeneracy which can be thought of as the entanglement of classical ground states and in addition they have various exotic properties like fractionalized charges and long range entanglement describing their physics.

Many examples of CSLs exist of which the most familiar are the Heisenberg antiferromagnet on the pyrochlore permitting a $U(1)$ gauge description at low temperatures as well as on other geometrically frustrated lattices such as honeycomb and kagome being described by the same low energy $U(1)$ gauge theory.

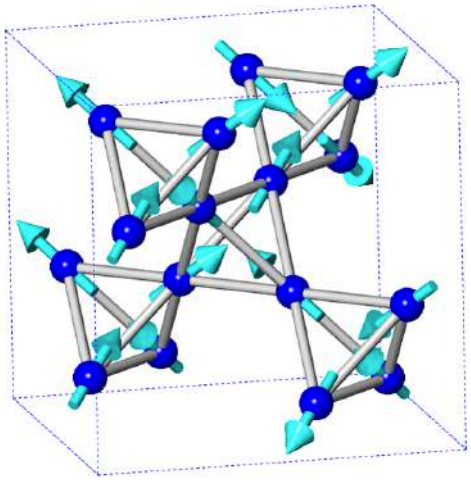

FIGURE 1.14: The structure of spin ice in the two-in-two-out configuration at each tetrahedron resulting in extensive degeneracy in the ground state and thus forming a classical spin liquid. Figure reproduced from [154].

The antiferromagnetic Heisenberg model on pyrochlore is well known *spin-ice* due to its resemblance to the physics of water ice where the tetrahedra [23] share a corner and the strong crystal field anisotropy imparts an Ising type magnetic interaction between the different spin moments. The ground state configuration is the famous "two-in-two-out" where two spins point inwards and the remaining two outwards in each tetrahedron. The residual entropy of this grounds state is extremely large and goes like $S/n \sim R\ln(3/2)$ [167]. The spin-ice rule can be summarized as a general Gauss law $\nabla \cdot \vec{B} = 0$ [38] where the spin at each site is associated with the magnetic field at that site $\vec{B}_i = \vec{S}_i$ thus permitting a $U(1)$ gauge description in analogy with classical electromagnetism. Also this analogy further implies that the correlator decays in an algebraic fashion between the spins $\langle S(0)S(r)\rangle \sim 1/r^3$ [81] in accordance with the dipolar decay form in electromagnetism. The "violation" of the Gauss law leads to the creation of a pair of magnetic monopoles with a Dirac string between them and these constitute the fractionalized excitations with energy half of that associated with a spin flip thus completing the analogy with $U(1)$ electromagnetism.

This is a recurrent theme in most of the CSLs of having an extensive ground state degeneracy due to a constraint equation which can be interpreted as a Gauss law leading to its low energy description with a gauge theory complete with fractionalized excitations. CSLs are interesting in their own right as they provide the gateway for some very interesting physics and give us a better grip on understanding QSLs. However despite all their glory they are not the main focus of this thesis but rather the magnetically ordered states in highly frustrated regimes.

1.4 Machine Learning

Almost every third news article today includes the words machine learning (ML) or artificial intelligence (AI) in some form or the other and has spewed a range of opinions from the conspiracy theorists to the experts predicting the future of humanity, especially with the popularity of chat GPT4 [64]. To give even a review of the history and development and the current state of ML is next to impossible and would require a thesis in itself but we shall stay humble here and briefly brush over the many topics of ML and refer the interested reader to a wealth of resources to deep dive into each topic. Machine learning has existed in one form or the other and has become so

ubiquitous in our lives that we barely think about them anymore from self driving cars to text prediction to chess games to email spam filters to name a few.

In the simplest terms machine learning is the " The ability of the machine to learn without being explicitly programmed ". Any ML program takes a set of inputs $(\vec{X})$ and corresponding outputs (y) and figures out the set of rules relating them i.e. tries to find a hypothesis function $\tilde{f}$ such that $\tilde{f}(\vec{X}) \approx y$ approximating the true function f , $f(\vec{X}) = y$.

Classical ML is usually broadly classified into deep and shallow algorithms where the classification is done based on the depth of the circuit. Deep algorithms such as convolutional neural networks (CNNs) [242] have multiple layers and the algorithms can run deep with many intermediate(hidden) layers whereas algorithms such as support vector machines (SVMs) [50] or logisitic/linear regressions have just a few layers. The other broad classification is how the algorithm uses data to make predictions and are classified as supervised, unsupervised and reinforcement learning respectively.

In *supervised learning* the algorithm is provided with labelled output data which might be discrete (classification problem) or continuous (regression problem where the goal is to find a decision/separating boundary) and the goal is to predict the label for unseen data.

In *unsupervised learning* the algorithm is provided with unlabelled data and the aim is to find structures or correlations between the data sets and group them together. The advantage of this method which is also exploited in the course of this thesis is that the user does not need to have any prior information about the structure of the data but at the same time interpreting the results is a challenge and requires experience of the researcher/domain expert.

In *reinforcement learning* which is the most commonly used strategy in evolution or extinction situations such as self driving cars or chess/video game or GPT the algorithms are trained using "survival of the fittest" strategy. The algorithm tries to optimize the set of actions it needs to take in order to achieve a reward (such as winning the game) and it keeps on trying different strategies (set of actions) till the best one (the fittest) is found.

There exist other algorithms which are a combination of the broad ones stated above. While machine learning has certainly proved more than useful in a multitude of tasks there do remain drawbacks as requiring lots of data to make conclusions as well as being very expensive to run and which algorithm is appropriate for the particular data set depends more on the expertise of the data scientist. If the data set has certain errors the algorithm would be biased and lead to inaccurate models which cause more harm than good in making decisions based on these models. Also it is next to impossible to understand the workings of many deep algorithms and make sense of the recommendations or predictions which makes it harder to check for biases or errors and fine tune the algorithms.

The most common observed trend in AI in general is that there is a breakthrough that causes a lot of buzz and media hype and inflated expectations and when not met there is a reality check and causes disillusionment amongst people and funding agencies and this pattern repeats over. In the future there need to be more ethical questions regarding machine intelligence that need to be addressed such as how much video surveillance or categorization of people based on the choices they make is acceptable. There are undoubtedly many areas where machines would play a crucial role in the future but it is left to us to thread these paths carefully.

1.4.1 Applications to Physics

Machine learning in physics has an entire Wikipedia page dedicated to it. ML these days is becoming an indispensable tool in different branches of physics ranging from astrophysics to quantum information theory [35, 151]. They have proved a useful tool in quantum state tomography which involves the reconstruction of a quantum state from measurements and learning Hamiltonians from phases of matter and phase transitions [138, 141].

In cosmology [56, 124] one of the main tools to study physical phenomena at the galactic scale is through simulations which requires preparing large data sets and also clustering and finding patterns or rather anomalies in data which prove essential to the detection of galaxies/ supernova.

Neural networks or boosted decision trees have proved crucial in N-body simulations simulating the interactions of millions of particles at low temperatures forming clusters. In particle physics outlier events such as *particle selection* is the prime focus and this is just a regression problem in the language of ML.

The application of ML to condensed matter physics began with the seminal work of Carleo and Troyer [34] where they showed a proof of concept by using artificial neural networks to find the ground states in prototypical interacting spin models in one and two dimensions. This initiated a wider adoption of ML in condensed matter physics from detecting phases and phase transitions to solving for the ground state quantum wave functions [34, 37, 54, 82, 168, 220] as well as analysing experiments [163, 243, 28] and designing algorithms [138, 141]. Interpreting ML results has always been a major drawback of the application of ML where we are not just interested in a classification but also wish to understand why the machine "thinks/learns" in that particular way which is much harder to decipher. There is always a trade-off in any algorithm between expressibility and interpretability where the former refers to the applicability to a wider variety of problems of varying dimensionality and linearity while the latter refers to the interpretation of the results (why the machine thinks that way). The algorithm used is generally problem specific and there is a huge promise and effort in the physics community in general, to integrate machine learning as an essential tool to understand these complex systems better.

1.5 Motivation of this thesis

The major focus of this thesis is the understanding Kitaev physics in the classical limit employing machine learning as a tool to investigate and explore the parameter space of extended Kitaev models. We shall focus on the parameter regimes which are relevant for the Kitaev candidates and in particular $\alpha - RuCl_3$ and discuss the possible phases we find as well as they underlying structures and dynamics of incommensurate spiral ground states which has experimental relevance. The main focus of this thesis is on exploring magnetic orders as well as incommensurate spirals as opposed to classical spin liquids.

Even though the original Kitaev model is a quantum model dealing with $S = 1/2$ spins on a honeycomb lattice we see that we are able to uncover many features of this quantum model even at the classical level which can be thought of as the large-S limit of the theory and can make a clear distinction between the "quantumness" and classical nature of the results. We demonstrate the usefulness of our machine in detecting and categorizing all the phases correctly in the frustrated parameter regime without any prior knowledge of the underlying physics and then interpret the machine learnt results. This is sufficient encouragement for future works on frustrated magnetism and uncovering new physics combining usefulness of machines as well as insights we derived in this thesis.

Chapter 2

Methods

In this chapter we introduce the reader to the major concepts and methodologies used in this thesis. We shall begin with a brief introduction to Monte Carlo methods followed by machine learning methods, though by no means exhaustive we shall dwell on TK-SVM which is the main algorithm used in the rest of this thesis and subsequently spin dynamics and transport which serves to bridge the gap between theory and experiment.

2.1 Classical Monte Carlo

We shall begin by introducing the classical Monte Carlo (MC) methods [22, 129], with particular focus on the methods used for sampling spin configurations (thermal ensembles) in thermal equilibrium which are then used to train the Machine, discussed in the subsequent sections.

Monte Carlo methods rely on using randomness to solve problems even when they are deterministic in nature, when analytical or other approaches are difficult to use. Monte Carlo sampling is applicable in any system which has a probabilistic interpretation.

The law of large numbers ***(LLN)*** *states that the expectation value of a large number of trials would converge to the "true" expected value and this convergence gets better by increasing the number of trials.*

As a direct consequence of LLN [153], any integral which can be represented as an expectation value can be approximated by taking an average over independent samples of the random variable. Hence this *finite and sparse* sampling plays a crucial role in overcoming the **curse of dimensionality** where the dimensions of the configuration space grow exponentially with the size of the system. For any finite subset of the total configuration space $\mathcal{J} \subset \mathcal{I}$, we can approximate the true expectation by a MC estimate

$$\langle A \rangle = \sum_{i \in \mathcal{I}} P(x_i) A(x_i) \approx \frac{1}{N_{MC}} \sum_{j \in \mathcal{J}} A(x_j) := \langle A \rangle_{MC} \tag{2.1}$$

the samples x_j used in the MC sampling , in general can be drawn from any underlying probability distribution, it could be uniform, Gaussian or any other distribution. In our case, since we wish to sample spins at thermal equilibrium we sample the configurations x_j according to the canonical distribution function,

$$x_j \sim P(x) = e^{-\beta E(x)}/Z \qquad Z = \sum_{x \in \mathcal{I}} e^{-\beta E(x)} \tag{2.2}$$

here $\beta = 1/T$ [29] is the inverse temperature of the thermal equilibrium. This allows for a better approximation of the true expectation value as the configurations more likely to be visited by the system during its time evolution are sampled, since most of the relevant configurations are sampled this is known as **importance sampling**. The error of the approximation vanishes as $1/\sqrt{N}$ independent of the dimension of configuration space, which is one of an inherent feature of MC sampling.

2.1.1 Sampling Procedure

We explain, in this section, why the approximation of drawing configurations from a canonical distribution makes sense. For any system in thermal equilibrium with its heat bath, the probability that the system is in a particular state **x** is given as a function of the state energy $E(\mathbf{x})$ and temperature as

$$p(\mathbf{x}) = \exp(-E(\mathbf{x})/T)/\sum_{\mathbf{x}} \exp(-E(\mathbf{x})/T) := \exp(-E(\mathbf{x})/T)/Z \tag{2.3}$$

This distribution maximizes the entropy function $S = -\sum_x p(x)\log p(x)$ subject to the normalization condition $\sum_x p(x) = 1$ and the mean value of energy is given by $E = \sum_x p(x)E(x)$.

The thermal average for any observable as a function of the states in the canonical distribution would be

$$\langle O \rangle = \frac{1}{Z}\sum_x \exp(-E(\mathbf{x})/T)O(x) \tag{2.4}$$

With no prior knowledge about the distribution of samples we compute the average as

$$\langle O \rangle = \frac{1}{N}\sum_{i=1}^{n} O(x_i) \tag{2.5}$$

The problem with random sampling (simple sampling) is that we sample a lot of configurations that lie outside the *importance area* of the configuration space i.e. the configurations that have the highest probability of being visited by the system at any given temperature, this under represents the information about distribution of configurations. Hence to circumvent this problem we sample from an associated probability distribution, which is known as **importance sampling** , $P(x)$ and the above equation can be rewritten as

$$\langle O \rangle = \frac{\sum_x \exp(-E(\mathbf{x})/T)/P(x)O(x)}{\sum_x \exp(-E(\mathbf{x})/T)/P(x)} \tag{2.6}$$

Now choosing $P(x) = \exp(-E(\mathbf{x})/T)$, the above equation reduces to a simple average. In conclusion, by sampling from a Boltzmann distribution for the expectation value of any observable we are justified in using a simple average of the observable at these points.

2.1.2 Markov Chains

Having justified in the previous section why importance sampling is needed, the natural question is how does one generate these configurations.

Generating these configurations from scratch is highly computationally inefficient, instead we employ a stochastic method, where we evolve the system through a series of steps $x_0 \rightarrow x_1 \rightarrow x_2 ....x_t \rightarrow x_{t+1} \rightarrow ...x_N$ and the transition to configuration from to to time t+1 depends on the probability P $P(x_0, x_1 ...x_t \rightarrow x_{t+1})$ which guarantees that we sample according to our desired importance distribution. In principle this probability depends on the history of evolution till t . In the simplest non-trivial case , the transition probability is path independent and depends only the current state i.e. $P(x_t \rightarrow x_{t+1})$, and such a stochastic process is known as a **Markov chain Process** [149] and its application to Monte Carlo sampling is known as Markov chain Monte Carlo (MCMC).

The requirement of having a stationary thermal distribution i.e. the importance probability distribution is time independent imposes on the transition probabilities a detailed balance equation (though it is only a sufficient condition)

$$P(x_i)P(x_i \rightarrow x_j) = P(x_j)P(x_j \rightarrow x_i) \quad \forall i \neq j \tag{2.7}$$

Since the stationary probability density is Boltzmann we compute the ratio of the transition probabilities in terms of energy differences

$$\frac{P(x_i \to x_j)}{P(x_j \to x_i)} = \frac{P(x_j)}{P(x_i)} = \exp\left(-(E_j - E_i)/T\right) = \exp\left(-\triangle E/T\right) \tag{2.8}$$

Additionally, we require that the update scheme be **ergodic** i.e. we could access all possible configurations in the allowed configuration space in a finite number of MC steps. We define a Markov chain as ergodic if ,

For all pairs of states (i, j) *in a Markov chain, there exists* $T \in \mathbb{N}$, *such that* $t = 0$ *the system started in state i, the probability of being in state j is always greater than 0,* $P(j) > 0$ *for all* $t > T$. The two technical requirements for the ergodicity of the Markov chain are of 1. **irreducibility** which means there is a sequence of transitions with non-zero probability from one state to another and 2. **aperiodicity** which ensures we don't get trapped in a cyclical transition between states.

We could recast the detailed balance equation [30] as a matrix equation and define a matrix T of transition probabilities $T_{ij} = P(x_i \to x_j) \geq 0$. Since all the entries are non-negative we could use the *Perron-Frobenius theorem* which states that T has a unique largest eigenvalue and the corresponding eigenvector can be chosen to have strictly positive components i.e $P(x) > 0 \ \forall x$). This ensures that we also have a (fixed-point) equilibrium thermal distribution. Since T is a matrix of transition probabilities , it has a maximal eigenvalue of 1 and all other eigenvalues , have an absolute value which is lesser than this maximal value. This ensures convergence starting from any initial configuration.

The second largest absolute eigenvalue determines the characteristic time of thermalization **(thermalization time)** though this is hard to access/determine in practice and one just waits for a sufficiently long time for the system to thermalize before beginning to collect snapshots of spin configurations. In addition, since the updates are only local, the updated configurations after thermalization are not entirely decorrelated from the preceding ones. The autocorrelations between successive configurations decays exponentially in a characteristic time scale known as the "autocorrelation time". In practice , one waits for a sufficient number of MC steps before measuring or collecting spin configurations for thermal averaging which is defined as the **(measuring time)**. The longer the thermalization time the lower the error on the averages of measurements and as a rule of thumb the thermalization times is orders of magnitude larger than the autocorrelation time.

2.1.3 Spin Updates

In the MC algorithm, on a lattice of N spins a single spin is chosen at random and updated. This update from $S_i \to S_i'$ might involve flipping the spins as in the case of Ising spins or rotating the spin around an effective magnetic field or any other update method. Each MC step comprises on N single spin updates such that on average, per MC step the spins are updated at least once. Single spin updates, even though are quite inefficient computationally as they involve local updates which lead to large thermalization and auto-correlation times are the only update method applicable in a majority of frustrated or disordered systems under consideration. A single spin update is also referred to as a sweep.

We shall discuss two such methods below, the Metropolis-Hastings algorithm and the Heat bath algorithm.

Metropolis-Hastings Algorithm

In this section we discuss the general Metropolis-Hastings algorithm [152]. The Markov chain can be engineered using this scheme , which decides if a particular configuration is accepted or rejected [230]. We propose an update from $x_i \to x_f$ and in general accept this proposed update only if it is "thermally" acceptable i.e. at the given temperature , the system can access these energy states. This algorithm is designed for importance sampling (sampling from a Boltzmann

distribution) and is essential in calculating thermal averages or sampling configurations. Main steps of the algorithm are illustrated below,

Algorithm 1 Metropolis Hastings Algorithm

For $i = 1...N$ repeat N times
Randomly Initialize State x_i
Compute energy $E_i = E(x_i)$
Randomly perturb the state (flip/ rotate spin) to create new state x_f
Compute $\triangle E = E_f - E_i$
if $\triangle E < 0$ **then**
    Accept x_f
else if $\triangle E \geq 0$ **then**
    Choose a random number $r \in rand(0, 1)$
    if $r < \exp(-\triangle E/T)$ **then**
        Accept x_f
    else
        Reject x_f

The above steps are repeated N times (each MC update comprises of N single updates) in order to find configurations at equilibrium before we measure physical observables and finally take thermal averages to get the expectation values [53].

In case of classical spin systems $S \in SO(3) = (\sin\theta\cos\phi, \sin\theta\sin\phi, \cos\theta)$ we could propose an update to any random point on the $O(3)$ sphere (θ, ϕ). For most spin interaction Hamiltonians which can be written as $\mathcal{H} = \sum_i \vec{S}_i \cdot \vec{B}_i$ where $\vec{B}_i$ is the effective magnetic field, the difference in energies is given by $\triangle E = (\vec{S'}_i - \vec{S}_i) \cdot \vec{B}_i$. At low temperatures a random spin update has a low chance of being accepted and in order to ensure acceptance we could propose a spin update to a cone around the original spin of aperture 2θ. This captures the low temperature classically ordered ground states well but would not be very useful in capturing frustrated or disordered ground states.

Heat Bath algorithm

The Metropolis algorithm has update acceptance based on the energy difference between the current and proposed spin configurations. This method of sampling has been shown to significantly reduce acceptance rate in simulations dealing with disordered or frustrated systems. An alternate solution that has been shown to perform better is the heat bath algorithm where the transition probability is proportional to the normalized probability of the updated state

$$P(x_i \to x_j) = \frac{P(x_j)}{\sum_k P(x_k)} \qquad \sum_k P(x_i \to x_k) = 1 \tag{2.9}$$

where we sum over all possible allowed updated configurations x_k. For systems with discrete possible updates the heat bath algorithm [51] can be implemented efficiently but for systems with continuous degrees of freedom, it is not in general possible to formulate a heat bath update. Although in certain special cases it is possible and fortunately in our case of frustrated Heisenberg interactions, we can formulate such an algorithm [232].

The general idea is that we propose a local spin update, where the new spin direction is drawn from a suitable probability distribution ensuring the updated configuration is from a canonical ensemble , i.e. is an allowed configuration in the Boltzmann distribution. The new update is determined by testing all possible allowed states in the "heat bath" of its neighbours which are fixed. All terms not involving the spin $\vec{S}_i$ at site i cancel and hence only a small number of computations involving the spin and its neighbours are required for the computation making the algorithm efficient.

In a system with n discrete energy levels $(E_1..E_n)$ the probability of being in a particular energy level k is given by the Boltzmann weight

$$P_k = \frac{e^{-E_k/T}}{\sum_i e^{-E_i/T}} \tag{2.10}$$

We could alternatively state that the system is in the energy level m , if for any random number R in the range 0 to 1 , $0 < R < 1$ we have

$$\sum_{i=1}^{m-1} P_i < R < \sum_{i=1}^{m} P_i \tag{2.11}$$

when the distribution of energy levels is continuous the above equation modifies to $R = \int_1^m diP_i := F(m)$ and the state m is given by the inverse function $m = F^{-1}(R)$.

For the Heisenberg spin model where $\mathcal{H} = -J\sum_{i,j\in N(i)} \vec{S}_i \cdot \vec{S}_j$ where $N(i)$ constitute all the nearest neighbours of spin at site i we can define a local "heat-bath" or effective magnetic field as $\vec{B}_i = J\sum_{j\in N(i)} \vec{S}_j$ and the local Hamiltonian becomes $h_i = \vec{S}_i \cdot \vec{B}_i = -JB\cos\theta$. The probability of finding the spin i at a particular (θ, ϕ) in a solid angle $d\omega = d\phi d\cos\theta$ around the heat bath is

$$P(\theta,\phi)d\phi d\cos\theta = \exp\left(-h_i/T\right)d\phi d\cos\theta / \int d\phi \int d\cos\theta \exp\left(-h_i/T\right) \tag{2.12}$$

We determine (θ, ϕ) through the equations

$$R = \int_0^{2\pi} d\phi' \int_{-1}^{\cos^{-1}\theta} d\cos\theta' P(\theta',\phi') \tag{2.13a}$$

$$R' = \phi/2\pi \tag{2.13b}$$

where $0 < R, R' < 1$ are just two random numbers. The reason we choose the azimuthal angle ϕ randomly is because energy does not depend on it i.e. $E(\theta,\phi) = E(\theta) = -JB\cos\theta$. We solve the above equations and obtain

$$\cos\theta = \frac{1}{BK}\log[\exp(BK)(1-R) + R\exp(-BK)] \quad ; \quad K = J/T \tag{2.14a}$$

$$\phi = 2\pi R' \tag{2.14b}$$

As can be seen from the figure above, when $BJ \ll T$ the values of $\cos\theta$ are almost uniformly distributed with respect to R i.e. the spins are randomly oriented at high temperatures. When $BJ \gg T$, the values of $\cos\theta$ are almost 1 for most values of R i.e. the spins are oriented parallel to each other at low temperatures.

Having solved for θ and ϕ we update the current spin configuration using the generalized Euler rotation matrix $\vec{S}'_k = R(\theta,\phi)\vec{S}_k$. This algorithm can be easily generalized to the frustrated Hamiltonians considered in this thesis and is summarized below

Algorithm 2 Heat bath Algorithm

1: **For** $i = 1...N$ repeat N times
2: Randomly choose spin at site i: $\vec{S}_i$
3: Compute the heat bath $\vec{B}_i = \sum_{j\in N(i)} \hat{J}_{ij}\vec{S}_j$
4: Choose $\phi \in rand(0, 2\pi)$
5: Choose $R \in rand(0, 1)$
6: Update $\cos\theta \leftarrow \frac{1}{BK}\log[\exp(BK)(1-R) + R\exp(-BK)]$
7: Having solved for θ, ϕ update spin $\vec{S}'_k = R(\theta,\phi)\vec{S}_k$

Over relaxation

In addition to the stochastic update algorithms discussed above, we implement over relaxation in order to reduce the *auto correlations* between successive updated spin configurations. Having found the effective magnetic field from the neighbouring spins we propose a θ precession of the spin about this vector where θ is either chosen randomly or is chosen to be π in the extreme case [52, 31]. It is done in order to ensure that no updated configuration is stuck in a local minimum from which it is usually hard to get out. The proposed configuration lies on the same energy isoline around a local minima (random θ) or opposite to the local minima (π update) and since the energies are comparable to the stochastic update, the update is accepted with the added benefit of not being stuck in any local minima. This update is micro canonical in the sense that it **does not** change the energy of the configuration i.e. $\vec{S}_k \rightarrow \vec{S}'_k$ such that $E_k = E'_k$. This update is a deterministic and all spins are updated sequentially.

Algorithm 3 Over relaxation Algorithm

1: **For** $i = 1...N$
2: Choose spin at site i: $\vec{S}_i$
3: Compute the heat bath $\vec{B}_i = \sum_{j \in N(i)} \hat{J}_{ij} \vec{S}_j$
4: Update spin $\vec{S}_i \leftarrow 2\frac{\vec{S}_i \cdot \vec{B}_i}{|\vec{B}_i|^2}\vec{B}_i - \vec{S}_i$

2.1.4 Parallel Tempering

In parallel tempering (PT) or replica exchange methods we consider an extended configuration space, hosting canonical configurations at different temperatures $(T_1 < T_2 ... < T_m)$. We then define a joint partition function as a product of individual partition functions at different temperatures.

$$\mathcal{Z}_{PT} = \prod_{i=1}^{m} \mathcal{Z}(T_i) = \prod_{i=1}^{m} \sum_{s} \exp(-\mathcal{H}(s)/T_i) \tag{2.15}$$

For each of the m temperatures, the configurations are simulated and updated using the Monte Carlo methods discussed above, as parallel process (on separate nodes of a cluster). The main idea behind PT is that, after a certain number of spin updates on individual nodes a swap of configurations at two different temperatures T_i, T_j is proposed and this swap is accepted based on Metropolis probability. Thus for 2 configurations x_i and x_j with energies E_i, E_j and at temperatures T_1, T_2 respectively, the Metropolis acceptance of a swap is given by

$$P((x_i, x_j) \rightarrow (x_j, x_i)) = min\{1, \exp(-\triangle E_{ij}/\triangle T)\} \tag{2.16}$$

where $\triangle E_{ij} = E_i - E_j$ and $\triangle T = T_2 - T_1$. In order to have a successful swap , there needs to be considerable overlap of probability distributions at the temperatures considered and larger the difference in temperatures lower the overlap, hence we consider only nearest neighbour (adjacent) temperatures. In most implementations , instead of swapping configurations between temperatures , temperatures are swapped keeping the configurations fixed. In this case one needs to simply compute $E(x)/\triangle T$ to see if an exchange is possible or not. The reason we use PT is to ensure that configurations at lower temperatures are not stuck in any local energy minima , thus have long auto correlation times, by heating them to a higher temperatures and subsequently cooling them back to the lower temperature reaching a different local minima. It is particularly useful in systems that have a high ground state degeneracy. This method is quite robust and can be trivially parallelized on any GPU system, and the simulations used in this thesis use a generic implementation of PT from the ALPSCore library. The PT algorithm is summarized below

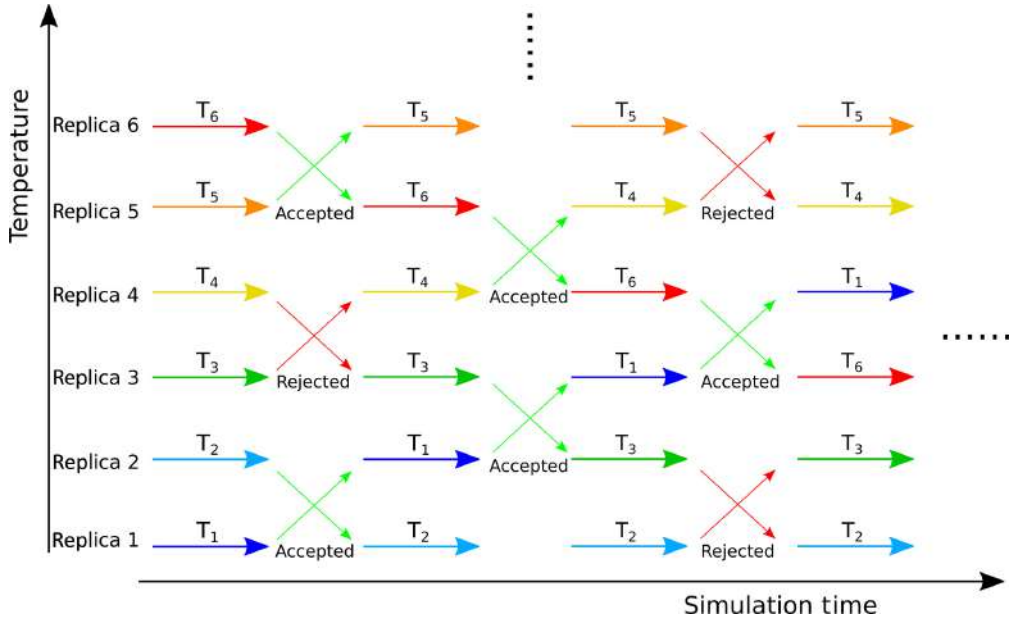

FIGURE 2.1: Parallel tempering process shown above.The neighbouring replicas are exchanged when the Metropolis criterion is met. Figure reproduced from [139]

Algorithm 4 Parallel Tempering Algorithm

1: Initial m temperatures $T_1 < T_2 ... < T_m$
2: Run parallel L MC updates (L Sweeps) on different nodes of the cluster at each T_i
3: Swap configurations between T_i and T_{i+1} for $i \in \{1, 3...m-1\}$ with Metropolis probabilities
4: Run parallel L MC updates (L Sweeps) on different nodes of the cluster at each T_i
5: Swap configurations between T_i and T_{i+1} for $i \in \{2, 4...m-2\}$ with Metropolis probabilities
6: Repeat $N_{MC}/2L$ times

2.2 Machine learning (SVMs)

In this section we shall introduce the machine learning methods that are relevant for this thesis and in particular focus on support vector machines (SVMs) with a tensorial kernel (TK). Machine learning in condensed matter physics is a very broad topic and different kinds of algorithms from artificial neural networks to reinforcement learning routinely used. It is an almost impossible task to discuss all the applications and we shall leave the reader to quench their thirst for knowledge of other applications. Our goal here is more well defined and revolves around phase classification of symmetry broken phases in frustrated magnets. We shall see how SVMs help in extracting useful (information) " features" from a configuration space of classical spins and be able to interpret the learnt results which is a strength of the SVMs [192, 24, 86]. We shall also see how the bias parameter plays a crucial role in phase classification and confers upon TK-SVM its strength of being an *unsupervised* learning algorithm. In unsupervised learning the machine finds correlations in unlabelled data and assigns a label itself and this has the great advantage that the user does not need to have deep insights about the topology of the phase diagram or intimate knowledge of the underlying physics but rather uncover physical insights thanks to the interpretability of the algorithm. We shall further illustrate most of the ideas discussed below using examples from the Heisenberg-Kitaev model on a two dimensional honeycomb lattice. The reader need not worry about the underlying physics as it is discussed in the subsequent chapters and can ignore the physics as a "black box" instead focusing on the illustration of concepts.

Support vector machines are a form of supervised classifiers, which means that they learn from discretely labelled data and can then be used to predict the label of any new data. In machine learning literature it is conventional to represent data with $\mathbf{X}^{(k)}$ and the target or labels with

$y^{(k)}$, where $k = 1...n$ is the index of the sample. In addition we usually consider data in an m-dimensional space i.e. consisting of m features $\mathbf{X} \in \mathbb{R}^m = [x_1, x_2...x_m]$ and the labels belong to a 1 dimensional space $y \in \mathbb{R}$. The general flow of ML is then

$$(\mathbf{X^{(k)}}, y^{(k)}) \rightarrow \textbf{Algorithm} \rightarrow \textbf{Model} \rightarrow y^{(pred)} \ (given \ \ \mathbf{X^{new}}) \tag{2.17}$$

We shall illustrate in the subsequent sections all the essential features of SVMs in the case of a binary classification i.e. we just have two classes of labels $y^{(k)} = \pm 1, \ \forall k$. SVMs map the training samples into the hyperspace and try to find a hyperplane *decision boundary* which maximizes the gap between the two classes of samples. New samples are then mapped to the same hyperspace and based on which side of the decision boundary they fall, they are assigned the label accordingly.

In addition to classification of linear data using a hyperplane, SVMs also classify non linear data efficiently using the *Kernel trick* [24, 86] where the non linear data is projected into a higher dimensional space making it linearly separable and we find a linear hyperplane in the higher dimensional space separating the data. We shall dwell into kernel methods in much more detail in the sections below.

We shall begin by discussing linearly separable data with binary labels. The hyperplane or decision boundary between the sets of training samples is,

$$\mathbf{w} \cdot \mathbf{X} - \rho = 0 \tag{2.18}$$

defined by the normal vector also known as the *parameters* $\mathbf{w} \in \mathbb{R}^d$ and the y-intercept ρ also know as the *bias*.

2.2.1 Hard-Margin

Ideally, if the data is completely linearly separable then can define two parallel hyperplanes separating the data and define the hyperplane that lies midway between these two hyperplanes as the *decision boundary*. We then have the following equations for the 2 hyperplanes,

$$\begin{aligned} &\mathbf{w} \cdot \mathbf{X^{(k)}} - \rho \leq -1, \ when \ y^{(k)} = -1 \\ &\mathbf{w} \cdot \mathbf{X^{(k)}} - \rho \geq 1, \ when \ y^{(k)} = 1 \\ &y^{(k)}(\mathbf{w} \cdot \mathbf{X^{(k)}} - \rho) \geq 1, \ \forall k \end{aligned} \tag{2.19}$$

where the last equation is the combined form of the two hyperplane equations.

In general for separable data we have infinitely many solutions for the hyperplane and to choose one we slightly modify our separation requirement. We impose a **margin** around the decision boundary which does not contain any of the training samples and we maximize the width of the margins to then choose the optimal decision boundary [204]. The width of the margin is then given by $2/|\mathbf{w}|$ and maximization of the width is equivalent to minimization of the norm of the normal vector and then our optimization problem becomes

$$\max \ 2/|\mathbf{w}| \equiv \min \ \frac{|\mathbf{w}|^2}{2} \ subject \ to \ \ y^{(k)}(\mathbf{w} \cdot \mathbf{X^{(k)}} - \rho) \geq 1 \ wrt \ \ \mathbf{w}, \rho \tag{2.20}$$

The decision boundary is actually determined by all points that lie on the margin or within it and these sample points are known as **support vectors**.

2.2.2 Soft-Margin

When the data is not perfectly separable it doesn't make sense to find a "perfect boundary" which classifies all the training examples perfectly with over complicated boundary neglecting the noise. In this case we want to use a boundary with a "soft margin" than a hard one. We relax the above constraint and allow for incursions into the margin introducing a regularization parameter $C > 0$

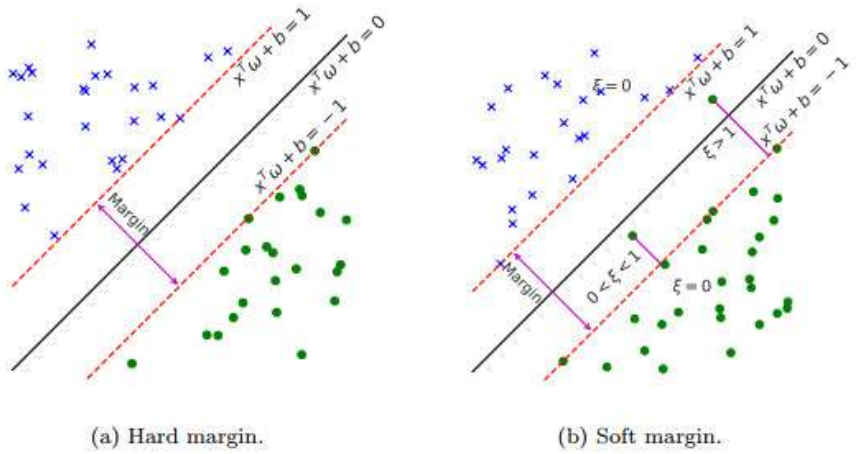

(a) Hard margin. (b) Soft margin.

FIGURE 2.2: The samples on the margins that determine the boundaries are known as support vector where the data is perfectly separable (left) having an optimal hard margin and requires a soft margin (right) where the classifier is penalized for misclassifications. Figure reproduced from [140]. The penalty coefficient for misclassification C. Larger the value of C greater the penalty for misclassification and hence narrower the margin (hard-margin limit). Decreasing the value of C leads to a softer margin and hence more misclassifcation. In general a smaller value of C is preferred to avoid overfitting.

and softening the optimization objective. This is robust to outliers and can "accept" outliers in a tolerance step as

$$\min \frac{|\mathbf{w}|^2}{2} + C\sum_k \chi_k \; subject\ to \;\; y^{(k)}(\mathbf{w}\cdot\mathbf{X^{(k)}} - \rho) \geq 1 - \chi_k \; wrt \;\; \mathbf{w}, \rho, \{\chi_k\} \tag{2.21}$$

where the slack variables $\chi_k > 1$ for misclassified samples else is $\chi_k \geq 0$. It is most convenient to calculate the optimal value of the slack variables through the *hinge loss* which determines the value completely in terms of the parameters $\mathbf{w}, \rho$ as,

$$\chi_k = h(\mathbf{X^{(k)}}, y^{(k)}) = \max\{0, 1 - y^{(k)}(\mathbf{w}\cdot\mathbf{X^{(k)}} - \rho)\} \tag{2.22}$$

Only samples that violate the margin incur a hinge loss and for all other correctly classified samples the loss is 0. The minimization objective using the Hinge loss can be written in an equivalent manner as,

$$\min \lambda\frac{|\mathbf{w}|^2}{2} + \frac{1}{n}\sum_{k=1}^{n} \max\{0, 1 - y^{(k)}(\mathbf{w}\cdot\mathbf{X^{(k)}} - \rho)\} \tag{2.23}$$

where $\lambda > 0$ is the trade-off parameter between increasing the margin size and ensuring the samples are correctly classified. The parameter λ is inversely related to C.

Decreasing the value of λ (increasing C) yields a hard-margin classifier with extremely narrow margin. The cost of having a hard-margin is that we overfit the samples. Increasing the value of λ leads to softening the classification criterion and broadening the margin. In the extreme limit we allow many misclassifications and hence underfit the data and discard useful information about structures in the underlying data set. The optimal value of λ is problem specific and one needs to test the performance on a range of values before choosing the best suited value.

It is worthy to note that since in the constraints, the samples appear only in a dot product with the parameters, we can safely conclude that the optimal parameters lie in the span of the samples, as any orthogonal components of the parameters would be of no significance to the optimization objective. We instead solve a simplified *Lagrangian dual* problem which can be solved efficiently using *quadratic programming algorithms*. Thus we have the dual optimization problem,

$$\begin{aligned} &\max f(\lambda_1, \lambda_2, ...\lambda_n) := \sum_{i=1}^{n} \lambda_i - \frac{1}{2} \sum_{i=1}^{n} \sum_{j=1}^{n} y^{(i)} \lambda_i \mathbf{X^{(i)}} \cdot \mathbf{X^{(j)}} \lambda_j y^{(j)} \\ &\textit{subject to } \sum_{i=1}^{n} \lambda_i y^{(i)} = 0, \textit{ and } 0 \leq \lambda_i \leq \frac{1}{2n\lambda} \ \forall i \end{aligned} \tag{2.24}$$

where we define λ_i through the equation,

$$\mathbf{w} = \sum_{k=1}^{n} \lambda_k y^{(k)} \mathbf{X^{(k)}} \tag{2.25}$$

$\lambda_i = 0$ when the sample $\mathbf{X^{(i)}}$ is correctly classified and $0 < \lambda_i < 1/2n\lambda$ when the sample $\mathbf{X^{(i)}}$ lies on the margin i.e. is a support vector and has a non zero hinge loss.

For a new sample $\mathbf{X}$ we predict the class it belongs to using the distance of the learnt hyperplane and its sign which can be solved entirely in terms of the support vectors and the bias,

$$d(\mathbf{X}) = \mathbf{w} \cdot \mathbf{X} - \rho = \sum_{k=1}^{n} \lambda_k y^{(k)} \mathbf{X^{(k)}} \cdot \mathbf{X} - \rho, \ y^{pred} = sign(d(\mathbf{X})) \tag{2.26}$$

In a multiclassification problem with P distinct labels we use binary classifications pairwise on $P(P-1)/2$ pairs of labels where we consider only training samples belonging to either labels. Each binary classification produces a single decision function and in all we have $P(P-1)/2$ decision functions. The support vectors of this multiclassification problem constitute all samples with a nonzero Lagrangian multiplier λ_i.

For a new test sample ideally the assignment of a label between all the classifiers is unambiguous. If this is not the case then most SVM algorithms use *majority vote* to decide the label, wherein each decision function assigns a label and the final label assigned is the mode(majority) of all the $P(P-1)/2$ labels. The SVM used in this thesis considers decision functions individually and may discard some based on physical insights, not using majority voting in the classification problem since in certain situations they might not correspond to the underlying physics and end up either not distinguishing between labels or assigning multiple labels to the same class.

2.3 The Kernel trick

When the data is not linearly separable we wish to learn a non-linear decision function by mapping the samples to a higher dimensional space $\phi : \mathbf{X} \in \mathbb{R}^d \rightarrow \phi(\mathbf{X}) \in \mathbb{R}^D$, $D > d$ where the samples are linearly separable and then project back the learnt linear hyperplane into the space of the original samples. Furthermore since the decision function and the optimization problem involve only inner products we use the Kernel trick which involves computing the Kernel function in the original space defined as the inner product of the mapped feature vectors.

$$K(\mathbf{X}, \mathbf{Y}) := \phi(\mathbf{X}) \cdot \phi(\mathbf{Y}) \tag{2.27}$$

As long as one is able to compute this function one doesn't need to be bothered about the precise form of mapping (ϕ) or the dimensionality of the mapped space (D) (which might be possibly infinite dimensional).

$K(\mathbf{X}, \mathbf{Y})$ is an "inner product" in higher some dimension which measures how *"similar"* the features are, if the features are very similar we require K to be large and in the opposite case we require K to be small. We could in principle define any "similarity function" to be a kernel function as long as we can define a mapping ϕ to the hyper space. This is guaranteed by the Mercer's theorem

Mercer's Theorem : Let $\{x^{(1)}...x^{(d)}\}$ *be d points in any dimensional space we then define a "grand Kernel matrix"* $K \in R^{d\times d}$ *s.t.* $K_{ij} = K(x^{(i)}x^{(j)})$. *K is a valid kernel function, if for any vector z (*$z \in \mathbb{R}^d$*), K is semi positive definite* $z^T Kz \geq 0 \Leftrightarrow K(x,z) = \phi^T(x)\phi(z)$.

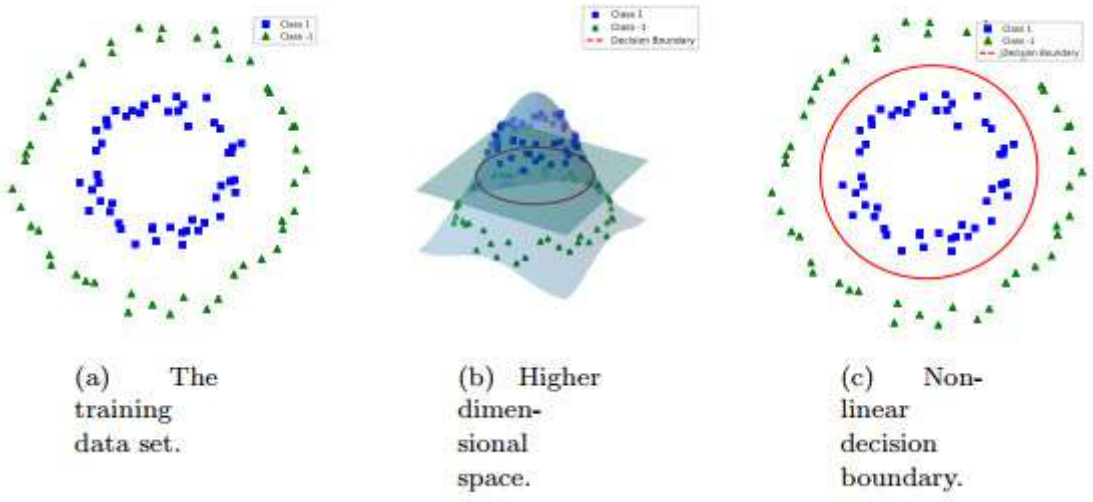

(a) The training data set.

(b) Higher dimensional space.

(c) Non-linear decision boundary.

FIGURE 2.3: The geometrical interpretation of the Kernel trick where data that is not separable in the original space is projected to a higher dimension where it is linearly separable and the decision boundary is projected back to the original space which now becomes a non linear boundary. Figure reproduced from [140].

In the decision functions and the optimization objective we replace the inner products between samples with an evaluation of the Kernel function,

$$d(\mathbf{X}) = \sum_{k=1}^{n} \lambda_k y^{(k)} \mathbf{X^{(k)}} \cdot \mathbf{X} - \rho \rightarrow \sum_{k=1}^{n} \lambda_k y^{(k)} K(\mathbf{X^{(k)}}, \mathbf{X}) - \rho \tag{2.28}$$

and in the optimization algorithm where we minimize the width of the margin and replace the norm of width expressed in terms of the support vectors by a Kernel evaluation,

$$\begin{aligned} \max f(\lambda_1, \lambda_2, ...\lambda_n) &:= \sum_{i=1}^{n} \lambda_i - \frac{1}{2} \sum_{i=1}^{n} \sum_{j=1}^{n} y^{(i)} \lambda_i \mathbf{X^{(i)}} \cdot \mathbf{X^{(j)}} \lambda_j y^{(j)} \\ &\rightarrow \sum_{i=1}^{n} \lambda_i - \frac{1}{2} \sum_{i=1}^{n} \sum_{j=1}^{n} y^{(i)} \lambda_i K(\mathbf{X^{(i)}}, \mathbf{X^{(j)}}) \lambda_j y^{(j)} \\ &subject\ to \sum_{i=1}^{n} \lambda_i y^{(i)} = 0,\ and\ 0 \leq \lambda_i \leq \frac{1}{2n\lambda}\ \forall i \end{aligned} \tag{2.29}$$

where the coefficients λ_i are again solved using quadratic programming. Using the Kernel trick [42, 172] of replacing all dot products with (non-linear) Kernel functions and using the SVM algorithm in the transformed hyperspace doesn't absolve us from the choice of the Kernel function which is much easier to engineer based on physical insights than dwelling in the details of the mapping function ϕ. Some common choices of Kernel functions are listed below -

$$\begin{aligned} &1.\ Polynomial\ :\ K(\mathbf{X^{(i)}}, \mathbf{X^{(j)}}) := (\mathbf{X^{(i)}} \cdot \mathbf{X^{(j)}})^d\ \ (d = 1,\ linear, d = 2,\ quadratic) \\ &2.\ Gaussian\ Radial\ Function\ :\ K(\mathbf{X^{(i)}}, \mathbf{X^{(j)}}) := \exp(-|\mathbf{X^{(i)}} - \mathbf{X^{(j)}}|^2/2\sigma^2) \\ &3.\ Sigmoid\ Function\ :\ K(\mathbf{X^{(i)}}, \mathbf{X^{(j)}}) := \tanh(\kappa \mathbf{X^{(i)}} \cdot \mathbf{X^{(j)}} - \beta),\ \kappa, \beta > 0 \end{aligned} \tag{2.30}$$

We illustrate how the quadratic Kernel function in 2 dimensions can be described as the inner product of a feature mapping in 3 dimensions,

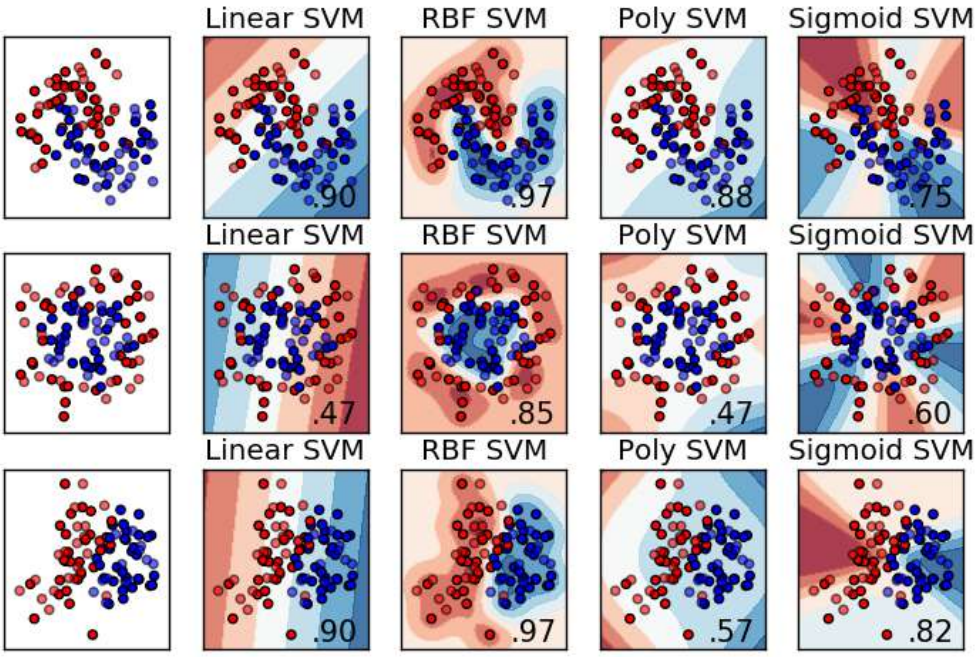

FIGURE 2.4: The different kernels used to find the decision boundary are shown and it is quite evident that in most cases RBF kernel performs pretty well but also risks overfitting the data. Figure reproduced from [27]

$$
\begin{aligned}
&K(\mathbf{x},\mathbf{y}) = (\mathbf{x}\cdot\mathbf{y})^2 = (x_1y_1 + x_2y_2)^2 = x_1^2y_1^2 + x_2^2y_2^2 + 2x_1y_1x_2y_2 \\
&= [x_1^2\ \sqrt{2}x_1x_2\ x_2^2]\cdot[y_1^2\ \sqrt{2}y_1y_2\ y_2^2] := \phi(\mathbf{x})\cdot\phi(\mathbf{y}) \\
&\phi(\mathbf{x}):\ (x_1,x_2) \rightarrow [x_1^2,\ \sqrt{2}x_1x_2,\ x_2^2]
\end{aligned}
\tag{2.31}
$$

A useful property of the quadratic Kernel is the reshuffling of indices to express the quadratic dot products in terms of coefficient matrix (C), where the summation over indices of the features is interchanged with the summation over the support vectors,

$$
\begin{aligned}
d(\mathbf{x}) &= \sum_k \lambda_k y^{(k)}(\mathbf{x}^{(\mathbf{k})}\cdot\mathbf{x})^2 = \sum_k \lambda_k y^{(k)} \sum_{i,j=1}^{d}(x_i^{(k)}x_i)(x_j^{(k)}x_j) \\
&= \sum_{i,j=1}^{d}[\sum_k \lambda_k y^{(k)}x_i^{(k)}x_j^{(k)}]x_ix_j := \sum_{i,j=1}^{d} C_{ij}x_ix_j
\end{aligned}
\tag{2.32}
$$

Thus using a quadratic Kernel gives us a decision function which is also quadratic in the sample coordinates [43, 193]. The coefficient matrix C can be diagonalized to find the principal axes and thus admit the extraction of the analytical form of the decision boundary. This interpretation of the decision boundary in terms of a coefficient matrix forms the basis of the SVM method used in this thesis.

2.4 Tensorial Kernel (TK) SVMs

Building upon the ideas discussed in the previous sections we introduce SVMs that use a tensorial Kernel introduced by [75, 77]. In general we can view the distinction between ordered and

disordered phases as a binary classification problem given a labelled set of microscopic spin configurations. We then naturally interpret the decision function as the phase boundary which would then play the role of an order parameter. Ponte and Melko [172] pointed out in their work that the decision function would always reproduce the true order parameter given a suitable Kernel. In their work the authors used quadratic kernels to study linear orders as a proof-of-concept which is not particularly enlightening in terms of physics. On the other hand, tensorial kernels are extremely suitable to capture the physics of symmetry broken classical $O(3)$ orders while remaining easy to interpret. In the subsequent sections we introduce the construction of the tensorial kernel and discuss the complexity and implementation and the role of the bias parameter in distinguishing phases.

2.4.1 Constructing the tensorial Kernel

We consider all components of the spins at the lattice sites as the training data which are labelled. $\mathbf{X} = \{\vec{S}_i \in O(3)\} = \{S_{i,a}\}$ where $i \in \{1, 2...N\}$ indexes the lattice site and $a \in \{x, y, z\}$ are the spin components. The labels assigned need not reveal any information about which particular phase the spin configurations belong and just be a trivial label to distinguish the points. Then with respect to a feature mapping, the tensorial Kernel is just defined as a quadratic Kernel,

$$K(\mathbf{X}, \mathbf{Y}) = [\phi(\mathbf{X}) \cdot \phi(\mathbf{Y})]^2 \tag{2.33}$$

where the feature mapping ϕ maps the sample to a monomial of spin components,

$$\phi : \mathbf{X} \to \phi(\mathbf{X}) = \{\phi_\mu\} = \{\langle S_{a_1}^{\alpha_1} S_{a_2}^{\alpha_2} .... S_{a_n}^{\alpha_n} \rangle_{cl}\} \tag{2.34}$$

Here we further partition our lattice into clusters containing r spins each and the index $\alpha \in \{1, 2, ...r\}$ represents a spin in the cluster. The index $\mu = (\alpha_1, a_1; ...; \alpha_n, a_n)$ represent the collective indices of the spin and component indices in a cluster [162, 75]. Here we crucially assume that the r spins in the cluster suffice to represent the underlying local orders and constraints. We further do a cluster average in order to reduce the dimension of the data. This implies any local order parameter can be described as a function over the $3r$ spin components as a lattice average over all clusters

$$\langle f(\{S_a^\alpha\}) \rangle_{cl} = \frac{r}{V} \sum_{I \in cl} f(\{S_{I,a}^\alpha\}) \tag{2.35}$$

where V is the total volume of the system and I is the cluster index. The motivation behind this tensorial mapping is that local orientational orders can be represented by finite rank tensors constructed from finite number of vector fields. As an illustration, rank 1 tensors represent magnetic orders, rank 2 tensors represent quadrupolar orders and so on. The choice of the cluster is a hyper parameter input by the user with some hindsight based on the geometry of the lattice or information about the symmetry broken phases of the Hamiltonian and is not an output of the algorithm. In most circumstances a single cluster choice mostly would not be able to accommodate all orders, but a sufficiently large cluster would serve the purpose albeit it being an overkill as for spin orders accommodated on smaller clusters one would find a reducible form of the larger cluster thereby inferring indirectly the optimal cluster size.

The monomials of degree n correspond to a $rank - n$ product of sublattice spins from which the local order or constraints are constructed as a linear combination of basis tensors

$$\mathbb{O} = \sum_\alpha c_\alpha S^{\alpha_1} \otimes S^{\alpha_2} ... \otimes S^{\alpha_n} \tag{2.36}$$

The decision function now using the monomial mapping can be expressed as

$$d(\mathbf{X}) = \sum_k \lambda_k y_k [\phi(\mathbf{X}^{(\mathbf{k})}) \cdot \phi(\mathbf{X})]^2 - \rho := \sum_{\mu\nu} C_{\mu\nu} \phi_\mu \phi_\nu - \rho \tag{2.37}$$

$$C_{\mu\nu} = \sum_k \lambda_k y_k \langle S^{\alpha_1}_{a_1} S^{\alpha_2}_{a_2} .... S^{\alpha_n}_{a_n} \rangle^{(k)}_{cl} \langle S^{\alpha'_1}_{a'_1} S^{\alpha'_2}_{a'_2} .... S^{\alpha'_n}_{a'_n} \rangle^{(k)}_{cl} \tag{2.38}$$

here $C_{\mu\nu}$ is the coefficient matrix calculated from the learned support vectors. The coefficient matrix $C_{\mu\nu}$ is a $(3r)^n \times (3r)^n$ symmetric matrix but the number of independent elements are much smaller due to redundancies discussed later. This matrix can simultaneously capture multiple coexisting orders as well as emergent local constraints as shall be shown in the subsequent sections and later chapters.

In TK-SVM one can probe tensor correlations upto a maximum rank of $n_{max} = 6$ by successively applying the mapping ϕ_μ at different ranks from $n = 1....6$ one can extract the relevant physics at the orders probed. At $n = 1$, from the coefficient matrix we extract all the spin-spin correlations of the spins in a cluster and this shall be illustrated with an example later. The choice of the optimal spin cluster is guided by insights on the lattice and a trial cluster consists of a number of lattice cells.

Even though the dimension of the sampled spins is extremely large and extensively dependent on the lattice size L i.e. $dim(\mathbf{X}) = 3L^d$ but there is a lot of redundancy as the monomials are identical under a simultaneous swap of spin and component indices, e.g. $\langle S^{\alpha_1}_{a_1} S^{\alpha_2}_{a_2} .... S^{\alpha_n}_{a_n} \rangle_{cl} = \langle S^{\alpha_2}_{a_2} S^{\alpha_1}_{a_1} .... S^{\alpha_n}_{a_n} \rangle_{cl}$. This implies that the dimension of the monomials just depend on the monomial degree n and the number of spins in each cluster r and we then consider a reduced dimensional feature space where we impose an ordering on the rank-n monomials,

$$\langle S^{\alpha_1}_{a_1} S^{\alpha_2}_{a_2} .... S^{\alpha_n}_{a_n} \rangle_{cl} \in \phi(\mathbf{X}) \iff (\alpha_1, a_1) \leq (\alpha_2, a_2) ... \leq (\alpha_n, a_n) \tag{2.39}$$

This imposition of ordering of monomials now implies that the number of distinct monomials of rank-n are $(3r + n - 1)!/n!(3r - 1)!$ which in general is significantly smaller than the original input space and also scales much slower and hence speeds up the computation for most physically relevant magnetic orders we encounter in this thesis.

2.4.2 Bias Parameter

The SVM optimization in addition to learning the coefficient matrix also learns the bias parameter ρ and even though at first sight it seems a trivial offset of the decision boundary it indeed admits a physical meaning and indicates the presence or absence of a phase transition or a crossover. Since the bias parameter is learnt independently of the interpretation of the coefficient matrix and the subsequent order parameters and local constraints, it can be used to graph partition the phase diagram hence making TK-SVM an *unsupervised and interpretable* machine learning algorithm. This feature of exploring and analysing unknown phase diagrams through unsupervised graph partitioning, without explicitly devising order parameters is the strength of TK-SVM and the subsequent chapters illustrate and allude to it.

The main motivation of this interpretation is easy to illustrate. Let us consider a simple magnetic order where we have fully ordered and fully disordered spin configurations. The quadratic part of the decision boundary (which at rank-1 is just the square of the magnetization) would attain a finite value in the ordered phase and vanish in the disordered phase. Thus for a configuration in the disordered phase we have $d(\mathbf{X}) = -\rho = \pm 1$ which implies all the disordered configurations would (ideally) lie on the margin boundaries of the classifier. Thus the bias ρ serves as an indicator of the absence or presence of phase transitions, where $\rho = \pm 1$ indicates that the samples belong to the ordered and disordered phases respectively and $\rho \neq \pm 1$ indicates that the samples are from the same phase or there are significant mislabelled samples.

In a binary classification over 2 samples A and B belonging to the ordered and disordered phases respectively the SVM learns the correct order parameter of the phase (to which A belongs)

and in addition learns a bias with the ideal values $\rho = \pm 1$. The sign learnt by ρ is a matter of convention and in this thesis we use the convention $\rho(A|B) = -\rho(B|A) = -1$ when A is in the ordered phase and B is in the disordered phase.

The value of the bias parameter $\rho = \pm 1$ refers to an ideal case where the quadratic part completely vanishes in one phase and has a non zero value in the other. This has been shown to be the case ref ke, jonas for crossovers as well as phase transitions, which lets us make some conclusions on phase transitions based on the bias parameter.

If the 2 samples A and B belong to the same phase and hence are characterized in the same way we have $|\rho| \gg 1$ but the sign of ρ indicates if we are deep in the ordered or the disordered phase. In the case of partial symmetry breaking where some orders vanish and the remaining orders only decrease in magnitude we have $|\rho| > 1$ as a result of to the contributions from the remaining orders. Finally, in the case of samples A and B from different non-trivial phases with distinct characteristics we usually have $\rho \in (-1, 1)$ and even though $C_{\mu\nu}$ can be used to interpret the order parameter the bias has no simple interpretation and cannot distinguish the samples belonging to a simple order-disorder transition. These results are summarized below

$$|\rho(A|B)| \begin{cases} \gg 1 \ A \text{ and } B \text{ in the same phase} \\ \lesssim 1 \ A \text{ and } B \text{ in different phases} \end{cases} \tag{2.40}$$

2.5 Graph Construction

In the previous section we discussed the general implementation of SVMs and the construction of tensorial kernels SVM and its implementation in binary classification. We further alluded to the bias parameter as having a *"physical interpretation"* which confers TK-SVM its unsupervised learning capabilities. In this section we shall explain how we build a graph from the bias parameter criterion in conjunction with spectral cluster analysis which is then the learnt phase diagram of the physical Hamiltonian under consideration without any prior knowledge of the system.

Any mutliclassification problem can be reduced to set of binary classifications which is the strategy exploited by TK-SVM. In a high dimensional parameter space, with multiple parameters (eg. Temperature, Magnetization or other interactions) we consider M points that are spaced uniformly and at each of these parameter points we consider multiple spin configurations assigned the same label. Of course spin configurations belonging to different parameter points have distinct labels. It is essential to remember that this labelling does not require any information about the underlying topology or structure of the phases in the phase diagram and unravelling the topology without prior knowledge is the main objective of the SVM optimization. We now have training samples with M distinct labels to which we apply TK-SVM multiclassification which is equivalent to $M(M-1)/2$ binary classifications between pairs of M distinct labels. At each rank-n and spin cluster, we obtain $M(M-1)/2$ decision boundaries with their own coefficient matrix and bias parameters.

These M parameter points then serve as vertices of the graph we wish to construct and based on the values of the bias parameters we introduce edges between two vertices. Thus we end up with a graph containing M vertices and M(M-1)/2 edges. This graph is further partitioned based on Fiedler clustering [58] which we shall describe below. This spectral clustering of the graph into subgraphs unravels the topology of the phase diagram and we interpret the distinct subgraphs as distinct phases in the phase diagram. This partitioning depends intimately on the rank-n as well as the spin cluster chosen as hyperparameters and one would need to (without any prior knowledge of the topology of the phase diagram) scan a few combinations of these hyperparameters to get a good understanding of the topology. Once we have the phase diagram, we then implement TK-SVM to learn the coefficient matrix for phase points deep in each phase and analyses the order parameters or local constraints to get a better understanding of the physics.

The graph edges could be weighted or unweighted. In unweighted graphs, we consider an edge between 2 vertices only if the magnitude of the bias parameter is orders of magnitude greater than unity ($|\rho| \gg 1$), which from the previous discussion implies that the 2 vertices belong to the

same phase else the edge is absent. This construction leads to a graph where vertices belonging to the same subgraph (phase) are densely connected and those belonging to different subgraphs are disconnected or barely connected. This construction has the advantage that for symmetry broken phases it is very easy to interpret the phase diagram and capture the transition between phases well but the downside to unweighted graphs is that we neglect a lot of information provided by the bias parameter and also cannot capture crossovers. A possible solution is to use weighted graphs where each edge is assigned a weight in the range $(0,1)$ based on value of the bias parameter. In this construction we consider all the $M(M-1)/2$ edges and further we can capture crossovers and correlations between different subgraphs (phases) really well.

A common weighting function for the bias parameters is the Lorentzian weighting function,

$$w(\rho) = 1 - \frac{\rho_c^2}{(|\rho| - 1)^2 + \rho_c^2} \in (0,1) \tag{2.41}$$

where for points in the same phase $|\rho| \gg 1 \implies w \approx 1$ and for points in different phases $|\rho| \approx 1 \implies w \approx 0$ and ρ_c is a cut-off parameter which sets a characteristic scale of $\gg 1$ in the bias criterion. However in practice the choice of ρ_c is not very crucial and it has been shown that across several orders of magnitude the clustering is clear and robust.

2.5.1 Fiedler clustering

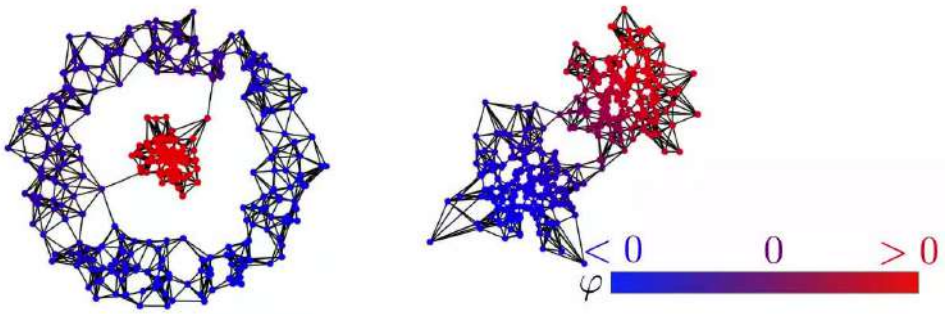

FIGURE 2.5: The graph contains fully connected two subgraphs shown here by red and blue. All the vertices in a subgraph have very similar values as shown by the color code here. Here algebraic connectivity, the second largest eigenvalue of the Laplacian λ_2, refers to the number of edges that need to be cut to disconnect the graphs.Figure produced from [74]

We now describe how the spectral clustering (Fiedler clustering) [57] of a connected graph (with vertices and edges) into subgraphs that lets us interpret the subgraphs as different phases thus letting us study the topology of the phase diagram. The decision made is whether or not a pair of labels is assigned the same phase or not. This is easiest to accomplish through a simple, undirected graph construction. We construct a symmetric $M \times M$ Laplacian matrix $\hat{L}$ which requires information only about the bias parameter $\rho_{i,j}$ connecting any 2 vertices i, j as

$$\hat{L} = \hat{D} - \hat{A} = \begin{bmatrix} d_1 & -w_{12} & \dots & -w_{1M} \\ -w_{21} & d_2 & \dots & -w_{2M} \\ \vdots & & & \vdots \\ -w_{M1} & -w_{M2} & \dots & d_M \end{bmatrix}. \tag{2.42}$$

where the off-diagonal entries, $w_{ij} = w_{ji} = w(\rho_{ij})$, represent all the edge weights and are collected by the adjacency matrix $\hat{A}$. These weights are given by the Lorentizan weighting discussed

above. The diagonal entries, $d_i = \sum_{j \neq i} w(\rho_{ij})$, represents degrees of the vertices i.e. the number of edges at each vertex and forms the degree matrix $\hat{D}$.

We solve for the eigenvalues and eigenvectors of $\hat{L}$. It is easy to see that the sum over any row or column is zero and L turns out to be positive semidefinite with the smallest eigenvalue being 0 and a trivial corresponding eigenvector $[1, 1, ...1] \in \mathbb{R}^M$. In an ideal partitioning we could identify the phases with the lowest eigenvalue but in practice there is always some misclassification hence we consider the *second smallest eigenvalue - Fiedler value* λ_2 and the corresponding eigenvector *Fiedler vector* $\mathbf{f}_2$. λ_2 represents the minimum number of edges that need to be cut to disconnect the graph. Entries of $\mathbf{f}_2$ have a one-to-one correspondence with vertices of the graph. Vertices (the physical parameter points) in the same subgraph are assigned nearly identical Fiedler entries in the Fiedler vector, while those in different subgraphs will be assigned contrasting values. Thus the Fiedler vector effectively partitions the graph and renders a natural interpretation to a phase diagram.

In case of crossover between phases the Fiedler vector entries gradually extrapolate between the values in the two phases, this is not a drawback of the method but rather illustrates the correct physics and the nature of a transition or a crossover. In conclusion the main strength of the above approach is that one does not need to monitor individual phase transitions or tune parameters across the parameter space rather gets the topology of the phase space over the entire parameter space at once. This is particularly useful when the phase diagram is multidimensional and the underlying phases have complex structures.

2.6 Extracting Order parameters

Here we shall discuss how does one extract useful information of the underlying physics from the coefficient matrix $C_{\mu\nu}$. As an illustration we shall discuss the stripy order which is one of the phases in the JK model. The spins orient themselves in stripes of opposite orientations. This phase has a four-site unit cell as shown in the figure below.

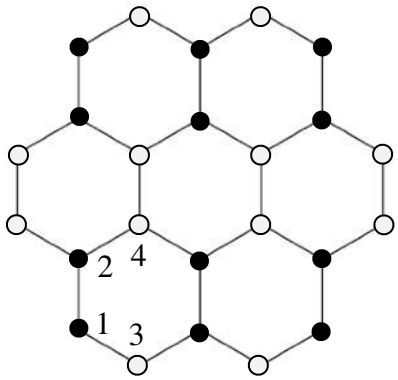

FIGURE 2.6: Figure showing the stripy order where the white and black dots (spins) have opposite orientations. The four-site unit cell here is shown labelled from 1-4.

The SVM is trained at rank $n = 1$ as this is a simple magnetic order and we can extract the analytical order parameter easily. From the coefficient matrix we can analyse the resulting decision function to infer the analytical structure.

The decision function is now

$$d(x) = \sum_{\mu\nu} C_{\mu\nu}\phi_\mu\phi_\nu - \rho = \sum_{a,b} C_{ab}\langle S_a^n\rangle\langle S_b^n\rangle - \rho \tag{2.43}$$

where $a, b \in x, y, z$ and n goes over all the spins used in the cluster and for the optimal choice $n = 1 - 4$ since this is a four-site order i.e. we just investigate the correlation $\langle S_i^{\alpha_k} S_j^{\alpha_l}\rangle$ with $\alpha \in$

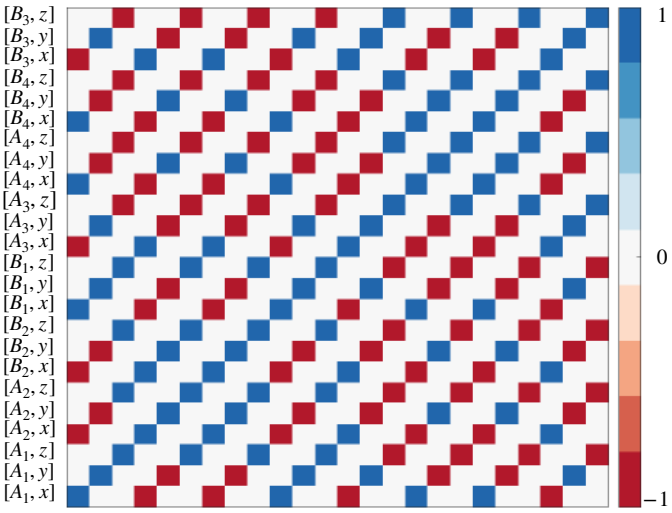

FIGURE 2.7: The $C_{\mu\nu}$ matrix learned by a rank-1 TK-SVM in the ST/D_2. Each entry represents a correlation between two spin components defined by the weighted sum of the support vectors. Results of an eight-spin cluster (2×2 honeycomb unit cells), which is the minimal unit of the D_2.

$\{1,2,3,4\}$ and $i \in \{x,y,z\}$ and each block at rank 1 is a 3×3 matrix elucidating all possible correlations between the components. This matrix is further symmetric owing to the invariance under interchange of labels. Choosing a convention where the correlation of the first spin in the cluster with itself is positive i.e. $\langle S_i^{\alpha_1} S_j^{\alpha_1} \rangle = +1\delta_{ij}$ we observe that all other correlations are diagonal and *strictly* the same or oppositely correlated. Further the strength of the coefficients is encoded in the color scale used but in the case illustrated here is ± 1. The learnt coefficient matrix at rank 1 is shown above and as expected we are able to observe four distinct 3×3 matrices as the components at rank 1 are just the 3 spin components and at rank-r is $3^r \times 3^r$ [76]. The correlations learnt explicitly corresponding to the 4 correlators $\langle S_1 S_1 \rangle, \langle S_1 S_2 \rangle, \langle S_1 S_3 \rangle, \langle S_1 S_4 \rangle$ are shown below.

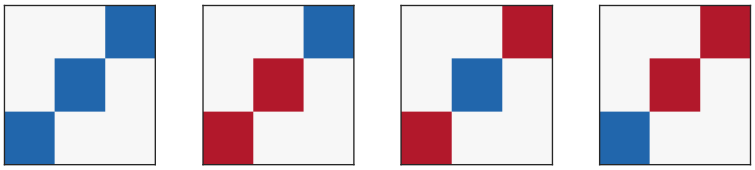

FIGURE 2.8: The four distinct ordering matrices inferred from rank 1 coefficient matrix for the stripy/D_2 order. These correspond to the four correlations $\langle S_1 S_1 \rangle, \langle S_1 S_2 \rangle, \langle S_1 S_3 \rangle, \langle S_1 S_4 \rangle$ for the spins at sites 1-4.

Once we have inferred the ordering matrices it is equivalent to knowing the order i.e. given a FM distribution of spins with a base spin $\vec{S}_A = (S_x \; S_y \; S_z)^{\mathrm{T}}$ we could know all other spins by successively applying the appropriate ordering matrices or inversely given the order we could apply these ordering matrices and retrieve the ferromagnetic spin distribution.

2.7 Spin dynamics

In this chapter we introduce spin dynamics, the time evolution of classical spins in response to an effective magnetic field. This description of spin dynamics is valid for systems with localized magnetic moments which are subject to exchange interactions, that can be described by an effective spin Hamiltonian. We introduce, in analogy to the Heisenberg equations of motion for quantum operators, a classical equation of motion for spin evolution better known as the the **Landau - Lifschitz** spin dynamics equation [129].

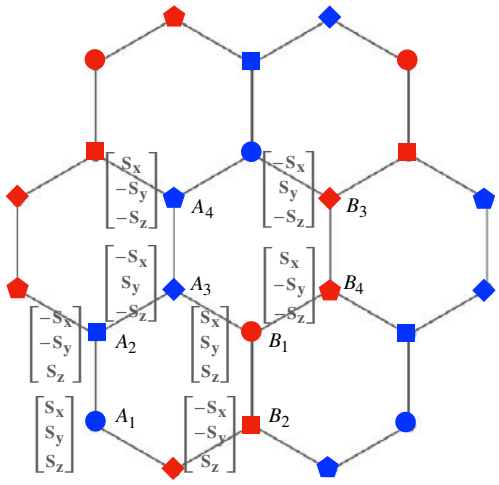

FIGURE 2.9: Configurations of an arbitrary D_2 state. The spin $\vec{S}_{A_1} = (S_x\ S_y\ S_z)^{\mathrm{T}}$ is used as the reference spin, while orientations of other spins are determined according to the respective ordering matrices.

We discuss the effects of evolving spins in a heat bath which include fluctuation and dissipation effects resulting in the relaxation of spins around an effective field. We shall subsequently discuss the analytical solution of the equations of motion known as the spin waves approach as well as the numerical methods of integration. Finally we shall implement spin dynamics in the study of structure factors as well as transport properties, which are not only relevant experimentally but also provide us further insights into the underlying physics of these classical systems.

2.7.1 Classical equations of Motion

In this thesis we primarily concern ourselves with spin Hamiltonians, which describe the interaction between localized magnetic moments, to be of the *Zeeman form*, i.e. a spin coupled to a magnetic field which need not necessarily be an external field rather an effective field which arises due to interactions with the neighbouring spins. A magnetic moment $(\vec{\mu})$ interacts with a magnetic field $(\vec{B})$ by precessing around it and this evolution is described by the Zeeman Hamiltonian

$$\mathcal{H}_{Zeeman} = \vec{\mu} \cdot \vec{B} = -g\mu_B \vec{S} \cdot \vec{B} := \vec{S} \cdot \vec{B} \tag{2.44}$$

where we relate the angular momentum $\vec{S}$ of the spin to its magnetic moment as $\vec{\mu} = -g\mu_B \vec{S}$ and g is the Landé-g factor and μ_B is the Bohr magneton which we shall absorb into a redefinition of spins and henceforth ignore. The spin Hamiltonians considered here describe the interaction of the spin at the site "i" with its neighbouring spins at site "j", which can be interpreted as being coupled to a local effective magnetic field (due to neighbouring spins),

$$\mathcal{H} = \sum_i \sum_j \vec{S}_i \hat{J}_{ij} \vec{S}_j = \sum_i \vec{S}_i \sum_j (\hat{J}_{ij} \vec{S}_j) := \sum_i \vec{S}_i \cdot \vec{B}_i \tag{2.45}$$

here $\hat{J}_{ij}$ are the interaction matrices between the spins at sites i and j on the lattice and the effective magnetic field at site i due to all interactions is $\vec{B} := \sum_j \hat{J}_{ij} \vec{S}_j$.

Classical spin could be interpreted as the "rotation" of a finite sized particle around its symmetry axis and in the presence of a magnetic field, Lorenz force leads to the precession of spin. Classically a magnetic moment placed in a magnetic field experiences a torque which causes a change in the angular momentum and the two are related by the classical equation

$$\vec{\tau} = \frac{d\vec{L}}{dt} = \vec{\mu} \times \vec{B} \tag{2.46}$$

Considering the spin as a classical angular momentum, the precession of the spin in an effective magnetic field is given by

$$\vec{\tau}_S = \frac{d\vec{S}}{dt} = \vec{S} \times \vec{B} = \vec{S} \times \sum_j \hat{J}_{ij}\vec{S}_j \tag{2.47}$$

The solution of this system of coupled differential equations gives the time evolution of the spin. Thus far we have motivated the equation of motion using heuristic arguments and analogy with classical mechanics. In the next section we shall derive the same equation of motion in analogy with the quantum mechanical Heisenberg equation of motion for any operator.

2.7.2 Analogy with Quantum mechanical equation of motion

In the Heisenberg picture in quantum mechanics, where the states are time independent and operators are time dependent the time evolution of any operator $(\hat{O})$ is given by the Heisenberg equation of motion,

$$\frac{d\hat{O}(t)}{dt} = i[\hat{H}, \hat{O}(t)] + \frac{\partial \hat{O}(t)}{\partial t} \tag{2.48}$$

and if there is no implicit time dependence of the operator $\hat{O}$ the last term drops out. Here $[\hat{A}, \hat{B}] = \hat{A}\hat{B} - \hat{B}\hat{A}$ defines the quantum commutator and for the quantum mechanical spin operators at sites i and j on the lattice, satisfying SU(N) algebra, obey the commutation relation

$$[\hat{S}_i^\alpha, \hat{S}_i^\beta] = i\epsilon_{\alpha\beta\gamma}\delta_{ij}\hat{S}_i^\gamma \tag{2.49}$$

where $\epsilon_{\alpha\beta\gamma}$ is the fully antisymmetric levi-civita tensor and $\alpha, \beta, \gamma \in \{x, y, z\}$ refer to the spin components.

In the classical approximation of spins we just replace the quantum mechanical spin operators with c-numbers and in our case we just replace with a set of 3 c-numbers $\hat{S} \to (S_x, S_y, S_z)$ with the constrain that $|\vec{S}| = S_x^2 + S_y^2 + S_z^2 = 1 \implies \vec{S} \in SO(3)$. We define a classical counterpart to the commutators known as the Poisson Bracket (PB) which is defined as follows for any two functions depending on spins $f(\vec{S}), g(\vec{S})$,

$$\{f, g\}_{PB} = \sum_n \epsilon_{\alpha\beta\gamma} \frac{\partial f}{\partial S_n^\alpha} \frac{\partial g}{\partial S_n^\beta} S_n^\gamma = \sum_n \vec{S}_n \cdot \left(\frac{\partial f}{\partial \vec{S}_n} \times \frac{\partial g}{\partial \vec{S}_n} \right) \tag{2.50}$$

By choosing $f = S_i^\alpha$ and $g = S_j^\beta$ we derive a classical counterpart of the quantum spin commutator $\{S_i^\alpha, S_j^\beta\}_{PB} = \epsilon_{\alpha\beta\gamma}\delta_{ij}S_i^\gamma$.

Continuing the analogy between the commutator and the Poisson bracket we define the classical equation of motion for any classical observable as

$$\frac{dO}{dt} = \{\mathcal{H}, O\}_{PB} \tag{2.51}$$

Thus the classical equation of motion for the spin at site i is then given by,

$$\begin{aligned} \frac{d\vec{S}_i}{dt} &= \{\mathcal{H}, \vec{S}_i, \}_{PB} = \sum_n \vec{S}_n \cdot \left(\delta_{in} \times \frac{\partial \mathcal{H}}{\partial \vec{S}_n} \right) \\ &= \left(\frac{\partial \mathcal{H}}{\partial \vec{S}_i} \times \vec{S}_i \right) = \vec{B}_i \times \vec{S}_i, \quad B_i = \sum_j \hat{J}_{ij}\vec{S}_j \end{aligned} \tag{2.52}$$

which is exactly the equation for spin evolution we derived in the previous section, which describes the precession of a spin around its local magnetic field. In the subsequent sections we shall see how to solve the evolution equation both analytically and numerically and how the

conservation of spin magnetization and energy result in spin and thermal currents respectively which play a crucial role in understanding dynamics.

2.7.3 Damping effects

The spin evolution equations discussed in the previous section lead to an infinite precession of the spin about its effective magnetic field, since as the system is isolated (there are no couplings to the environment/ external baths) which result in a loss of energy and ultimately relax to the effective magnetic field, which is the ground state of the system. This behaviour at low temperatures is *unphysical*, since assuming infinite precession at any temperature contradicts the expectation of the system relaxing into a ground state(at zero temperature). At high temperatures too, one would expect such behaviour to be unphysical as increased rate of collisions between spins or other thermal and lattice effects would lead to a change in the spin energy causing it to precess randomly.

Physically, relaxation effects are brought about by the interaction of the spin system with the lattice or electronic structure of the molecules (other particles) causing the spins to lose energy and relax to the ground state. This modeling of relaxation is more **phenomenological** and is introduced by hand, without differentiating the origin of damping, by adding additional terms friction terms in the equations of motion as introduced by Landau and Lifschitz in 1935 [129],

$$\frac{d\vec{S}_i}{dt} = \vec{B}_i \times \vec{S}_i - \lambda(\vec{B}_i \times \vec{S}_i) \times \vec{S}_i \tag{2.53}$$

The damping constant λ is chosen to be positive and the direction of the damping term is towards the effective field i.e. the spin system always relaxes along $\vec{B}_i$. Gilbert proposed a damping term [67] proportional to the precessional frequency (angular speed) of the spin similar to the friction term in classical mechanics,

$$\frac{d\vec{S}_i}{dt} = \vec{B}_i \times \vec{S}_i + \alpha(\vec{S}_i \times \frac{d\vec{S}_i}{dt}) \tag{2.54}$$

The two definitions are equivalent upto first order and a trivial redefinition as shown below starting from the Gilbert definition,

$$\begin{aligned}
&\frac{d\vec{S}_i}{dt} = \vec{B}_i \times \vec{S}_i + \alpha(\vec{S}_i \times \frac{d\vec{S}_i}{dt}) \\
&= \vec{B}_i \times \vec{S}_i + \alpha(\vec{S}_i \times \vec{B}_i \times \vec{S}_i + \vec{S}_i \times \alpha(\vec{S}_i \times \frac{d\vec{S}_i}{dt})) \\
&= \vec{B}_i \times \vec{S}_i - \alpha[(\vec{B}_i \times \vec{S}_i) \times \vec{S}_i] - \alpha^2 S_i^2 \frac{d\vec{S}_i}{dt} \\
&\implies (1 + \alpha^2 S_i^2)\frac{d\vec{S}_i}{dt} = \vec{B}_i \times \vec{S}_i - \alpha[(\vec{B}_i \times \vec{S}_i) \times \vec{S}_i] \\
&:= \frac{d\vec{S}_i}{d\tau} = \vec{B}_i \times \vec{S}_i - \alpha[(\vec{B}_i \times \vec{S}_i) \times \vec{S}_i]
\end{aligned} \tag{2.55}$$

where we used the vector triple cross product identity $\vec{A} \times [\vec{B} \times \vec{C}] = (\vec{A} \cdot \vec{C})\vec{B} - (\vec{A} \cdot \vec{B})\vec{C}$ and the fact that spin length is conserved $d\vec{S}_i^2/dt = 0$ and a trivial redefinition of time $\tau := t(1 + \alpha^2 S_i^2) = t(1 + \alpha^2)$. Hence we see that the two definitions are indeed equivalent. This renormalization of time leads to an important difference in the high damping limit,

$$\begin{aligned}
\lambda \to \infty \implies d\vec{S}/dt \to (-)\infty \quad (Landau - Lifschitz) \\
\alpha \to \infty \implies d\vec{S}/dt \to 0 \quad (Gilbert)
\end{aligned} \tag{2.56}$$

In the Gilbert equation, due to the renormalization of time $\alpha \to \infty$ implies that the spins are completely relaxed to their ground states as implied by the requirement that $(1+\alpha^2)d\vec{S}_i/dt \to finite$. This is more in line with the physical expectation that increasing damping leads to stopping/arresting of the mechanics. The damping term could also be interpreted as a energy loss term, in which the Landau Lifschitz interpretation of case higher the damping higher the loss of energy makes sense. Most numerical methods utilize the Gilbert interpretation and choose a value of damping between $\alpha \in (0.0001, 0.01)$.

2.7.4 Heat Bath effects

At higher temperatures there are thermal effects such as lattice vibrations or interactions with other particles that play an important role in the dynamics by exciting the spins. We expect that at high temperatures (above the Curie temperature) the spins don't precess about a fixed direction but randomly thus destroying any underlying magnetic order (paramagnetic phase). In the preceding sections we have discussed about evolution of isolated spins i.e. spins without being coupled to a heat bath and realise that such a description is unphysical in the high temperature regime hence needing to modify our description of dynamics which we do here.

We model the coupling to a heat bath via a stochastic force term which simulates the acceleration of a particle due to random temperature induced collisions. The interplay between the stochastic and damping terms determines the equilibrium state of the system. We simulate the stochasicity in the equation of motion as $\vec{\xi}_i \times \vec{S}_i$, where the spin is coupled to a fluctuating term ($\vec{\xi}$) drawn from a stochastic distribution. As the vector is perpendicular to the spin we as guaranteed of the conservation of spin length.

The fluctuating terms can be drawn from any distribution such as a Poisson , Bose or Gaussian distribution to name a few. The most common choice without prior knowledge of the underlying interactions is to use white noise i.e. draw from a Gaussian distribution. The large number of random collisions (applying the central limit theorem) make the Gaussian distribution plausible. We further assume there is no preferred direction i.e. the system does not drift in a preferred direction as a result of collisions implies the distribution has a vanishing mean. We also assume the fluctuations are uncorrelated between different spins as well as at different times. These assumptions are only valid if the mean free path of the collision is larger than the lattice spacing and the time interval between two successive collisions is shorter than the time scale of spin dynamics , these assumptions imply that for the fluctuating forces we have ,

$$\langle \xi_i^\alpha(t) \rangle = 0 \qquad \langle \xi_i^\alpha(0) \xi_j^\beta(t) \rangle = \delta_{ij}\delta_{\alpha\beta}\delta(t)\sigma^2 \tag{2.57}$$

where $\sigma^2 = 2\alpha T$ with α being the damping parameter and T temperature of the heat bath. We choose the variance of the distribution in such a way that the distribution of single particle energies in thermal equilibrium still follows the Boltzmann distribution. It is also simple to see that using a Gaussian distribution we get a spectral density that is independent of ω and hence the name *white noise*.

Combining the effects of damping as well as coupling to a heat bath we get the **Landau-Lifschitz-Gilbert** equation describing the evolution dynamics of a spin ,

$$\frac{d\vec{S}_i}{dt} = \vec{B}_i \times \vec{S}_i - \alpha(\vec{B}_i \times \vec{S}_i) \times \vec{S}_i + \vec{\xi}(t) \times \vec{S}_i \tag{2.58}$$

The energy as expected is not conserved, even though the spin length is conserved. In practice the value of the damping constant α is chosen small enough such that the variance of the distribution $\sigma^2 \sim 2\alpha T \sim 0.01$ and since energy goes as the spin square ($E \sim S \cdot S$) we have an error in energy conservation in the 4th order $E \sim \mathcal{O}(10^{-4})$. The numerical integration of the equation of motion using finite difference methods (which will be discussed below) again leads to a further error in energy of the same or lesser order and in practice for most simulated systems this is within the acceptable error range [91].

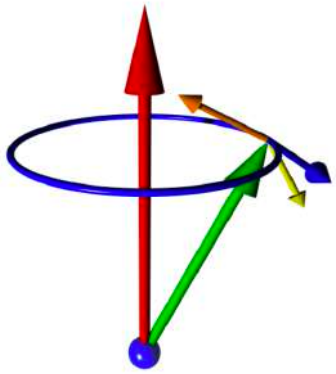

FIGURE 2.10: The visualization of spin dynamics which is described by the Landau Lifschitz Gilbert (LLG) equation. The spin (green) precesses around its effective magnetic field (red) with direction of motion shown by the blue arrow. The damping force driving the spin system towards its effective field is shown by the orange arrow and the random fluctuations as a result of coupling to a heat bath is shown by the yellow arrow. All these three are perpendicular spin (green) establishing the conservation of spin length. Figure reproduced from [20].

In this thesis we follow a different approach where we don't introduce phenomenological noise or damping and instead use the Landau-Lifschitz equation without Gilbert contributions for spin configurations sampled from Monte Carlo canonical ensembles [122, 206]. It has been shown in other studies that the two approaches are equivalent. We prefer to use the first approach since we are interested in dynamics that are completely intrinsic to the system and do not have to dwell in the subtleties of using uncorrelated noise or correlated noise to model the nature of interactions and further justify the value of damping parameters which are chosen arbitrarily in literature and lead to broadening of the spin wave spectrum which are indistinguishable from cosmetical implementations such as Gaussian energy convolution which shall be discussed in the subsequent sections. Furthermore we are interested in transport dynamics and within the conductivities in the linear response theory are defined without damping or noise terms and hence in the spirit of self consistency we persist with spin dynamics that don't include these terms either.

2.8 Analytical solutions - Spin Waves

Having setup the equation of motion for spin evolution in the previous section, we shall solve it analytically to get a better understanding of the underlying physics. The LLG equation of spins coupled to a heat bath with damping , is a coupled differential equation whose solution leads to a Fokker-Planck equation describing the time evolution of non-equilibrium probability distributions. This obscures and complicates the underlying physics and in the spirit to simplify things and build up our intuition of spin dynamics we shall consider the simple undamped, decoupled LL equation. We shall further illustrate the key concepts using the simple nearest neighbour AFM and FM Heisenberg model and the general algorithm to study spin waves in more complicated systems [206, 68].

We being by considering the classical nearest neighbour Heisenberg interaction Hamiltonian $\mathcal{H} = -J\sum_{<i,j>} \vec{S}_i \cdot \vec{S}_j$ where the Heisenberg coupling $J > 0$ leads to the alignment of spins in the same direction (the ferromagnetic phase) and $J < 0$ leads to the opposite alignment of neighbouring spins (the anti-ferromagnetic phase). The equation of motion is then ,

$$\frac{d\vec{S}_i}{dt} = \vec{B}_i \times \vec{S}_i = -J \sum_{j \in N(i)} \vec{S}_j \times \vec{S}_i \tag{2.59}$$

This equation of motion governs the precession of spins in its effective neighbouring field whose solutions we shall discuss below.

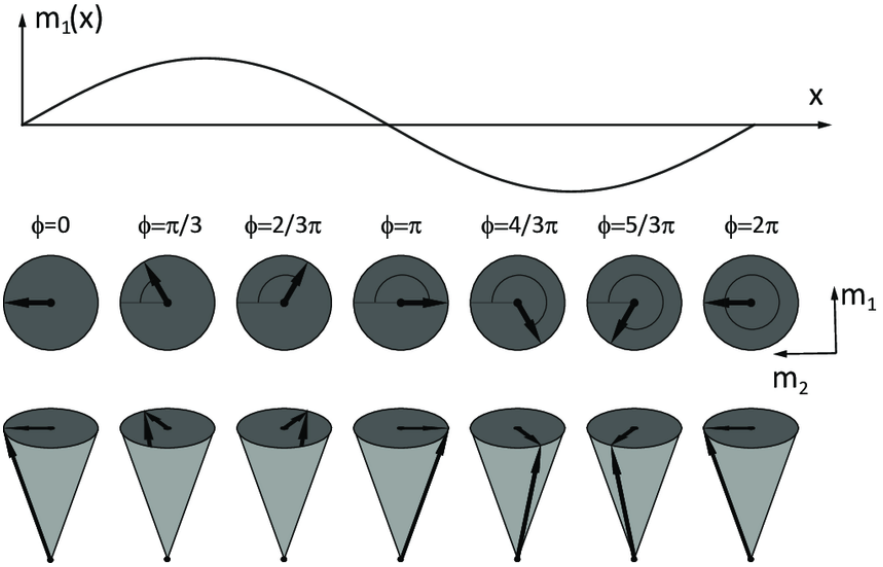

FIGURE 2.11: The precession of spins around an effective magnetic field which when superposed on the perpendicular plane appears as the collective excitation of the spins. The number of spins in the unit cell correspond to the total number of spin wave modes though some of these modes might be degenerate. Figure reproduced from [121]

2.8.1 Ferromagnetic spin waves

Here since all spins are aligned in the same direction we assume each spin is slightly tilted away from a common equilibrium direction

$$\vec{S}_i = \vec{S}_0 + \delta\vec{S}_i \; \forall i \tag{2.60}$$

where $\delta\vec{S}_i$ is the small tilt perpendicular to $\vec{S}_0$. Substituting this into the equation of motion we get

$$\frac{d\delta\vec{S}_i}{dt} = 2J \sum_{j\in N(i)} [\delta\vec{S}_j - \delta\vec{S}_i] \times \vec{S}_0 \tag{2.61}$$

we use the ansatz that the precessional motion propagates in a wave like fashion and therefore look for solutions of the form,

$$\delta\vec{S}_i = \frac{1}{2}[\vec{A}_k \exp(i(\vec{k}\cdot\vec{R}_i - \omega_k t)) + \vec{A}_k^* \exp(-i(\vec{k}\cdot\vec{R}_i - \omega_k t))] \tag{2.62}$$

which when inserted into the above equation gives

$$-i\omega_k\vec{A}_k = 2J \sum_{j\in N(i)} [1 - \exp(i\vec{k}\cdot(\vec{R}_i - \vec{R}_j))]\vec{A}_k \times \vec{S}_0 \tag{2.63}$$

further assuming the common direction of magnetization to be the z axis i.e. $\vec{S}_0 = S_0\hat{z}$ and since the perturbation is in a plane perpendicular to the common direction which is the xy plane we have $\vec{A}_k = A_k(\hat{x} - i\hat{y})$ resulting in the equation for the angular frequency of spins to be of the form

$$\omega_k = 2JS \sum_{j \in N(i)} [1 - \exp(i\vec{k} \cdot (\vec{R}_i - \vec{R}_j))] \tag{2.64}$$

For spins on a 1D lattice the nearest neighbours for any site i is $i \pm 1$ which when substituted in the above equation evaluates to

$$\omega_k = 2JSz(1 - \cos(2ka)) \sim k^2 \tag{2.65}$$

Thus the spin waves in a ferromagnet in the long wavelength limit have a quadratic dispersion which is a consequence of the fact that magnetization commutes with the Hamiltonian [130].

2.8.2 Anti-ferromagnetic spin waves

In the AFM ground state, neighbouring spins are aligned opposite to each other which can be characterized by a wave vector $\vec{k}_0$ and subsequently a phase factor $\exp(i\vec{k}_0 \cdot \vec{R}_i) = \pm 1$ based on the position of the spin $\vec{S}_i$ referring to the two possible orientations. The fluctuation away from the ground state is now characterised as,

$$\vec{S}_i = \vec{S}_0 \exp(i\vec{k}_0 \cdot \vec{R}_i) + \delta\vec{S}_i \; \forall i \tag{2.66}$$

Substituting this into the equation of motion we get,

$$\frac{d\delta\vec{S}_i}{dt} = 2J \sum_{j \in N(i)} [\delta\vec{S}_i \times \vec{S}_0 \exp(i\vec{k}_0 \cdot \vec{R}_j) + \delta\vec{S}_j \times \vec{S}_0 \exp(i\vec{k}_0 \cdot \vec{R}_i)] \tag{2.67}$$

We again assume the magnetization axis to be $\hat{z}$ and study the fluctuations in the xy plane perpendicular to the magnetization direction by introducing $S^{\pm} = \delta S^x \pm i\delta S^y$ and further seeking solutions of the plane-wave form now with 2 amplitudes (A_k, B_k) for the 2 sublattices of spins ,

$$\begin{aligned} S_i^+ &= \sqrt{2/N} \sum_k [A_k \exp(i(\vec{k} \cdot \vec{R}_i - \omega_k t)) + B_k \exp(i((\vec{k} - \vec{k}_0) \cdot \vec{R}_i - \omega_k t))] \\ S_i^- &= \sqrt{2/N} \sum_k [A_k^* \exp(-i(\vec{k} \cdot \vec{R}_i - \omega_k t)) + B_k^* \exp(-i((\vec{k} - \vec{k}_0) \cdot \vec{R}_i - \omega_k t))] \end{aligned} \tag{2.68}$$

substituting these in the equation of motion and solving we find the precessional frequency to be

$$\omega_k = \pm 2S \sqrt{[J(\vec{k}_0) - J(\vec{k})][J(\vec{k}_0) - J(\vec{k} - \vec{k}_0)]} \tag{2.69}$$

where

$$J(\vec{k}) = J \sum_{j \in N(i)} \exp(i\vec{k} \cdot (\vec{R}_i - \vec{R}_j)) := Jz\gamma_k \tag{2.70}$$

where z is the number of nearest neighbours and $z\gamma_k = \sum_{j \in N(i)} \exp(i\vec{k} \cdot \vec{\delta}_j)$ and $\vec{\delta}_j$ is the vector to the jth nearest neighbour. The precessional frequency now reduces to a simple form

$$\omega_k = \pm 2zJS(1 - \gamma_k^2)^{1/2} \sim k \tag{2.71}$$

The spin waves in the long wavelength limit in an anti-ferromagnet are linear as opposed to the quadratic nature in ferromagnets. This dispersion is similar to the acoustic dispersion of phonons. The spins in the two sublattices precess with the same frequency ω_k but different amplitudes A_k, B_k and since the sublattices are equivalent there are two types of spins waves possible for each permutation.

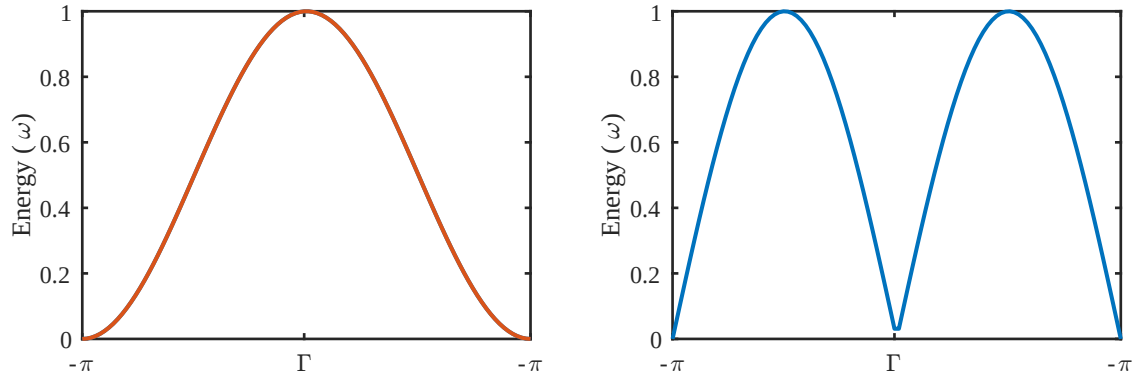

FIGURE 2.12: The FM(left) and AFM(right) dispersion calculated from the formulas discussed above. The main difference is the quadratic and linear dispersion near the zone center (Γ).

2.8.3 Quantum-Mechanical treatment

We now discuss the quantum mechanical treatment of the precession dynamics of spins. Analogous to the quantization of classical lattice vibrations leading to *phonons*, the quantization of classical spin precession (spin waves) leads to *magnons* i.e. the energy is quantized or changes only in integral multiples of the precessional frequency ω_k. There is although a crucial and important difference between magnons and phonons which is a result of the commutation relations. For phonons the commutation relation between the position and momentum operator imply a bosonic commutation relation between the phonon creation and annhilation operators inferring a *"true bosonic"* nature to phonons while for magnons, the commutation relation between the spin operators infers only an *"approximate bosonic"* nature.

We shall illustrate the quantization in the simple case of a Heisenberg ferromagnet and later summarize the general algorithm to quantize spin waves for any ordered spin configuration. We begin with the quantum Heisenberg Hamiltonian and consider spins aligned along the quantization axis which we denote as the z-axis,

$$\mathcal{H} = -J\sum_{ij}\hat{S}_i\cdot\hat{S}_j = -J\sum_{ij}\frac{1}{2}(S_i^+S_j^- + S_i^-S_j^+) + S_i^zS_j^z \tag{2.72}$$

where $S^\pm = S^x \pm iS^y$. It is easy to see that the state where all spins are projected maximally ($m = S$) (or minimally ($m = -S$)) along the quantization axis is an exact eigenstate of the above Hamiltonian as the spin raising (or lowering) operator annihilates the state and S^z simply measures the projection along z. Thus for a state with an azimuthal quantum number m we have,

$$\begin{aligned} S^z|m\rangle &= m|m\rangle \\ S^\pm|m\rangle &= \sqrt{(S\mp m)(S\pm m+1)}|m\pm 1\rangle \end{aligned} \tag{2.73}$$

It is easy to see that the ground state is $2NS+1$ fold degenerate with a spin of magnitude NS. We now map the spin operators to the boson creation and annihilation operators which for a state with occupation number n satisfies,

$$\begin{aligned} \hat{N}|n\rangle &= a^\dagger a|n\rangle = n|n\rangle \\ a|n\rangle &= \sqrt{n}|n-1\rangle \\ a|n\rangle &= \sqrt{n+1}|n+1\rangle \end{aligned} \tag{2.74}$$

and also map the fully polarized state $|m = S\rangle$ to the vacuum state $|n = 0\rangle$ and with the substitution $m = S - n$. Reorganizing and rearranging terms we get to the lowest order the **Holstein-Primakoff transformation**

$$\begin{aligned} S^+|n\rangle &= \sqrt{(2Sn)(1-\frac{n-1}{2S})}|n-1\rangle \approx \sqrt{2S}\sqrt{n}|n-1\rangle := \sqrt{2S}a|n\rangle \\ S^-|n\rangle &= \sqrt{2S(n+1)(1-\frac{n-1}{2S})}|n+1\rangle \approx \sqrt{2S}\sqrt{n+1}|n+1\rangle := \sqrt{2S}a^\dagger|n\rangle \\ S^z &= S - N = S - a^\dagger a \end{aligned} \tag{2.75}$$

The S^z operator measures the deviation from the fully polarized state $|m = S\rangle$. We also neglect the terms in red since we here only consider the approximation to linear order and ignore higher order terms which give the interaction between the quantized particles. This linear approximation is known as the linear spin wave theory and the quantized particles in this theory are free magnons.

We also define the Fourier transform of the Holstein-Primakoff operators as

$$a_l = \frac{1}{\sqrt{N}}\sum_k \exp(-i\vec{k}\cdot\vec{R}_l)a_k \quad , \quad a_l^\dagger = \frac{1}{\sqrt{N}}\sum_k \exp(i\vec{k}\cdot\vec{R}_l)a_k^\dagger \tag{2.76}$$

The commutation relation between the creation and annihilation operators now become

$$\begin{aligned} [a_k, a_q^\dagger] &= \frac{1}{N}\sum_l\sum_m \exp(i\vec{k}\cdot\vec{R}_l)\exp(-i\vec{q}\cdot\vec{R}_m)[a_l, a_m^\dagger] \\ &\approx \frac{1}{N}\sum_l\sum_m \exp(i\vec{k}\cdot\vec{R}_l)\exp(-i\vec{q}\cdot\vec{R}_m)\frac{1}{2S}[S_l^+, S_m^-] \\ &= \frac{1}{N}\sum_l\sum_m \exp(i\vec{k}\cdot\vec{R}_l)\exp(-i\vec{q}\cdot\vec{R}_m)\frac{1}{2S}2S_l^z\delta_{lm} \\ &= \frac{1}{NS}\sum_l \exp(i(\vec{k}-\vec{q})\cdot\vec{R}_l)S_l^z \approx \frac{1}{N}\sum_l \exp(i(\vec{k}-\vec{q})\cdot\vec{R}_l) = \delta_{kq} \end{aligned} \tag{2.77}$$

where we have used the approximation $S^z \approx S$ which is exactly true for the ground states but only holds approximately for the excited states where the magnetization differs slightly from the fully polarized value. We also only considered here the linear part of the relation between the spin and magnon operators. Hence we conclude that the magnon creation and annihilation operators are **"approximately bosonic"**. Now substituting this into the Heisenberg Hamiltonian to linear order and considering only quadratic terms we get,

$$\begin{aligned} \mathcal{H} &= -J\sum_{ij}\frac{1}{2}(S_i^+S_j^- + S_i^-S_j^+) + S_i^zS_j^z = -J\sum_{ij} S(a_ia_j^\dagger + a_i^\dagger a_j) + (S - a_i^\dagger a_i)(S - a_j^\dagger a_j) \\ &= -JS^2Nz - JS\sum_{ij} a_ia_j^\dagger + a_i^\dagger a_j - a_i^\dagger a_i - a_j^\dagger a_j \\ &= E_0 - JS\sum_{ij}\frac{1}{N}\sum_{kq} e^{-i\vec{k}\cdot\vec{R}_i}e^{i\vec{q}\cdot\vec{R}_j}(\delta_{kq} + a_q^\dagger a_k) + e^{i\vec{k}\cdot\vec{R}_i}e^{-i\vec{q}\cdot\vec{R}_j}a_k^\dagger a_q - e^{-i(\vec{k}-\vec{q})\cdot\vec{R}_i}a_k^\dagger a_q \\ &- e^{-i(\vec{k}-\vec{q})\cdot\vec{R}_j}a_k^\dagger a_q \\ &= E_0 + JSz\sum_k [2 - \exp(-i\vec{k}\cdot\vec{\delta}_j) - \exp(i\vec{k}\cdot\vec{\delta}_j)]a_k^\dagger a_k \\ &= E_0 + 2JSz\sum_k [1 - \cos(\vec{k}\cdot\vec{\delta}_j)]a_k^\dagger a_k = E_0 + \sum_k \omega_k a_k^\dagger a_k \end{aligned} \tag{2.78}$$

where $\omega_k = 2JSz[1-\cos(\vec{k}\cdot\vec{\delta}_j)] \sim k^2$ which is the same expression derived in the above section on the classical waves in ferromagnets but with a different interpretation of quantized excitations of spin waves with energy of n magnons being $E = n\omega_k$. Finally we discuss the general algorithm.

Algorithm 5 Linear Spin wave Algorithm

1: In the spin Hamiltonian express all spin vectors as spin operators $\vec{S} = (S^x, S^y, S^z) \rightarrow (S^+, S^-, S^z)$
2: Map the spin operators to magnon raising and lowering operators via Holstein-Primakoff transformation $(S^+, S^-, S^z) \rightarrow (a^\dagger, a)$
3: Expand the Hamiltonian and keep only linear terms in $a^\dagger a$
4: Fourier transform the Hamiltonian
5: Diagonalize the Hamiltonian (using Bogoliubov transformations if necessary)

In general for a magnetic unit cell with N sublattices we need N bosons to diagonalize the Hamiltonian and if it is non diagonal we further need a Bogoliubov transformation to diagonalize it.

Once we have the energy dispersion $\omega(\vec{k})$, we understand the nature free magnon propagation in the magnetic phase but this is only to the linear order. In order to understand magnon propagation as well as magnon-magnon interactions we compute the dynamical structure factor which is probed by neutron scattering experiments as well. The dynamic structure factor gives the spin-spin correlation is space and time and doesn't involve any approximation on the nature of the interactions [7].

2.8.4 Runge-Kutta method of numerical integration

In the classical RK method also known as RK-4 we discretize time and evaluate the dynamical equation as a finite difference method as known as the Euler method,

$$\frac{d\vec{S}_i}{dt} = \left(\frac{\partial \mathcal{H}}{\partial \vec{S}_i} \times \vec{S}_i\right) = \vec{B}_i \times \vec{S}_i \rightarrow \vec{S}_i(t+\delta t) = \vec{S}_i(t) + (\vec{B}_i \times \vec{S}_i)\delta t \tag{2.79}$$

We observe in the Euler method that the error accumulated in spin length at each step is $\mathcal{O}(\delta t)$ and the error in energy is $\mathcal{O}(\delta t^2)$. Instead we use a fourth order method such that the total error accumulated in spin length is $\mathcal{O}(\delta t^4)$. Of course we could use other higher order methods (such as RK-8 where the accumulated error is $\mathcal{O}(\delta t^8)$) but for most practical purposes find such methods an overkill which is both computationally expensive and adds little to our understanding of physics and hence limit ourselves with fourth order methods which is sufficient to understand the physics discussed in this thesis.

We compute the spin at the next time step given a spin configuration at a particular time as,

$$\vec{S}(t+\delta t) = \vec{S}(t) + \frac{\delta t}{6}(k_1 + 2k_2 + 2k_3 + k_4) \tag{2.80}$$

here we use a weighted average of 4 increments where each increment k_i is an estimate of the slope with greater weight given to slopes at the midpoints, the 4 increments which are approximations to the true slope are

$$
\begin{aligned}
k_1 &= \sum_j \hat{J}_{ij}\vec{S}_j \times \vec{S}_i \equiv \vec{B}_i \times \vec{S}_i \\
k_2 &= \sum_j \hat{J}_{ij}(\vec{S}_j + \delta t * k_1/2) \times (\vec{S}_i + \delta t * k_1/2) \\
k_3 &= \sum_j \hat{J}_{ij}(\vec{S}_j + \delta t * k_2/2) \times (\vec{S}_i + \delta t * k_2/2) \\
k_4 &= \sum_j \hat{J}_{ij}(\vec{S}_j + \delta t * k_3) \times (\vec{S}_i + \delta t * k_3)
\end{aligned}
\tag{2.81}
$$

It is easy to see that if we just have the first term (k_1) we reduce back to the Euler method. The convergence in RK-4 is higher compared to Euler methods due to a higher degree of accuracy at each time step and the coefficients weighting the slopes are carefully chosen as to cancel the error till the fourth order giving us accuracy till the fourth order as compared to Euler method which gives us accuracy to the first order. For short time dynamics where the total time of evolution is $T \sim 10^{2-3}$ a step size of $\delta t \sim 0.001 - 0.01$ is computationally efficient and we get a total error in energy of the order $\mathcal{O}(T * \delta t^4) \sim \mathcal{O}(10^{-5})$. To study auto-correlation exponents $\langle S(0)S(t)\rangle \sim t^{-\alpha}$ which reveal information about the nature of dynamics whether it be ballistic ($\alpha = 0.5$) or diffusive ($\alpha = 1$) or anomalous (eg. KPZ $\alpha = 2/3$) we need to evolve to long times $T \sim 10^{6-8}$ and this is beyond the acceptable error limit in the classical RK methods. We could extend the RK method to an eight order method but this is extremely expensive and slow within any reasonable limit as the time step limits the computation and applicability of the method. In such circumstances we use a different integration scheme also known as the discrete time odd-even (DTOE) update, which we shall discuss briefly below.

2.8.5 Dynamical Structure factors

Neutron scattering experiments provide vital information of the structure as well as the magnetic excitations of the solid. Since neutrons are charge neutral species they are an ideal probe interacting directly with the nuclei and through magnetic interactions with other species possessing a magnetic moment. Neutron scattering experiments probe magnetic excitations (magnon propagation) through inelastic scattering where the Intensity of scattering is related to the scattering cross-section via

$$
I(\vec{q},\omega) \propto d^2\sigma/d\Omega dE \propto \sum_{\alpha\beta}\left(\delta_{\alpha\beta} - \frac{q_\alpha q_\beta}{q^2+\eta^2}\right) S^{\alpha\beta}(\vec{q},\omega) \tag{2.82}
$$

where the spin correlation function is known as the **Dynamical structure factor**,

$$
S^{\alpha\beta}(\vec{q},\omega) = \frac{1}{N}\int_{-\infty}^{\infty} dt \sum_{i,j}^{N} e^{-i\vec{q}\cdot(\vec{r}_i - \vec{r}_j)} e^{i\omega t} \langle S_i^\alpha(0) \cdot S_j^\beta(t)\rangle \tag{2.83}
$$

and the **static structure factor** which measures the spatial correlation between spins and shows up as Bragg peaks in the scattering experiments is just given by the integral over energy of the dynamical spin structure factor

$$
S^{\alpha\beta}(\vec{q}) = \int d\omega S^{\alpha\beta}(\vec{q},\omega) = \frac{1}{N}\sum_{i,j}^{N} e^{-i\vec{q}\cdot(\vec{r}_i - \vec{r}_j)} \langle S_i^\alpha(0) \cdot S_j^\beta(0)\rangle \tag{2.84}
$$

There is a slight subtlety between static structure factor $S^{\alpha\beta}(\vec{q})$ and the elastic part of dynamical structure factor $S^{\alpha\beta}(\vec{q},\omega = 0)$. The later is a Fourier transform of the snapshot of configurations of spins at a particular instant of time (equal time correlator) while the former is a long time average of the dynamical correlator.

It is possible to express the dynamical structure factor as a sum of elastic and inelastic contributions as

$$S(\vec{q},\omega) \propto \sum_G \delta(\vec{q}-\vec{G})\delta(\omega) + \sum_k \frac{|\vec{q}\cdot e(\vec{k}))|}{\omega(k)}[n(k)\delta_{\omega,-\omega(k)}\delta(\vec{q}+\vec{k}-\vec{G}) \tag{2.85}$$

$$+(n(k)+1)\delta_{\omega,\omega(k)}\delta(\vec{q}-\vec{k}-\vec{G})+...] \tag{2.86}$$

where $e(\vec{k})$ is the polarization vector and $n(k) = 1/(\exp(\omega(k)/T)-1)$ is the Bose-Einstein distribution of the magnons at a particular temperature. The first term corresponds to elastic scattering and the second and third terms correspond to inelastic scattering processes to linear order where magnons are absorbed and created.

Algorithm 6 Computing Dynamical Structure factors

1: Find the path in momentum q - space along which to compute the DSF
2: Compute time evolution of spins using Euler methods or RK methods
3: Compute the Fourier transformation of spins in q space $\vec{S}_{\vec{q}}(t) = \frac{1}{\sqrt{N}}\sum_{i=1}^{N} e^{-i\vec{q}\cdot\vec{r}_i}\vec{S}_i(t)$
4: Compute spin correlators in time $S^{\alpha\beta}(q,t) = (\langle S^{\alpha}_{\vec{q}}(0)S^{\beta}_{-\vec{q}}(t)\rangle)$
5: Compute the Fourier transform in time to get the DSF $S^{\alpha\beta}(q,\omega) = FT(S^{\alpha\beta}(q,t))$

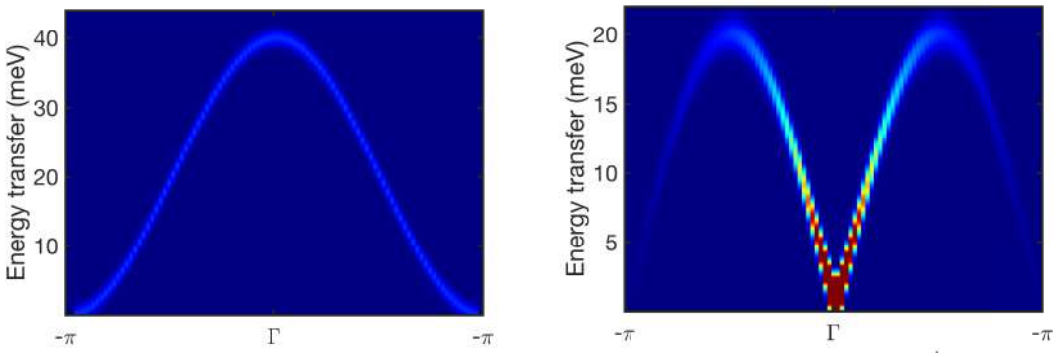

FIGURE 2.13: The dynamical structure factors computed for the 1D FM(left) and AFM(right) chains using SpinW program. These are exactly the same as the spectrum in Fig 2.12 and show that for ordered systems it is possible to recover information about the magnetic order as well as the effective Hamiltonian by looking at the DSF spectrum.

2.8.6 Numerical details

Numerically, we have a finite time step parameter (δt) from the dynamical evolution of spins, which means we store spin snapshots at discrete intervals of time implying that we need to modify our definition of the dynamical structure factor as,

$$S^{\alpha\beta}(\vec{q},\omega) = \frac{1}{\sqrt{N_t}N}\sum_{i,j}^{N} e^{-i\vec{q}\cdot(\vec{r}_i-\vec{r}_j)}\sum_{n}^{N_t} e^{i\omega n\delta t}\langle S^{\alpha}_i(0)\cdot S^{\beta}_j(n\delta t)\rangle \tag{2.87}$$

here $\delta t = T_{max}/N_t$ is the minimal time step for the spin evolution. This imposes a limit on the energy resolution from the Heisenberg energy time uncertainty relation, with the resolution being $\delta\omega \sim 1/\delta t$.

Since the underlying lattice is discrete, the reciprocal momentum is discrete too with a maximal resolution given by $\delta q = 2\pi/(L\cdot a)$ where L is the system size and a is the lattice constant. The

dynamical structure factors are usually calculated along a path through momentum/reciprocal space, where path $\subset \{\vec{q}_i = \frac{2\pi}{La}(n_1\vec{b}_1 + n_2\vec{b}_2)\}$ here $\vec{b}_i$ are reciprocal lattice vectors and $n_i \in \{0, ..., 2\pi/L\}$.

Once the values of $\{q\}$ for the path are determined it is easiest to compute the DSF by first Fourier transforming with respect to $\vec{q}$

$$\vec{S}_{\vec{q}}(t) = \frac{1}{\sqrt{N}} \sum_{i=1}^{N} e^{-i\vec{q}\cdot\vec{r}_i} \vec{S}_i(t) \tag{2.88}$$

Subsequently, the DSF is computed using any discrete Fast Fourier Transform (dFFT) package as

$$S^{\alpha\beta}(\vec{q}, \omega) = \langle S^{\alpha}_{\vec{q}}(\omega) S^{\beta}_{-\vec{q}}(-\omega) \rangle = \mathbf{FFT}(\langle S^{\alpha}_{\vec{q}}(0) S^{\beta}_{-\vec{q}}(n\delta t) \rangle) \tag{2.89}$$

and to compare with experiments which measures the scattered intensity $I(\vec{q}, \omega) \propto d^2\sigma/d\Omega dE$ we compute

$$I(\vec{q}, \omega) = \sum_{\alpha\beta} \left(\delta_{\alpha\beta} - \frac{q_\alpha q_\beta}{q^2 + \eta^2} \right) S^{\alpha\beta}(\vec{q}, \omega) \tag{2.90}$$

here $\eta \approx 0.01$ is a small renormalization parameter added to avoid a $0/0$ division.

The DSF are very strongly peaked around high symmetry points, which show as Bragg peaks in the static structure factors as can be seen by integrating over energy $S(\vec{q}) = \sum_\omega S(\vec{q}, \omega)$, and obfuscate the salient features of magnon propagation which have an intensity almost 3 orders of magnitude lesser than the Bragg peaks. The resolution is a naive subtraction of high symmetry points from the path or rescaling of intensities around high symmetry points to amplify the background magnon propagation.

An additional resolution to compare with experiments is to multiply the intensity with a form factor of the form $\mathcal{F}(\vec{q}) = A \exp\left(-a|\vec{q}|/4\pi\right)^2$ where the coefficients are known from literature or other experiments.

To avoid numerical artefacts which come from discretization of time and discontinuities at the time boundaries $(0, T_{max})$ we need to convolute the intensity with a Gaussian envelop and impose a Gaussian energy resolution with FWHM $(\sim 2\pi\delta t)$. A further energy convolution is added if one wishes to compare with experiments reflecting the finite energy resolution of the measurements.

2.9 Currents and conductivities

In this section we shall give a broad overview of spin and thermal currents in the purview of semiclassical dynamics [146]. We shall also highlight the connection between conservation and conductivities given in the context of linear response theory by the Kubo formula.

For every constants of motion a system possess, the equation of conservation (in time) implies a continuity equation and an associated local current density $j(r, t)$ with the conserved operator O. We obtain the net current by integrating the current density over all space,

$$\mathcal{J}_O(t) = \int d\vec{r} j_O(\vec{r}, t) = \int d\vec{r}\vec{r} \frac{\partial}{\partial t} O(\vec{r}, t) \equiv \sum_i \vec{r}_i \frac{\partial}{\partial t} O_i(t) \tag{2.91}$$

where an integral over r and integration by parts is carried out excluding the boundary terms and the sum over all lattice points represents a discretized version of the same.

2.9.1 Kubo Formula

We shall begin with a general derivation of the Kubo-Green formula [123, 239] and subsequently derive the formulas for spin and thermal conductivities used in this thesis.

Let us consider an isolated system describable by Hamiltonian $\mathcal{H}$ with a true ground state represented by $|G\rangle$ coupled to an external weak perturbation whose dynamics could be described by $\mathcal{H}_{ext}$ and let $O(\vec{x},t)$ be a local observable such as energy density or magnetization in whose measurement we are interested. The full Hamiltonian describing the interaction of the system with the external force is given by

$$\mathcal{H}_T(t) = \mathcal{H} + \mathcal{H}_{ext}(t) \tag{2.92}$$

The expectation values of the local observable under this coupling is describable in the interaction picture where the observables evolve according to the unperturbed Hamiltonian (the Heisenberg picture) but the states evolve according to the external perturbation (Schödinger picture) which is written using the time ordering operator (T) to preserve causality as

$$\langle O(\vec{x},t)\rangle = \langle G|U(t)O(\vec{x},t)U^{\dagger}(t)|G\rangle \ , \ U(t) := T\exp(-i\int_{-\infty}^{t} d\tau \mathcal{H}_{ext}(\tau)) \tag{2.93}$$

Linear response is the response of the system to the lowest order in the external perturbation which can be written by expanding out the unitary operator and retaining the first term as

$$\delta\langle O(\vec{x},t)\rangle = i\int_{-\infty}^{t} d\tau \ \langle[\mathcal{H}_{ext}(\tau), O(\vec{x},t)]\rangle \tag{2.94}$$

it is also important to note that causality is always maintained as the external perturbation drives the system for times earlier than the time at which we make a measurement on the local observable O i.e. $\tau < t$.

In most scenarios the external perturbation is linearly coupled to the observable we wish to measure, for example when we wish to measure the magnetization response we couple the system to an external magnetic field which couples to the spins in a Zeeman fashion as $\vec{B}\cdot\vec{S}$ and can be expressed in terms of a linear force $f(\vec{x},t)$ term as

$$\mathcal{H}_{ext}(t) = \int d\vec{x} O(\vec{x},t) f(\vec{x},t) \tag{2.95}$$

resulting in the expression for the linear response to the external linear force as

$$\delta\langle O(\vec{x},t)\rangle = i\int_{-\infty}^{t} dt' \int d\vec{x}' \langle[O(\vec{x}',t'), O(\vec{x},t)]\rangle f(\vec{x}',t') = \int_{-\infty}^{t} dt' \int d\vec{x}' \chi(\vec{x}'t',\vec{x},t) f(\vec{x}',t') \tag{2.96}$$

where χ is just the correlator between the local observables and is known as *generalized susceptibility* or the retarded Green's propagator. Taking a Fourier transform in time leads to expressing the susceptibility in frequency space which is known generalized *Kubo formula*

$$\chi(\vec{x},\vec{x}';\omega) = -i\int_{-\infty}^{0} d\tau \exp(-i\omega\tau)\langle[O(\vec{x}',0), O(\vec{x},\tau)]\rangle \tag{2.97}$$

From the Fick's law of diffusion we can express the flux of flow $\vec{j}$ in terms of gradient of a concentration $C(\vec{r},t)$ as

$$\vec{j} = -D\vec{\nabla}C \tag{2.98}$$

where D is the diffusion constant. From the equation of conservation i.e. $\dot{C} = 0 = \partial C/\partial t + \vec{\nabla} \cdot \vec{j}$ we get solution for the concentration in terms of the diffusion constant describing the diffusion in time as an exponential decay with distance as ,

$$\frac{\partial C(\vec{r},t)}{\partial t} - D\nabla^2 C(\vec{r},t) = 0 \implies C(\vec{r},t) = \frac{1}{(4\pi Dt)^{d/2}} \exp(-\frac{r^2}{4Dt}) \tag{2.99}$$

measuring the time derivative of the mean squared displacement then gives us the diffusion constant which is also known as the *Einstein relation* following his work on Brownian motion and random diffusion i.e.

$$\frac{\partial}{\partial t} \int d\vec{r} r^2 C(\vec{r},t) = D \int d\vec{r} r^2 \nabla^2 C(\vec{r},t) \implies \frac{\partial}{\partial t} \langle r^2(t) \rangle = 2dD \tag{2.100}$$

We can instead express diffusion constant as a correlator in time by expressing displacement as an integral of velocity i.e. $\vec{r}(t) = \int_0^t dt' \vec{v}(t')$ which results in the mean squared displacement being expressed in one dimension for simplicity as

$$\langle r^2(t) \rangle = \int_0^t \int_0^t dt' dt'' \langle v(t') v(t'') \rangle = 2 \int_0^t \int_0^{t'} dt' dt'' \langle v(t') v(t'') \rangle \tag{2.101}$$

at equilibrium since only the difference in time is relevant we have

$$D = \lim_{t\to\infty} \frac{1}{2} \frac{\partial}{\partial t} \langle r^2(t) \rangle = \lim_{t\to\infty} \int_0^t dt' \langle v(t') v(0) \rangle \tag{2.102}$$

and this equation is known as the *Green-Kubo* formula. If we consider the flux as just a flow of charge i.e. $\vec{j} = q\vec{v}$ then the diffusion constant (in two or more dimensions) attains a tensor character corresponding to the possible correlations between the different directions of diffusion i.e. with respect to the mean squared displacement $\langle r_\mu r_\nu \rangle$ $\mu, \nu = \{x, y, z..\}$ and can be written in terms of these fluxes as

$$D_{\mu\nu} = \frac{1}{q^2} \lim_{t\to\infty} \int_0^t dt' \langle j_\mu(t') j_\nu(0) \rangle \tag{2.103}$$

This general theory can also be extended to spin systems where we could consider the diffusion of energy or of spin magnetization corresponding to the coupling of the spin system either with an external thermal bath giving rise to energy diffusing through the system or with an external magnetic field gradient giving rise to the diffusion of spin magnetization.

The interaction of thermal ∇T and magnetic field ∇H gradients with magnetic moments are responsible for magnon mediated thermal and spin currents respectively. Linear response theory then gives a relation between the driving forces and the response.

$$\begin{pmatrix} j_s \\ j_{th} \end{pmatrix} = \begin{pmatrix} L_{s,s} & L_{s,th} \\ L_{th,s} & L_{th,th} \end{pmatrix} \cdot \begin{pmatrix} \nabla H \\ -\nabla T/T \end{pmatrix} \tag{2.104}$$

In 1D systems $L_{m,n}$ are scalars and in 2D systems they are 2×2 tensors as required by the dimensionality of the lattice. The spin and thermal conductivities are then given as,

$$\sigma = L_{s,s} \quad , \quad \kappa = \frac{1}{T} \left(L_{th,th} - \frac{L_{s,th}^2}{L_{s,s}} \right) \tag{2.105}$$

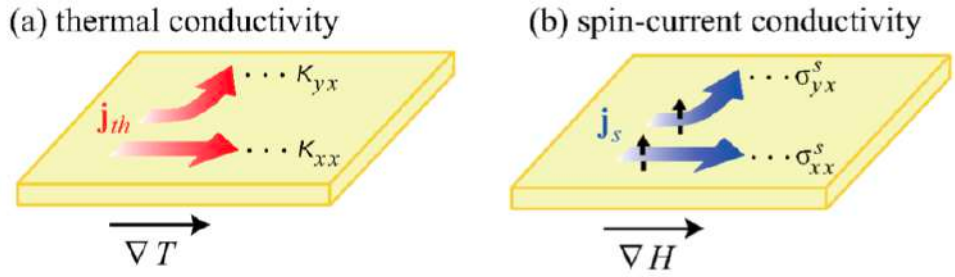

FIGURE 2.14: The thermal and magnetic field gradients responsible to thermal and spin currents are shown here. The spin polarization (shown by the black arrow) is assumed perpendicular to the plane which refers to the conserved component of spin magnetization. Figure reproduced from [9]

In the models we consider in this thesis, without an external magnetic field, we have $L_{s,th} = L_{th,s} = 0$ as these quantities are odd with respect to the spins. From the Green Kubo formula we then have

$$L^{\mu,\nu}_{m,n} = \frac{1}{VT} \lim_{\tau\to\infty} \int_0^\tau dt \langle \mathcal{J}^\mu_m(0) \mathcal{J}^\nu_n(t) \rangle \tag{2.106}$$

here $m, n \in \{s, th\}$ and $\mu, \nu = \{x, y\}$ indicate the physical lattice directions.

$$\sigma_{\mu\nu}(T) = \frac{1}{TL^2} \lim_{\tau\to\infty} \int_0^\tau dt \langle \mathcal{J}^\mu_s(0) \mathcal{J}^\nu_s(t) \rangle_T \tag{2.107a}$$

$$\kappa_{\mu\nu}(T) = \frac{1}{T^2L^2} \lim_{\tau\to\infty} \int_0^\tau dt \langle \mathcal{J}^\mu_{th}(0) \mathcal{J}^\nu_{th}(t) \rangle_T \tag{2.107b}$$

here $\langle ... \rangle_T$ denotes an ensemble thermal average with respect to a canonical equilibrium distribution $e^{-\beta H}/Z$ where Z is the canonical partition function and $\beta = 1/T$ is the inverse temperature [9, 156]. It has to be emphasised that we don't approximate the interactions between spins to linear order or the nature of spins and consider only first order perturbations as done in spin waves. LL(G) dynamics is exact in the sense that includes all orders of magnon-magnon interactions. In particular any relaxation or damping effects of the currents, has its origins purely in the higher order magnon-magnon and magnon-phonon interactions and hence is intrinsic to the system under consideration.

Chapter 3

Hidden Symmetries in the JK model

In the previous chapters we introduced TK-SVM and discussed about the techniques and methodology which makes it an *interpretable and unsupervised* machine learning algorithm. This chapter and the subsequent chapters are devoted to the application of TK-SVM in analyzing the physics of Kitaev magnets and in particular investigate the phase diagram as well as the dynamics and transport of the generalized $JK\Gamma$ model and its extensions on the 2D hexagonal lattice introduced in the first chapter (Chapter 1).

In this chapter we focus on the JK model and elucidate various aspects of TK-SVM discussed in the previous chapters and also highlight its applicability in detecting hidden orders at high symmetry points.

Symmetries form the basis of our understanding of physics as exemplified by Noether theorem, which states that the existence of continuous symmetries implies conserved quantities. Symmetries (invariance under continuous translations/deformations) in time, space, and rotations lead to the conservation of energy, momentum, and angular momentum respectively. These kinds of symmetries are well understood in physics. Additionally, in certain many-body systems there often exists an effective symmetry also known as *hidden symmetry* which as the name suggests is not apparent.

At these hidden symmetry points a complex spin ordering pattern may be transformed into a simple one [39, 40, 92] and the existing knowledge of conventional phases could be applied to analyze the phase. Recently there has been a lot of interest in extended Kitaev systems as they are close to Kitaev spin liquids (KSLs) [119] and other exotic phases [94, 41, 208, 97, 228] where high-symmetry points exist. Others examples of these high symmetry points are the Bethe-ansatz solvable $SU(3)$ point in the spin-1 bilinear-biquadratic chain [216, 125, 205, 19] and the emergent $O(4)$ symmetry in the spin-1/2 J-Q model [244] and the $SO(4)$ points for the Hydrogen atom and CFT3 point at the tip of the lobe in Bose-Hubbard models.

In general identification of high-symmetry points is a non-trivial task and is very much problem-dependent requiring experience and insights from the investigators. Here we demonstrated how TK-SVM facilitates the identification of *high symmetry SO(3) points* in the JK model and the correct characterization of the complete order parameters for the zigzag and stripy phases given by the D_2 and D_{2h} ordering matrices respectively.

3.1 Model and methods

We investigated the Heisenberg Kitaev (JK) model on the 2D hexagonal lattice defined by the Hamiltonian,

$$\mathcal{H} = \sum_{<ij>_\gamma} J\vec{S}_i \cdot \vec{S}_j + KS_i^\gamma S_j^\gamma, \tag{3.1}$$

where J and K denote the Heisenberg and Kitaev interaction, respectively, and parametrized by the phase angle $\varphi \in [0, 2\pi)$ with $K = \sin\varphi$, $J = \cos\varphi$ and $\gamma \in \{x, y, z\}$ labels the three types of nearest-neighbor bonds on the hexagonal lattice between neighbouring spins $\vec{S}_i, \vec{S}_j$ as $< ij >_\gamma$. Thus is depicted in Figure 3.1 above.

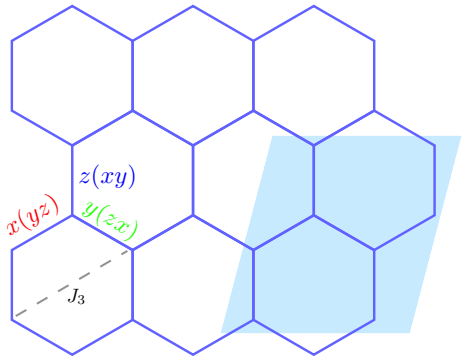

FIGURE 3.1: Depiction of the a honeycomb lattice and the D_{2h} and D_2 magnetic cell, which contain eight spins and two sectors marked by A (blue) and B (red). This choice of magnetic cell fits zigzag and stripy patterns along different directions and also applies to states at the hidden $O(3)$ points which cannot be captured by a four-site zigzag or stripy cell. x, y, and z label the three distinct bonds in the Kitaev interaction.

The quantum spin-$\frac{1}{2}$ version of the JK model was shown by Chaloupka [41, 40] to accommodate four simple magnetic orders, antiferromagnet, zigzag, ferromagnet and stripy in addition to the two extended regions of quantum spin liquids under finite Heisenberg perturbation. We found that in the large-S limit of classical spins corresponding to $S \to \infty$, the four magnetic orders are persistent and shared similar phase boundaries of the corresponding phases in the quantum model expect the regions of the classical spin liquids which were shrunk to only a single point at $K = \pm 1$ at low temperatures ($T \sim 10^{-3}$). In addition we found the high symmetry points with the $SO(3)$ symmetry hidden deep inside the zigzag and stripy phases respectively at the phase point $K = -2J$ and the transformations identifying these points were the same as in the quantum case described by Chaloupka et al signifying the applicability of our machine in detecting hidden symmetries.

To implement TK-SVM and study the topology of the phase diagram via Fiedler partitioning we introduced a uniformly spaced fictitious grid in the 1D parameter space where our only parameter is φ, with a spacing of $\delta\varphi = \frac{\pi}{48}$ and a total of $M = 96$ parameter points between $[0, 2\pi)$. To train the machine we then sampled 500 spin configurations from a classical parallel tempered Monte Carlo ensemble on a $L = 72$ lattice of 10,368 spins at a low temperature ($T = 10^{-3}\sqrt{J^2 + K^2}$) at each of the parameter points . We then performed an SVM classification on the data and found that rank $r = 1$ was sufficient to learn the topology of the phase diagram, which was expected as the phases in the quantum model had simple magnetic orders. This Fiedler partitioning resulted in a graph of $M = 96$ vertices and $M(M-1)/2 = 4,560$ edges to which we added an additional dimension (by adding a random value to each phase point) as the parameter space was one dimensional to show the results of the spectral clustering and the topology of the phase diagram in two dimensions 3.2.

3.2 Topology of the Phase Diagram

Each of the edges in the above graph partitioning were Lorentzian weighted with a characteristic cutoff parameter ρ_c which sets the scale for points belonging to the "sameness" of vertices. However we found that the choice of ρ_c as shown in Figure 3.4 was **not very crucial** and the partitioning is robust over a wide range of the critical parameters. We compared the Fiedler vector decomposition using a wide range of ρ_c from $10^{-1} - 10^4$. and found that at $\rho_c = 0.1$ the partitioning is less obvious as all Fiedler vector entries are very similar and hence it did not help us in distinguishing the phases. We then used $\rho_c = 10^3$ since it gave us the most clearly distinguishable Fiedler vector segregation.

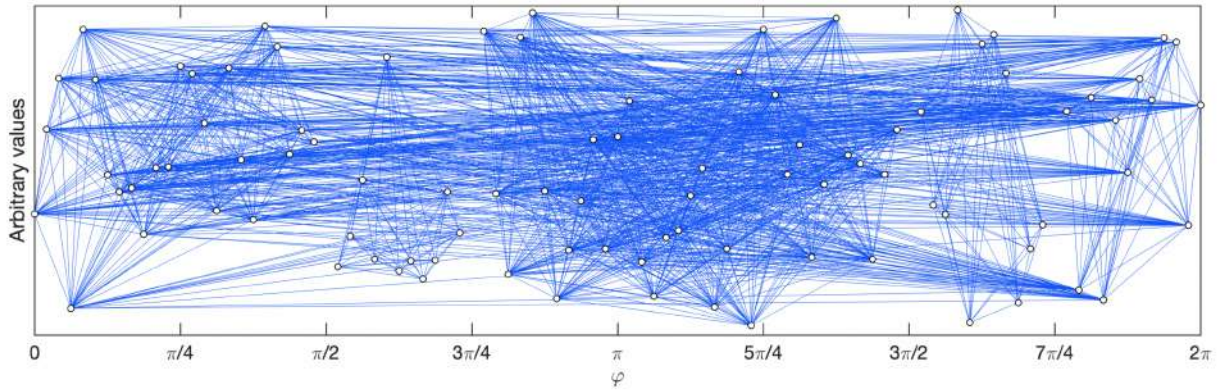

FIGURE 3.2: The Lorentzian weighted graph with M vertices and $M(M-1)/2$ edges. In order to produce a 2D graph (as there is only 1 parameter φ) an additional random value is added as the y component. From the figure we identify 5 densely populated subgraphs which are further analysed by Fiedler partitioning where parameter points in each subgraph have similar Fiedler vector values.

Visually there appeared to be 5 strongly connected subgraphs Fig 3.2 and however Fiedler vector analysis showed that two of the subgraphs correspond to the same phase and hence in total there are 4 distinct subgraphs corresponding to the 4 distinct magnetic phases as expected. These distinct phases appear as plateaus corresponding to the constant Fiedler values as discussed in Chap 2 and the Fiedler decomposition is shown in Fig 3.3.

We were able to successfully reproduce the classical JK phase diagram known in literature [174, 96]. The four plateaus starting from the left correspond to the antiferromagnetic (AFM), zigzag (ZZ), ferromagnetic (FM) and stripy (ST) phase, following the labeling in Figure 3.3 (a). However, as we shall discuss subsequently, by analyzing the coefficient matrix we found that the "traditional" zigzag and stripy orders in the regions $\varphi \in (\frac{\pi}{2}, \frac{3\pi}{4})$ and $(\frac{3\pi}{2}, \frac{7\pi}{4})$ were better characterized by the D_2 and D_{2h} order parameters respectively.

The discrete jumps in the Fiedler vector entries are interpreted as phase transitions which occur at $J = 0$, $K = \pm 1$ ($\varphi = \frac{\pi}{2}, \frac{3\pi}{2}$) and $J = -K$ ($\varphi = \frac{3\pi}{4}, \frac{7\pi}{4}$). The jumps at $\varphi = \pi/2, 3\pi/2$ at $K = \pm 1$ correspond to the Kitaev limits where the classical spin liquids are shrunk to a point. When we analyzed the $C_{\mu\nu}$ matrix at rank 1, we found that since the spins are uncorrelated and there is no underlying magnetic order these matrices appeared random inline with our expectations .

We remind the reader that the learning of Figure 3.3 is completely unsupervised which means one does not require any prior knowledge of the phase diagram or order parameters and all the four phases were discriminated simultaneously by a *single* partitioning. Once we determined the global topology of the phase diagram, whose resolution is set by the given training data set, we dug deep into each phase and analyzed the coefficient matrices at ranks 1 and 2 to infer the local constraints as well as the order parameters. Once we had these order parameters it became more convenient to *refine phase boundaries* by examining the change in magnetization with parameter values. This is the general strategy one employs with TK-SVM when dealing with unknown phase diagrams and also demonstrates its strength and utility.

3.2.1 Constructing Explicit Order Parameters

Having constructed the phase diagram using Fiedler clustering we investigated each subgraph by exploiting the strong interpretability of TK-SVM. We chose a particular parameter point deep in each subgraph and extracted the analytical order parameters from the the corresponding coefficient matrix $C_{\mu\nu}$ trained at rank 1 and averaged using a 8 spin cluster as it was the optimal choice to capture all the orders. The extraction and interpretation of the trivial FM and AFM orders is skipped and we shall illustrate the inference of orders from the non trivial zigzag and stripy phases.

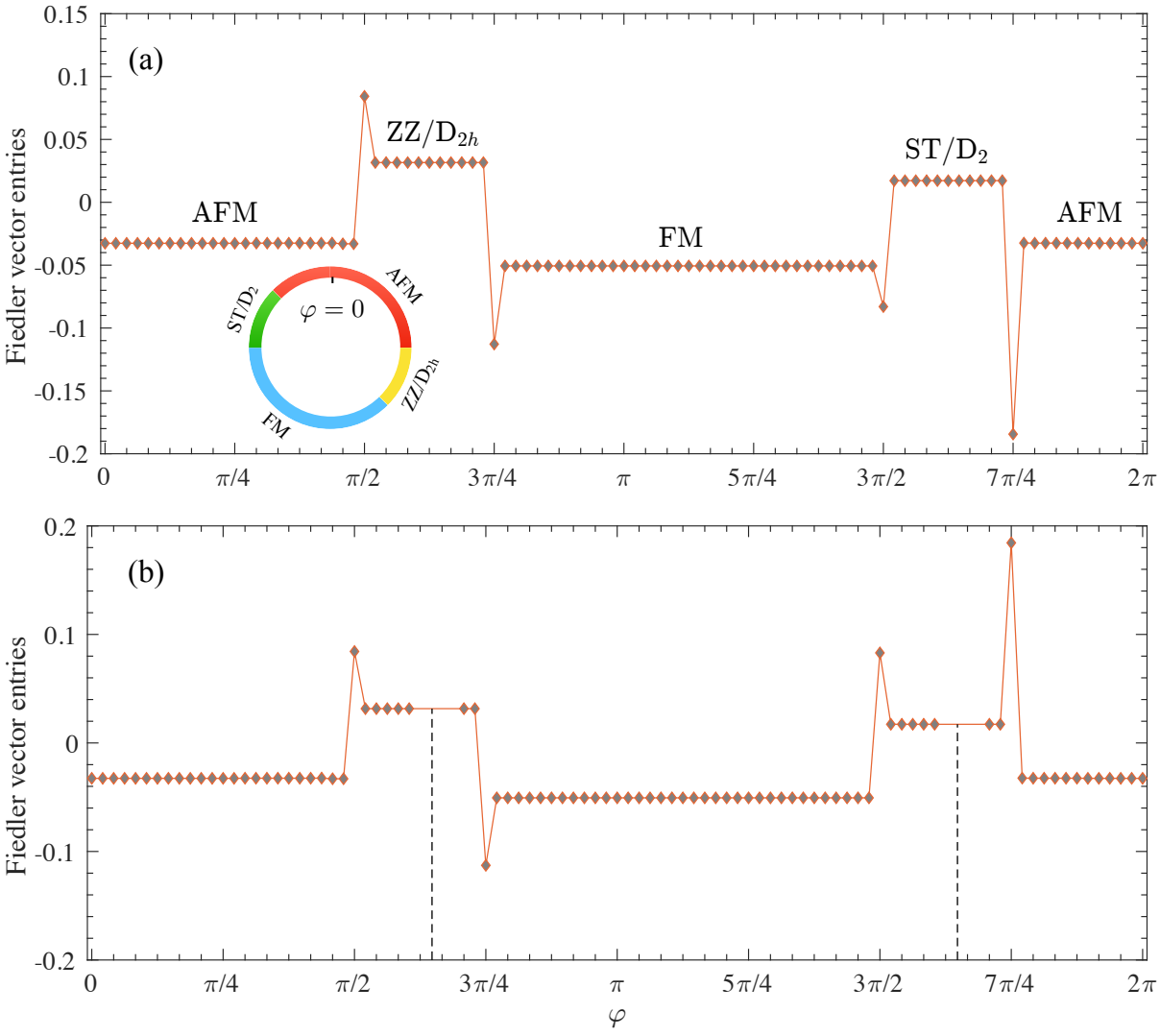

FIGURE 3.3: The Fiedler vector acts as the phase diagram of the Heisenberg-Kitaev model. (a) Gradients in Fiedler vector entries reflect the clustering of the graph. The plateaus indicate stable phases, and the jumps signal phase transitions. The phases are labeled following the common convention: AFM, antiferromagnet; ZZ, zigzag; FM, ferromagnet; ST, stripy. In addition, the ST and ZZ region are also marked according to the D_2 and D_{2h} magnetization. The inner panel shows a circular representation of the phase diagram. (b) Another partitioning removing data near the high-symmetry points $\varphi = \arctan(-2) \sim 0.65\pi$ and 1.65π (indicated by the dashed lines; the graph is not shown), to demonstrate that data of these special points are not needed for revealing the hidden $O(3)$ symmetry. The partitioning is reflected by contrasts between Fiedler vector entries, rather than the absolute values. Panels (a) and (b) lead to the same topology of the phase diagram.

From the coefficient matrices for the zigzag henceforth called D_{2h} and stripy phases labelled D_2 as we discussed in Chapter 2 we extracted the corresponding order order parameters are given in Table 3.1. Just as a reminder to the reader, we reiterate that the $C_{\mu\nu}$ matrix at rank 1 gives the correlation between the spin components of the 8 spins corresponding to the cluster we chose i.e. the correlations $\langle S_i^{\alpha_k} S_j^{\alpha_l} \rangle$ with $\alpha_k \in \{1, 2...8\}$ and $i \in \{x, y, z\}$ and each block is a 3×3 matrix elucidating all possible correlations between the spin components. This alternate labelling of the phases corresponds to the symmetry group to which the ordering matrices belong.

In the case of D_2 a spin cluster of 4 spins was sufficient but in case of D_{2h} we required a minimal cluster of 8 spins to accommodate all spin correlations. The correlation matrices between the 8 spins are described by the ordering matrices which when applied to a cluster of uniformly aligned

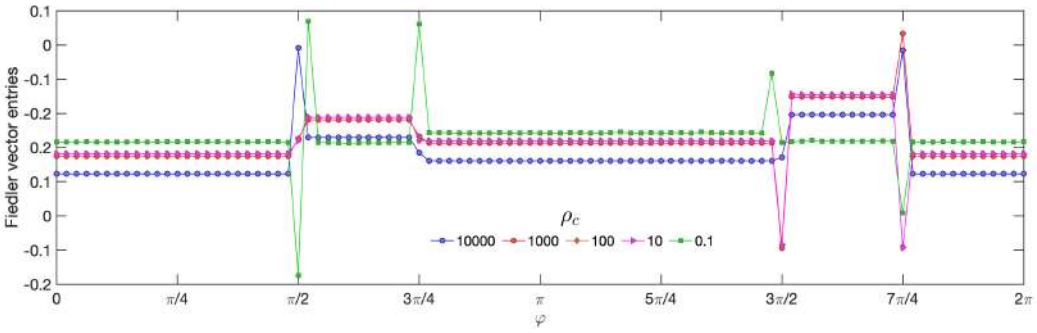

FIGURE 3.4: Fiedler vectors obtained with different choices of ρ_c. In all cases, where ρ_c is large enough to set a characteristic scale "$\gg 1$" for the reduced ρ criterion, the clustering is evident and robust. The profound jumps at $\varphi = \frac{\pi}{2}, \frac{3\pi}{4}, \frac{3\pi}{2}, \frac{7\pi}{4}$ correspond to phase boundaries, as they do not belong to any plateaus (stable phases).

spins i.e. spins in the FM phase would give the respective orders or inversely when applied to the existing order would give the FM order. The FM and AFM phases the ordering matrices were trivial $\hat{T}_{FM,all} = \mathbf{I}$ and $\hat{T}_{AFM,odd} = \mathbf{I}$, $\hat{T}_{AFM,even} = -\mathbf{I}$. The ordering matrices for the non-trivial phases are shown below in the table below

Phases	**Ordering Matrices**	
$D_2(ST)$	$\hat{T}_1^{A,B} = \begin{pmatrix} 1 & 0 & 0 \\ 0 & 1 & 0 \\ 0 & 0 & 1 \end{pmatrix}$,	$\hat{T}_2^{A,B} = \begin{pmatrix} -1 & 0 & 0 \\ 0 & -1 & 0 \\ 0 & 0 & 1 \end{pmatrix}$,
	$\hat{T}_3^{A,B} = \begin{pmatrix} -1 & 0 & 0 \\ 0 & 1 & 0 \\ 0 & 0 & -1 \end{pmatrix}$,	$\hat{T}_4^{A,B} = \begin{pmatrix} 1 & 0 & 0 \\ 0 & -1 & 0 \\ 0 & 0 & -1 \end{pmatrix}$
$D_{2h}(ZZ)$	$\hat{T}_1^{A,B} = \pm\begin{pmatrix} 1 & 0 & 0 \\ 0 & 1 & 0 \\ 0 & 0 & 1 \end{pmatrix}$,	$\hat{T}_2^{A,B} = \pm\begin{pmatrix} 1 & 0 & 0 \\ 0 & 1 & 0 \\ 0 & 0 & -1 \end{pmatrix}$,
	$\hat{T}_3^{A,B} = \pm\begin{pmatrix} -1 & 0 & 0 \\ 0 & 1 & 0 \\ 0 & 0 & -1 \end{pmatrix}$,	$\hat{T}_4^{A,B} = \pm\begin{pmatrix} -1 & 0 & 0 \\ 0 & 1 & 0 \\ 0 & 0 & 1 \end{pmatrix}$

TABLE 3.1: D_2 and D_{2h} ordering matrices. Their magnetic cells are shown in Figure 3.1, which consist of two sectors, labeled by A, B, and in total eight sublattices. The D_2 and D_{2h} orders involve four and eight distinct spin orientations, respectively, and are described by the respective three-dimensional dihedral groups.Their ordering matrices also define the sublattice transformations that identify the hidden $O(3)$ points in the Heisenberg-Kitaev model.

The magnetizations can be defined in terms of the ordering matrices as

$$\overrightarrow{M} = \frac{1}{8} \sum_{A,B} \sum_{k=1}^{4} \hat{T}_k^{A,B} \vec{S}_k. \tag{3.2}$$

where the ordering matrices $\hat{T}_k^{A,B}$ describing the relative spin orientations in the cluster are tabulated in Table 3.1 above.

The stripy phase (ST) comprised of four matrices in the dihedral group D_2 with $\hat{T}_k^A = \hat{T}_k^B$. These matrices were proposed in the study of orbital degeneracy of Mott insulators [111, 110] and play a crucial role in the identification of hidden symmetries of the JK model [41, 39] as we shall discuss below. The zigzag phase (ZZ) could be viewed as an AFM version of the Stripy phase with $\hat{T}_k^A = -\hat{T}_k^B$ and hence represented by the dihedral group $D_{2h} \cong D_2 \times Z_2$.

3.2.2 Measuring the order parameters

We confirmed that we had correctly interpreted the coefficient matrices and also sharpened our phase boundaries, which in this simple model coincided with the ones derived from Fiedler partitioning, by measuring the appropriate order parameters including the trivial FM and Néel orders, at $T = 10^{-3}\sqrt{J^2 + K^2}$ the temperature at which we trained our TK-SVM. The results of this measurement are shown below in Fig 3.5 where in each phase as a consequence of the correct interpretation the magnetization saturated to 1 but in all other phases vanished. We however observed a small overlap between magnetizations at the phase boundaries $\varphi = 3\pi/4, 7\pi/4$ which could be interpreted as finite size effects and in addition we found that the classical ground states have a subextensive degeneracy with chains of decoupled FM and AFM Ising chains.

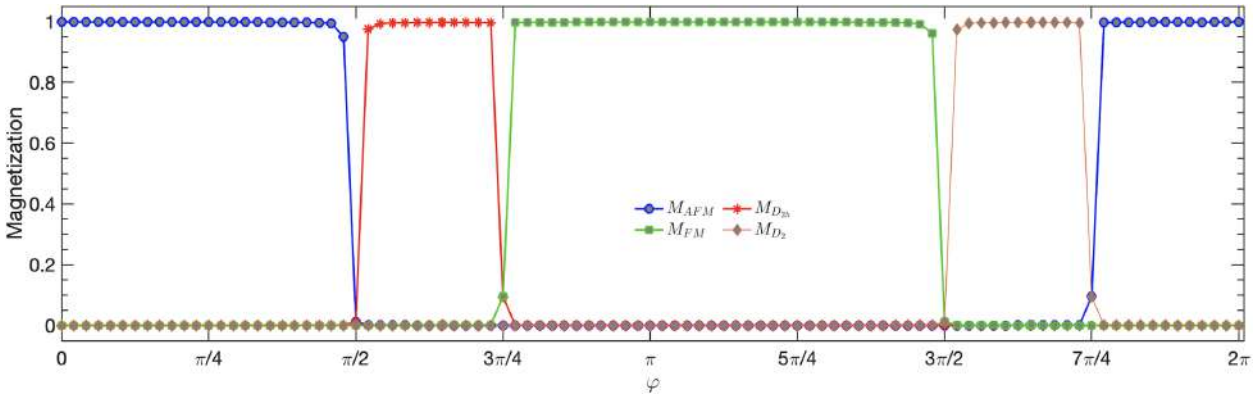

FIGURE 3.5: Measurements of order parameters. The FM, AFM, D_2 and D_{2h} magnetization are measured as a function of φ at low temperature $T = 10^{-3}\sqrt{J^2 + K^2}$. In each phase, the respective magnetization ($M = \langle|\frac{1}{N_{cell}}\sum_{cell}\vec{M}|\rangle = 1$) saturates to unity, while others vanish, where $\vec{M}$ is the ordering moment in one magnetic cell, $\sum_{cell}$ sums over magnetic cells, and $\langle ...\rangle$ denotes the ensemble average. The small residual moments at $\varphi = 0.75\pi$ and 1.75π are finite-size effects. At these points, the classical ground states form decoupled FM and AFM Ising chains with a subextensive degeneracy.

3.3 Discussion on D_2 and D_{2h} phases

The measurements of D_{2h} and D_2 order parameters and their saturation to unity in the respective phases validated our claim that they are the correct order parameters for the regions $\varphi \in (\frac{\pi}{2}, \frac{3\pi}{4})$ and $(\frac{3\pi}{2}, \frac{7\pi}{4})$. described in literature by zigzag and stripy orders respectively [175, 174, 96].

We shall now elaborate the differences and similarities between these orders. From the static structure factors plotted we observed that D_{2h} and ZZ, D_2 and ST have very similar SSFs as shown in Figure 3.7, 3.6. As expected all of them had Bragg peaks at M high symmetry point in the first Brillouin zone and only D_2 and ST had additional (higher intensity) Bragg peaks at X points in the second Brillouin zone. The only difference between the two plotted structure factors was the difference in Bragg peaks at all M points in D_2, D_{2h} and Bragg peaks at only 2 (out of the 6 possible) M points in ZZ, ST. The reader might naively guess that D_2/D_{2h} are a *complete characterization* of the phases i.e. we considered all the three possible spin orientations of the spin at site 1 in the cluster $\vec{S}_1 \in \{(0,0,\pm1),(0,\pm1,0),(\pm1,0,0)\}$ while in the ST/ZZ phase we considered only one possibility and hence *partially characterized* the phase. This naive intuition is the right one indicating that it is better to characterize the phases using D_2 and D_{2h} ordering matrices respectively.

In Figure 3.8 we show the configurations of D_2 and D_{2h} state, which were generated by fixing one spin, e.g. $\vec{S}_{A_1} = \vec{S}_1$, and the orientation of other spins were determined according to the respective ordering matrices in Table 3.1. In general, the reference spin (the first spin in the cluster) $\vec{S}_1$ could point along any arbitrary direction in the $SO(3)$ space. However, there the particular

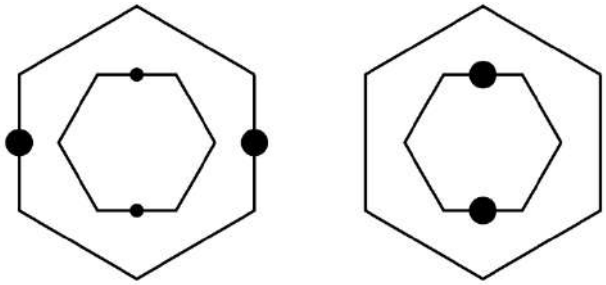

FIGURE 3.6: The static structure factor $S(\vec{K})$ for Stripy (ST) and Zigzag (ZZ) phases respectively (reproduced from [39]). The first and second Brillouin zones are shown with Bragg peaks at $\vec{K} = M$ high symmetry points. As is evident in the stripy phase we have Bragg peaks of higher intensity as shown by the size of the circle at the X points in the second Brillouin zone and low intensity at the M points. In contrast in the Zigzag phase we have no peaks in the second Brillouin zone and only high intensity Bragg peaks at the M points.

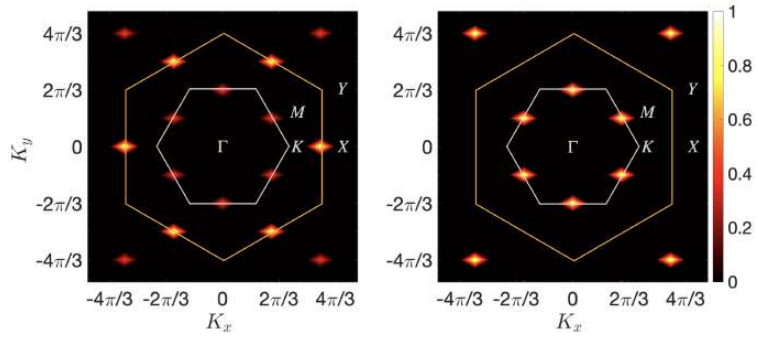

FIGURE 3.7: Static spin-structure factor, $S(\vec{K})$, for the (ST) D_2 (left) and (ZZ) D_{2h} order (right). The gray and orange hexagons denote the first and second Brillouin zones respectively, and high-symmetry points are indicated. $S(\vec{K}) = \left\langle \frac{1}{N} \sum_{ij} \vec{S}_i \cdot \vec{S}_j \, e^{i\vec{K}\cdot(\vec{r}_i - \vec{r}_j)} \right\rangle$, where $\vec{r}_i$ is the position of a spin at site i, and a nearest-neighbor bond of the honeycomb lattice is set to unit length. We find Bragg peaks at the M points and additionally at the X points in the case of D_2.

instances where the D_{2h} and D_2 structures reduced to the zigzag and stripy orders are worthy of a comment. As the reader expected when we have just one of the three possible orientations we reduce to the literature description. For example, the case $\vec{S}_1 = (0\ 0\ \pm 1)$ reduces to the Z-type zigzag and stripy state shown in Figure 3.9. Similarly, if we chose $\vec{S}_1 = (\pm 1\ 0\ 0)$ and $(0\ \pm 1\ 0)$, we reduce to the X- and Y-type zigzag and stripy state, respectively. This observation implies the manifold of the zigzag (stripy) and D_{2h} (D_2) order have overlaps but the two are not isomorphic.

In the ZZ/D_{2h} and ST/D_2 regions, away from the hidden symmetry points ($K = -2J$, $O(3)$ points at $\varphi \approx 0.65\pi, 1.65\pi$), the above special states were realized as the ground states of the JK model owing to the discrete symmetry of the Kitaev term; as visualized in Figure 3.10. While at the high symmetry points the distinction between D_{2h} (D_2) and zigzag (stripy) orders is superfluous as there was no locking of the spins to any of the axes and spins can point along any direction along the $O(3)$ sphere which implied that these cannot be described by staggered arrangements of $\pm\vec{S}$ as in the zigzag or stripy structure.

We shall illustrate the difference further by considering a Z-type zigzag (stripy) moment. As measured in Figure 3.11, the expectation value at the hidden symmetry $O(3)$ point was $M = \frac{1}{2}$ at low temperatures $T \to 0.001$ while for the D_2 phase it saturated to $M = 1$. This could be simply explained by parametrizing the reference spin to point any direction along the $O(3)$ sphere which in general polar coordinates could be described by $\vec{S}_1 = (\sin\theta \sin\phi \ \ \sin\theta \cos\phi \ \ \cos\theta)$, where θ, ϕ are Euler angles. Since spins at the hidden symmetry points deep within these phases were actually

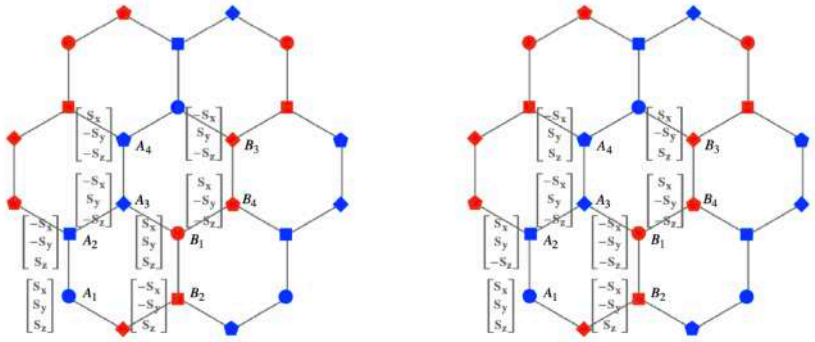

FIGURE 3.8: Configurations of an arbitrary D_2 and D_{2h} state. The spin $\vec{S}_{A_1} = (S_x\ S_y\ S_z)^{\mathrm{T}}$ is used as the reference spin, while orientations of other spins are determined according to the respective ordering matrices. Compared to stripy and zigzag orders, which are staggered arrangements of $\pm\vec{S}$, the sign flip in a D_2 and D_{2h} pattern can occur at individual components. In special cases $\vec{S}_{A_1} = (0\,0\,\pm 1)^{\mathrm{T}}$, these patterns are equivalent to the Z-type zigzag and stripy patterns shown in Figure 3.9, with a reduced four-site magnetic cell $\{A_1, A_2, A_3, B_3\}$. When choosing $\vec{S}_{A_1} = (\pm 1\ 0\ 0)^{\mathrm{T}}$ and $(0\ \pm 1\ 0)^{\mathrm{T}}$, X- and Y-type zigzag and stripy states will be realized, where the magnetic cells are given by $\{A_1, A_2, A_3, B_1\}$ and $\{A_2, A_3, B_1, B_2\}$, respectively. In general cases, the D_{2h} (D_2) and zigzag (stripy) orders are different, and the magnetic cell cannot be reduced to four sites.

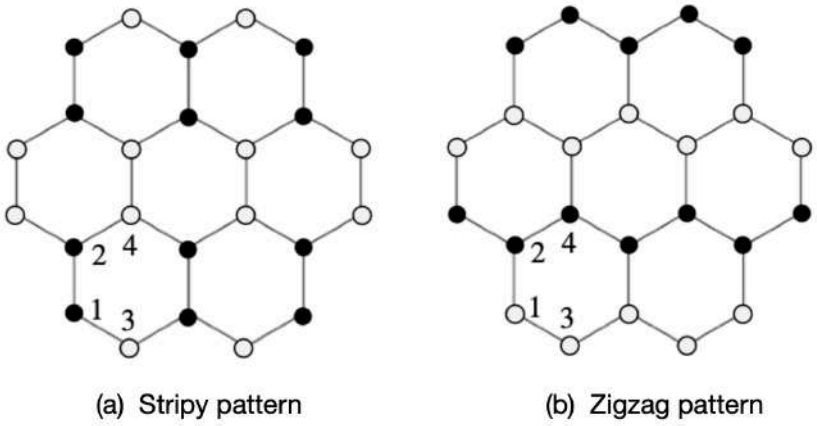

FIGURE 3.9: Representative configurations of a stripy (ST) and zigzag (ZZ) order. White ($\vec{S}$) and black ($-\vec{S}$) cycles denote opposite spins. The corresponding magnetization can be defined as $M_{\mathrm{ST}} = \langle|\frac{1}{N_{\mathrm{cell}}}\sum_{\mathrm{cell}}(\vec{S}_1 + \vec{S}_2 - \vec{S}_3 - \vec{S}_4)|\rangle$, and $M_{\mathrm{ZZ}} = \langle|\frac{1}{N_{\mathrm{cell}}}\sum_{\mathrm{cell}}(\vec{S}_1 - \vec{S}_2 + \vec{S}_3 - \vec{S}_4)|\rangle$, respectively, where the numbers label the four sublattices. In general, $\vec{S}$ may point to arbitrary directions. However, in the ground states of the Heisenberg-Kitaev model, the realization of these above configurations will be accompanied by $\vec{S} = (0\,0\,\pm 1)^{\mathrm{T}}$. We hence refer to them as Z type. Such states are present in the intersection of zigzag (stripy) and D_{2h} (D_2) manifolds.

arranged according to D_{2h} or (D_2) patterns, the zigzag or stripy moment of an individual configuration of spins was $\vec{m} = (0\ 0\ \cos\theta)$ (for a Z type configuration), and the corresponding ensemble average, by integrating over all allowed states, was $M_{ZZ/ST} = \frac{1}{4\pi}\int|\vec{m}|\sin\theta d\theta d\phi = \frac{1}{2}$ while a similar calculation for the D_{2h} order showed $M_{D_2,D_{2h}} = \frac{1}{4\pi}\int|\vec{m}|\sin\theta d\theta d\phi = \frac{1}{4\pi}\int 1\sin\theta d\theta d\phi = 1$. Thus we could definitively conclude that the D_{2h} and D_2 orders provide a more universal and

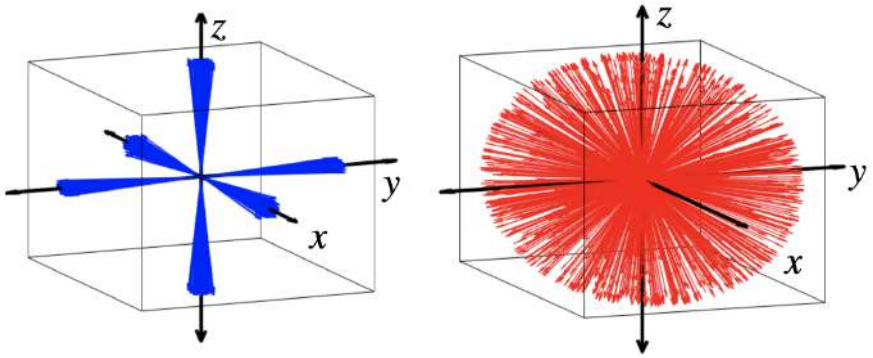

FIGURE 3.10: Distribution of spin orientations for states in the ZZ or D_{2h} and ST or D_2 phases away (left) and at (right) the hidden $O(3)$ points, at a low temperature $T = 0.001$.

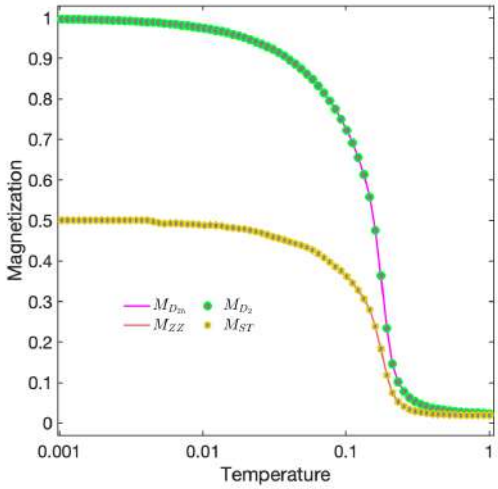

FIGURE 3.11: Magnetization as a function of temperature at the $O(3)$ points, with $\varphi \approx 0.65\pi$ for the zigzag (ZZ) and D_{2h} orders and $\varphi \approx 1.65\pi$ for the stripy (ST) and D_2 orders. The D_{2h} (ZZ) and D_2 (ST) curves show the same behavior as the Heisenberg-Kitaev model is symmetric under a sub-lattice transformation $J \to -J, K \to -K$, and meanwhile $S_i \to -S_i$ for either of the honeycomb sublattices.

complete description for the magnetization as compared to the zigzag and stripy order.

It has to be noted that there is **no phase transition or crossover** separating the high symmetry $O(3)$ points from the neighboring points with discrete three-fold symmetries at $T \to 0$. The ground-state energy of the ZZ/D_{2h} phase could be calculated to be $E_{ZZ} = \frac{1}{3}(-K + J)$ per bond which happens to be degenerate with that of the Néel or the FM order, $E_{AFM} = -\frac{1}{3}(K + J)$ and $E_{FM} = \frac{1}{3}(K + J)$, at $J = 0$ and $J = -K$, respectively, which form the two phase boundaries at $\varphi = \pi/2, 3\pi/4$ this explains why we observed the overlap in the magnetization Fig 3.5.

We could distinguish between the high symmetry $O(3)$ points and the neighbouring points within the purview of TK-SVM by analyzing rank 2 coefficient matrix which showcases another strength of our machine which enabled us to make the distinction with little to no effort

At rank 2, the sub-block matrices are 9×9 and they describe the correlations between a pair of spin quadratic components $S_i^{\alpha} S_j^{\beta}$ and $S_{i'}^{\alpha'} S_{j'}^{\beta'}$. The rank 2 matrix away from the high symmetry point shown above by (a) shows a finite quadratic correlations (which is nothing but a "redundant" representation of the order parameter we learnt at rank 1) and hence we gained no additional information about the phase which wasn't already understood at rank 1. The rank-2 $C_{\mu\nu}$ pattern away from the high-symmetry point where the spins are locked to the three axes

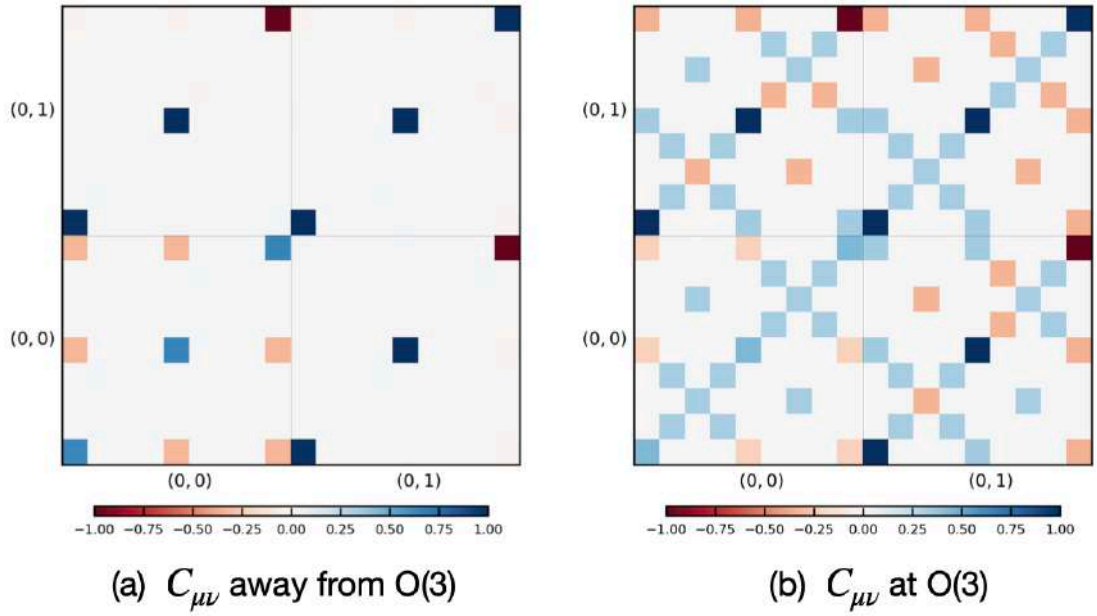

FIGURE 3.12: Representative blocks of the $C_{\mu\nu}$ matrices of the [a] ZZ/D_{2h} phase learned by a rank-2 TK-SVM with the eight-spin [b] D_{2h} magnetic cell, away from (a) and at (b) the $O(3)$ point. Blocks are labeled by the spin indices (i, j). Non vanishing entries in a block correspond to correlations between quadratic components $S_i^\alpha S_j^\beta$ and $S_{i'}^{\alpha'} S_{j'}^{\beta'}$. Negative elements in the $(0,0)$ block reflect the spin normalization $|\vec{S}| = 1$. Non-trivial entries in (a) are the diagonal ones in each 9×9 sub block.

displayed nontrivial quadratic correlations only between the diagonal elements in each sub-block which correspond to the 3 axes i.e. we have correlations only between $S_i^\alpha S_j^\alpha$.

The more interesting coefficient matrix is the one at the hidden symmetry point where we found cross term correlations like $S_i^\alpha S_j^{\beta\neq\alpha}$ which reflected the fact that spins were not locked to any of the axes and could be freely parameterized in the $SO(3)$ sphere. This absence/presence of cross correlations linked with the unlocking/locking of spins to the axes could be analyzed using rank 2 correlations giving us a way to detect these hidden symmetry points.

3.4 Hidden Symmetries

By interpreting the coefficient matrices deep in each phase we discovered that the D_2 and D_{2h} ordering matrices in Table 3.1 accurately described the stripy and zigzag phases respectively. These orders comprise of a finite set of orthogonal matrices, which not only preserve the spin length but also are invertible. As explained before we could start with a simple ferromagnetic configuration and successively apply these transformation matrices on each spin in the cluster and get the respective phase or invert those transformations to convert the D_2 and D_{2h} orders into simple ferromagnets.

Specifically, one could define spin orientations in a sublattice-dependent coordinate as,

$$\tilde{S}_k = \hat{T}_k^{A,B} \vec{S}_k \tag{3.3}$$

The magnetization Eq. (3.2) of the transformed system of spins is then just $\overrightarrow{M} = \tilde{M} = \sum_k \tilde{S}_k$ which describes a ferromagnetic alignment of $\tilde{S}$ spins.

The above transformation acts on spin patterns transforming them at any parameter point into a simple ferromagnet. The transformation of the Hamiltonian in the same coordinate system

could be rewritten in terms of interactions on a local bond $\langle ij\rangle_\gamma$ connecting spins $\vec{S}_i, \vec{S}_j$ as,

$$H_{ij} = \vec{S}_i^{\mathrm{T}} \hat{J}_\gamma \vec{S}_j, \tag{3.4}$$

where $\hat{J}_\gamma$ corresponds to the three types of bonds in the JK Hamiltonian Eq. (6.1) with $\gamma \in \{x, y, z\}$,

$$\hat{J}_x = \begin{bmatrix} K+J & & \\ & J & \\ & & J \end{bmatrix}, \ \hat{J}_y = \begin{bmatrix} J & & \\ & K+J & \\ & & J \end{bmatrix}, \ \hat{J}_z = \begin{bmatrix} J & & \\ & J & \\ & & K+J \end{bmatrix}. \tag{3.5}$$

Under the sublattice-dependent coordinate transformations, Eq. (3.4) becomes

$$\widetilde{H}_{ij} = \tilde{S}_i^{\mathrm{T}} \hat{T}_i^{\mathrm{A,B}} \hat{J}_\gamma \left(\hat{T}_j^{\mathrm{A,B}}\right)^{\mathrm{T}} \tilde{S}_j. \tag{3.6}$$

The three different bonds transform under the sublattice spin transformations as

$$\begin{gathered} \hat{J}_x \to \left(\hat{T}_2^{\mathrm{A,B}}\right)^{\mathrm{T}} \hat{J}_x \hat{T}_3^{\mathrm{A,B}}, \ \left(\hat{T}_4^{\mathrm{A,B}}\right)^{\mathrm{T}} \hat{J}_x \hat{T}_1^{\mathrm{A,B}} \\ \hat{J}_y \to \left(\hat{T}_{3(1)}^{\mathrm{A(B)}}\right)^{\mathrm{T}} \hat{J}_y \hat{T}_{1(3)}^{\mathrm{B(A)}}, \ \left(\hat{T}_{4(2)}^{\mathrm{A(B)}}\right)^{\mathrm{T}} \hat{J}_y \hat{T}_{2(4)}^{\mathrm{B(A)}} \\ \hat{J}_z \to \left(\hat{T}_1^{\mathrm{A,B}}\right)^{\mathrm{T}} \hat{J}_z \hat{T}_2^{\mathrm{A,B}}, \ \left(\hat{T}_3^{\mathrm{A,B}}\right)^{\mathrm{T}} \hat{J}_z \hat{T}_4^{\mathrm{A,B}}, \end{gathered}$$

leading to

$$\tilde{J}_x = \pm \begin{bmatrix} K+J & & \\ & -J & \\ & & -J \end{bmatrix}, \ \tilde{J}_y = \pm \begin{bmatrix} -J & & \\ & K+J & \\ & & -J \end{bmatrix}, \ \tilde{J}_z = \pm \begin{bmatrix} -J & & \\ & -J & \\ & & K+J \end{bmatrix}, \tag{3.7}$$

where "$+$" ("$-$") corresponds to the D_2 (D_{2h}) orders respectively. The transformed bond dependent Hamiltonian can now be written at any parameter point (i.e. any arbitrary J,K value) as

$$\tilde{H}_{ij} = \tilde{S}_i^{\mathrm{T}} \tilde{J}_\gamma \tilde{S}_j, \tag{3.8}$$

where $\tilde{S}$ are spins describe a simple ferromagnet. It has to be noted that the two descriptions are completely equivalent and the difference is just in the way we view the interaction and transformation between the spins which is common in physics and the reader might remember them as active and passive transformations. In the first picture we consider the spins to be transformed (as described in the appropriate phase) and the interaction matrices between them as untransformed (active picture) while in the second point of view we consider spins as untransfomed (all in the same ferromagnetic phase) and the interaction matrices between them as transformed (passive picture).

Identification of the hidden symmetry point becomes apparent in the transformed frame of reference, where at the parameter point $\mathbf{K} = -\mathbf{2J}$ or equivalently $\varphi = \tan^{-1}(-2)$, the couplings in the sublattice coordinate reduce to isotropic matrices, $\pm J\mathbf{I}$, where $\mathbf{I}$ denotes the identity matrix. $\widetilde{H}_{ij}$ now just describes a the local interaction for a ferromagnetic Heisenberg model of spin $\tilde{S}$, with $J > 0$ (< 0) in the D_2 (D_{2h}) phase.

With this identification we precisely reproduced the hidden $O(3)$ symmetries of the JK model, reported previously by Chalopuka in Ref. [39] through a dual transformation. This was also evident in the spin configurations we sampled at and away from the high symmetry points as shown in Figure 3.10. At the high symmetry point since we are reduced to the isotropic case the spins have all possible orientations reflecting the $O(3)$ symmetry and away from these points this symmetry reduces to a three-fold degeneracy where the spins are locked to the axes.

This way of identifying hidden symmetries was straightforward and did not require any specific properties or prior insights of the Hamiltonian on behalf of the researchers. The high-symmetry points were self-evident once the order parameters were detected. This is also shown

in Figure 3.3 (b) where data from the high-symmetry points are *not* needed in the training.

3.5 Local constraints at phase boundaries

We discovered that at the phase boundaries the competition between two magnetic orders usually led to more subtle properties such as an enhanced symmetry or emergent local constraint. We shall discuss the local constraints we learned at the phase boundaries in the phase diagram of Figure 3.3 at $\varphi = \frac{3\pi}{4}$ and $\frac{7\pi}{4}$ between the zigzag and FM phases and stripy and AFM phases respectively. We postpone the discussion of the cases $\varphi = \frac{\pi}{2}$ and $\frac{3\pi}{2}$ which correspond to pure Kitaev models and the ground-state constraints for classical Kitaev spin liquids learnt by TK-SVM to Chapter 5.

In order to detect the local constraints we used rank-2 TK-SVM to detect quadratic correlations between spins.

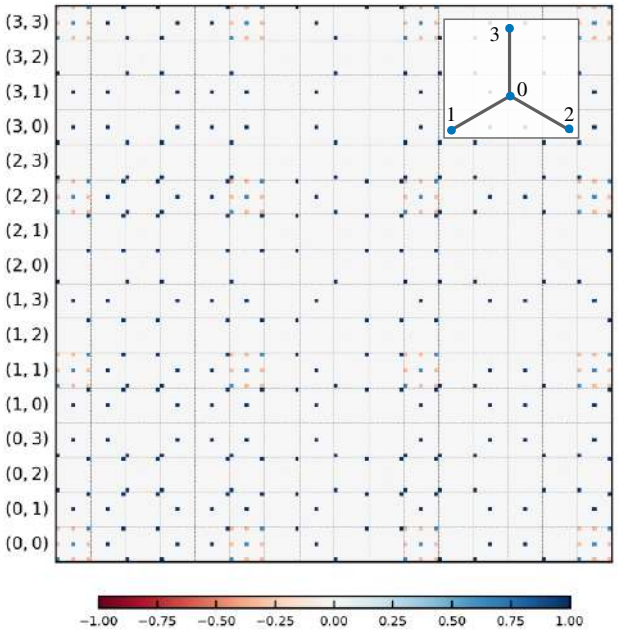

FIGURE 3.13: The $C_{\mu\nu}$ matrix learned by a rank-2 TK-SVM with a four-spin triad cluster (inner panel) at the boundary point $\varphi = \frac{3\pi}{4}$. The axes iterate over spin indices (i, j) and spin components (α, β) in a lexicographically order, from bottom (left) to top (right). The spin indices divide the $C_{\mu\nu}$ matrix into 9×9 sub blocks. Non-vanishing entries in a block represent the form of correlations between quadratic components $S_i^\alpha S_j^\beta$ and $S_{i'}^{\alpha'} S_{j'}^{\beta'}$. Blocks with $i = j$ and $i' = j'$ lead to constants owing to the trivial normalization $|\vec{S}| = 1$. Other blocks corresponds to the local constraints G_1 and G_2. The pattern learned for $\varphi = \frac{7\pi}{4}$ (not shown) has a similar structure with sign flips in certain entries.

Figure 3.13 shows the rank-2 $C_{\mu\nu}$ matrix for $\varphi = \frac{3\pi}{4}$. The pattern for $\varphi = \frac{7\pi}{4}$ had a similar structure but displays different signs for certain entries.

From the above coefficient matrix we could infer two local constraints, G_1 and G_2 as,

$$G_1 = \langle S_0^x(S_2^x + S_3^x) + S_0^y(S_1^y + S_3^y) + S_0^z(S_1^z + S_2^z)\rangle_{\text{td}} = \pm 2, \tag{3.9a}$$

$$G_2 = \langle S_2^x S_3^x + S_1^x S_3^x + S_1^x S_2^x\rangle_{\text{td}} = 1, \tag{3.9b}$$

with all other nearest neighbor and next-nearest neighbor correlations vanishing. Here, $\langle\cdot\rangle_{\text{td}}$ denotes a lattice average over triad clusters involving three bonds and four spins (see the inner panel of Figure 3.13), and "+", "−" correspond to $\varphi = \frac{3\pi}{4}, \frac{7\pi}{4}$, respectively. To verify that we had

correctly inferred the constraints we measured them explicitly and the results are shown in Figure 3.15. We see that at low temperatures at the phase boundaries the constraints exactly saturated to the values we expect from the above equations.

We further noticed that the local constraints G_1 and G_2 are invariant under the following local spin component transformations,

$$S_0^x,\, S_2^x,\, S_3^x \to -S_0^x,\, -S_2^x,\, -S_3^x, \tag{3.10a}$$
$$S_0^y,\, S_3^y,\, S_1^y \to -S_0^y,\, -S_3^y,\, -S_1^y, \tag{3.10b}$$
$$S_0^z,\, S_1^z,\, S_2^z \to -S_0^z,\, -S_1^z,\, -S_2^z. \tag{3.10c}$$

However, since every spin is shared by two triads, these transformations do not define a local, but rather a *subdimensional* symmetry. For instance, Eq. (3.10c) corresponds to a transformation flipping the S_z component of spins in a chain formed by x- and y-bonds, as depicted in Figure 3.14.

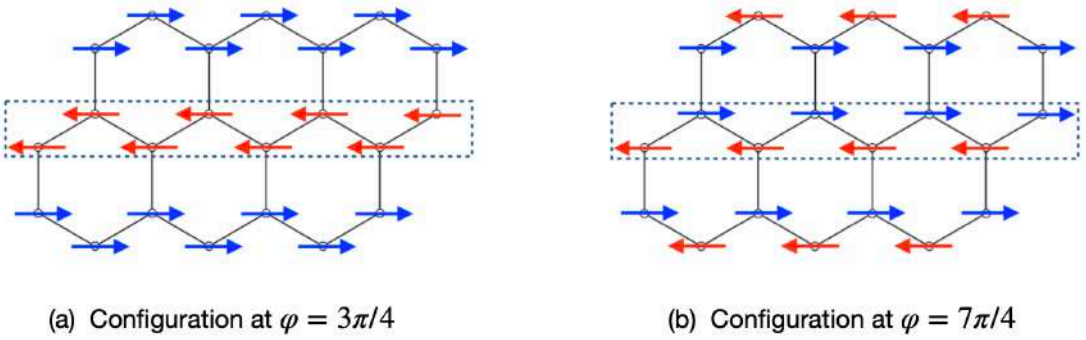

FIGURE 3.14: Representative classical ground-state configuration at $\varphi = \frac{3\pi}{4}, \frac{7\pi}{4}$. The system forms ferromagnetic (a) or anti-ferromagnetic (b) Ising chains. The subdimensional symmetry leads to a classical subextensive degeneracy by flipping one entire chain of spins.

The solutions of constraint equations, Eqs.(3.9a) and (3.9b) give the classical ground states. The absence of cross terms, such as $S_i^{\alpha} S_j^{\beta\neq\alpha}$, indicated that each spin has only a single non-vanishing component in the ground state and hence all the ordering matrices are diagonal. The solution to the above equations was also satisfied by a system forming ferromagnetic ($\varphi = \frac{3}{4}\pi$) and anti-ferromagnetic ($\varphi = \frac{7}{4}\pi$) Ising chains as shown in the figure 3.14. As a consequence of the subdimensional symmetry, flipping of one Ising chain does not cost energy which leads to a subextensive line degeneracy with 3×2^L classical ground states. This implied ZZ/D_{2h} (ST/D_2) order was degenerate with the AFM (Néel) order at these boundary points. In the spin-$\frac{1}{2}$ JK model, the subextensive degeneracy is lifted by quantum fluctuations by a quantum order-by-disorder mechanism [41, 40] which does not happen in the classical system. The Hamiltonian is *not* input to the machine but rather learnt from the spin configurations illustrating the potential application of TK-SVM to learn non-trivial spin Hamiltonians from samples of simple orders.

3.6 Summary and Outlook

In this chapter we successfully demonstrated using TK-SVM to identify hidden $O(3)$ symmetry in the JK model on the 2 dimensional honeycomb lattice at the phase point $K = -2J$ deep in the stripy and zigzag phases respectively. We also successfully reproduce the classical phase diagram and measured the magnetization in each phase demonstrating conclusively that we correctly interpreted the order parameters with the help of the machine. This approach can be extended to other complicated systems with hidden symmetries in unconventional magnetic phases. We emphasize again that, this identification of high symmetry points and learning of the topology of the phase diagram happened in an **unsupervised** manner without prior knowledge on behalf of the

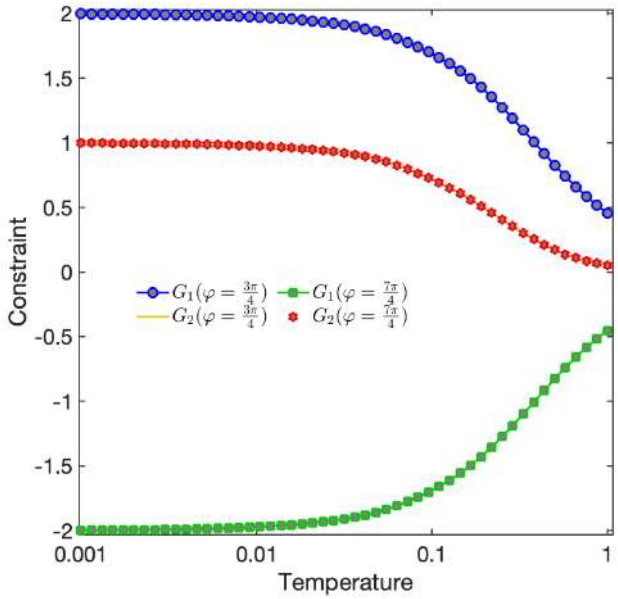

FIGURE 3.15: Local constraints at $\varphi = \frac{3\pi}{4}, \frac{7\pi}{4}$ as a function of temperature. G_1 and G_2 satisfy Eqs. (3.9a) and (3.9b) in the ground state. (The G_2 curves at the two φ values overlap.)

researchers on the topology of the phase space which makes it an important tool in investigating complex systems. This has to be contrasted to other constructions which are **contingent on the skill and experience of the researcher**.

We additionally showed that the D_{2h} and D_2 orders provide a more universal and accurate description of the magnetization compared to zigzag and stripy order described in literature. The interpretation of rank 1 and 2 coefficient matrices which are just the correlations between polynomials of spin components emphasized the significance of being able to express the order parameters and local constraints explicitly in many-body spin systems, which is a consequence of the **interpretable** nature of our machine-learning method.

Our machine also successfully unravelled subdimensional symmetries. On one hand, this identification complements the studies reported in Ref. [143] where TK-SVM was used to identify the local Z_2 symmetries of classical Kitaev spin liquids by probing their ground-state constraints. On the other, as subdimensional symmetries are typically related to degenerate competing orders, their identification by machine learning methods implied a potential generative use of these machines i.e. to *learn non trivial Hamiltonians from data*.

In the future, as hidden symmetries are ubiquitous in symmetry-protected topological states [79, 44, 170] such as the hidden $Z_2 \times Z_2$ symmetry in the celebrated Haldane phase [3, 4, 109, 108] one could employ a machine like ours see if the machine is capable of learning these hidden symmetries which would prove invaluable to the advances in the condensed matter community in general. While it might be easier to construct an *ad hoc* machine for this particular SPT phase, devising a versatile machine that is applicable to a (reasonably) wide class of topological phases however remains a challenging task.

Chapter 4

Phase Diagram of Generalized Kitaev Magnets

In the previous chapter, we discussed the application of TK-SVM to the JK model and its applicability in detecting hidden symmetries as well as subdimensional symmetries. In this chapter we extend our efforts to the complete $JK\Gamma$ model on the two dimensional hexagonal lattice. This shows the applicability and usefulness of TK-SVM to operate in an *unsupervised* manner in a high dimension parameter space and find the topology of the phase diagram without requiring any input or insights on part of the researchers about the underlying spin Hamiltonian.

Kitaev materials [208, 97, 228] have been prime candidates for ML applications as they are nontrivial and complex, hosting various disordered and unconventionally ordered phases, proving a challenge to most ML algorithms and going beyond bench marking models. Experimentally, the bond-dependent anisotropic interactions relevant for Kitaev physics is realized as a consequence of the interplay between electron correlations coupled with spin-orbit coupling [94, 41] (see Chapter 1 for more details). Following this seminal work by Chaloupka et al, the Kitaev community began searching in earnest for the holy grail of condensed matter physics, which is a compound that hosts spin liquid phases at low temperatures. A number of suitable candidates have been proposed over the years but the most promising ones are compounds which are $4d$ and $5d$ transition-metal-based Mott insulators with the chemical representation A_2IrO_3 (A = Na, Li, K) and α-$RuCl_3$ [228, 14, 16, 176, 233, 234, 39]. $\alpha - RuCl_3$ in particular has been postulated to host a field-induced quantum spin liquid as evidenced by the half-quantized thermal Hall plateau under an external in plane magnetic field [103, 240] suppressing the zigzag order, while spectroscopic [171, 186, 147] and thermodynamic [11, 10] measurements indicate a topologically trivial partially-polarized phase. We refer the reader to chapter 1 where we discussed the various Kitaev candidates and the extended Kitaev Hamiltonian as well as a brief overview of the experiments therein, in case the reader wants to refresh their memory.

In an ideal scenario we would expect to find a compound that faithfully exhibits the Kitaev physics but in reality non-Kitaev terms, such as the Heisenberg exchange and the symmetric off-diagonal Γ exchange, permitted by the underlying cubic symmetry and ubiquitously exist in real Kitaev materials [180, 181] leading to ordering at low temperatures. In addition, longer-range interactions such as the third nearest neighbour interactions and structural distortions provide further hopping channels [179, 92, 147] resulting in magnetic ordering. These additional terms enrich the Kitaev physics [222, 72, 71, 197, 134, 100, 73, 92, 128, 143] but also pose a significant challenge to the analysis because of the large parameter space and the emergence of complicated structures. This then becomes an ideal playground for an interpretable and unsupervised learning method such as TK-SVM which can efficiently detect patterns and construct the associated phase diagrams in this high dimensional parameter space.

We found that our machine not only reproduced all the classical phases reported in literature but also a hitherto missed phase which we christened as the *nested zigzag-stripy order* and also established the robustness of the complicated spiral phase $S_3 \times Z_3$ reported in [143] against Heisenberg interactions in the extended phase diagram. We arrived at the conclusion that in the restricted parameter space spanned by the three primary exchange interactions—J, K, and Γ, the representative Kitaev material α-$RuCl_3$ thought to host the elusive Kitaev spin liquid, lies close to

the boundaries of several phases, including a simple ferromagnet, the unconventional $S_3 \times Z_3$ and nested zigzag-stripy as well as a correlated paramagnet which on one hand explains the experimentally observed zigzag magnetic order at low temperatures but on the other hand complicates experimental analyzes due to proximity to a multitude of magnetic orders. We further found that the presence of a finite Γ' and/or J_3 term stabilized the zigzag order, whereas the four magnetic orders might compete if Γ' is anti-ferromagnetic.

In this chapter we illustrate one of the earliest non trivial examples where ML goes beyond the current state-of-art methods and provides nontrivial information in strongly correlated Kitaev physics.

4.1 Model and Methods

We investigated the generalized Heisenberg-Kitaev-Γ model on a two dimensional honeycomb lattice defined by the Hamiltonian

$$\begin{aligned} H &= H_{JK\Gamma} + H_{\Gamma'} + H_{J_3}, \\ &= \sum_{\langle ij\rangle_\gamma} \mathbf{S}_i \cdot \hat{\mathcal{J}}_\gamma \mathbf{S}_j + \sum_{(ij)} J_3 \mathbf{S}_i \cdot \mathbf{S}_j, \end{aligned} \tag{4.1}$$

where we subdivided the Hamiltonian into nearest neighbour interactions

$$H_{JK\Gamma} = \sum_{\langle ij\rangle_\gamma} \left[J\mathbf{S}_i \cdot \mathbf{S}_j + K S_i^\gamma S_j^\gamma + \Gamma(S_i^\alpha S_j^\beta + S_i^\beta S_j^\alpha) \right], \tag{4.2a}$$

$$H_{\Gamma'} = \sum_{\langle ij\rangle_\gamma} \left[\Gamma'(S_i^\gamma S_j^\alpha + S_i^\gamma S_j^\beta + S_i^\alpha S_j^\gamma + S_i^\beta S_j^\gamma) \right]. \tag{4.2b}$$

and the third nearest neighbour interactions

$$H_{J_3} = \sum_{(ij)} J_3 \mathbf{S}_i \cdot \mathbf{S}_j \tag{4.3}$$

Here, γ labels the three distinct nearest-neighbor (NN) bonds $\langle ij\rangle$, which is the standard convention used in all chapters in this thesis, with mutually exclusive $\alpha, \beta, \gamma \in \{x, y, z\}$ as illustrated in Figure 4.1; $\hat{\mathcal{J}}_\gamma$ is a 3×3 matrix comprising all exchanges on a NN bond $\langle ij\rangle_\gamma$, and (ij) denotes the third NN bonds with a Heisenberg interaction J_3.

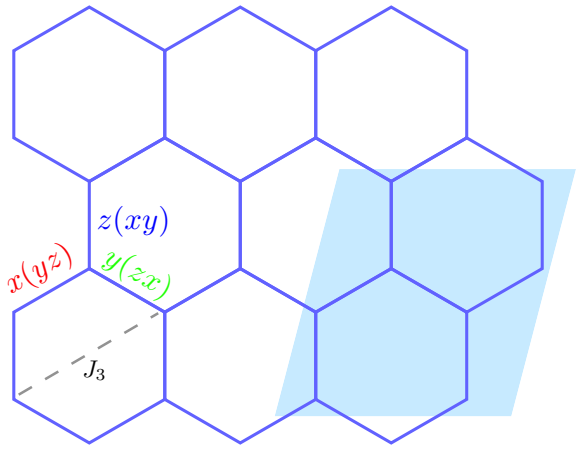

FIGURE 4.1: A honeycomb lattice with anisotropic bonds $\gamma(\alpha\beta)$. The shaded region marks a symmetric cluster of $m \times m$ unit cells. A lattice with linear size L is then partitioned into $(\frac{L}{m})^2$ such clusters. Here, $m = 2$ is shown for example. Larger clusters with $m = 4, 6, 12$ are considered in training TK-SVMs.

The most general form of the NN interaction matrices $\hat{\mathcal{J}}_\gamma$ for each bond in the above Hamiltonian could be written as

$$\hat{J}_x = \begin{bmatrix} K+J & \Gamma' & \Gamma' \\ \Gamma' & J & \Gamma \\ \Gamma' & \Gamma & J \end{bmatrix}, \; \hat{J}_y = \begin{bmatrix} J & \Gamma' & \Gamma \\ \Gamma' & K+J & \Gamma' \\ \Gamma & \Gamma' & J \end{bmatrix}, \; \hat{J}_z = \begin{bmatrix} J & \Gamma & \Gamma' \\ \Gamma & J & \Gamma' \\ \Gamma' & \Gamma' & K+J \end{bmatrix}. \tag{4.4}$$

The $JK\Gamma$ Hamiltonian Eq. (4.2a) comprises of all generic NN exchanges allowed by cubic symmetry [94, 180] of the octahedra surrounding the d^5 magnetic ions. The Kitaev (K) term is of utmost interest naturally as it is crucial for the realization of (Kitaev) spin liquids. However, in realistic materials in addition to Kitaev interactions, the Heisenberg (J) and the symmetric off-diagonal (Γ) exchanges ubiquitously exist whose presence leads to magnetic ordering.

The Γ' term is a secondary symmetric off-diagonal interaction whose origins lie in the trigonal distortion of the octahedral cage where a negative (positive) Γ' corresponds to trigonal compression (expansion) of the edge-sharing oxygen or chlorine octahedra [179] while the inclusion of the J_3 term reflects the extension of d-electron wave functions between the magnetic ions. These terms in literature were considered as perturbative to the $JK\Gamma$ model but we found in this work that even a weak presence of these terms almost always led to a zigzag ordering, hence complicating the effective Hamiltonian model describing real materials as different Hamiltonians give the same ordering. Although second nearest-neighbor exchanges are also possible, experiments and ab-inito quantum chemistry calculations showed that the third-neighbor exchanges was more significant including the intensely studied compounds Na_2IrO_3, α-Li_2IrO_3, α-$RuCl_3$ and the more recently (re-)characterized cobalt-based compounds $Na_3Co_2SbO_6$ and $Na_2Co_2TeO_6$ [219, 203]. In most materials, the Γ' and J_3 exchange terms were introduced phenomenologically to stabilize and explain magnetic orders observed in experiments [16, 92, 131, 147], in particular the zigzag-type orders found in most two-dimensional Kitaev candidates [208].

We emphasize that the "model" Hamiltonian for Kitaev candidates are a combination of experimental inputs and phenomenological insights. In general as in any other complex spin system, different combinations of parameters lead to a multitude of phases and correlated paramagnets, which makes the scanning of this multidimensional parameter space computationally extremely expensive. Since they lead to the same phase, the problem of "reverse engineering" the parameters upon the observation of a particular phase (experimentally) becomes a challenge. in Kitaev materials. In literature, the primary physics of Kitaev materials is governed by the $JK\Gamma$ model, whose phase diagram for a fixed Γ' and J_3 motivated through experiments remains the prime focus of this chapter.

Moreover, motivated by the microscopic models proposed for α-$RuCl_3$ by Maksimov et al [147, 131] based on the INS and THz data for $Na_3Co_2SbO_6$ and $Na_2Co_2TeO_6$ [203], we focused on the parameter space with $K < 0$, $\Gamma > 0$ and a moderate range of ferromagnetic Heisenberg ($J < 0$) exchange terms.

We parameterized the Kitaev and Γ interactions through the angle θ as $K = \sin\theta$, $\Gamma = \cos\theta$ and scanned over $\theta \in [3\pi/2, 2\pi)$ ensuring $K < 0, \Gamma > 0$ and further restricted the Heisenberg interaction to be of the ferromagnetic type $J \in [-0.3, 0]$. For higher values of the Heisenberg parameter we got trivial ferromagnetic phases and hence restricted our values in line with experiments.

We also subsequently investigated slices of the phase diagram with the addition of secondary contributions Γ', J_3 motivated by experimentally relevant values of $J_3 = 0, 0.1$ and $\Gamma' = 0, \pm 0.1$. We considered both ferromagnetic as well as anti-ferromagnetic Γ' (referring to the trigonal compression and expansion respectively) covering both the cases of its disputed sign in α-$RuCl_3$.

4.1.1 Methods

In tune with the rest of the thesis, we considered classical spins ($\vec{S} \in O(3)$) and trained our TK-SVM with classical Monte Carlo spin data collected at very low temperature of $T = 10^{-3}\sqrt{K^2 + \Gamma^2}$ for large system sizes $L = 72$. During training we simulated 400 (θ, J) parameter points at fixed

Γ' and J_3 slice, and in total we simulated the 6 combinations of (Γ', J_3) with the values $(\Gamma', J_3) \in \{(0,0), (0.1,0), (-0.1,0), (0,0.1), (0.1,0.1), (-0.1,0.1)\}$.

We performed a multi-classification using TK-SVM for these six combinations of parameters to unravel the topology of the phase diagram which is interpreted as the phase diagram. Then deep in each phase we sampled a few points and extracted the physical order parameters at rank 1 by interpreting the coefficient matrix and refined the phase boundaries to verify that we had correctly interpreted the orders. We measured the order parameters in new simulations lowering the temperature further to $T = 10^{-4}\sqrt{K^2 + \Gamma^2}$, in the most frustrated parameter regimes.

In the training phase, for Monte Carlo sampling we chose $N_T = 64$ logarithmically distributed temperatures between $T = 0.5 \times 10^{-3}$ and 10 for the majority of the (θ, J) points, while we also used $N_T = 128$ logarithmical temperatures for a small subset of special parameter points in the frustrated regimes. In the testing stage, we used $N_T = 128$ temperatures in $[0.75 \times 10^{-4}, 10]$ for most points measured in Figs. 4.8, 4.6 and 4.9, but also used $N_T = 256$ logarithmical temperatures as and when needed for a few points.

We typically ran 8×10^6 Monte Carlo (MC) sweeps for simulations using $N_T = 64$ and 1.6×10^7 sweeps for those requiring more temperature partitions. We reserved half of the total sweeps for thermalization and in the training stage, we collected 500 samples per parameter point from the second half of the MC sweeps, this meant we sampled once every 800 or 1,600 MC sweeps. In the testing stage, new Monte Carlo simulations were performed to measure the learned order parameters (Figs. 4.8, 4.6 and 4.9), and we compared several independent simulations to confirm the ergodicity and sufficient thermalization of our simulations.

We discovered that the phase diagrams of the investigated parameter regions were dominated by various magnetic orders as expected for the extended Kitaev model. This indicates that our classical phase diagrams qualitatively, or even semi-quantitatively, reflects the phase diagrams in literature with a finite spin-S values. Indeed, we successfully reproduced all the classical orders reported in literature - the ferromagnetic, zigzag and 120° orders [180, 92, 147] and in addition found new phases missed in the previous literature surveys.

4.2 Topology of the General Phase Diagram

The topology of the phase diagram is unraveled through the Fiedler partitioning via the *unsupervised* learning of TK-SVM at rank 1 and 2. For the $JK\Gamma$ phase diagrams considered here with fixed Γ' and J_3 couplings we sampled 500 configurations at each of the 400 parameter points in the (J, θ) subspace. These points were uniformly distributed in the parameter space with $J \in [-0.3, 0]$ with a uniform spacing of $\Delta J = 0.02$ and $\theta \in [3\pi/2, 2\pi]$ with a spacing of $\Delta\theta = \frac{1}{48}\pi$. This protocol of uniform sampling is the standard strategy when exploring unknown phase diagrams. If we have prior knowledge about the topology we can importance sample instead.

In all six cases, the phase diagrams were mapped using just the rank-1 classification, while a universal choice of the cluster for the averaging was simply chosen to be the symmetric $m \times m$ honeycomb unit cells (see Figure 4.1) where we checked and confirmed the consistency of a phase diagram by using clusters of different sizes with $m = 4$, 6, 12 (32, 72, 288 spins).

Figure 4.3 shows the histograms of the Fiedler vector entries. The pronounced peaks were identified with the well-separated phases we observed in the graph partitioning while the flat regions indicated disordered regimes and/or crossovers between the phases with the Fielder entries randomly distributed. Having determined the topology of the phase diagram, the next step was to analyze and interpret the coefficient matrices $C_{\mu\nu}$ learnt in each phase in order to extract the order parameter. We did this at rank 1 and if we detected no magnetic order/pattern we performed an additional rank-2 analysis to identify the phase either as a spin liquid where a stable ground-state constraint exists or as a correlated paramagnet or incommensurate phase where no such local constraints exist.

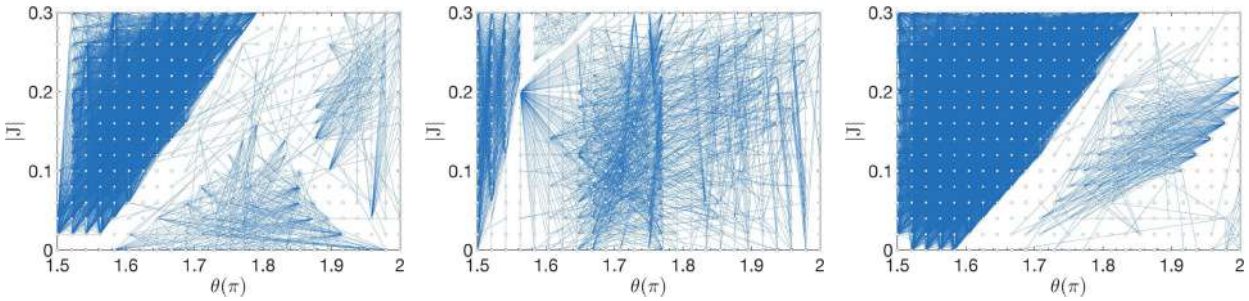

(a) $J_3 = 0, \Gamma' = 0$ (b) $J_3 = 0, \Gamma' = -0.1$ (c) $J_3 = 0, \Gamma' = 0.1$

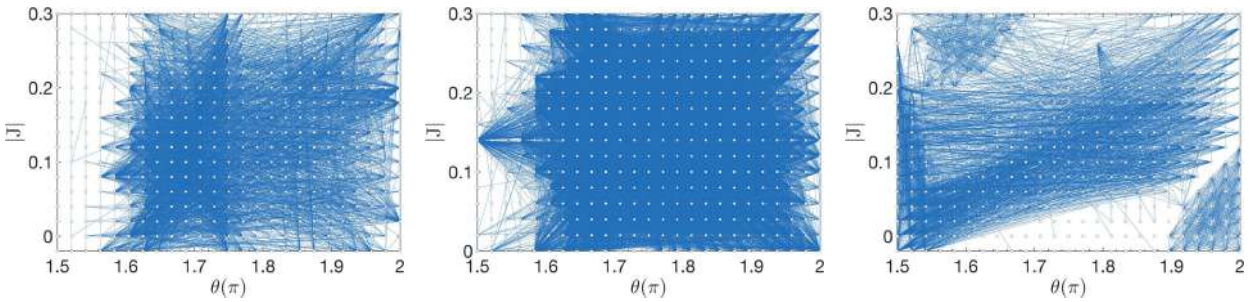

(d) $J_3 = 0.1, \Gamma' = 0$ (e) $J_3 = 0.1, \Gamma' = -0.1$ (f) $J_3 = 0.1, \Gamma' = 0.1$

FIGURE 4.2: Graphs associated with the phase diagrams discussed. Each vertex (white circle) represents a (θ, J)-point with fixed J_3 and Γ', from which training samples are collected. The edge (blue line) connecting two vertices is determined by the learned bias parameter ρ. Here $\rho_c = 10^4$ is imposed in the weight function.Each graph contains 400 vertices and 79,800 edges. Edge weights are suppressed in the figure for visualization purposes.

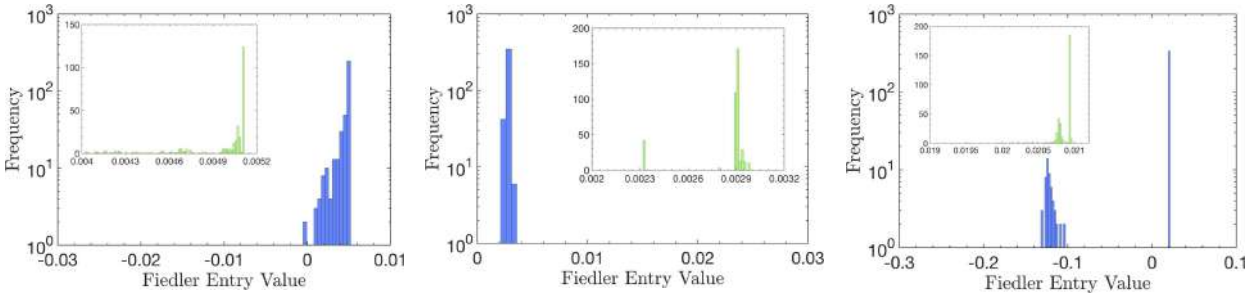

(a) $J_3 = 0, \Gamma' = 0$ (b) $J_3 = 0, \Gamma' = -0.1$ (c) $J_3 = 0, \Gamma' = 0.1$

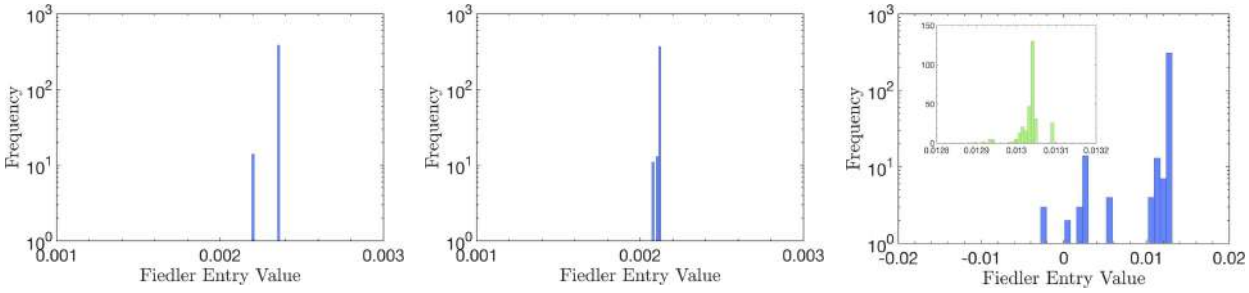

(d) $J_3 = 0.1, \Gamma' = 0$ (e) $J_3 = 0.1, \Gamma' = -0.1$ (f) $J_3 = 0.1, \Gamma' = 0.1$

FIGURE 4.3: Histograms for the dominating Fiedler entries of the six graph partitioning problems. The main panels have a logarithmic scale on the vertical axis because the distribution spans several orders of magnitude. The insets show the main part of the distribution on a linear scale for easier comparison.

4.2.1 $JK\Gamma$ Phase diagram

We shall now discuss the $JK\Gamma$ phase diagram with the secondary interactions set to zero. This particular phase diagram has been thoroughly explored by several authors in the past Refs. [180, 222, 92, 39]. We found that while the results in these works with dominating Heisenberg and Kitaev interactions i.e. the JK phase diagram we discussed in the previous chapter, were quite consistent with each other albeit through different methods, the physics of competing Kitaev and Γ interactions was however more subtle with different methods giving different results.

In the Kitaev-Heisenberg dominated regions we again found the trivial/nontrivial magnetic orders ferromagnetic, zigzag, anti-ferromagnetic, and stripy orders which we previously encountered in the pure JK phase diagram [41, 96] and found that these orders also extend to regions of finite Γ [180, 92]. The conclusion we can make is that these phases are quite robust against perturbations by the symmetric Γ exchange interaction.

In the parameter regime relevant for Kitaev candidate α-$RuCl_3$ with $K < 0$, $\Gamma \sim |K|$ and a small but finite ferromagnetic J term, the study by Rau et al [180] based on Luttinger-Tisza analysis suggested a zigzag order. However, the zigzag order was not confirmed by the 24-site exact diagonalization (ED) carried out in the same work, and a more recent study [92] equipped with 32-site ED and cluster mean-field calculations showed that the physics depends on the size and shape of clusters making the unravelling of the topology more subtle.

However, our machine found that the $JK\Gamma$ phase diagram in the above parameter regime is quite rich as expected and shown here in Figure 4.4. We reproduced the ferromagnetic and zigzag phases in the large K and Γ with a finite J regions reported in literature [180, 222, 92]. In addition our machine identified a novel *nested zigzag-stripy* (ZZ-ST) phase and also showed the extension of the helical $S_3 \times Z_3$ phase which is robust against moderate Heisenberg perturbations. The $S_3 \times Z_3$ phase which results from the competition between the Kitaev and Γ spin liquids and features a spin-orbit entangled modulation, with magnetic Bragg peaks at $\frac{2}{3}\mathbf{M}$ points [143] will be discussed in the next chapter (Chapter 5).

We, most importantly, reported the novel nested ZZ-ST order for the first time and to our best knowledge it has not been reported previously in literature . In this phase, whose representative ground-state configuration is shown below in Figure 4.5, the spins can be divided into two groups, $\{\vec{S}_A, \vec{S}_B\}$. One set of spins, e.g., the A-spins in Figure 4.5, form the regular zigzag pattern with a doubled lattice constant while the other set of spins (B-spins) form the stripy patterns, intricately nested with the zigzag pattern of the A-spins. This interlacing of nested and stripy orders has an enlarged magnetic cell which when averaged using smaller cluster sizes appears as a random pattern and hence might be the reason why it was missed by the previous studies. This nested order has an enlarged ground-state manifold: The global three-fold rotation (C_3) and spin-inversion symmetry $(S \to -S)$ of the (generalized) $JK\Gamma$ model trivially allows six ground states. This degeneracy is further doubled as the two sets of spins $A \leftrightarrow B$ can be swapped, leading to twelve distinct ground states, which we observed and verified in our Monte Carlo simulations.

In addition, the robustness of the nested zigzag stripy order was also confirmed as shown in Figure 4.6 by scanning θ at different J values. We found that this order completely saturates at larger values of J and θ (or greater the Γ parameter). This nested phase is sandwiched between the zigzag and the trivial ferromagnetic phase.

The evolution of spin structure factors (SSFs) at a fixed J as a function of θ is also interesting. As shown in Figure 4.7 for a fixed $J = -0.1$, in the ferromagnetic phase at small Γ, the magnetic Bragg peak develops at the Γ point (zone center) of the first Brillouin zone. Increasing the Γ coupling led to the magnetic Bragg peaks moving outwards to the $\frac{1}{2}M$ for the nested phase, $\frac{2}{3}M$ for the helical $S_3 \times Z_3$ phase and finally to the M points for the zigzag phase.

We also found that these magnetic phases were separated by broad crossover areas where the machine didn't learn any magnetic order or constraints at rank 1 and 2 even down to the temperature $T = 10^{-3}$ and were hence marked as incommensurate or paramagnetic (IP) regimes . Explicit measurements of the learned order parameters at a lower temperature $T = 10^{-4}$ further showed all magnetic moments in the region marked as IP were remarkably fragile, as plotted in Figure 4.8

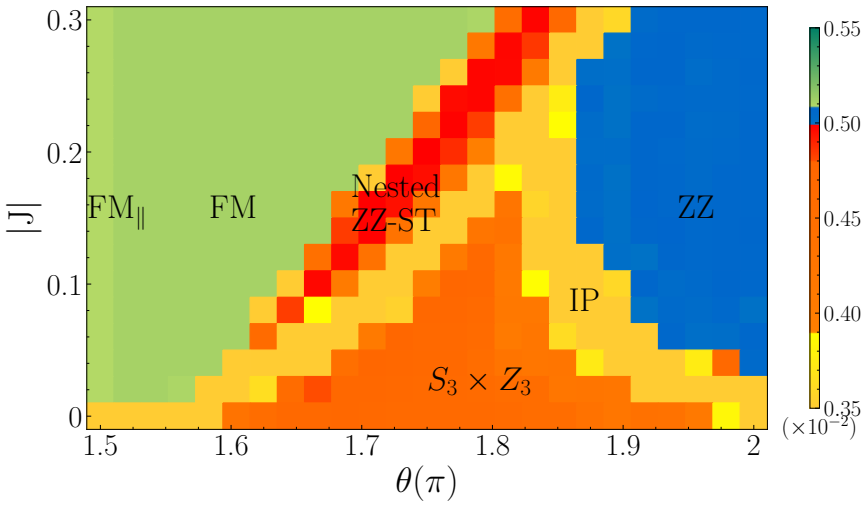

FIGURE 4.4: Machine-learned J-K-Γ phase diagram for parameters $J < 0$, $K = \sin\theta < 0$, $\Gamma = \cos\theta > 0$, at $T = 10^{-3}$. Interactions and temperature are in units of $\sqrt{K^2 + \Gamma^2}$. Each pixel represents a (θ, J) point with $\Delta\theta = \frac{1}{48}\pi$ and $\Delta J = 0.02$; same for the phase diagrams below. A rank-1 TK-SVM with symmetric cluster of 12×12 lattice cells is used. The color represents the Fiedler entry value (FEV) for the corresponding (θ, J) point, and the choice of the color bar is guided by the histogram of FEVs. Parameter points in the same phase have the same or very close values. The blurry regions indicate phase boundaries and crossovers. The Kitaev and Γ spin liquids reside at the corner of $(\theta, J) = (\frac{3}{2}\pi, 0)$ and $(2\pi, 0)$, respectively, which are not distinguished from disordered IP regime as the rank-1 TK-SVM detects magnetic orders. FM: ferromagnetic, where FM$_\parallel$ indicates easy-axis states; Nested ZZ-ST: nested zigzag-stripy; IP: incommensurate or (correlated) paramagnetic.

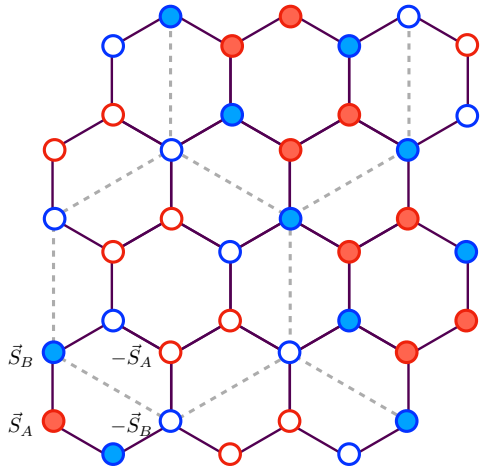

FIGURE 4.5: A ground-state configuration of the *nested* zigzag-stripy order. The red (A) and blue (B) colors label two inequivalent reference spins, $\vec{S}_A \neq \vec{S}_B$. The filled ($+$) and empty ($-$) cycles indicate the sign of a spin. Here the A-spins (B-spins) form zigzag (stripy) structures on a honeycomb lattice with a doubled lattice spacing. The dashed lines are a guide to the eye.

with a fixed $J = -0.1$. Although we trained the machine with data from a finite-size lattice at low but non zero finite temperature, we cannot conclusively exclude lattice incommensuration and long-range orders as $T \to 0$ in these regimes. We could make the conclusion that at our large system size any stable magnetic orders at the low temperatures we investigated is absent. However, we speculate that in the finite-S quantum limit, these regions could potentially host spin liquid phases as quantum fluctuations might suppress conventional magnetic ordering. At rank 1 we cannot distinguish between Kitaev and Γ spin liquids and the disordered IP regimes in the phase

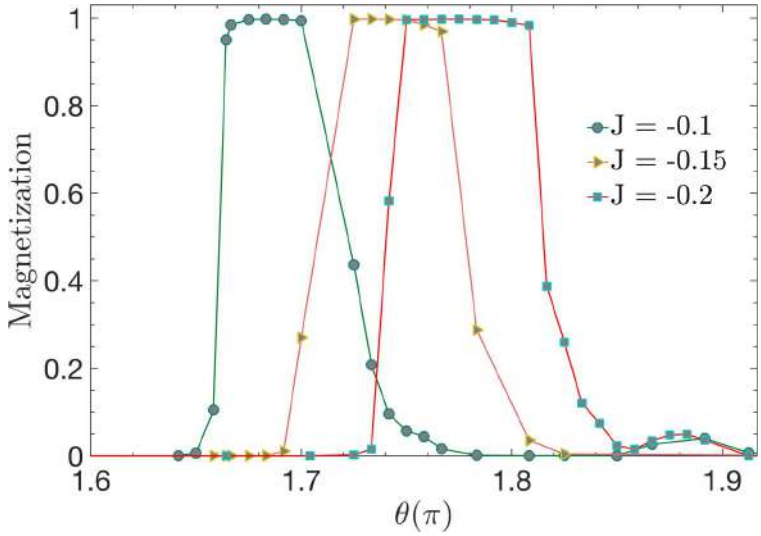

FIGURE 4.6: Monte Carlo measurements of the nested zigzag-stripy magnetization at different J's, with $\Gamma' = J_3 = 0$, $T = 10^{-4}$. Consistent with the phase diagram Figure 4.4 learned at $T = 10^{-3}$, the nested zigzag-stripy order is preferred by larger $|J|$ and Γ.

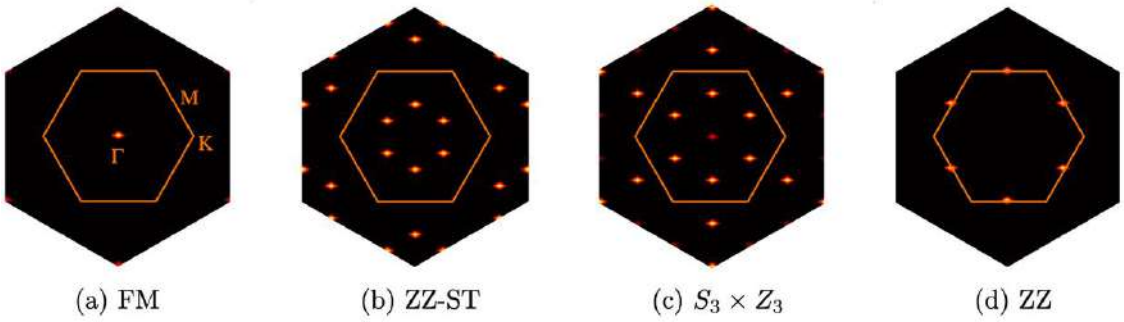

FIGURE 4.7: Evolution of the spin structure factor $S(q)$. The inner (outer) area denotes the first (second) honeycomb Brillouin zone; high symmetries points are indicated. Here $S(q) = \left\langle \frac{1}{2L^2} \sum_{ij} S_i \cdot S_j \, e^{iq\cdot(r_i - r_j)} \right\rangle$ is measured at $J = -0.1$ and $T = 10^{-3}$. Upon increasing Γ, the magnetic Bragg peaks pass by the Γ (FM), $\frac{1}{2}M$ (nested ZZ-ST), $\frac{2}{3}M$ (modulated $S_3 \times Z_3$) and M (zigzag) points. The length of the wave factors are stable within each phase.

diagram Figure 4.4. However we discovered and show in the next chapter 5 the classical ΓSL is less robust than the classical KSL when against competing interactions. Having discussed the pure $JK\Gamma$ model we next discuss the influence of adding secondary terms.

4.2.2 Phase diagram and effects of adding Γ' and J_3 terms

As motivated previously, the addition of these secondary terms are part phenomenological and part guided by experiments. We disentangled the two secondary terms and separately studied their influence.

We began by neglecting the J_3 interactions and only considered the influence of the secondary off-diagonal Γ' interaction whose origins lie in the trigonal distortion. We observed that the presence of a small ferromagnetic $\Gamma' = -0.1$ stabilizes and expands the the zigzag order in the $JK\Gamma$ phase diagram significantly as shown in Figure 4.10 (a). We also additionally observed the presence of the AFM S_3 phase , a type of 120° order [180, 92] in corner at large Γ near the ΓSL point. These results were consistent with the works in literature for the quantum spin-1/2 model in Ref. [92].

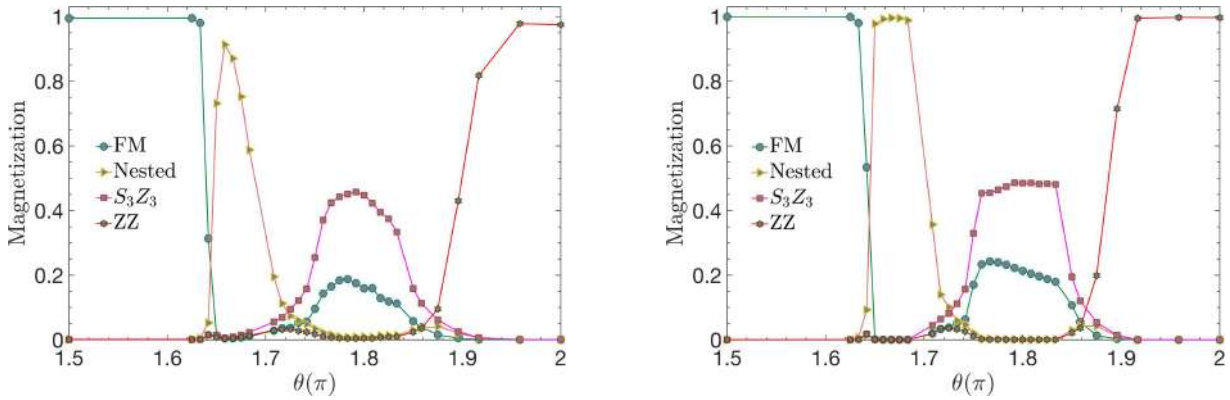

(a) $T = 10^{-3}$ (b) $T = 10^{-4}$

FIGURE 4.8: Monte Carlo measurements of the magnetization at fixed $J = -0.1$, $\Gamma' = J_3 = 0$. Results for $T = 10^{-3}$ and $T = 10^{-4}$ are compared. The magnetic order of each phase in Figure 4.4 is confirmed. The broad IP regions are narrower at very low temperature $T = 10^{-4}$ but remain quite sizable, indicating that these regions are highly frustrated and the orders fragile.

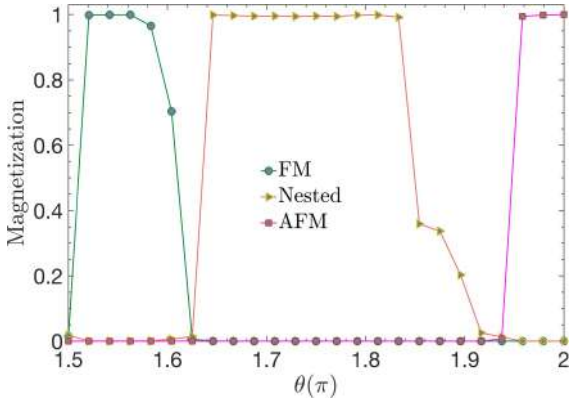

FIGURE 4.9: Monte Carlo measurements of the magnetization with fixed $J = 0$, $\Gamma' = 0.1$, $J_3 = 0$, at $T = 10^{-4}$. The wide window between the nested zigzag-stripy and anti-ferromagnetic orders corresponds to the IP regime in the phase diagram Figure 4.10 (b).

For the ferromagnetic $\Gamma' = 0.1$ case, the machine found more interesting orders than the trivial zigzag phase. As shown in Figure 4.10 (b), we found three stable magnetic phases. A ferromagnet and the nested ZZ-ST magnet dominated the parameter regimes of small and large Γ, while at the large Γ and small J we found an anti-ferromagnet phase. These magnetic orders were found to be separated by broad crossovers. In particular, as shown in Figure 4.9 along the $J = 0$ line, in the regime between the nested and anti-ferromagnetic phase, no strong ordering was observed even down to extremely low-temperature $T = 10^{-4}$ and there was a small overlap between multiple orders leading to random spin patterns and an undefined magnetic ordering, hence we labelled these regimes too as incommensurate or correlated paramagnetic (IP).

We next added the third nearest neighbour Heisenberg J_3 interaction which phenomenologically is the consequence of extension of d-orbitals of the magnetic ions. We considered a small but positive anti-ferromagnetic J_3 as shown in Figure 4.12 (a) and (b). We observed that in the cases $\Gamma' = 0, -0.1$, the J_3 exchange term strongly favored and stabilized the zigzag order resulting in a simple phase diagram with a single phase over all ranges of parameters considered.

However as shown in Figure 4.11 the measured zigzag moment we found preferred the directions of easy axes for $\Gamma' = 0$ denoted on the extreme left by $ZZ_{\parallel}$ and easy planes, denoted to the extreme left of the phase diagram by $ZZ_{\perp}$ in Figure 4.12 (a) and (b) for $\Gamma' = -0.1$ at small $\Gamma = 0$, and both evolved towards $\langle \bar{1}11 \rangle$ directions upon increasing Γ. An exception in the phase diagram

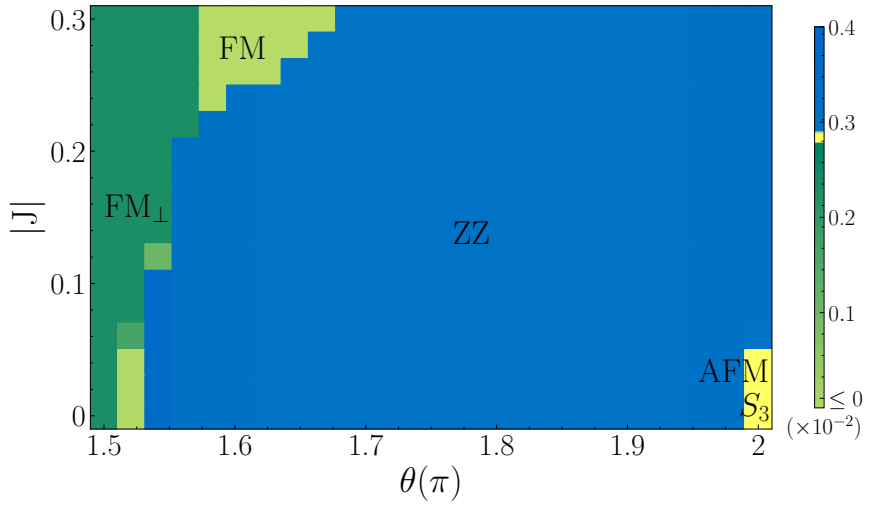

(a) $\Gamma' = -0.1$

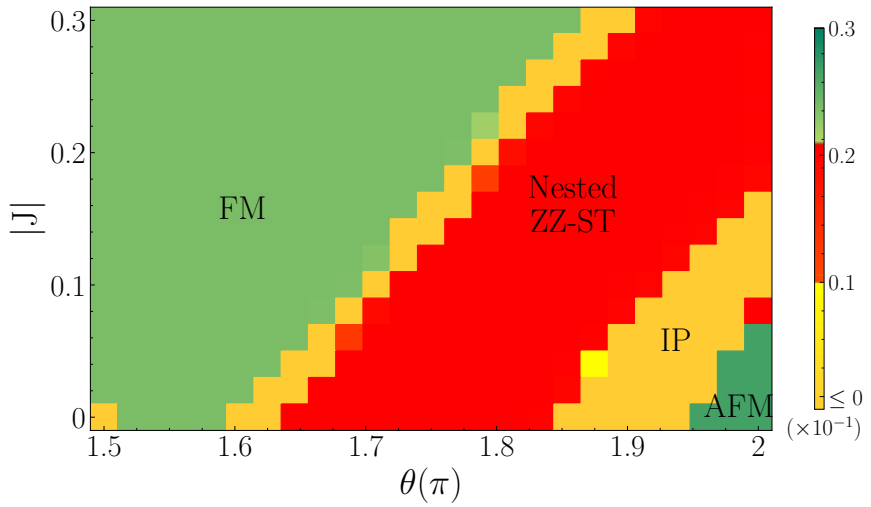

(b) $\Gamma' = 0.1$

FIGURE 4.10: Machine-learned J-K-Γ phase diagram, with $J_3 = 0$, $\Gamma' = \pm 0.1$ at $T = 10^{-3}$. A zigzag phase prevails over the phase diagram when a ferromagnetic $\Gamma' = -0.1$ is considered, while an anti-ferromagnetic S_3 order is stabilized in the large Γ limit. All orders in (a) are unfrustrated. By contrast, in the case of an anti-ferromagnetic Γ' (b), the nested zigzag-stripy phase expands significantly, and there remains a highly frustrated IP region at larger Γ values. Panels (a) and (b) are learned with a symmetric 6×6 and 4×4 cluster, respectively. The resolution of (θ, J) points is same as in Fig. 4.4, namely, $\Delta\theta = \frac{1}{48}\pi$ and $\Delta J = 0.02$.

was found top left corner which constitutes an incommensurate phase. This regime might be the remnant of a spiral order in the $O(3)$-symmetric $J_1 - J_3$ honeycomb Heisenberg model reported in these references [178, 59]. We found that it is present only in a narrow window around $J_3/J \sim -\frac{1}{3}$ along the $\Gamma = 0$ line which then becomes a trivial ferromagnet at larger values of the Heisenberg coupling $|J|$.

The regime of a positive J_3 and positive Γ' led to a more complex topology, as shown in Figure 4.12 (c). While the zigzag phase still dominated the phase diagram, we found the ferromagnetic and the $S_3 \times Z_3$ phase and the anti-ferromagnetic phase in the vanishing J_3 but positive Γ' case at the bottom right hand corner (Figure 4.10). The nested ZZ-ST order which dominated in the $J_3 = 0$ phase diagrams, was replaced by an IP regime and a zigzag order. We conclude that a positive Γ' competes with J_3 and this added to the frustration of the system and resulted in a more complex phase diagram. Having discussed all possible phase diagrams we now focus on

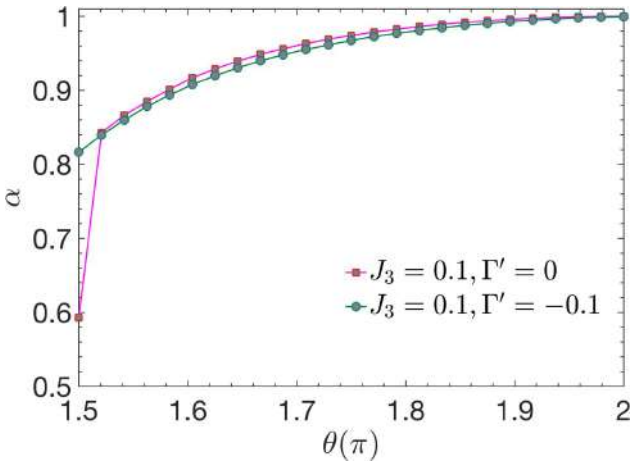

FIGURE 4.11: Evolution of the zigzag moment (m_{ZZ}) along the $J = -0.1$ line, for $J_3 = 0.1$, $\Gamma^{'} = 0, -0.1$, at $T = 10^{-3}$. Spins prefer easy-axes (easy-planes) for the case of $\Gamma^{'} = 0$ ($\Gamma^{'} = -0.1$) at small Γ, but evolves towards $n \in \langle \bar{1}11 \rangle$ with increasing Γ. $\alpha = \langle |m_{ZZ} \cdot \mathbf{n}| \rangle$ measures the projection of the magnetic moment on directions of $\langle \bar{1}11 \rangle$, and $\langle ... \rangle$ denotes an ensemble average.

the relevance to the current Kitaev candidates.

4.3 Implication to materials

In this section we shall look at the representative parameters reported in literature for the model we discussed in various Kitaev compounds. From the phase diagram discussed in previous sections and the parameter values discussed we conclude the most plaussible phases these materials would be found in at low temperatures and if they would be suitable Kitaev candidates. The parameter values reported in Ref. [203] based on inelastic neutron scattering (INS), the two cobaltate systems both $Na_2Co_2TeO_6$ and $Na_3Co_2SbO_6$ have a dominating ferromagnetic Kitaev exchange and a small AFM J_3 with $J_3 \sim 0.1|K|$. We found based on these values that they fall deep in the zigzag phase as shown in the phase diagrams of Figure 4.12 (a) and Figure 4.12 (b), which agree with the experimental result reported in Ref. [203].

	J	K	Γ	Γ'	J_3
α-$RuCl_3$[227]	-0.97	-8.21	4.16	-0.93	
α-$RuCl_3$[115]	-1.67	-6.67	6.6	-0.87	2.8
α-$RuCl_3$[226]	-0.5	-5.0	2.5		0.5
α-$RuCl_3$[147]	$[-4.1, -2.1]$	$[-11, -3.8]$	$[3.9, 5.0]$	[2.2,3.1]	$[2.2, 3.1]$
$Na_2Co_2TeO_6$[203]	$-0.1(8)$	$-9.0(5)$	1.8(5)	0.3(3)	0.9(3)
$Na_3Co_2SbO_6$[203]	$-2.0(5)$	$-9.0(10)$	0.3(3)	$-0.8(2)$	0.8(2)

TABLE 4.1: A selection of representative microscopic interactions (in meV) proposed for three Kitaev materials. A more complete collection of models suggested for α-$RuCl_3$ can be found in Refs. [131] and [147].

Recent studies have shown that the main Kitaev candidate compound α-$RuCl_3$ resides in the zigzag phase, provided that the Γ' term is negligible or is negative as suggested by the *ab initio* calculation and the INS fit of Ref. [226] and the DFT calculations of Refs. [115, 227]. Nevertheless, as we saw above if Γ' is antiferromagnetic, which was recently advocated in Ref. [147], the Kitaev material it falls into the far more complex phase diagram Figure 4.12(c) in the proximity with

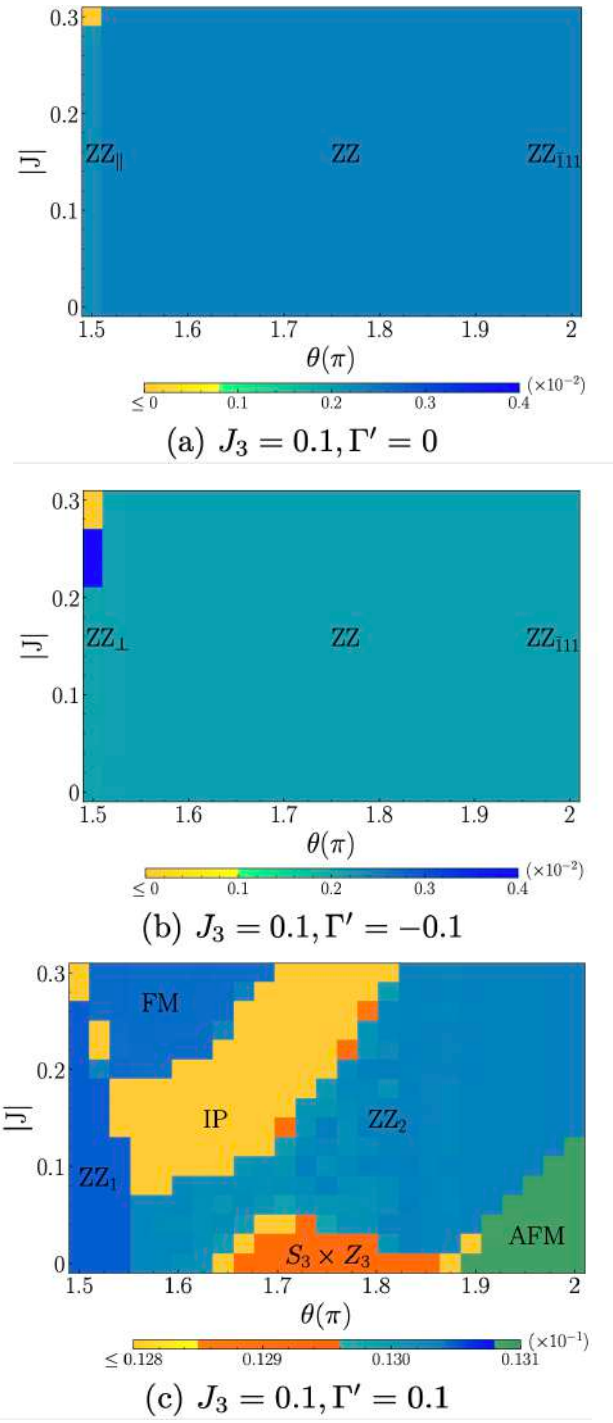

FIGURE 4.12: Machine-learned phase diagrams with $J_3 = 0.1, \Gamma' = 0, \pm 0.1$ at $T = 10^{-3}$. The J_3 term universally prefers zigzag states. Special zigzag states are marked in (a) and (b). The system is more frustrated for anti-ferromagnetic Γ' (c). The zigzag phase closely competes with other orders and a broad IP region. ZZ_1 and ZZ_2 distinguish different zigzag configurations. Panels (a) and (b) are learned with a symmetric 4×4 cluster, and panel (c) uses a 6×6 cluster. Colors reflect the value of Fiedler entries at each (θ, J) points, whose histograms are provided in shown above.

several competing phases. This conclusion is consistent with the linear spin-wave analysis of Ref. [147] where they found the zigzag-like magnet α-$RuCl_3$ lies adjacent to an incommensurate or disordered regime.

However if we just consider the pure $JK\Gamma$ model then (see Figure 4.4), α-$RuCl_3$ lies close to several competing phases. If we consider the commonly suggested range in literature for the three major exchange interactions , $\Gamma \sim 0.5 - 1|K|$ ($\theta \sim 1.65 - 1.75\pi$), $J \sim -0.1|K|$ [227, 176, 115, 226, 131, 147] we conclude from our phase diagram the relevant possible location in the $JK\Gamma$ phase diagram Figure 4.4 is close to the boundary of, the $S_3 \times Z_3$, the nested ZZ-ST, a ferromagnetic phase and a broad paramagnetic regime making the definite prediction of the phase without secondary factors non trivial.

4.4 Summary and Outlook

In this chapter we demonstrated the interpretable and unsupervised nature of TK-SVM, to learn the phase diagram of a generalized Heisenberg-Kitaev-Γ model on a honeycomb lattice which is relevant for most Kitaev materials that are a hot topic of research as they host a myriad of exotic and unconventional magnetic orders. We, here, not only successfully reproduced all known magnetic orders reported in literature which include incommensurate or paramagnetic-like regimes thus establishing the usefulness of the machine in unravelling vital information about the phases high-dimensional parameter space, but also went ahead and detected hitherto unreported new phases in the parameter regions relevant for the compounds α-$RuCl_3$, $Na_2Co_2TeO_6$ and $Na_3Co_2SbO_6$, which include a nested zigzag-stripy phase and an extended region of the modulated $S_3 \times Z_3$ phase under finite Heisenberg interactions.

In particular, our machine-learned phase diagrams suggests that, in the $JK\Gamma$ subspace relevant for the actively studied compound α-$RuCl_3$, the material is situated at the boundary of several competing phases, including a simple ferromagnet, the modulated helical $S_3 \times Z_3$ and the nested zigzag-stripy magnets, and possibly a correlated paramagnet. But we found that when we included secondary couplings based on phenomenological considerations such as Γ' and J_3, these terms act to stabilize the zigzag order as known in the literature. However, interestingly if the Γ' exchange is instead anti-ferromagnetic and sufficiently strong to compete with J_3, as recently proposed by Ref. [147], the proposed parameter point is in the vicinity of incommensurate or correlated paramagnetic regime which may originate from the competition of the magnetic orders indicated above.

In this chapter we have treated spins as classical $O(3)$ vectors which correspond to the large-S limit of quantum spins. What remains to be examined is the fate of these novel phases reported here against quantum fluctuations. Nevertheless, as long as strong symmetry-broken orders dominate over fluctuations, the phase diagrams reported here would act as a useful reference for all future quantum simulations. Moreover, by recognizing the unconventional orders and indicating the paramagnetic-like regimes, our phase diagrams also guide the understanding of existing Kitaev materials and the search for new ones.

Chapter 5

Phase Diagram of the $K\Gamma$ model unravelling new phases

Having seen already a few applications of our machine in analyzing the phase diagrams of certain models of Kitaev magnets in the previous few chapters, we continue on the same journey and in this chapter discuss the application of TK-SVM to the $K\Gamma$ model in a magnetic field. We found that this minimalistic model is much more interesting than the simple JK model which hosts well studied magnetic orders [39]. Our machine unravelled a complex phase diagram in the $K\Gamma$ phase space and in addition to the well known 120° vortex phase S_3 we also discovered a complex modulated helical phase which we christen "the modulated helical vortex" or by its symmetry group name $S_3 \times Z_3$. Our motivation to investigate this model is primarily due to the fact that a lot of the critical parts of the physics of Kitaev materials such as extension of Kitaev spin liquids or field induced suppression of spin orders can be already understood at classical level through this model. Kitaev materials have been at the forefront of present day research in condensed matter with a prime motivation to search for quantum Kitaev spin liquids (KSLs) [119]. In literature there is scarce conceptual understanding beyond the exactly solvable Kitaev limit and most investigations largely rely on mean-field or spin-wave methods [180, 181, 39, 92, 97, 164] and these different numerical calculations more often than not are qualitatively in conflict with each other [100, 222, 73, 134, 197, 72, 71].

We deployed our machine TK-SVM [75, 142, 77] to learn the global phase diagram of the honeycomb $K\Gamma$ model under a $[111]$ field in an unsupervised manner, which remains disputed even in the (semi-) classical large-S case and then use its interpretability to analyze each of the phases learnt by the machine. Our machine found complicated magnetic spin orders which we understood to be a direct consequence of *competition* and *cooperation* between Kitaev and Γ spin liquids. This chapter again provided another instance where our machine is able to detect new physics and unravel a lot of information in complex many-body systems.

5.1 Model and methods

We studied the $K\Gamma$ model on a two dimensional honeycomb lattice in a uniform $[111]$ magnetic field. The spins were treated as classical $O(3)$ vectors in order to achieve large system sizes $L = 72$ of 10368 spin which are crucial to capture competing orders induced by the Γ interaction. The Kitaev term is a result of Ising like interactions of spins on different bonds of the hexagonal lattice and induces bond frustration as a result of not being able to satisfy the bond constraints simultaneously. The introduction of the symmetric off-diagonal Γ term is phenomenological with its microscopic origins lying in the direct overlap of d orbitals or hopping mediated by the $d - p$ orbitals (see Chapter 1 for more details). In most realistic Kitaev materials it is thought that these terms are comparable [176, 115, 233, 227, 223] and it leads to macroscopic degeneracies and classical spin liquids [182].

The Hamiltonian we investigated is,

$$H = \sum_{\langle ij\rangle_\gamma} \left[K S_i^\gamma S_j^\gamma + \Gamma (S_i^\alpha S_j^\beta + S_i^\beta S_j^\alpha) \right] - \sum_i \vec{h} \cdot \vec{S}_i, \tag{5.1}$$

where K and Γ denote the strength of Kitaev and off-diagonal interactions, respectively and $\gamma \in \{x, y, z\}$ labels the three different nearest-neighbor (NN) bonds $\langle ij\rangle_\gamma$; α, β, γ are mutually orthogonal; and the magnetic field is $\vec{h} = h(1\,1\,1)/\sqrt{3}$. We further parametrized the interactions using the angle θ as $K = \sin\theta$, $\Gamma = \cos\theta$, with $\theta \in [0, 2\pi)$. The region $\theta \geq 3\pi/2$ corresponds to parameters of $4d/5d$ transition metals with ferromagnetic (FM) Kitaev coupling ($K < 0$) [208], while $\theta \in [\pi/2, \pi)$ relates to $4f$-electron based systems with anti-ferromagnetic (AFM) Kitaev coupling ($K > 0$) [95].

The Hamiltonian studied above features a global $C_6^R C_3^S$ symmetry which acts simultaneously on the real(R) and spin space(S), where C_6^R rotates the six spins on the hexagon (anti-)clockwise in the real space and C_3^S (anti-)cyclically permutates $\{S^x, S^y, S^z\}$. The Hamiltonian, in the absence of a magnetic field ($h = 0$), is additionally symmetric under a sublattice transformation $K \to -K$, $\Gamma \to -\Gamma$ and $S_i \to -S_i$ for either of the honeycomb sublattices A, B. This sublattice symmetry indicates equivalence between the $K\Gamma$ model of FM and AFM Kitaev interaction, which this is evident from the $h = 0$ phase diagram shown in Figure 5.3 (a) and the associated order parameters.

In order to study the phase diagram and implement TK-SVM we first collected samples from the parameter space (θ-h space) of interest. To do so, we partitioned the phase space into a uniform grid with a spacing of $\Delta h = 0.01$ in the y axis and considered magnetic fields in the range from $h \in [0, 0.2]$ and considered a spacing of $\Delta\theta = 0.02\pi$ in the x axis with the parameter θ in the range $\theta \in [0, 2\pi)$. Thus in total we considered 1250 points uniformly covering the entire phase space. At each phase point in the parameter space we then carried out large-scale parallel-tempering Monte Carlo simulations [89, 53] to generate the 500 spin configurations at low temperature $T = 10^{-3}\sqrt{K^2 + \Gamma^2}$, with system sizes up to $N = 10,368$ spins (72×72 honeycomb unit cells). As major parts of the phase diagram are unknown, we distributed the phase points (almost) uniformly, which is the common strategy in exploring unknown phase diagrams .

We then performed a SVM multi-classification on the sampled MC data and used a critical bias parameter of $\rho_c = 10^4$ to generate the topology although we crosschecked the consistency of our partitioning over a wide range of ρ_c. We then built a graph using the unsupervised aspect of TK-SVM with $M = 1250$ vertices and $M(M-1)/2 = 780,625$ edges [58, 57], which we interpret as the phase diagram.

The histogram of the Fiedler entries which is just the count of parameter points in each distinct subgraph, interpreted as an individual phase or the wide bumps interpreted as either crossover or phase boundary is shown below in Fig 5.1, 5.2 ,

Having learnt the topology of the phase diagram, we then collected more samples (typically a few thousands) deep in each phase at certain phase point and performed a separate multiclassification with the aim of learning the $C_{\mu\nu}$ matrices of high quality in order to be able to extract analytical quantities such as order parameters or local constraints. We learnt the coefficient matrices at rank 1 and 2. Finally, in order to confirm our interpretation, we measured these learned quantities.

5.2 $K\Gamma - h$ Phase Diagram

We shall now discuss the $K\Gamma$-h phase diagram which is just the colour coded representation of the Fielder vector decomposition. We found a rich and complex phase diagram that included a variety of classical spin liquids and exotic magnetic orders. We also found that in the region adjacent to the ferromagnetic Kitaev limit with $\Gamma \gtrsim 0$ (i.e. $\theta \gtrsim 3\pi/2$), which has been extensively studied for the quantum spin-1/2 $K\Gamma$ model, the classical phase diagram shares a number of important features with the quantum counterpart. In the subsequent sections we shall make clear to the reader, the

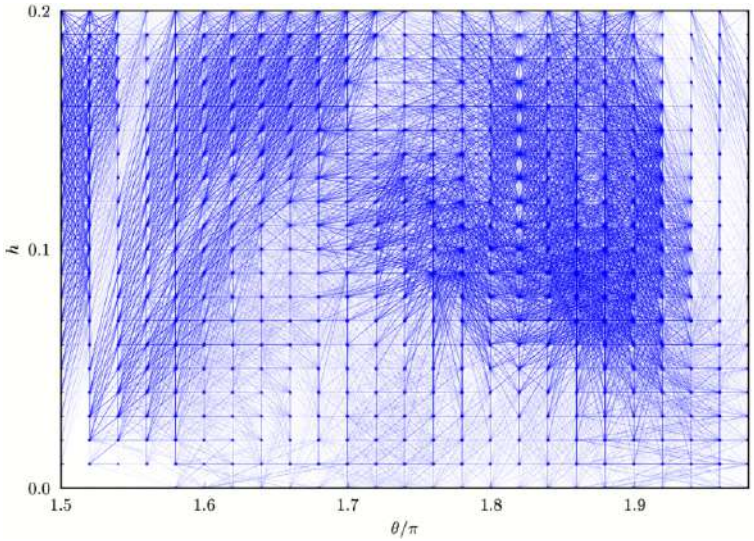

FIGURE 5.1: The $\theta \in [\frac{3\pi}{2}, 2\pi)$ sector of the graph is shown for visualization. Each vertex labels a (θ, h) point, following a uniform distribution $\Delta\theta = 0.02\pi$, $\Delta h = 0.01$. The edges connecting two vertices are determined by ρ in the corresponding decision function and the Lorentzian weight function. Edge weights are weakened to reduce visual density. The entire graph contains $M = 1{,}250$ vertices with $\theta \in [0, 2\pi)$ and $M(M-1)/2 = 780{,}625$ edges, whose partition gives the phase diagram Figure 5.3 (c).

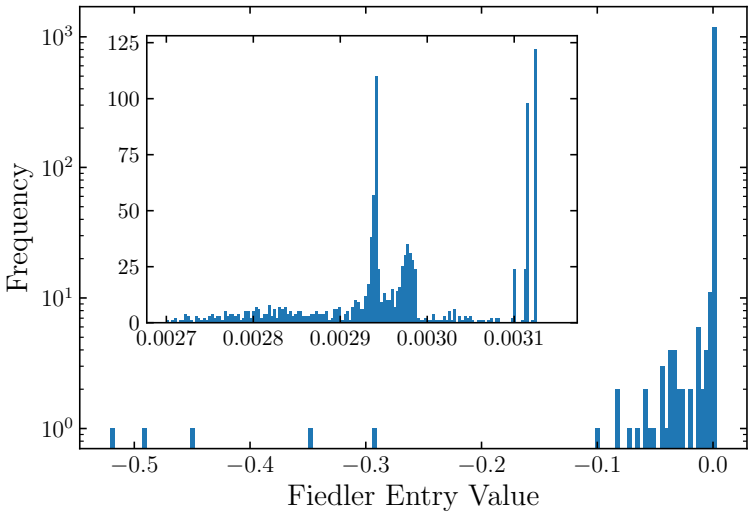

FIGURE 5.2: Histogram of Fiedler vector entries. Each entry corresponds to a vertex of the graph, namely, a (θ, h) point. Their values are color-coded by the phase diagram Figure 5.3 (c). A logarithmic scale is used in the main panel as the histogram is spanning several orders. The inner panel uses a linear scale and shows a zoom-in view of the bulk of the distribution. From left to right, the five profound peaks in the inner panel correspond to the two $S_3 \times Z_3$ phases, the FM S_3, the AFM S_3 phase and the full polarized phase, respectively. Flat regions correspond to correlated paramagnets and indicate wide crossovers to neighboring phases.

similarities between the classical and quantum phase diagrams and the specific properties of each phase and devote this section only to the features we observed in the phase diagram.

We shall first focus our attention to the pure $K\Gamma$ model without a magnetic field which is shown in Figure 5.3 (a). The Hamiltonian Eq. (5.1) has four limits at $(K, \Gamma) = (\pm 1, 0)$ and $(0, \pm 1)$ which corresponds to the classical spin liquids with two KSLs and two ΓSLs. These CSLs partitioned the phase diagram into four regions. When both the Kitaev and Γ interactions were either ferromagnetic or antiferromagnetic indicated here by $(+)$, the system is unfrustrated, while when they are

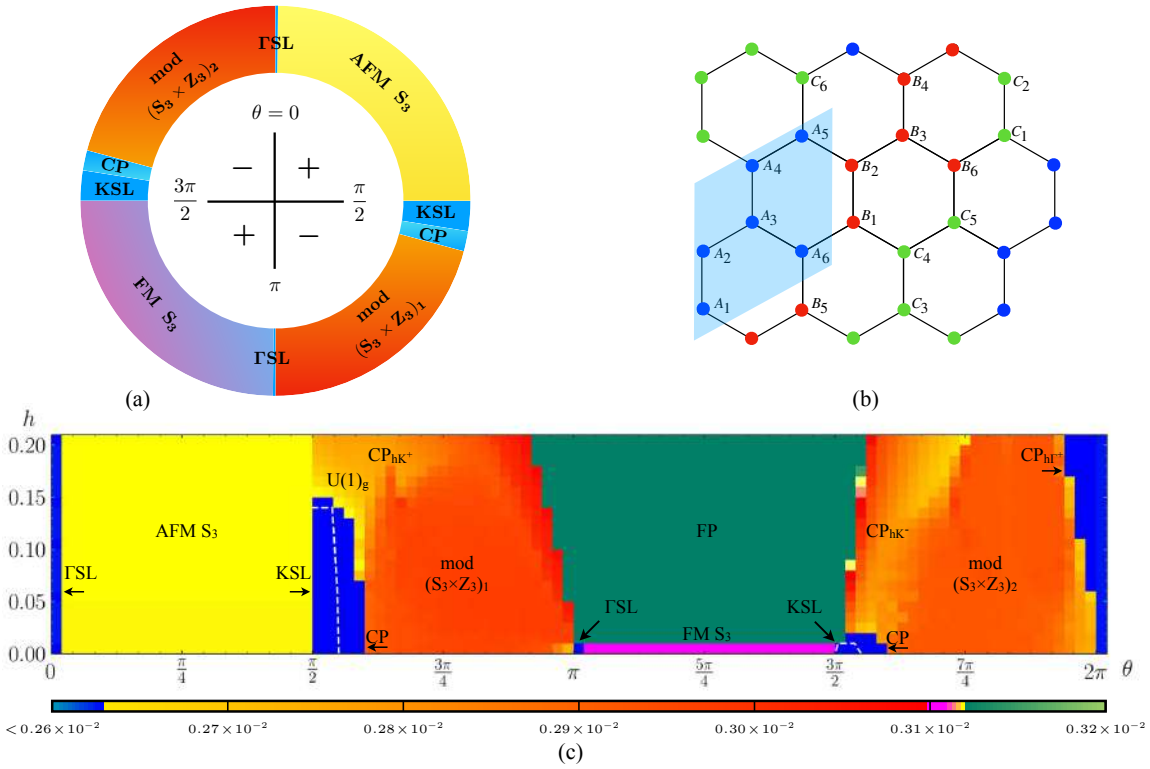

FIGURE 5.3: Machine-learned phase diagram for the honeycomb K-Γ model in a $[111]$ magnetic field, with $K = \sin\theta, \Gamma = \cos\theta$ and at temperature $T = 10^{-3}\sqrt{K^2+\Gamma^2}$. (**a**) Circular representation of the $h = 0$ phase diagram as a function of angle θ. Classical Γ (ΓSLs) and Kitaev (KSLs) spin liquids reside in the limits $\theta \in \{0, \frac{\pi}{2}, \pi, \frac{3\pi}{2}\}$ $[(K,\Gamma) = (0,\pm1),(\pm1,0)]$. These special limits divide the phase diagram into two frustrated ($K\Gamma < 0$) and two unfrustrated ($K\Gamma > 0$) regions, labeled by "$-$" and "$+$', respectively. While ΓSLs exist only in the two large Γ limits, KSLs extend into the frustrated regions, until $|\Gamma/K|_1 \sim 0.16$ ($\theta \sim 0.551\pi, 1.551\pi$). The $h = 0$ phase diagram is symmetric under $\theta \to \theta + \pi$ and a sublattice transformation . (**b**) Magnetic cells of the S_3 and modulated $S_3 \times Z_3$ orders. The shaded sites show a magnetic cell for the FM and AFM S_3 order, comprised of six spins. The modulated $S_3 \times Z_3$ orders consist of three distinct S_3 sectors (labeled by A, B, C) and in total eighteen sublattices. (**c**) Finite h phase diagram. The FM S_3 and the KSL (ΓSL) for $K = -1$ ($\Gamma = -1$) will be fully polarized (FP) once the $[111]$ field is applied. However, an antiferromagnetic Γ extends the FM KSL to a small, but finite, $h \sim 0.01$. AFM ΓSL and AFM KSL are robust against external fields. The former persists until $h \geq 0.2$, while the latter is non-trivially polarized from $h \sim 0.14$ with global $U(1)$-symmetric correlations $[U(1)_g]$. In the frustrated regions and intermediate fields, there are areas of different partially-polarized correlated paramagnets (CP_hs). In particular, in the sector of $K < 0, \Gamma > 0$, the CP_{hK^-} and $CP_{h\Gamma^+}$ regimes erode the modulated $(S_3 \times Z_3)_2$ phase, as field-induced suppression of magnetic order takes hold. Each pixel in the phase diagram represents a (θ, h) point and is color-coded by the corresponding Fiedler vector entry. Dashed lines separate a spin liquid from a correlated paramagnet, based on susceptibility of the associated ground state constraint (GSC). The Fiedler vector and the GSCs are computed from rank-1 and rank-2 TK-SVM, respectively.

of opposite sign indicated here by $(-)$, the system remained highly frustrated. This frustration or unfrustration based on the signs of the interactions was associated with the "competition" or "cooperation" between the classical spin liquids as we shall discuss below further in the section on constraints.

In the two unfrustrated regions when K and Γ are both finite, the system immediately changed from a spin liquid to a vortex magnetic order described in literature as the 120° state [180, 39].

Since the explicit order parameters of the two phases corresponded to the symmetric group S_3, we refered to them in this thesis by their symmetry group name as the FM S_3 and AFM S_3 phase, respectively, to distinguish them from other types of 120° states. These phases emerged as a result of the *cooperation* between the Kitaev and Γ spin liquids which we shall ruminate further below.

We observed in the frustrated regions that the two KSLs extended to a finite value of Γ suggesting that these spin liquids are robust to perturbations from non-Kitaev interactions in conjunction with mounting evidence suggesting that quantum KSLs survive against perturbations by some non-Kitaev interactions [103, 240, 72, 71, 134, 222, 73, 166, 70]. This finite extension of classical KSLs in the large-S limit was quite remarkable and suggested that certain features in the quantum regime might already be understood in the classical counterparts. We used the corresponding ground state constraint (GSC) and estimated that up till $|\Gamma/K| \sim 0.16$ the KSL extended. One possible explanation is that for the finite extension of classical KSL lies in the large extensive ground-state degeneracy (exGSD) of classical KSLs. On the other hand, we found that the two classical ΓSLs only exist in the limit $\Gamma = \pm 1$, which agreed with the extensive GSD calculations which showed that the exGSD is much smaller than that for KSLs.

The modulated helical phases occupied the majority of the frustrated regions. In the ferromagnetic K sector, it was recently proposed to accommodate incommensurate orders or disordered states by numerical studies based on small system sizes [100, 73, 197]. However, having analyzed the explicit order parameter, our machine revealed a much more intriguing structure in these modulated helical phases. These phases were found to posses three-folds of the magnetic structure present in the FM and AFM S_3 phase, leading to a total of eighteen sublattices. In addition, the three S_3 sectors mutually cancelled each other via a novel modulation and hence we referred to this phase as the modulated $S_3 \times Z_3$ phase or the modulated helical order. This phases emerged as a result of the *competition* between a Kitaev and a Γ spin liquid.

We found an additional structure in the phase diagram between each modulated $S_3 \times Z_3$ phase and the corresponding KSL, a window of another correlated disordered region. We understood this region as a crossover between the two phases. We referred these regions as correlated paramagnets (CP), which however we hypothesized may shrink in size if the phase transitions get sharper and the system sizes get larger and the temperature of classical simulations was lowered.

Having discussed the phase diagram in zero field thus far, we shall now discuss the influence of the magnetic field on the phase diagram. When we turned on the $[111]$ magnetic field, we discovered that the fate of each phase strongly depended on the sign of its interactions, as is shown in Figure 5.3 (c). Those which featured only ferromagnetic interactions, including the FM S_3 phase, the FM Kitaev and Γ spin liquids, immediately polarized which we represented by the fully polarized (FP) phase above. However, interestingly we found that the phases with one or both antiferromagnetic interactions were quite robust against finite h. Specifically, the AFM KSL persisted up to $h \sim 0.14$. Before the KSL was trivial polarized at much stronger fields, an intermediate region dubbed as $U(1)_g$ emerged, where the magnetic field induced two different correlations with a *global* $U(1)$ symmetry. This shall be discussed in more detail below. Interestingly, this region appeared to coincide with a gapless spin liquid phase which was recently proposed for quantum spin-1/2 and spin-1 systems [159, 249, 84, 85, 248].

We again found that even in the case of a finite magnetic field, the frustrated $K\Gamma < 0$ regions were the most interesting and richest in physics. The FM KSL extended to a small but finite region upto field $h \sim 0.01$ while on the other hand the AFM KSL extended over a much greater area. We additionally found that at intermediate h, there are disordered regions that separate a $S_3 \times Z_3$ phase from a spin liquid or a trivially polarized state. These phases are referred to as partially-polarized correlated paramagnets (CP_hs) in order to distinguish them from the parent spin liquid. The correlated paramagnets CP_{hK^-} and $CP_{h\Gamma^+}$ were found to be responsible for the erosion of the modulated $(S_3 \times Z_3)_2$ phase. Gohlke et al recently proposed a field-induced unconventional paramagnet for the quantum spin-1/2 in the $\mathrm{CP}_{\mathrm{hK}^-}$ region [134, 71] which matches with what we found here. This agreement between classical and quantum phase diagrams indicates that certain features and critical properties of Kitaev materials with a significant Kitaev and Γ interaction, might already be understood at the classical level.

5.2.1 Discussion of the S_3 and $S_3 \times Z_3$ orders

In this section we shall discuss the two non-trivial magnetic orders found by our machine namely S_3 and $S_3 \times Z_3$ orders. We interpreted the coefficient matrix $C_{\mu\nu}$ at rank 1 and 2 to derive the ordering matrices and the local constraints. To ensure that we had correctly interpreted the phases we measured the corresponding magnetization in these phases and observed that they are finite in the respective phases and zero elsewhere thus further confirming the phase boundaries derived from the unsupervised graph partitioning. In many body physics, one way to get a disordered phase (or a spin liquid phases) is to have a non-decomposible superposition of competing magnetic orders. Here, in contrast to this familiar scenario, we hypothesised the emergence of these magnetic orders (S_3 , $S_3 \times Z_3$) is due to either the *cooperation* or the *competition* between two spin liquids ($KSL, \Gamma SL$).

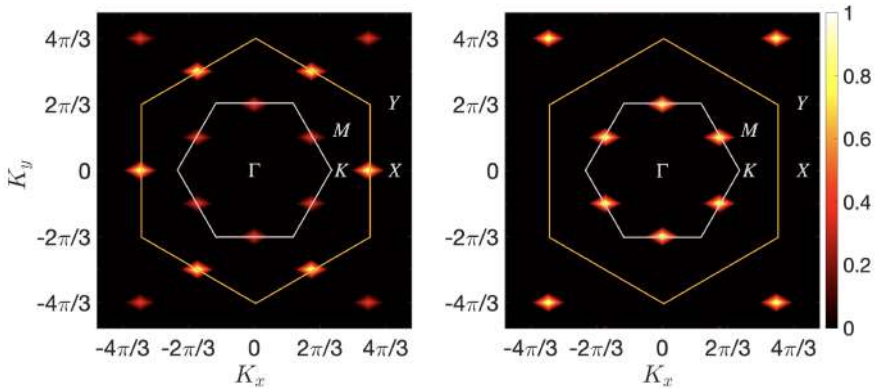

FIGURE 5.4: Static spin-structure factors (SSFs), $S(\vec{K}) = \left\langle \frac{1}{N} \sum_{ij} \vec{S}_i \cdot \vec{S}_j \, e^{i\vec{K}\cdot(\vec{r}_i - \vec{r}_j)} \right\rangle$, where $\vec{r}_i$ is the position of a spin at site i, and $\langle . \rangle$ denotes the ensemble average. The two S_3 orders develop magnetic Bragg peaks at the **K** points of the honeycomb Brillouin zone (orange hexagon). The two $S_3 \times Z_3$ orders show Bragg peaks at $\frac{2}{3}\mathbf{M}$ points, owing to the larger magnetic cell. The length of nearest-neighbor bonds of the honeycomb lattice is set to unity.

The static structure factor that was computed from the configuration of spins obtained from Monte Carlo sampling at low temperatures $\sim 10^{-3}$ is shown above in 5.4 which was generated by averaging over 500 samples from the canonical ensemble.

We observed that the two S_3 orders (FM,AFM) developed the exact same SSF with magnetic Bragg peaks at the K points of the first honeycomb Brillouin zone (Figure 5.4), which we identified with the well-known $\sqrt{3} \times \sqrt{3}$ order. Similarly we observed that the SSF of the two $S_3 \times Z_3$ phases, shown in Figure 5.4 (b), developed magnetic Bragg peaks at the $2/3M$ points of the first honeycomb Brillouin zone. We understood the reduced BZ was a consequence of the large magnetic cell. Nevertheless in both scenarios the SSF pattern only revealed partially information on the ordering and did not reveal any information on the differences in magnetization between AFM and FM or the spin-lattice entangled modulation in Eq. (5.4). This ability to indistinguish orders just based on SSFs highlights the importance of knowing and compels us to find the explicit order parameters in order to accurately classify and interpret the phase.

The coefficient matrix $C_{\mu\nu}$ learnt at rank 1 with a 18 site spin cluster for the two phases is shown below and the learnt ordering matrices (order parameters) for the two phases is shown in Table 5.1

We observed that in the interpretation of the S_3 phase the 18 site cluster is redundant and we could fit three sets of repeating patterns of six matrices (3×3) each starting from the bottom left. While for the $S_3 \times Z_3$ phase the 18 site cluster accommodated all the ordering matrices (without repetitions/ redundancies) as shown in Figure 5.5.

We shall now discuss the two phases separately.

Unfrustrated S_3 orders

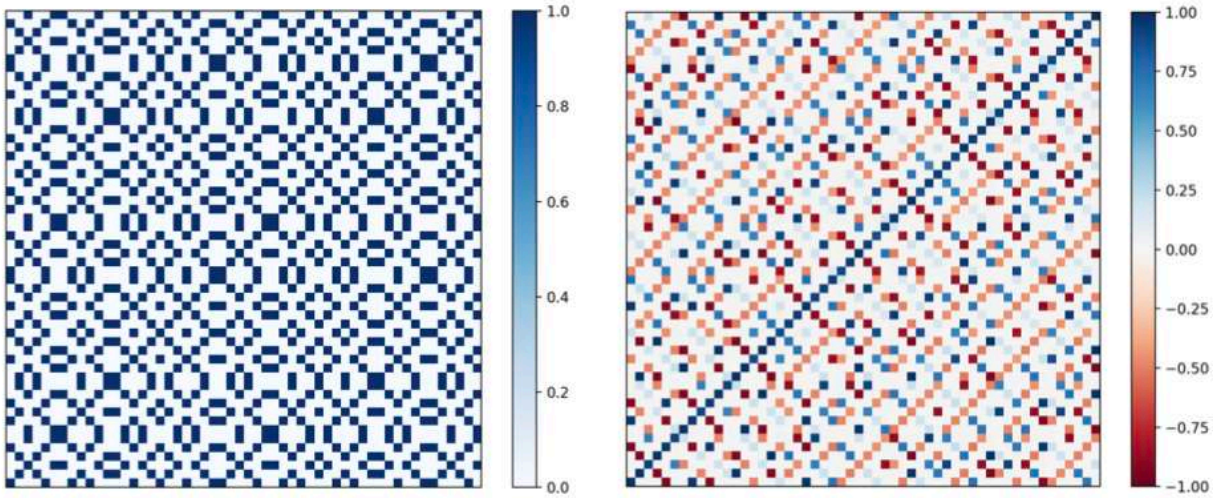

FIGURE 5.5: Visualization of the $C_{\mu\nu}$ matrix of the FM S_3 and the mod $(S_3 \times Z_3)_2$ phase. Each pixel corresponds to an entry of $C_{\mu\nu}$. Non-vanishing entries identify the relevant components of ϕ_μ entering the order parameter. Here results of a 18-spin cluster are shown for demonstration, while much larger clusters are used for the phase diagram Figure 5.3. The S_3 order is represented multiple times as its magnetic cell has six sublattices.

The S_3 orders exist in the unfrustrated region of the phase diagram where both the interaction terms have the same sign $K\Gamma > 0$.

From the $C_{\mu\nu}$ matrices we learnt that both S_3 orders have six magnetic sublattices with an order parameter magnetization defined as

$$\overrightarrow{M}_{S_3} = \frac{1}{6}\sum_{k=1}^{6} T_k \vec{S}_k, \tag{5.2}$$

where T_k are ordering matrices, given in Table 5.1, and the only different between FM and AFM S_3 orders is that the ordering matrices T_2, T_4, and T_6 differ by a global sign. These six matrices form a closed symmetric group known as the S_3 group and hence the name of the phase. This group comprises of three rotations and three reflections with $C_3 := \{T_1, T_3, T_5\}$ cyclic subgroup indicating three-fold rotations about the $[111]$ direction in spin space and T_2, T_4 and T_6 corresponding to reflection about the planes $(110), (011), (101)$ respectively. These findings were also reported in Chaloupka et al [39] and these exact six matrices reproduce a dual transformations, that transformed this vortex phase to a simple ferromagnet thus uncovering a hidden $O(3)$ symmetry at $K = \Gamma$ phase point which is another instance of hidden symmetries we discussed in the previous chapter 3.

Frustrated $S_3 \times Z_3$ ***orders*** The modulated $S_3 \times Z_3$ orders exist in the frustrated regimes of the phase diagram where the interactions have opposite signs $K\Gamma < 0$. From the $C_{\mu\nu}$ matrix we learnt eighteen ordering matrices shown in the Table 5.1 and we defined the corresponding (order parameter) magnetization as

$$\overrightarrow{M}_{S_3\times Z_3} = \frac{1}{18}\sum_{\alpha}^{A,B,C}\sum_{k=1}^{6} T_k^\alpha \vec{S}_k^\alpha, \tag{5.3}$$

where T_k^α are given in Table 5.1, and $\alpha = A, B, C$ refer to the three distinct S_3 sectors illustrated in Figure 5.3 (b). The only difference between the AFM and FM phases was that $(S_3 \times Z_3)_1$ differed from $(S_3 \times Z_3)_2$ by a global sign for all even k's. We also noticed that this order exhibited a very

S_3

$$T_1 = \begin{pmatrix} 1 & 0 & 0 \\ 0 & 1 & 0 \\ 0 & 0 & 1 \end{pmatrix}, \quad T_2 = \pm\begin{pmatrix} 0 & 1 & 0 \\ 1 & 0 & 0 \\ 0 & 0 & 1 \end{pmatrix}, \quad T_3 = \begin{pmatrix} 0 & 0 & 1 \\ 1 & 0 & 0 \\ 0 & 1 & 0 \end{pmatrix},$$

$$T_4 = \pm\begin{pmatrix} 0 & 0 & 1 \\ 0 & 1 & 0 \\ 1 & 0 & 0 \end{pmatrix}, \quad T_5 = \begin{pmatrix} 0 & 1 & 0 \\ 0 & 0 & 1 \\ 1 & 0 & 0 \end{pmatrix}, \quad T_6 = \pm\begin{pmatrix} 1 & 0 & 0 \\ 0 & 0 & 1 \\ 0 & 1 & 0 \end{pmatrix}$$

Mod $S_3 \times Z_3$

$$T_1^A = \begin{pmatrix} 1 & 0 & 0 \\ 0 & 1 & 0 \\ 0 & 0 & 1 \end{pmatrix}, \quad T_2^A = \pm\begin{pmatrix} 0 & 1 & 0 \\ 1 & 0 & 0 \\ 0 & 0 & -a \end{pmatrix}, \quad T_3^A = \begin{pmatrix} 0 & 0 & 1 \\ -1/2 & 0 & 0 \\ 0 & -1/2 & 0 \end{pmatrix},$$

$$T_4^A = \pm\begin{pmatrix} 0 & 0 & -a \\ 0 & a-1 & 0 \\ -a & 0 & 0 \end{pmatrix}, \quad T_5^A = \begin{pmatrix} 0 & -1/2 & 0 \\ 0 & 0 & -1/2 \\ 1 & 0 & 0 \end{pmatrix}, \quad T_6^A = \pm\begin{pmatrix} 1 & 0 & 0 \\ 0 & 0 & a-1 \\ 0 & a-1 & 0 \end{pmatrix}$$

$$T_1^B = \begin{pmatrix} -1/2 & 0 & 0 \\ 0 & -1/2 & 0 \\ 0 & 0 & -1/2 \end{pmatrix}, \quad T_2^B = \pm\begin{pmatrix} 0 & a-1 & 0 \\ a-1 & 0 & 0 \\ 0 & 0 & 1 \end{pmatrix}, \quad T_3^B = \begin{pmatrix} 0 & 0 & -1/2 \\ -1/2 & 0 & 0 \\ 0 & 1 & 0 \end{pmatrix},$$

$$T_4^B = \pm\begin{pmatrix} 0 & 0 & 1 \\ 0 & -a & 0 \\ 1 & 0 & 0 \end{pmatrix}, \quad T_5^B = \begin{pmatrix} 0 & 1 & 0 \\ 0 & 0 & -1/2 \\ -1/2 & 0 & 0 \end{pmatrix}, \quad T_6^B = \pm\begin{pmatrix} a-1 & 0 & 0 \\ 0 & 0 & -a \\ 0 & -a & 0 \end{pmatrix}$$

$$T_1^C = \begin{pmatrix} -1/2 & 0 & 0 \\ 0 & -1/2 & 0 \\ 0 & 0 & -1/2 \end{pmatrix}, \quad T_2^C = \pm\begin{pmatrix} 0 & -a & 0 \\ -a & 0 & 0 \\ 0 & 0 & a-1 \end{pmatrix}, \quad T_3^C = \begin{pmatrix} 0 & 0 & -1/2 \\ 1 & 0 & 0 \\ 0 & -1/2 & 0 \end{pmatrix},$$

$$T_4^C = \pm\begin{pmatrix} 0 & 0 & a-1 \\ 0 & 1 & 0 \\ a-1 & 0 & 0 \end{pmatrix}, \quad T_5^C = \begin{pmatrix} 0 & -1/2 & 0 \\ 0 & 0 & 1 \\ -1/2 & 0 & 0 \end{pmatrix}, \quad T_6^C = \pm\begin{pmatrix} -a & 0 & 0 \\ 0 & 0 & 1 \\ 0 & 1 & 0 \end{pmatrix}$$

TABLE 5.1: Ordering matrices in the S_3 and modulated $S_3 \times Z_3$ magnetizations. "+" ("−") corresponds to the FM (AFM) S_3 order and the modulated $(S_3 \times Z_3)_{1(2)}$ order. $a \in [0,1]$ is $|\Gamma/K|$ dependent. The S_3 matrices form the symmetric group S_3. The $S_3 \times Z_3$ matrices consist of three distinct S_3 sectors, featuring a spin-lattice entangled modulation $T_k^A + T_k^B + T_k^C = 0$. A global sign difference is in T_k with $k = 2, 4, 6$, reflecting the sublattice symmetry of the Hamiltonian Eq. (5.1) in zero field.

delicate *spin-lattice entangled* modulation where,

$$T_k^A + T_k^B + T_k^C = 0 \ \ \forall k = 1...6 \tag{5.4}$$

To elucidate this point further we noticed that $T^{\alpha}_{1,3,5}$, $\alpha = \{A, B, C\}$ represented rotations about the [111] direction but there is an additional $\cos(2\pi/3) = -1/2$ factor entering some but not all spin components. This factor corresponded to an alternating 120° rotation in spin space and three subsequent rotations required to bring back the spin to its original configuration. The rotation factor, as shown in Table 5.1, alternates among the three S_3 sectors, to achieve the cancellation (or identity transformation) of the corresponding spin components. We also observed that in the case of mirror reflections (T_k^{α} with even k's) the same cancellation occurs resulting in a three-fold modulation but in contrast to rotations carried through the factor $\cos(2\pi/3)$ the reflections are carried through a factor $a \in [0,1]$ which is also learnt by TK-SVM and depends strongly on the relative strength $|\Gamma/K|$. This modulation occurred in a way that guarantees cancellation.

Thus the two modulations that result in identity transformations can succinctly be put together as

$$\cos(2\pi/3) + \cos(4\pi/3) + \cos(6\pi/3) = 0 \tag{5.5a}$$

$$(a-1) + (-a) + 1 = 0 \tag{5.5b}$$

It is important to note here that this spin modulation is very different from those in multiple-**q** orders and spin-density-wave (SDW) orders where the phase factors *universally act on all spin components* and not just on certain spin components which is the case here. Since we multiply spin components with these modulated matrices we do not explicitly conserve the spin norm and further the $S_3 \times Z_3$ magnetization does not saturate to unity, instead to a reduced value $|\vec{M}_{S_3\times Z_3}| \lesssim \frac{2}{3}$, indicating an intrinsic frustration.

To confirm that we have correctly identified the modulated phase we measured the $S_3 \times Z_3$ order parameter against finite magnetic field as well as thermal fluctuations. In Figure 5.9 (b) and (d), we confirmed their stability by varying the phase parameter $\theta = \arctan(K/\Gamma)$ at zero magnetic field over the entire frustrated region for both the AFM ($\theta \in [\pi/2, \pi)$) and FM ($\theta \in [3\pi/2, 2\pi)$) and we observed that the magnetization is non-zero (but does not saturate to one due to spin modulation explained above) in the entire region.

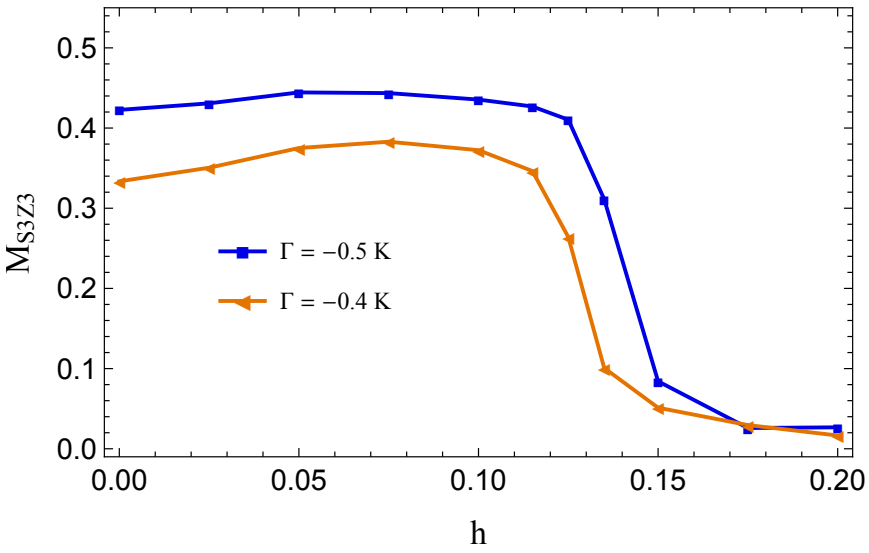

FIGURE 5.6: Monte Carlo measurement of the $(S_3 \times Z_3)_2$ magnetization as a function of the [111] field, in the region of FM K and intermediate AFM Γ. The $(S_3 \times Z_3)_2$ magnetization extends over a finite region of external field and is subsequently suppressed to a small but finite value, see Figure 5.3(c).

Moreover, the global phase diagram in a finite field already discussed above (Figure 5.3 (c)) showed that these modulated phases are robust and had a finite extension against finite [111] magnetic field. This feature was further confirmed by plotting the magnetization against finite field as shown in Figure 5.6. The magnetization was suppressed around $h \approx 0.15$ but the exact critical field for suppression depends intricately on the Γ interaction. The suppressed order entered a partially-polarized frustrated regime, owing to the competition between the external field and the Kitaev and Γ interactions and a further increase in field strength led to a full polarization of the phase resulting in a trivial ferromagnet where the second term in the Hamiltonian dominates over the first $H \approx -\sum_i \vec{h} \cdot \vec{S}_i$. Gohlke et al Ref. [71] discussed a similar classical regime where the classical paramagnet was considered to be the parent phase of two quantum nematic paramagnets in the quantum spin-1/2 $K\Gamma$ model [71, 134].

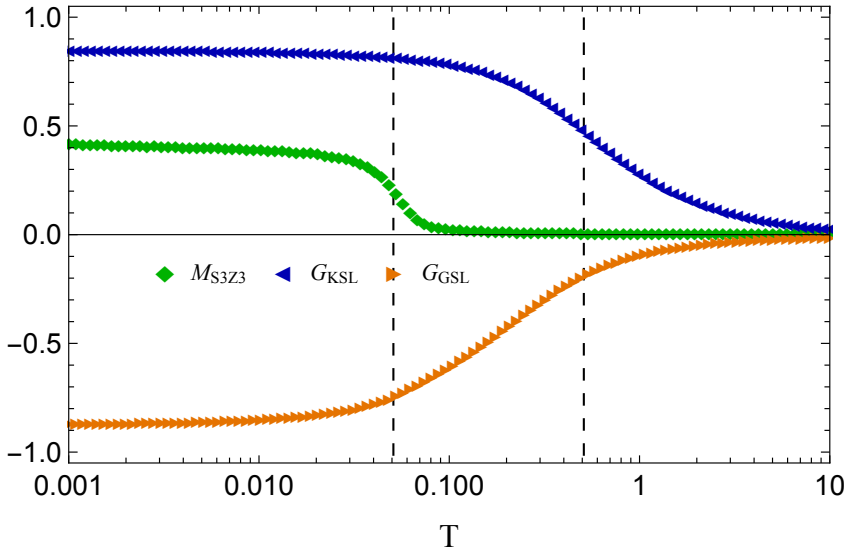

FIGURE 5.7: Temperature dependence of the $(S_3 \times Z_3)_2$ order and the corresponding Kitaev and Γ correlations for $h = 0$, $\Gamma = -0.5$, and $K > 0$. The system exhibits a two-step melting, dividing the temperature range into three regimes. In the low-temperature regime, the $(S_3 \times Z_3)_2$ order is established along with strong G_{KSL} and $G_{\Gamma SL}$. The intermediate regime is a correlated paramagnet, where the competing Kitaev and Γ correlations are already noticeable but not strong enough to stabilize magnetic order. A trivial paramagnet is found for high temperatures. The dashed lines mark the location of crossovers.

We also investigated how robust the order was against thermal fluctuations as shown in Figure 5.7, we evaluated the temperature dependence of the $(S_3 \times Z_3)_2$ magnetization as well as the corresponding Kitaev and Γ constraints. We conclude that the system exhibited two crossovers when increasing temperature. In the low temperature regime we have a finite order as shown by the finite values of the magnetization as well as constraints with strong G_{KSL} and $G_{\Gamma SL}$. This finite order on increasing temperature melted into an intermediate regime where the Kitaev and Γ correlations are developed but are not strong enough to stabilize magnetic order against thermal fluctuations. This intermediate regime was found to extend until nearly one order of magnitude below the Néel temperature set by the interaction strength, and may also be viewed as a finite-temperature correlated paramagnet.

Upon increasing the temperature further the finite temperature paramagnet melted into trivial paramagnet will all constraints and coefficients vanishing. While a two-step melting is often observed for spin liquids, including the quantum KSL [159, 160] and the classical ΓSL [185], as well as for spin nematics, such as the multipolar orders in the Kagome [247] and pyrochlore [207] anti-ferromagnets, such a phenomenon is quite unusual for a magnetically ordered system.

The $(S_3 \times Z_3)_1$ phase had the same temperature dependence because of the sub-lattice symmetry of the KΓ model at zero field which we alluded to in the section on the model and methods. However, the only difference was that sign of G_{KSL} and $G_{\Gamma SL}$ are swapped as exemplified in the case of Figure 5.9 (b) and (d).

5.3 Local constraints learnt by TK-SVM

In this section we shall expound on the local constraints that we learnt by interpreting the coefficient matrix $C_{\mu\nu}$ at rank 2. Since we were able to interpret as well as measure the order parameters for all the magnetic orders where the system breaks orientational symmetry (SSB) and entered a unique ordered ground state we shall focus on the constraints we learnt for the classical Kitaev and Γ spin liquids. Since a classical spin liquid, unlike magnetic orders, does not break any orientational symmetry we characterize them by the local symmetries in its *ground state constraints*

Correlations	Symmetry	
	Global	Local
$G_1 = \sum_{\langle ij\rangle\in\hexagon} S_i^\gamma S_j^\gamma$	$C_6^R C_3^S$	Z_2
$G_2 = \sum_{\langle ij\rangle\in\hexagon} \sum_{\alpha\beta} \lvert\varepsilon_{\alpha\beta\gamma}\rvert S_i^\alpha S_j^\beta$	$C_6^R C_3^S$	Z_2
$G_3 = \sum_{[ij]\in\hexagon} S_i^{\gamma_2} S_j^{\gamma_1}$	$C_6^R C_3^S$	Z_2
$G_4 = \sum_{[ij]\in\hexagon} \lvert\varepsilon_{\alpha\gamma_1\gamma_2}\rvert (S_i^{\gamma_1} S_j^\alpha + S_i^\alpha S_j^{\gamma_2})$	$C_6^R C_3^S$	
$G_5 = \sum_{(ij)\in\hexagon} S_i^c S_j^c$	$C_6^R C_3^S$	Z_2
$G_6 = \sum_{(ij)\in\hexagon} \sum_{ab} \lvert\varepsilon_{abc}\rvert S_i^a S_j^b$	$C_6^R C_3^S$	
$G_1^h = \sum_{\langle ij\rangle\in\hexagon} \sum_{\alpha\beta} S_i^\alpha S_j^\beta$	$U(1)$	
$G_2^h = \sum_{(ij)\in\hexagon} \sum_{ab} S_i^a S_j^b$	$U(1)$	

TABLE 5.2: Quadratic correlations classified by rank-2 TK-SVM. $G_{KSL} = \frac{1}{2}\langle G_1\rangle_\hexagon = \pm 1$ and $\langle G_{k\neq 1}\rangle_\hexagon = 0$ define the grounds states of FM and AFM KSLs, respectively. $G_{\Gamma SL} = \frac{1}{7}\langle G_2 \pm G_3 + G5\rangle_\hexagon = \pm 1$ and vanishing G_1, G_4, G_6 define the ground states of FM and AFM ΓSLs. For the two S_3 orders, all G_k contribute with an equal weight. No stable ground-state constraints are found in the modulated $S_3 \times Z_3$ phases and those correlated paramagnetic regions. All G_k preserve the global $C_6^R C_3^S$ symmetry of the $K\Gamma h$ Hamiltonian Eq. G_1 (G_2, G_3, G_5) is locally Z_2 invariant on a bond (hexagon). G_1^h, G_2^h are field-induced correlations for the AFM Kitaev model with a global $U(1)$ symmetry.

(GSC) which define the ground state manifold as well as the low-lying excitations of the spin liquid (see CSLs in Chapter 1 for better understanding).

Our machine learnt a distinct constraint for the two spin liquids shown in the phase diagram Figure 5.3. Since these constraints are learnt at rank-2, these constraints give the correlations between quadratic spin components on the hexagon. All the constraints we learnt could be classified into **six types at zero field** ($h = 0$) and another two field-induced correlations for the AFM KSL summarized in the Table below Table 5.2.

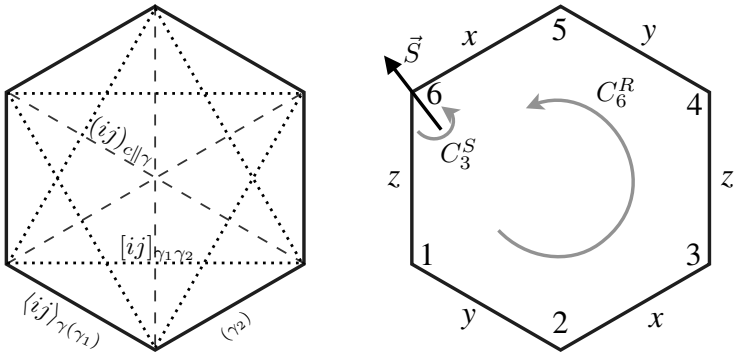

FIGURE 5.8: Convention of the quadratic correlations in Table 5.2. $\langle.\rangle$, $[.]$ and $(.)$ denote the first, second and third nearest-neighbor (NN) bonds, respectively. $\gamma = x, y, z$ label the type of a NN bond. γ_1, γ_2 correspond to the two connecting NN bonds. $c = \gamma$ is determined by the parallel NN bond. α, β, γ (a, b, c) are mutually orthogonal. C_6^R is a symmetry that rotates the six spins on a hexagon (anti-)clockwise. C_3^S denote (anti-)cyclic permutations of the three spin components.

5.3.1 Constraints for the magnetic phases

For the S_3 phase we identified by interpreting the rank-2 coefficient matrix the GSC,

$$G_{S_3} = \frac{1}{15}\langle \pm G_1 \pm G_2 + G_3 + G_4 \pm G_5 \pm G_6 \rangle_{\hexagon} = 1, \tag{5.6}$$

which equally comprised of the G_{KSL} and $G_{\Gamma SL}$ in Eqs. (5.7)-(5.8), with additional G_4 and G_6 terms owing to the normalization $|\vec{S}| = 1$. We see from the Figure 5.9 (a) and (c) that in the AFM case both the spin liquid constraints are equal and saturate to -1 i.e. $G_{KSL} = G_{\Gamma SL} = -1$ and is opposite to the S_3 magnetization. In the FM case they all are equal and saturate to 1 $G_{KSL} = G_{\Gamma SL} = 1$. This equal contribution of the two spin liquids could be interpreted as **"cooperation"** where the two spin liquids eliminate the macroscopic extensive ground state degeneracy of each other resulting in the unfrustrated phase.

It is worth noting here that the two S_3 phases represent a rare instance where a magnetic state possess a non-trivial GSCs, which are normally reserved only for classical spin liquids or multipolar orders [77].

We plotted the $S_3 \times Z_3$ magnetization along with the G_{KSL} and $G_{\Gamma SL}$ correlations as shown in Figure 5.9 (b) and (d) to better understand this modulated order. In order to exclude the $|K/\Gamma|$-dependence in the order parameters, we defined an alternate magnetization by including only odd k's in Eq. (5.3), $\overrightarrow{M}'_{S_3\times Z_3} = \frac{1}{9}\sum_{\alpha}^{A,B,C}\sum_{k}^{1,3,5} T_k^{\alpha}\vec{S}_k^{\alpha}$. From the Figure 5.9 we observed that in the frustrated regions, the characteristic Kitaev and Γ correlations developed towards opposite directions. Near the Kitaev limits, $\theta = \frac{\pi}{2}, \frac{3\pi}{2}$, G_{KSL} dominated and as a result the system stayed disordered, in either an extended KSL phase or a CP region. When $G_{\Gamma SL}$ was sufficiently strong to compete with G_{KSL}, at about $|\Gamma/K| \sim 0.27$, an $S_3 \times Z_3$ order emerged from the two conflicting quadratic correlations, and expanded till the large Γ limits owing to the small exGSD of the ΓSL. Thus the emergence of the modulated order could be thought of as the result of **"competition"** between the two spin liquids.

5.3.2 Constraints for the spin liquids

We successfully reproduced the GSC reported in Baskaran et al [17] obtained by a Jordan-Wigner construction,

$$G_{\mathrm{KSL}} = \frac{1}{2}\langle G_1 \rangle_{\hexagon} = \pm 1, \quad \langle G_{k\neq 1} \rangle_{\hexagon} = 0, \tag{5.7}$$

where " $\pm$ " corresponds to the FM and AFM KSLs respectively (the same convention used below) and $\langle \ldots \rangle_{\hexagon}$ denotes the thermal average over all hexagons. This cluster averaging is feature already implemented in TK-SVM. These constraints learnt here impose a degenerate dimer coverings on the honeycomb lattice which is in agreement with previous works discussed in Refs. [17, 198]. This degenerate dimer covering is precisely the ground states of a classical KSL.

Our machine identified two constraints in the case of ΓSLs,

$$G_{\Gamma SL} = \frac{1}{7}\langle G_2 \pm G_3 + G_5 \rangle_{\hexagon} = \pm 1, \tag{5.8}$$

$$\langle G_1 \rangle_{\hexagon} = \langle G_4 \rangle_{\hexagon} = \langle G_6 \rangle_{\hexagon} = 0, \tag{5.9}$$

where the sign of the G_3 correlation in the constraint equation served to distinguish the FM and AFM ΓSLs. The solution to the constraint equations naturally implied that the ground-state flux for every three hexagon plaquettes was $W \sim \{1, 0, 0\}$ which was also reported in Ref [182, 185], where the flux plaquette was defined in the usually way for each hexagon as $W = S_1^x S_2^z S_3^y S_4^x S_5^z S_6^y$.

The explicit GSC learnt also clarified the symmetry properties as well as the extensive degeneracy expected in any classical spin liquid. As discussed above the Hamiltonian has an intrinsic $C_6^R C_3^S$ symmetry in the real and spin space and we confirmed that the Kitaev and Γ constraints

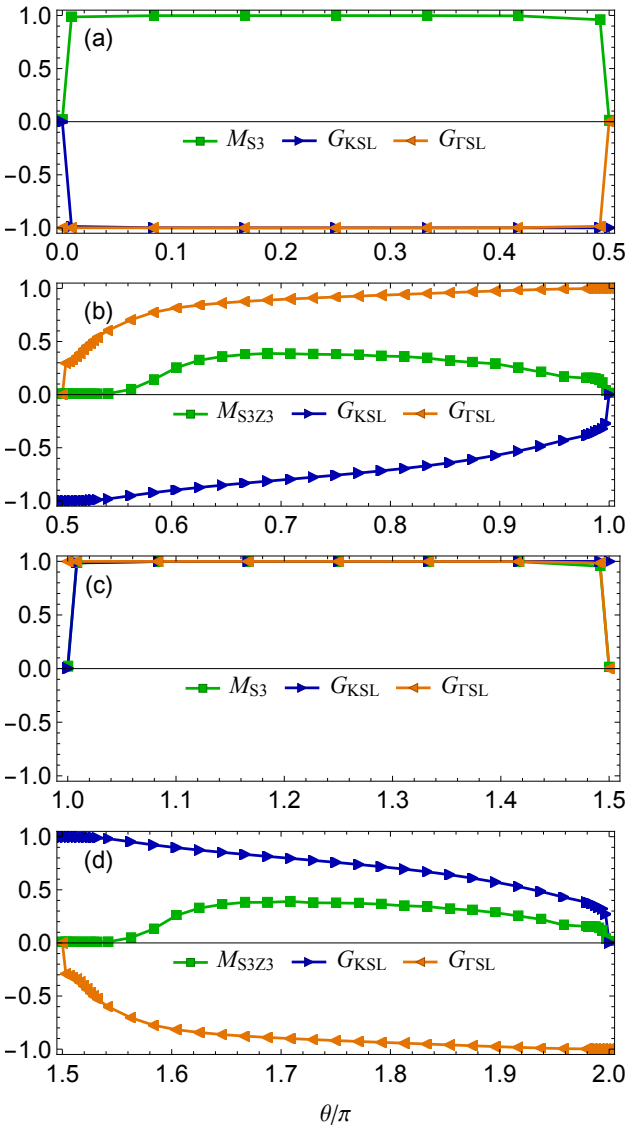

FIGURE 5.9: Measurements of the S_3 and modulated $S_3 \times Z_3$ magnetizations (green), and characteristic Kitaev (blue) and Γ (orange) correlations, with $K = \sin\theta$, $\Gamma = \cos\theta$, $h = 0$, $T = 0.001$. $M = \langle \frac{1}{N_{cell}} \sum_{cell} \vec{M} \rangle$ measures the magnitude of the respective magnetization, where $\vec{M}$ denotes the ordering moments in one magnetic cell, $\frac{1}{N_{cell}} \sum_{cell}(.)$ and $\langle ... \rangle$ indicate the lattice and ensemble average, respectively. At the Kitaev ($\theta = \frac{\pi}{2}, \frac{3\pi}{2}$) and Γ ($\theta = 0, \pi$) limits, either $G_{KSL} = \pm 1$ or $G_{\Gamma SL} = \pm 1$, satisfying the corresponding ground-state constraint. In the unfrustrated regions, $K\Gamma > 0$, Kitaev and Γ correlations behave in an equal footing as $G_{KSL} = G_{\Gamma SL} = \pm 1$, and cooperatively induce the AFM (a) or FM (c) S_3 order. In the frustrated regions, $K\Gamma < 0$ [(b), (d)], G_{KSL} and $G_{\Gamma SL}$ develop towards opposite directions. Though the system stays disordered near the Kitaev limits, from $|\Gamma/K| \sim 0.27$ up to the large Γ limits, the $S_3 \times Z_3$ orders are established owing to the competition between G_{KSL} and $G_{\Gamma SL}$.

also respected and preserved this global $C_6^R C_3^S$ symmetry. More importantly we discovered that in addition to this global symmetry the constraints also possessed a *local* Z_2 symmetry, which represents the different classical Z_2 spin liquids.

For the Kitaev constraints Eq. (5.7) when the γ component of a NN bond $\langle ij \rangle_\gamma$ was flipped it left the constraint invariant,

$$S_i^\gamma \to -S_i^\gamma,\ S_j^\gamma \to -S_j^\gamma,\ i,j \in \langle ij \rangle_\gamma \in G_1. \tag{5.10}$$

For the given dimer covering configuration that characterized the Kitaev spin liquid, this Z_2 symmetry gives rise to $(2^3)^{1/3}$ redundant degrees of freedom on each hexagon which together with the $1.381^{N/2}$ dimer coverings on a honeycomb lattice [231, 21, 105] gave a total of 1.662^N extensive degenerate ground states and a residual entropy $S/N \approx 0.508$ at zero temperature in agreement with the values reported in Baskaran et al [17]

The local Z_2 symmetry of the ΓSL constraint Eq. (5.8) has a different form,

$$S_i^{\alpha} \to -S_i^{\alpha},\ S_j^{\beta} \to -S_j^{\beta},\ \forall \langle ij \rangle_{\alpha,\beta\perp\gamma} \in G_2, \tag{5.11}$$

$$S_i^{\gamma_2} \to -S_i^{\gamma_2},\ S_j^{\gamma_1} \to -S_j^{\gamma_1},\ \forall [ij]_{\gamma_1\gamma_2} \in G_3, \tag{5.12}$$

$$S_i^{c} \to -S_i^{c},\ S_j^{c} \to -S_j^{c},\ \forall (ij)_{c\|\gamma} \in G_5. \tag{5.13}$$

where, α, β are the components normal to γ; "[.]" denotes the second nearest-neighbor bonds with γ_1, γ_2 corresponding to the two connecting NN bonds; "(.)" denotes the third nearest-neighbor bonds, and c equals the γ on a parallel NN bond; as depicted in Figure 5.8. This Z_2 symmetry was more involved than the simple one for KSLs but was also evident once the explicit GSC for the ΓSL was correctly identified.

The corresponding extensive ground state degeneracy was again accounted for the local redundancy on a each hexagon with a value of $2^{N/6} \approx 1.122^N$ and a residual entropy of approximately $S/N \approx 0.115$. When we compared to the degeneracy of KSLs the degeneracy of ΓSLs is orders of magnitude **smaller** which would explain why ΓSLs are more prone to fluctuations and are not as robust against perturbations as KSLs (see Figure 5.3 and 5.9).

Furthermore, in addition to the constraints for ground states, we identified two field-induced quadratic correlations in the $U(1)_g$ region of the phase diagram (see Figure 5.3 (c)) denoted as G_1^h and G_2^h in Table 5.2, which were found to be invariant under a global $U(1)$ rotation symmetry about the direction of the $\vec{h}_{111}$ fields which would result in gapless modes from general symmetry considerations. Thus our machine identified and characterized a host of gapless spin liquids in addition to the gapped spin liquids.

We remind the reader that the GSCs and other quadratic correlations learned here by TK-SVM are not just limited to classical spins but hold for any general spin-S and can be directly measured in the quantum $K\Gamma$ model. In comparison to other quantities used to characterize phases such as plaquette fluxes, Wilson/Polyakov loops, and spin structure factors, which may have similar behavior in different spin liquids, we emphasize that the GSCs are *unique* to a ground-state manifold and would be a more distinct characterization of the phases. The violation of the constraint would then serve to set boundaries on the extension of KSLs in a natural way.

Using the GSC, G, we characterized the classical spin liquids, by defining a susceptibility for the constraint as the variance in the constraint as follows,

$$\chi_{\mathrm{G}} = \frac{V}{T}\left(\langle G^2 \rangle - \langle G \rangle^2\right), \tag{5.14}$$

where $\langle ... \rangle$ is the ensemble average, and V denotes the volume of the system following Greitemann et al Ref. [77] which was the first to introduce the definition of a constraint susceptibility. The sharpness of the peak as well as its breadth showed the range of applicability of the constraint and in turn the range and breakdown of the associated classical spin liquid.

We estimated the extension of classical KSLs by defining the constraint susceptibility $\chi_{G_{KSL}}$ as a function of the Γ interaction as shown in Figure 5.10. In the zero field limit we observed a single sharp peak around $|\Gamma/K| = 0.15$ and an extension from 0.1 to 0.2 above which signified a break down of the constraint and a transition to a correlated paramagnet and then to the modulate $S_3 \times Z_3$ orders, this extension showed the robustness of the KSL against finite values of the Γ interaction. In contrast we observed that at a fixed $h\ (= 0.01)$, $\chi_{G_{KSL}}$ developed two peaks, reflecting the violation of the GSC.The sharper peak at a smaller $|\Gamma/K|$ again corresponded to the crossover between a KSL and a non-Kitaev correlated paramagnet and the broad bump at a larger $|\Gamma/K|$ corresponded to the second crossover to the modulated $S_3 \times Z_3$ phase. We remark here

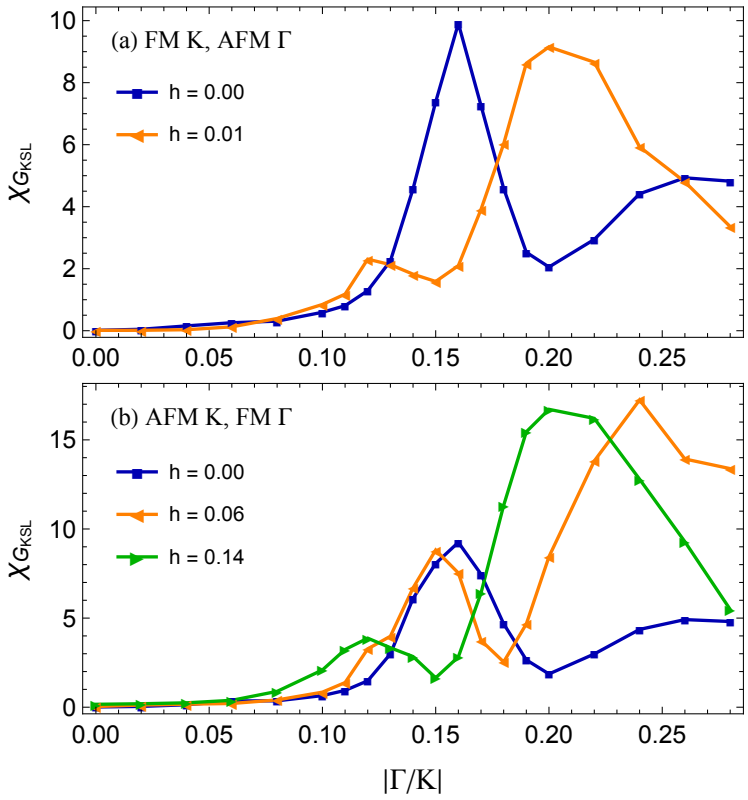

FIGURE 5.10: Susceptibility for the characteristic Kitaev correlation G_{KSL} as function of $|\Gamma/K|$, in the vicinity of the FM (a) and AFM (b) Kitaev limit with $K\Gamma \leq 0$. The first peak of $\chi_{G_{KSL}}$ in a fixed h identifies the crossover from a classical KSL to a non-Kitaev correlated paramagnet. At $h = 0$, the KSLs survive until $|\Gamma/K| \sim 0.16$. When magnetic fields are applied, the peak moves consistently towards a smaller value of $|\Gamma/K|$ with its width broadening. The wide bumps at lager $|\Gamma/K|$ signal the second crossover to a modulated $S_3 \times Z_3$ phase, for which the optimal quantity is the $S_3 \times Z_3$ magnetization.

that the optimal measure of this second crossover to the modulated phase would actually be the $S_3 \times Z_3$ order parameter instead of $\chi_{G_{KSL}}$ we used. However, the location of the second bump at least qualitatively agreed with the results based on measuring the $S_3 \times Z_3$ magnetization (see Figure 5.9).

In order to examine the effects of magnetic fields on the AFM KSL, we measured the field-dependent $U(1)_g$-symmetric correlations, G_1^h and G_2^h, and the magnetization per spin parallel ($m_{\parallel}$) and perpendicular ($m_{\perp}$) to the [111] field. We then plotted these quantities as a function of the magnetic field as is shown in Figure 5.11. We found that under weak and intermediate fields, most of the spins responded paramagnetically, that is $m_{\parallel}$ was small and $m_{\perp}$ completely vanished. While on the other hand G_1^h and G_2^h increased smoothly as a function of the external field, the bumps in their derivative (the derivative of the constraints with the magnetic field) around $h = 0.24$ might imply an effective change in the system, which we used to then estimate the robustness of the AFM KSL against polarization by an external field. The regime with intermediate field is marked as a $U(1)_g$ in order to distinguish it from a polarized state. This partially polarized region in the classical phase diagram coincided with a region in the quantum spin-1/2 and spin-1 AFM Kitaev model which was proposed to host a gapless U(1) spin liquid proposed [159, 249, 84, 85, 248]. Thus again emphasising that the classical phase diagram shares a lot of the physics of the quantum phase diagram.

We used the behavior of $\chi_{G_{KSL}}$, G_1^h, and G_2^h to sharpen the phase boundaries (depicted by the white dashed lines in the KSL phases in Figure 5.3 (c)) between the KSLs and other correlated paramagnets, supplementing the graph partitioning from Fiedler clustering. To remind the reader

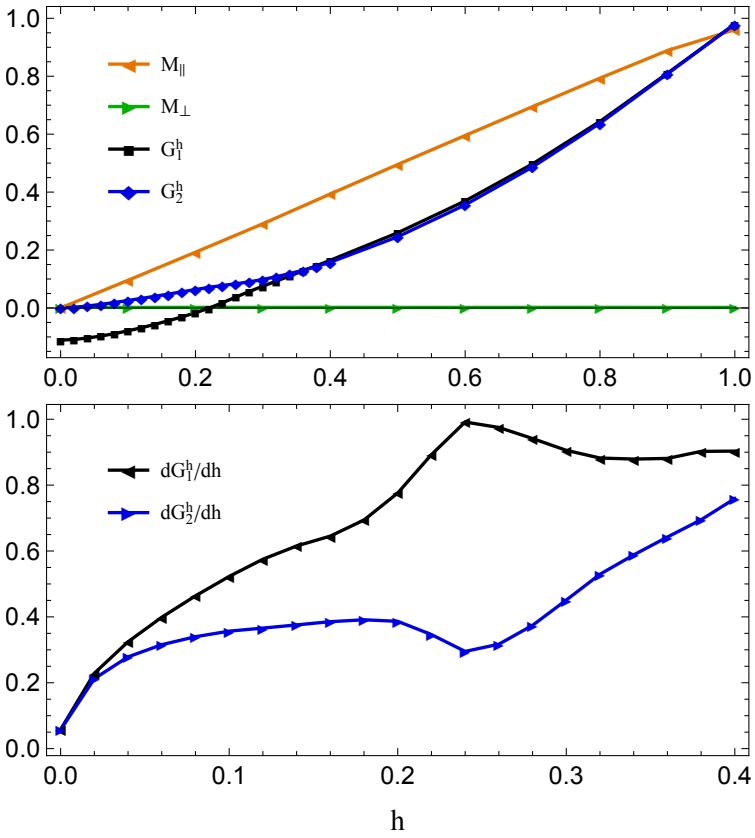

FIGURE 5.11: Field dependence of the magnetization per spin parallel ($m_{\parallel}$) and perpendicular ($m_{\perp}$) to the [111] field, and the normalized $U(1)_g$-symmetric correlations, G_1^h and G_2^h, at the AFM Kitaev limit $(K, \Gamma) = (1, 0)$. The spins are mostly paramagnetic under weak and intermediate fields. Bumps in dG^h/dh may imply prominent changes in the system.

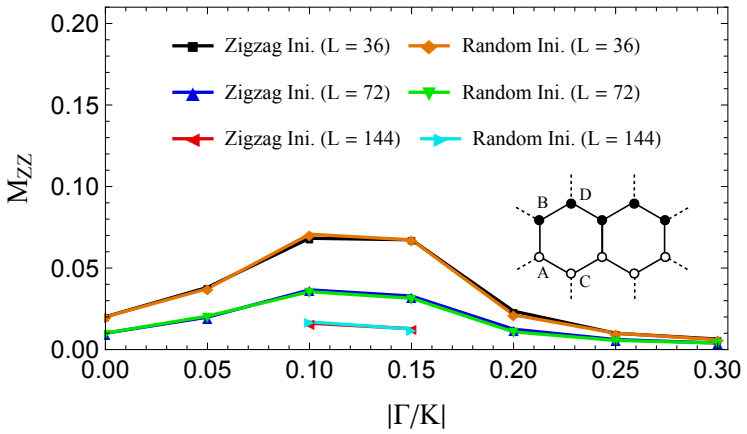

FIGURE 5.12: Monte Carlo measurement of the zigzag order in the region of FM K and small AFM Γ at $h = 0$, where the magnetization $M_{ZZ} = \left\langle \left| \frac{1}{N_{\text{cell}}} \sum_{\text{cell}} \left(\vec{S}_A - \vec{S}_B + \vec{S}_C - \vec{S}_D \right) \right| \right\rangle$, and A, B, C, D label the four sub-lattices. Simulations initiated with perfect zigzag states are compared with random initialization. The zigzag order appears to be unstable in all cases. The small residual moments are a finite-size effect and decrease significantly with increasing system sizes.

again, we partitioned the graph at rank-1 which only detected the presence or absence of magnetic orders and needed to interpret rank-2 to find GSCs to find the extent of the spin liquids. In principle, one could also have performed a graph partitioning using rank-2 TK-SVM. But this was not

required as at rank-1 we found a pretty good classification of all the phases and unraveled most of the phase diagram only requiring rank-2 at a few locations.

We additionally also evaluated the zigzag magnetization in Figure 5.12 in the extended KSL and CP region with FM K and AFM Γ and found that it is quite insignificant and unstable at low temperature and suffers strongly from finite-size effects. We did this, since the zigzag order has been considered as a Γ-induced competing order to a KSL. The insignificance of the zigzag order in the extended regions is consistent with the picture that, in order to stabilize the zigzag-like order found in α-$RuCl_3$ [15, 176], other terms, such as the first and third nearest-neighbor Heisenberg J_1, J_3 interactions [72, 65, 100] or the off-diagonal Γ' term [73, 134, 71, 197], are needed, which we thoroughly studied in the previous chapter 4.

5.4 Summary and Outlook

In this chapter we studied the $K\Gamma h$ model on the two dimensional honeycomb lattice by exploiting the interpretability and unsupervised nature of TK-SVM.

We found that the classical phase diagram of the $K\Gamma$ model in an $[111]$ field is exceptionally rich (see Figure 5.3), hosting several unconventional symmetry-breaking phases and a plethora of disordered states at very low temperature. The phase diagram clearly showed the finite extent of the KSLs, an intermediate disordered phase at the AFM Kitaev limit, and a field-induced suppression of magnetic orders, which were previously only reported for quantum systems. These common features emphasize that that certain aspects of the Kitaev materials might already be understood at a classical level and also motivates a systematic investigation of large spin models in order to find potential higher-S spin liquids.

The machine discovered, the modulated $S_3 \times Z_3$ phase with a complex modulation. This implied that the competition between Kitaev and non-Kitaev exchanges does significantly enrich the physics and lead to more unconventional phases than expected.

From a rank-2 interpretation we found the GSCs of the classical ΓSLs and reproduced the ones of the KSLs reported in literature. These constraints enhanced our understanding of the ΓSLs and their fragility to perturbations due to an exponentially small ground state degeneracy in comparison with KSLs, but also shed light on the emergence of the complicated orders in the K-Γ model. The unfrustrated S_3 phase emerged as a consequence of the characteristic Kitaev and Γ correlations "cooperatively" eliminating the macroscopic degeneracy of each other. In contrast, the modulated $S_3 \times Z_3$ phase could be understood as the consequence of "competition" between the KSL and ΓSL. This mechanism may be viewed as an alternative protocol for devising exotic phases.

The fate of the modulated $S_3 \times Z_3$ order in quantum K-Γ models, for the case of spin-1/2 as well as higher S values remains an open question and is worth investigating. It is not uncommon that, when a system establishes a robust magnetic order in the classical large-S limit, this order can persist in the quantum cases with a reduced ordering moment due to quantum fluctuations. There are many examples for various spin-liquid candidates discussed in the recent works, see for instance Refs. [246, 224, 137].

It might also be an useful endeavour to investigate the static spin structure of the modulated phases and understand if they give the complete characterization of the phase and also look into the dynamical and transport properties in this phase.

Chapter 6

Spin Helices in the $K\Gamma$ model

In the previous few chapters we discussed the application of machine learning methods, in particular TK-SVM to analyse the phase diagram of the Kitaev model with additional interactions motivated to search the parameter regime relevant for Kitaev materials.

In the present chapter and the next one we shall divert ourselves from machine learning and focus more on analysing the ground state in the modulated $S_3 \times Z_3$ phase the machine found in the previous chapters and in the next chapter we shall investigate the signatures of these complex phases on dynamical quantities and transport properties. In this short chapter we report the results of investigating the ground-state nature of the honeycomb Kitaev-Γ model in the material-relevant parameter regime through a combination of analytics and classical simulations. The classical ground state has a pretty complicated structure with a tangle of multiple inequivalent highly structured spin double helices. These findings would explain at least some of the dynamical effects observed in inelastic neutron scattering in real materials as well as enrich our understanding of Kitaev magnetism.

6.1 Model and Symmetry

We studied the same $K\Gamma$ model on a honeycomb lattice introduced in the previous chapter which comprised of two bond-dependent terms: a directional Ising-type interaction (K) and a symmetric off-diagonal Γ interaction whose origins lie in the overlap of the $d-d$ orbitals or through the intermediate hopping through the $d-p$ orbitals. The Hamiltonian for the model studied is,

$$H = \sum_{\langle ij \rangle_\gamma} K S_i^\gamma S_j^\gamma + \Gamma \left(S_i^\alpha S_j^\beta + S_i^\beta S_j^\alpha \right). \tag{6.1}$$

where, γ labels the three different types of bonds, and $\alpha, \beta, \gamma \in \{x, y, z\}$ are mutually exclusive [119] and we considered hopping (interactions) only between the nearest neighbours as exemplified by $\langle ij \rangle$. The above equation could also be written as a matrix equation as $H = \sum_{\langle ij \rangle_\gamma} \mathbf{S}_i \cdot \hat{J}_{ij}^\gamma \mathbf{S}_j$ where the interaction matrices on each of the three bonds are as follows

$$\hat{J}_{ij}^x = \begin{bmatrix} K & & \Gamma \\ & \Gamma & \end{bmatrix}, \hat{J}_{ij}^y = \begin{bmatrix} & \Gamma & \\ \Gamma & & K \end{bmatrix}, \hat{J}_{ij}^z = \begin{bmatrix} \Gamma & & \\ & K & \end{bmatrix}. \tag{6.2}$$

6.1.1 Hidden Symmetry

We discovered that the above Hamiltonian had a *hidden global* symmetry that intertwined the spatial and spin degrees of freedom which as a consequence led to an additional two-fold degeneracy. Under the following transformation with σ matrices, the interaction matrices are left invariant and hence form symmetries of the system under consideration

$$\sigma_i^{\alpha\beta} \hat{J}_{ij}^\gamma \sigma_j^{\alpha\beta} = \hat{J}_{ij}^\gamma, \tag{6.3a}$$

$$\sigma_i^{\alpha\gamma} \hat{J}_{ij}^\gamma \sigma_j^{\gamma\beta} = \hat{J}_{ij}^\gamma, \tag{6.3b}$$

where $\sigma_i^{\alpha\beta}$ denotes spin reflections where the spins are transformed as $\sigma_i^{\alpha\beta} S_i^{\gamma} = -S_i^{\gamma}$. This transformation flips only the mutually exclusive component of the spin on which it is acting (i.e. the spin on site i). We shall illustrate this with an example here. Let us consider the transformation being applied to the z bond. According to the index rules discussed above the only allowed transformations are

$$\sigma_{xy}\hat{J}^z\sigma_{xy} = \hat{J}^z \ , \ \sigma_{xz}\hat{J}^z\sigma_{zy} = \hat{J}^z \ , \ \sigma_{yz}\hat{J}^z\sigma_{zx} = \hat{J}^z \tag{6.4}$$

and we see that for all the spins in the $C-A-B-B-A-C$ chain along the z bonds (see Fig 6.2) these transformation matrices leave the chain and the spins along the z bond invariant hence forming a symmetry of the system. A similar set of transformations would apply for the x and y bonds respectively.

To make this more explicit to the reader, let us just consider the spins $\vec{S}_C, \vec{S}_A$ that are along the first z bond which is marked along the bottom left corner (see Fig 6.2). The Hamiltonian along this bond would be $H^z_{CA} = KS^z_C S^z_A + \Gamma\left(S^x_C S^y_A + S^y_C S^x_A\right)$. From the transformation shown on the right the spins get modified by σ_{xy} which flips only the z component. The action of the 3 spin reflection matrices are as shown below

$$\sigma_{xy}\begin{pmatrix} S^x \\ S^y \\ S^z \end{pmatrix} = \begin{pmatrix} S^x \\ S^y \\ -S^z \end{pmatrix} \ , \ \sigma_{xz}\begin{pmatrix} S^x \\ S^y \\ S^z \end{pmatrix} = \begin{pmatrix} S^x \\ -S^y \\ S^z \end{pmatrix} \ , \ \sigma_{yz}\begin{pmatrix} S^x \\ S^y \\ S^z \end{pmatrix} = \begin{pmatrix} -S^x \\ S^y \\ S^z \end{pmatrix} \tag{6.5}$$

These transformations alternate amongst the three spin reflections and cover the entire lattice and this hidden symmetry modifies the correlations in the system which results in two *distinct* orders becoming degenerate. Thus the above Hamiltonian under this transformation is left invariant which is shown explicitly

$$\begin{aligned} H^z_{CA} = (S^x_C, S^y_C, S^z_C)\hat{J}^z \begin{pmatrix} S^x_A \\ S^y_A \\ S^z_A \end{pmatrix} \rightarrow \tilde{H}^z_{CA} = \vec{S}_C\sigma_{xy}\hat{J}^z\sigma_{xy}\vec{S}_A \\ = (S^x_C, S^y_C, -S^z_C)\hat{J}^z \begin{pmatrix} S^x_A \\ S^y_A \\ -S^z_A \end{pmatrix} = H^z_{CA} \end{aligned} \tag{6.6}$$

The hidden symmetry we found implies that the 6 site pattern to the left is degenerate to the 18 site pattern on the right (see Fig 6.2). We observed from our Monte Carlo simulations that there were three different kinds of spins which we labelled as $\vec{S}_A, \vec{S}_B, \vec{S}_C$ and these spins in the 6 site pattern formed a regular $C-A-B-B-A-C$ pattern. Of course there is a C_3 rotation symmetry along the three bond directions and there is a global $\mathbb{Z}_2$ symmetry where all the spins are flipped $S \rightarrow -S$ which is apparent in the Hamiltonian as it comprises only of quadratic spin components. But the *non-trivial symmetry is the hidden symmetry* which is responsible for the additional degeneracy.

6.2 Method

Motivated to discuss the parameter regime for realistic Kitaev materials we focused on the regime away from the classical (K, Γ) spin liquids, where both the interactions are sizeable and competing i.e. in the frustrated regime $K\Gamma < 0$. In continuation with the previous chapter, we parameterized the two interactions by the angle θ as $K = \sin\theta$, $\Gamma = \cos\theta$ and considered a ferromagnetic K and an anti-ferromagnetic Γ ($1.5\pi < \theta < 2\pi$) which is the most relevant choice of parameters for the d-electron Ir- and Ru-based compounds [226, 234, 131]. We could easily map onto the

other frustrated regime with an anti-ferromagnetic K and ferromagnetic Γ through $\theta \rightarrow \theta + \pi$ and simultaneously flipping the spins on even and odd sublattices $\vec{S}_{2i} \rightarrow \vec{S}_{2i}$, $\vec{S}_{2i+1} \rightarrow -\vec{S}_{2i+1}$ [1], which is relevant for the physics at $0.5\pi < \theta < \pi$.

We utilized parallel tempering Monte Carlo methods to reach extremely low temperatures down to $T = 10^{-5}\sqrt{K^2 + \Gamma^2}$ for systems of linear size up to $L = 72, 90, 108$ with periodic boundary conditions. We further cooled the system to the classical lowest possible temperature $T \rightarrow 0$ by eliminating remaining thermal noise and allowing the system relax to its local magnetic field thereby "freezing" the spins. We found that such large systems sizes and low temperatures were necessary to manifest the spin helices. We used parallel tempering together with heat bath and over-relaxation algorithms to equilibrate the system at extremely low temperatures. We simulated around $N_T = 256$ logarithmically distant temperatures and 10^7 Monte Carlo sweeps were performed in each individual run to ensure we converged to the same states thereby confirming the ergodicity of our simulations. The Monte Carlo sampling generated spin configurations that lie slightly above the classical ground states by an energy scale $\Delta E \sim 10^{-5}$ preset by the lowest simulated temperature.

In order to freeze the spins to manifest the spiral we further cooled the system letting it approach its classical ground states by iteratively aligning the spins along their local molecular fields $\vec{B}_i^{\text{loc}}$ [96],

$$\vec{S}_i^{new} = \frac{\vec{B}_i^{loc}}{|\vec{B}_i^{\text{loc}}|}|\vec{S}_i^{old}|. \tag{6.7}$$

Here $\vec{B}_i^{loc} = \sum_{\langle ij \rangle_\gamma} \hat{J}_{ij}^{\gamma} \vec{S}_j$

This iterative alignment process continued until the maximum difference in energies of the spin configurations between successive iterations $|E^{\text{old}} - E^{\text{new}}|_{\text{max}}$ was less than 10^{-14}.

Evolution of energies and magnetizations in the freezing process is shown below in Fig. 6.1. We note that roughly after $300 - 500$ iterations of cooling the sub lattice magnetizations plateaued. However energy seemed to converge much earlier, that is around the 50^{th} iteration we reached the plateau. A plausible explanation of the observation might be that the energy is quadratic in spin as opposed to magnetization which is linear in spin and hence the convergence to the plateau value is faster in case of energy. To confirm the ergodicity of our simulations we examined, at a few fixed parameter point, a number of statistically uncorrelated configurations and found that they had identical energies up to the numerical machine precision.

6.2.1 Simulating Translationally invariant Ansatzes

Having discussed the model in the previous section the next natural step would be to find the solutions of this Hamiltonian. One approach to find the ground states is to use Monte Carlo simulations. While the other common strategy is to minimize the Hamiltonian with small periodic clusters where the choice of those clusters are guided by small-size trial simulations. The drawback of this approach is that it fails to capture the true ground states of the Kitaev-Γ model which has the imprinted modulated helix. Nonetheless, minimizing the energy based on a translationally invariant ansatz is still useful and it provides us vital information about longitudinal magnetization of the helical phase, in particular the sublattice structure and orientations of the helical axes.

We tried to minimize energy by making an ansatz for the three elementary spins (represented here with a tilde $\tilde{S}$ in order to distinguish them from the actual spins obtained from Monte Carlo) as follows $\tilde{S}_{A,B,C} = (\sin\alpha \sin\beta, \sin\alpha \cos\beta, \cos\alpha)_{A,B,C}$. This representation for the spins belong to has the phase angles $\alpha \in [0, \pi), \beta \in [0, 2\pi)$ which are the free parameters that need to be varied in order to optimize the energy. The end result of this optimization is that we get the spin configurations $\tilde{S}_{A,B,C}$ which form the classical ground state and once we know these base spins all other spins are related by trivial transformations.

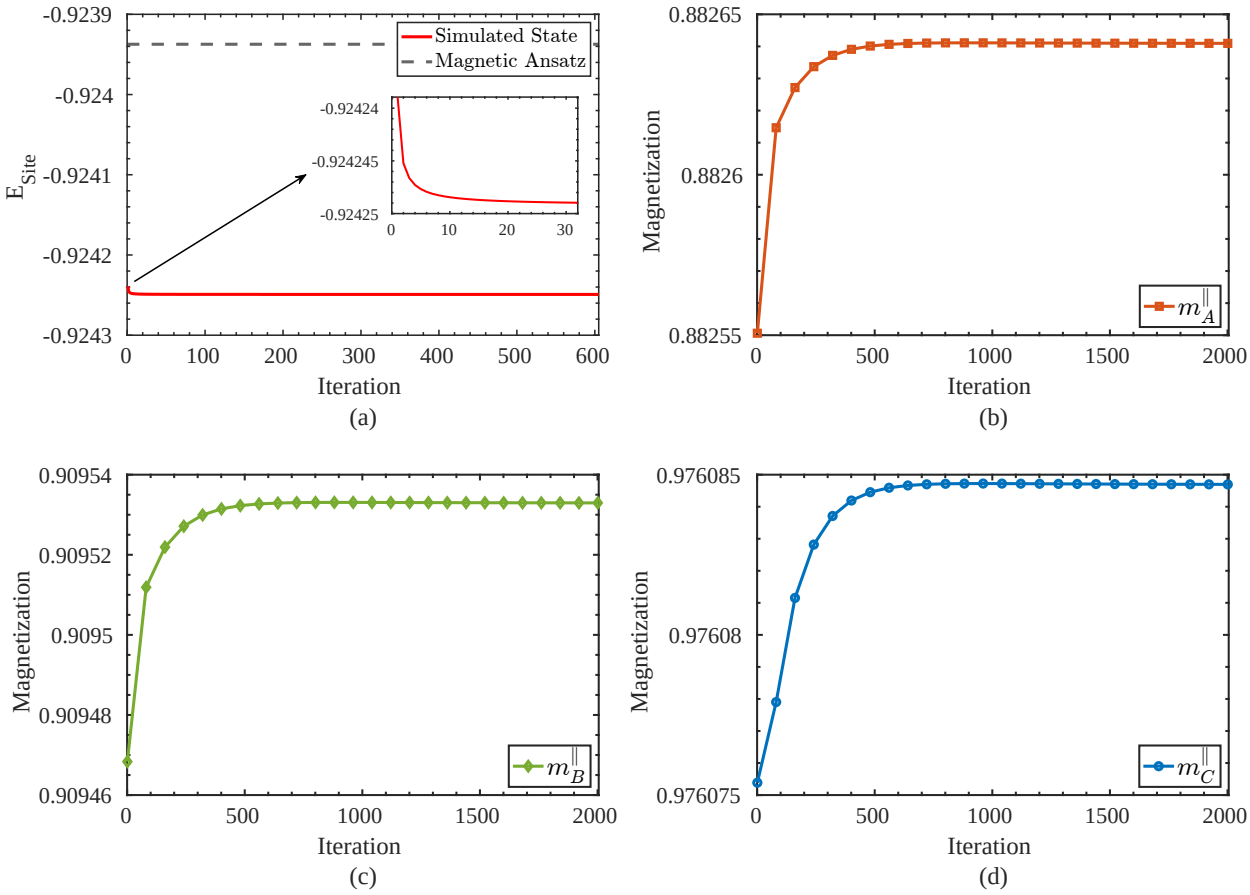

FIGURE 6.1: Cooling of a classical state simulated on a $L = 72$ lattice at $\Gamma = -K$ ($\theta = 1.75\pi$), with $|\mathbf{S}_i| = 1$. (a) Convergence of the energy. The energy per spin is $E_{\text{site}} = -0.92423895$ before the cooling and is $E_{\text{site}} = -0.92424917$ after the cooling (solid line); both are lower than the ansatz energy $E_{\text{site}} = -0.92393734$ (dashed line). The inset magnifies the evolution in a short time period. (b-d) Convergence of the sublattice (longitudinal) magnetizations, $m^{\parallel}_{A,B,C}$, of the helical axes. These magnetizations converge to values below unity owing to non-vanishing spiral magnetizations $m^{\perp}_{A,B,C}$.

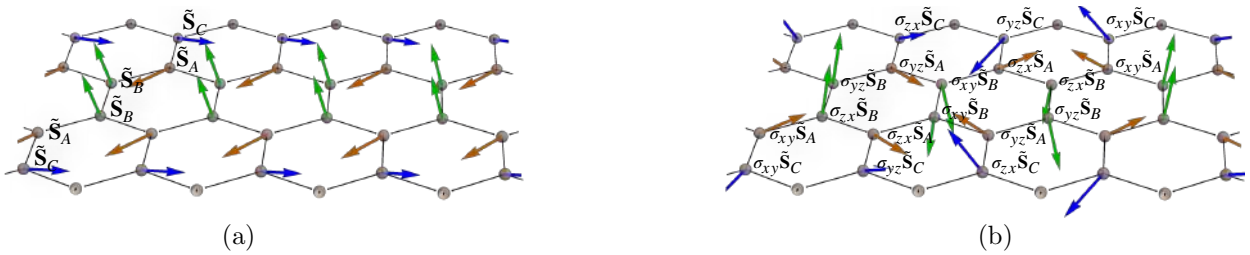

FIGURE 6.2: Two degenerate magnetic ansatzes obtained by enforcing a 3×3 periodic cluster at $K = -\Gamma$. (a) The three ansatz spins $\tilde{\mathbf{S}}_A, \tilde{\mathbf{S}}_B, \tilde{\mathbf{S}}_C$ form a 6-site repeating pattern *C-A-B-B-A-C*. (b) An 18-site degenerate repeating pattern is obtained by applying the hidden symmetry.

We then simulated all the other spins in the 3×3 cluster using the hidden symmetry transformations discussed above and we end up with two degenerate patterns one with 6 spins arranged as $C - A - B - B - A - C$ and the other hidden symmetry related 18 site pattern. The representations of these ansatz is shown in Fig 6.2

$$\tilde{E}_{\text{site}} = \frac{K}{6}\Big[2\cos\alpha_A\cos\alpha_B + 2\sin\alpha_A\big(\sin\beta_A\sin\alpha_B\sin\beta_B + \cos\beta_A\sin\alpha_C\cos\beta_C\big)$$
$$+ \sin^2\alpha_B\cos^2\beta_B + \sin^2\alpha_C\sin^2\beta_C + \cos^2\alpha_C\Big]$$
$$+ \frac{\Gamma}{3}\Big[\sin\alpha_B\big(\sin\alpha_A\sin(\beta_A+\beta_B) + \cos\alpha_A\cos\beta_B\big) + \cos\alpha_B\big(\sin\alpha_A\cos\beta_A + \sin\alpha_B\sin\beta_B\big)$$
$$+ \cos\alpha_C\big(\sin\alpha_A\sin\beta_A + \sin\alpha_C\cos\beta_C\big) + \sin\alpha_C\sin\beta_C\big(\cos\alpha_A + \sin\alpha_C\cos\beta_C\big)\Big]$$

This spin ansatz was solved by minimizing the energy shown above giving us the base spins $\tilde{S}_{A,B,C}$ found to be non-collinear and non-coplanar but crucially this ansatz varied with the ratio $|K/\Gamma|$.

On one hand, as seen in the Fig 6.1 (a) the energy of the magnetic ansatz and the true ground-state energy is very close only differing by a factor of $\sim 10^{-4}$. While on the other, this ansatz does *not* reflect the true nature of the ground state as the true state is not translational invariant and hosts an incommensurate spiral texture. The ansatz was found to be a good approximation for the longitudinal components while ignoring transverse components as $\mathbf{m}_\mu^{\parallel} = \frac{1}{N_{\text{cell}}}\sum_{\text{cells}}\mathbf{S}_\mu = \tilde{S}_\mu^{\parallel}$, which define the helical axes, with a very high precision. The spin ansatzes $\tilde{S}_{A,B,C}$ were nearly parallel to the longitudinal magnetization of actual spins. This was further confirmed by evaluating the cosine de-similarity between the *orientations* of $\tilde{\mathbf{S}}_\mu$ and $\mathbf{m}_\mu^{\parallel}$ as defined below,

$$D_\mu = \frac{1}{2}\left(1 - \tilde{\mathbf{S}}_\mu \cdot \frac{\mathbf{m}_\mu^{\parallel}}{|\mathbf{m}_\mu^{\parallel}|}\right) \in [0,1]\,, \tag{6.8}$$

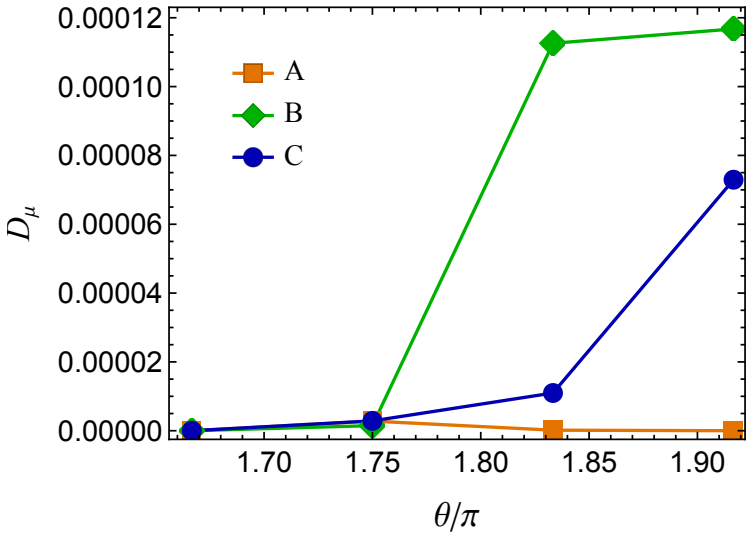

FIGURE 6.3: Cosine de-similarity $D_\mu \in [0,1]$ between the ansatz spin orientations $\tilde{\mathbf{S}}_{A,B,C}$ and the sublattice magnetizations $\mathbf{m}_{A,B,C}^{\parallel}$ simulated on a $L = 72$ lattice. D_μ generally rises with increasing Γ, which is expected due to the stronger spiral magnitudes. Nevertheless, even at the large Γ value $\theta \approx 1.92\pi$, the de-similarities remain remarkably small, and the magnetic ansatzes can still provide a proximate description of the correct sublattice structure.

As measured in Fig. 6.3 for small enough θ in the range of $1.5\pi < \theta < 1.68\pi$ the desimilarity is almost 0 which suggests that our magnetic ansatz is a pretty good one and the imprint of the helix

is negligible. The observation that in the parameter range where transverse magnetization $\mathbf{m}_\mu^\perp$ was comparable to the longitudinal magnetization $\mathbf{m}_\mu^\parallel$, the desimilarity D_μ remained extremely small ($\sim 10^{-4}$). This let us hypothesise that the longitudinal order could be well approximated by the magnetic ansatzes but the transverse components revealing the true spiral nature is absent.

The source of helicity might be understood by considering the exchange frustrations generated by Γ matrices which could be decomposed into a part generating reflections ($\sigma_{\alpha,\beta}$ which is the generator of reflections in the $\alpha\beta$ plane) and into a part generating rotations L_α (which is the generator of $SO(3)$ rotations about the α axis) as follows

$$\Gamma_z = -L_z \cdot \sigma_{xz} = \begin{pmatrix} 0 & 1 & 0 \\ 1 & 0 & 0 \\ 0 & 0 & 0 \end{pmatrix} = - \begin{pmatrix} 0 & -1 & 0 \\ 1 & 0 & 0 \\ 0 & 0 & 0 \end{pmatrix} \cdot \begin{pmatrix} 1 & 0 & 0 \\ 0 & -1 & 0 \\ 0 & 0 & 0 \end{pmatrix} \tag{6.9}$$

This combination of reflections and rotations favours a spiral structure. The observation that the spiral magnetization $m_\mu^\perp$ increased with increasing Γ gives further credence to the fact that the Γ interactions are responsible for the spiral structure. Furthermore, as the three types of lattice bonds host different Γ matrices, there is competition between different rotation axes and this interplay between helicity and competing interactions could lead to a modulation in the 18 helical axes. Even though Γ interactions are necessary for the spirals we cannot neglect a finite competing K. If the Kitaev interaction K vanished, the Hamiltonian would reduce to that of a pure Γ model featuring an emergent local Z_2 symmetry. As we saw in the previous chapter this would imply all magnetic orders are destroyed due to extensive degeneracy of the ground states and the system becomes a classical Γ spin liquid.

6.3 Ground state as a tangle of Helices

We shall here discuss the classical ground states we found through our Monte Carlo simulations followed by spin freezing in the selected parameter regime spanning $3\pi/2 < \theta < 2\pi$. Upon measuring the $S_3 \times Z_3$ magnetization, discussed in the previous chapter, we found there was a prominent *undersaturation* (Figure 6.5) of the magnetic order which suggested the lack of a perfect translationally invariant order [143].

This missing magnitude in the magnetization essentially holds the key to our understanding of the classical ground states and to unravel this information we had to use very large lattices and simulate spins at extremely low temperatures.

Each spin in the ordered phase could be decomposed into longitudinal(parallel) and transverse(perpendicular) components respectively and the direction of the longitudinal components is along the $\hat{z}$ direction at each spin,

$$\vec{S}_\mu = \vec{S}_\mu^\parallel + \vec{S}_\mu^\perp \,,\ \vec{S}_\mu^\parallel = (0, 0, m_\mu^\parallel) \quad \mu = 1, 2...18 \tag{6.10}$$

These longitudinal components form a 3×3 supercell containing 18 sublattices as depicted in Fig. 6.4. The corresponding magnetic moments for each of the sublattices were calculated by averaging over all the supercells in the entire lattice (similar to a cluster average) as $\mathbf{m}_\mu^\parallel = \frac{1}{N_{\text{cell}}} \sum_{\text{cells}} \mathbf{S}_\mu$, where $\mu = 1, 2...18$ is the index used to distinguish the 18 different sublattices. The general motive behind this definition of magnetization is that all the spins on a particular sublattice share the same parallel component and different perpendicular components. Hence the averaging would result in a destructive interference of perpendicular components resulting in only the parallel components surviving and adding up constructively. These parallel magnetic moments are the source of the stable $\frac{2}{3}\mathbf{M}$ magnetic Bragg peaks reported in the literature [143, 197], and also act as the rotation axes of the highly structured spin helices.

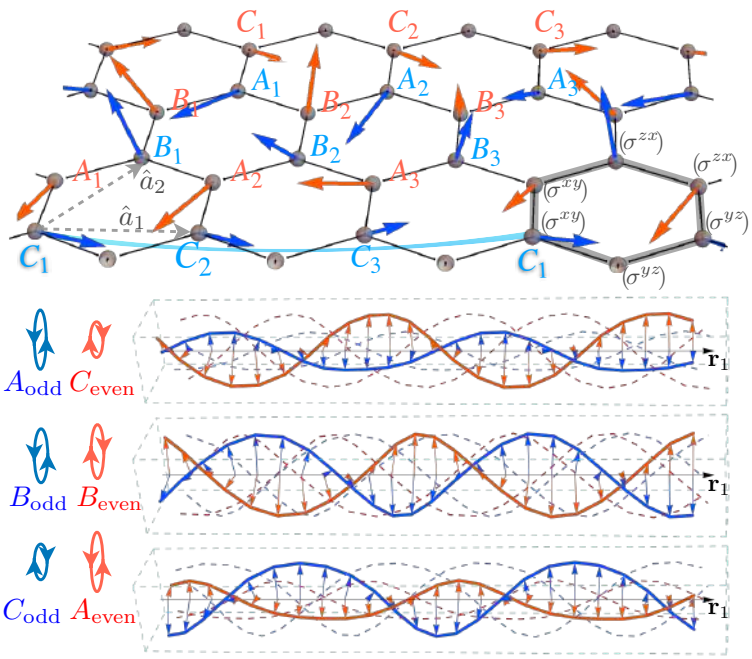

FIGURE 6.4: A classical ground state of the honeycomb Kitaev-Γ model at $\Gamma = -K$ on a $L = 72$ lattice. Upper panel: Structure of the 3×3 supercell determined from the helical axes (longitudinal components) of spins. A, B, C label three independent directions of the helical axes, and $j = 1, 2, 3$ distinguishes different orientations due to the hidden symmetry. Blue and red colors mark the odd and even honeycomb sublattices and the helices' chirality. A supercell specifies 18 *inequivalent* helices as spins form a helix *only if* they belong to the same sublattice, e.g., the linked blue C_1 spins. The grey hexagon marks a unit cell of the 6-site hidden symmetry transformation. Lower panel: Spiral (transverse) components of the 18 helices in their respective sublattice basis. Each helix consists of $\frac{L}{3}$ spins due to the 3×3 supercell structure. The helical pitches are *spontaneously anisotropic* and are $\frac{L}{6}$ and $\frac{L}{3}$ supercells in size along directions of the two lattice vectors $\hat{a}_{1,2}$. Cycles on the side reflect the strength and staggered chirality of the corresponding helix. The helix ensemble can be viewed as nine pairs of double helices.

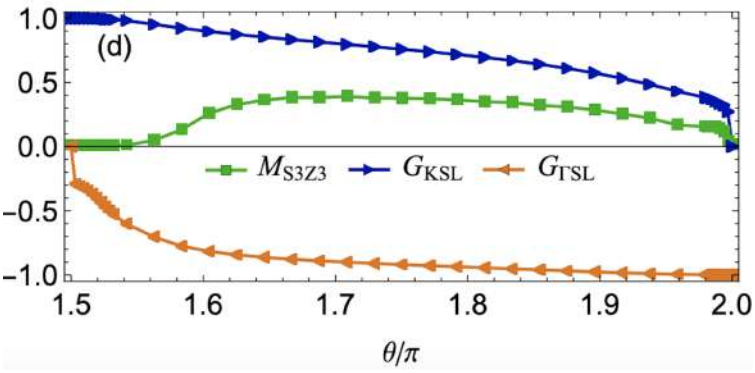

FIGURE 6.5: Figure showing the magnetization of the $S_3 \times Z_3$ phase for varying values of K/Γ. The magnetization shows a distinct understaturation for the measured order indicating the lack of a translationally invariant order and the presence of a helix.

As alluded in the previous section there is a 6 site pattern which is degenerate with the 18 site pattern as a consequence of the hidden symmetry. The Fig. 6.4 shows a sample configuration of this 18 site pattern at the phase point $K = -\Gamma$. To elucidate this point we note that all A_j spins have identical longitudinal components $\mathbf{S}^{\parallel}_{A_j} = \mathbf{m}^{\parallel}_{A_j}$ similarly for B_j and C_j spins with $j = 1, 2, 3$.

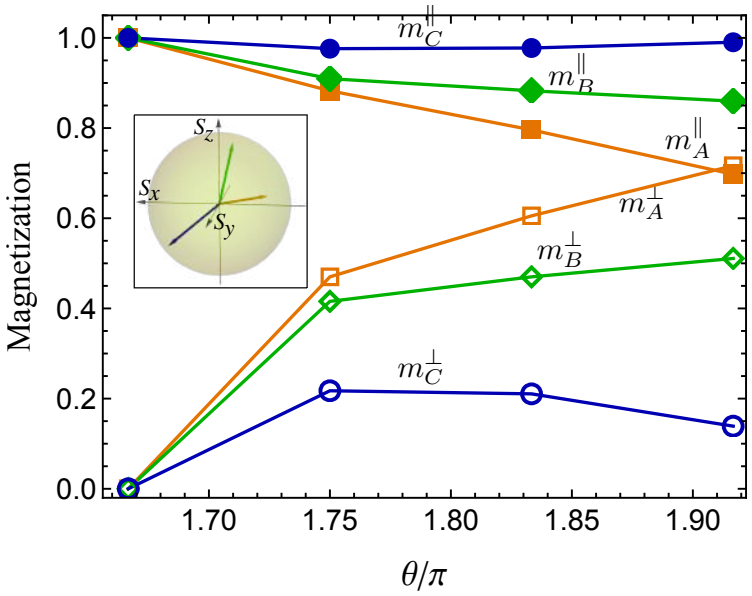

FIGURE 6.6: Magnetizations of the classical spin-helix tangle with comparable Kitaev and Γ interaction, $K = \sin\theta, \Gamma = \cos\theta$. The longitudinal and spiral components the order are measured by $m^{\parallel}_{A,B,C}$ and $m^{\perp}_{A,B,C}$, respectively, leading to saturated total magnetizations $\left(m^{\parallel}_{A,B,C}\right)^2 + \left(m^{\perp}_{A,B,C}\right)^2 = 1$. The spiral component at $\theta \approx 1.67\pi$ is small but non-vanishing (see Fig. 6.7). The inset exemplifies the orientations of $\mathbf{m}^{\parallel}_A$, $\mathbf{m}^{\parallel}_B$ and $\mathbf{m}^{\parallel}_C$ (distinguished by colors) at $\theta = 1.75\pi$.

The degenerate state is obtained by applying the hidden symmetry transformations Eqs. (6.3a) and (6.3b) as indicated by the grey hexagon, leading to nine distinct rotation axes distinguished by the numerical subscripts j. This is to be expected since we have just three reflection operators $\sigma_{xy}, \sigma_{xz}, \sigma_{yz}$ and them acting on the three helical axes would result in $3 \times 3 = 9$ distinct helical axes which we labelled as A_j, B_j, C_j. Since the hidden symmetry is exact, one can always infer all helical axes from the three independent moments $\mathbf{m}^{\parallel}_{A,B,C}$.

We further note that each of the 3 spins alternately occupies an even or odd site in the 6 site pattern $C - A - B - B - A - C$ and hence we end up with 18 distinct helices which could be viewed as a set of 9 distinct double helices to account for the odd and even sublattices. These magnetic moments are non-collinear and non-coplanar and vary with K/Γ in both magnitude and orientation. Most importantly, we would like to bring the readers attention to the fact that the spiral is not defined between spins in a supercell but rather between spins at the same sublattice point along different supercells. This is shown in Fig 6.4 where the two spins C_1 that belong to the same spiral structure are shown connected by a light blue line. We would also like to highlight to the reader that the supercell is only defined for the *longitudinal order* and not the transverse magnetization. The true ordering does not have a translational symmetry as a result of the *incommensurate transverse components*, as illustrated in the lower panel of Fig. 6.4.

In Fig. 6.6 shows the magnetizations of the three sublattices A, B, C measured as a function of the parameter angle θ. We made a few interesting observations. Firstly, inline with expectation, we observed an under saturation in the parallel components $m^{\parallel}_{A,B,C}$ with increasing angle. In the parameter range $1.5\pi < \theta < 1.66\pi$ the parallel components were found to be equal and completely saturate i.e. $m^{\parallel}_{A,B,C} = 1$ implying the absence of the helix. Upon increasing θ we observed that the degeneracy between the parallel components is lifted and the transverse components play an important role. The sum of the parallel and perpendicular components of course saturate to 1 as expected showing that our helical ansatz 6.11 is the right one.

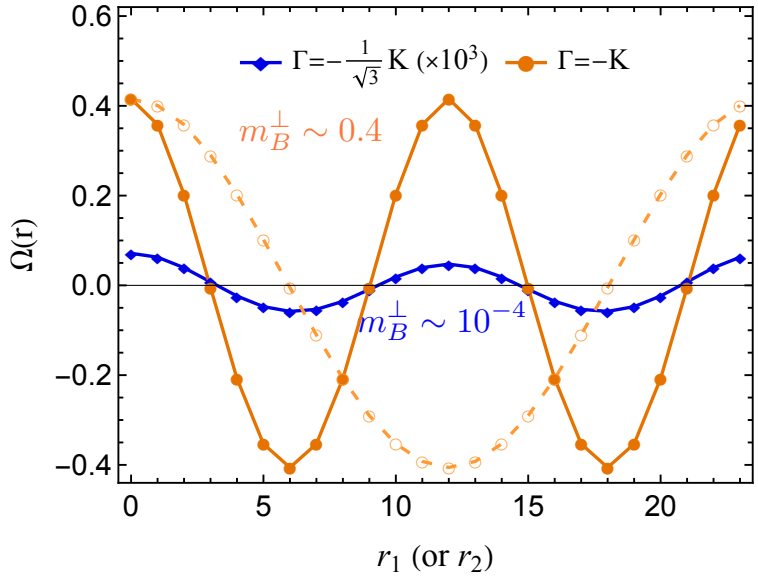

FIGURE 6.7: The spiral correlation function $\Omega_\mu(\mathbf{r})$ for B-helices at $\Gamma = -K/\sqrt{3}$ (blue; rescaled by 10^3) and $-K$ (orange) ($\theta = 1.67\pi, 1.75\pi$). The oscillation and the amplitude reflect the periodicity of the helices and strength of the spiral magnetization $m_B^\perp$, respectively. Filled and open symbols are measured along spontaneously chosen lattice $\mathbf{r}_1$ and $\mathbf{r}_2$ directions, with pitch sizes of $\frac{L}{6}$ and $\frac{L}{3}$ supercells, respectively. A $L = 72$ lattice is considered, and $r_1, r_2 = 0, 1, \ldots, \frac{L}{3} - 1$.

The proposed ansatz for the spiral components of a spin by carefully analyzing the frozen spin configurations at the appropriate sublattices is given by,

$$\vec{S}^\perp_{\mu,\mathbf{r}} = m^\perp_\mu \left(\cos\tfrac{6\pi}{L}(2r_1 + r_2), \mathrm{sgn}(\Gamma)^\eta \sin\tfrac{6\pi}{L}(2r_1 + r_2), 0\right) \tag{6.11}$$

We would like to stress that this ansatz is the **most important equation** of this chapter and is the one that establishes the true ground state structure of the classical model. The perpendicular magnetization $m^\perp_\mu = \frac{1}{N_{\text{cell}}} \sum_{cells} |\vec{S}^\perp_\mu|$ is defined by the transverse spin components and $\mathbf{r} = (r_1, r_2)$ with $r_1, r_2 = 0, 1, \ldots, \frac{L}{3} - 1$ label the 3×3 supercells and $\eta = 0, 1$ is used to distinguish the even and odd honeycomb sublattices and $\mu = 1...18$ label the different sublattices.

A significant feature of the above ansatz is the *chirality modulation* factor in front of the y component $sgn(\Gamma)^\eta$. This determines whether the spirals rotate clockwise or anti-clockwise with respect to the helical axis. In the parameter range we considered $\Gamma := \cos\theta > 0$, $3\pi/2 < \theta < 2\pi$ and as $sgn(\Gamma) > 0$ both the spirals have the same chirality rotating counterclockwise and the spin helices living on the odd and even honeycomb sublattices (blue and red sites in Fig. 6.4) could be viewed as nine pairs of double helices with uniform chirality. While in the other frustrated region with $\Gamma < 0$ and $K > 0$ the spirals had opposite chirality which we explicitly verified.

Another interesting feature is the *highly unusual anisotropy* in the spatial periodicity as seen by the factor of 2 before r_1. This suggests that the helix along one of the lattice directions has twice the pitch length as compared to the other helix or alternately the helix completes two revolutions (periods) along a spontaneously chosen $\mathbf{r}_1$ direction while it just does one (period) along the other direction albeit the same amplitude.

We explicitly showed this periodicity anisotropy (which is encoded in the ansatz Eq. (6.11)) by measuring the spiral correlation function as defined below

$$\Omega_\mu(\mathbf{r}) = \frac{1}{m^\perp_\mu}\left(\vec{S}_{\mu,\mathbf{r}_0} \cdot \vec{S}_{\mu,\mathbf{r}_0+\mathbf{r}} - |\mathbf{m}^\parallel_\mu|^2\right), \tag{6.12}$$

where the distance $\mathbf{r}$ is measured in unit of supercells i.e. we measure the spiral anisotropy at the spins belonging to the same sublattice on different supercells. The correlation function $\Omega_\mu(\mathbf{r})$

in Fig. 6.7 forms a cosine curve reflecting the periodicity of the underlying spin helix with its amplitude indicating the strength of the spiral magnetization $m_\mu^\perp$. For the orange curves where the helix is more pronounced which is the curve corresponding to the parameter point $K = -\Gamma$ the solid (orange) line measures the oscillation along r_1 and the dashed (orange) line with open markers measures the oscillation along r_2. We see that both the curves have the same amplitude but different periods and the period along r_1 is twice that of the period along r_2 highlighting the anisotropy in periods. We stress that the helical order is *genuinely incommensurate* implying pitch increases linearly with L.

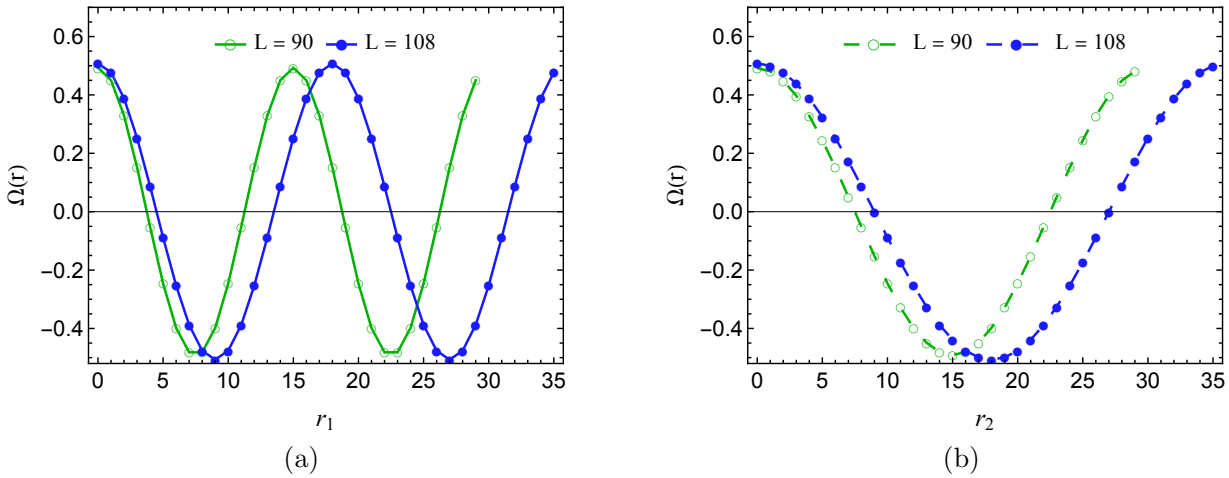

FIGURE 6.8: Finite-size dependence and spontaneous anisotropy of the helix pitches. The spiral correlation function $\Omega_\mu(\mathbf{r})$ for type-B helices is measured at $K = -\Gamma$ along the direction of two independent lattice vectors. (a) The oscillations show two periods along a spontaneously chosen r_1 direction, confirming the pitch sizes of $\frac{L}{6} = 15, 18$ supercells (45 and 54 lattice spacings) for lattices $L = 90, 108$, respectively. (b) There is only a single period along the r_2 direction, with pitch sizes of $\frac{L}{3} = 30, 36$ supercells (90 and 108 lattice spacings), justifying a spontaneous anisotropy in periodicity. Type-A and type-C helices have the same periodicity but differ in the oscillation amplitude as $|\Omega_\mu| \propto m_\mu^\perp$; $r_1, r_2 = 0, 1, \ldots, \frac{L}{3} - 1$ due to the 3×3 supercell structure.

In the Fig 6.8 we explicitly plotted the spin spirals oscillation parameter with different lattice sizes $L = 90, 108$ and verified that the incommensuration grows linearly with the system size. For the $L = 108$ we have $L/3 = 36$ supercells and for $L = 90$ we have $L/3 = 30$ supercells and by comparing the right (a) and left (b) figures we see that along r_1 we have helix with pitch lengths 15 and 18 and along r_2 we have pitch lengths 30 and 36 for $L = 90$ and $L = 108$ respectively with the same amplitude which justified our transverse magnetization ansatz.

The Fig. 6.7 also shows the oscillation parameter $\Omega_\mu(\mathbf{r})$ for the B-helix at $\Gamma = -K/\sqrt{3}$ at $\theta = 1.67\pi$ shown by the blue curve, where the parallel components account almost completely for the total magnetization and the transverse components have a very small imprint. We observed that despite the extremely small $m_B^\perp \sim 10^{-4}$, the expected cosine oscillation was present. This confirms that the spiral structure remains an imprinted feature over the entire frustrated phase $1.58\pi \lesssim \theta < 2\pi$ even though the imprint at smaller values of θ are hard to detect and does not play a major role in spin texture.

6.4 Summary and Outlook

In this chapter we studied the classical ground state of the honeycomb Kitaev-Γ model in the parameter regime relevant for realistic Kitaev materials which earlier our machine found and we recognized as the non trivial modulated $S_3 \times Z_3$ phase. Understanding the classical structure of the ground state is crucial for both interpreting experimental observations and exploring novel

phases in Kitaev magnets as well as making sense of the quantum results which could be done using DMRG, ED or iPEPs. We have investigated the classical ground-state properties through a combination of comprehensive Monte Carlo simulations followed by freezing the spin to its local molecular axis to generate a spin configuration at the lowest possible classical temperature. This chapter, in contrast to the previous chapters which were driven by machine learning methods, involved human effort in analysing the ground state and identifying the tangle of helices which we propose to have experimental signatures. We discovered the classical ground state features a tangle of highly structured spin double helices with the transverse component increasing with Γ values. This helix tangle distinguished itself from typical spiral magnets [158, 118, 112, 213] by a number of prominent features, including an intricate modulation of helical axes, a spontaneous periodicity anisotropy, and a well-regulated chirality pattern. The complete characterization of the classical ground state becomes particularly valuable given fundamental limitations in state-of-the-art quantum numerical algorithms. We expect the emergence of unconventional helicity to leave fingerprints on dynamical and transport behaviors, such as spectrum broadening and splitting, long-living currents, and anomalous diffusions [173, 98, 221] which we shall discuss in the next chapter.

Chapter 7

Dynamics and transport in the $JK\Gamma$ model

In the previous chapter we analysed the ground state in the $S_3 \times Z_3$ phase and found an extremely sophisticated tangle of double helices which we expect to have some imprint on neutron scattering experiments. In this final chapter we precisely answer this question and deal with the dynamics and transport in the $JK\Gamma$ model for one last time and understand what are the experimental signatures one expects thus bridging the gap between theory and experiments.

Transport phenomena along with dynamical response reflects the dynamical properties of interacting spins such as magnetic excitations and fluctuations moving away from the static properties such as spin orderings and phase diagrams we investigated in the previous few chapters. Recent developments in spintronics and magnonics has found that spin transport could be used as a probe to study magnetic properties [9, 60, 69].

Nonlinear spin structures such as skyrmions also show signatures in magnon meditated spin transport [156] and spin currents can also uncover extremely subtle topological phenomena such as $\mathbb{Z}_2$ vortex binding-unbinding [8] which remain elusive to static quantities such as specific heat and susceptibility showing only a weak signature. From a theoretical perspective we could also analyse transport properties and in particular thermal Hall effects and understand to what extent do classical results explain quantum signatures in Kitaev magnets [103].

Here we discovered that spin transport can be used as a probe in detecting phase transitions and consequently changes in spin textures while thermal transport does not. Along the way we defined and clarified the difference between total and virtual spin currents and highlighted how the equivalence of eigenvalues of the interaction matrix is essential in conservation of spin magnetizations. We also found that evolution of the spiral has signatures on dynamical structure factors which could serve as a further probe into the rich and exciting field of frustrated magnetism.

7.1 Model and Theoretical Framework

We investigated the classical Heisenberg-Kitaev-Γ ($JK\Gamma$) model on a 2D honeycomb lattice, with the interaction Hamiltonian between the classical spins $\vec{S}_i \in SO(3)$ given by [39, 45],

$$\begin{aligned}\mathcal{H}_{JK\Gamma} &= \sum_{<ij>_\gamma} \left[J\vec{S}_i \cdot \vec{S}_j + KS_i^\gamma S_j^\gamma + \Gamma(S_i^\alpha S_j^\beta + S_i^\beta S_j^\alpha)\right] \\ &= \sum_i \sum_{j\in N(i)} \vec{S}_i \hat{J}_{ij}^\gamma \vec{S}_j, \end{aligned} \tag{7.1}$$

here, γ labels the three distinct nearest-neighbor (NN) bonds $\langle ij \rangle$ on the hexagon with mutually exclusive $\alpha, \beta, \gamma \in \{x, y, z\}$ as illustrated in Figure 7.1 and $N(i)$ labels the nearest neighbours of the spin $\vec{S}_i$ (see eqn (7.1)). The interaction matrices applicable on the γ bonds are explicitly written as,

$$\hat{J}^x = \begin{bmatrix} J+K & 0 & 0 \\ 0 & J & \Gamma \\ 0 & \Gamma & J \end{bmatrix}, \hat{J}^y = \begin{bmatrix} J & 0 & \Gamma \\ 0 & J+K & 0 \\ \Gamma & 0 & J \end{bmatrix}, \hat{J}^z = \begin{bmatrix} J & \Gamma & 0 \\ \Gamma & J & 0 \\ 0 & 0 & J+K \end{bmatrix}.$$

The Heisenberg-Kitaev-Γ Hamiltonian (eqn (7.1)) comprises of generic NN exchanges allowed by the cubic symmetry of the octahedral cage surrounding the magnetic ion [147, 41]. Although the Kitaev (K) term is of prime interest for realizing quantum spin liquids, in real materials, the Heisenberg (J) and the symmetric off-diagonal (Γ) exchanges exist ubiquitously.

The dynamical evolution of spins is described by the Landau-Lifschitz (LL) equation [130],

$$\frac{\partial \vec{S}_i}{\partial t} = -\{\vec{S}_i, \mathcal{H}\} = \sum_j \vec{S}_i \times \vec{B}_i^j, \tag{7.2}$$

where $\vec{B}_i^j = \partial h_j / \partial \vec{S}_i$ is the effective magnetic field due to the neighbouring spins $\vec{S}_j$ on the spin $\vec{S}_i$. This equation describes the precession of spin around an effective local magnetic field and is the classical analogue of the Heisenberg equation of motion. In this scheme temperature effects are incorporated by Monte Carlo sampling of spins at the required temperature from thermal equilibrium ensembles.

The dynamical structure factor (DSF) investigates the dynamical response of the spin system which is unravelled by inelastic neutron scattering experiments and is defined as ,

$$S(\vec{q}, \omega) = \frac{1}{N} \sum_{i,j}^{N} e^{-i\vec{q}\cdot\vec{r}_{ij}} \int dt e^{i\omega t} \langle \vec{S}_i(0) \cdot \vec{S}_j(t) \rangle, \tag{7.3}$$

where the spin configurations $\vec{S}(t)$ at any time t are generated by integrating the classical equation of motion (eqn (7.2)). We refer the reader to Chapter 2 for more details on spin dynamics and the Landau-Lifschitz Gilbert [67] equation describing the spin evolution.

7.1.1 Currents and conductivities

Every conserved physical quantity implies a continuity equation and an associated local current density $j(r,t)$. We obtain the net current by integrating the current density over all space as [146],

$$\begin{aligned} \mathcal{J}_O(t) &= \int d\vec{r} j_O(\vec{r}, t) = \int d\vec{r} \vec{r} \frac{\partial}{\partial t} O(\vec{r}, t) \\ &= \sum_i \vec{r}_i \frac{\partial}{\partial t} O_i(t), \end{aligned} \tag{7.4}$$

where an integral over r and integration by parts is carried out excluding the boundary terms and the sum over all lattice points represents a discretized version.

In any spin model, where the total energy $\mathcal{H} = \sum_i h_i$ is a conserved quantity, we can define the *thermal current* integrating the time derivative of the energy density as,

$$\begin{aligned} \mathcal{J}_{th}(t) &= \sum_i \vec{r}_i \frac{\partial h_i}{\partial t} = \sum_i \vec{r}_i \sum_m \frac{\partial h_i}{\partial \vec{S}_m} \cdot \frac{\partial \vec{S}_m}{\partial t} \\ &= \sum_i \vec{r}_i \sum_m \vec{S}_m \cdot (\vec{B}_m^i \times \sum_l \vec{B}_m^l) \\ &= \sum_i \vec{r}_i \sum_{j \in N(i)} \vec{S}_j \cdot (\hat{J}_{ij} \vec{S}_i \times \sum_{k \in N(j)} \hat{J}_{jk} \vec{S}_k), \end{aligned} \tag{7.5}$$

where the effective magnetic field $\vec{B}_i^j = \hat{J}_{ij}\vec{S}_j$ was used in going from the second line to the third line. Finally this term can be rearranged to obtain the expression below,

$$\mathcal{J}_{th}(t) = \sum_i \sum_{j,k\in N(i)} (\vec{r}_j - \vec{r}_k)\vec{S}_i \cdot (\hat{J}_{ij}\vec{S}_j \times \hat{J}_{ik}\vec{S}_k). \tag{7.6}$$

The conservation of the α^{th} component of Magnetization $M^\alpha = \sum_i S_i^\alpha$ results in the *spin current* which can be derived using the above formalism as,

$$\begin{aligned}\mathcal{J}_s^\alpha(t) &= \sum_i \vec{r}_i \frac{d\vec{S}^\alpha}{dt} = \sum_i \sum_j \vec{r}_i (\vec{B}_i^j \times \vec{S}_i)^\alpha \\ &= \sum_{i,j\in N(i)} \vec{r}_i (\hat{J}_{ij}\vec{S}_j \times \vec{S}_i)^\alpha + \vec{r}_j (\hat{J}_{ij}\vec{S}_i \times \vec{S}_j)^\alpha.\end{aligned} \tag{7.7}$$

The above expression can be rewritten as,

$$\mathcal{J}_s^\alpha(t) = \Delta \sum_i \sum_{j\in N(i)} (\vec{r}_i - \vec{r}_j)(\vec{S}_i \times \vec{S}_j)^\alpha, \tag{7.8}$$

here $\hat{J}_{ij}$ are the interaction matrices between the spins $\vec{S}_i$ and $\vec{S}_j$ and Δ is the degenerate eigenvalue of the spin interaction matrix $\hat{J}^\gamma$ and $\vec{r}_i$ are the lattice vectors to the spin $\vec{S}_i$ from the origin.

The conservation of spin magnetization is related to the equivalence of eigenvalues of the interaction matrix. Assuming α^{th} component magnetization is conserved i.e. $dM^\alpha/dt = d\sum_i S_i^\alpha/dt = 0$ we have,

$$\begin{aligned}\frac{dM^\alpha}{dt} &= \sum_i [(B_i^i \times S_i) + \sum_{j\in N(i)} (B_i^j \times S_i)]^\alpha \\ &= \sum_i [(\sum_{k\in N(i)} \hat{J}_{ik}S_k \times S_i) + \sum_{j\in N(i)} S_j \hat{J}_{ji} \times S_i]^\alpha \\ &= 2\sum_i (\sum_{j\in N(i)} \hat{J}_{ij}S_j \times S_i)^\alpha \text{ index relabelling} \\ &= 2\sum_{i,j\in N(i)} [(\hat{J}_{ij}S_j \times S_i) + (\hat{J}_{ij}S_i \times S_j)]^\alpha \\ &= 2\sum_{i,j\in N(i)} \begin{bmatrix} (\Delta_y-\Delta_z)\cdot(S_i^z S_j^y + S_i^y S_j^z) \\ (\Delta_z-\Delta_x)\cdot(S_i^x S_j^z + S_i^z S_j^x) \\ (\Delta_x-\Delta_y)\cdot(S_i^x S_j^y + S_i^y S_j^x) \end{bmatrix}^\alpha = 0 \\ \frac{dM^\alpha}{dt} &= 0 \Leftrightarrow \Delta_\beta = \Delta_\gamma\end{aligned} \tag{7.9}$$

where $\Delta_{x,y,z}$ are the eigenvalues of $\hat{J}$ and α, β, γ are mutually exclusive and further we assumed $\hat{J}$ was *diagonal*. Thus the equivalence of eigenvalues is a necessary and sufficient condition for the conservation of magnetization. In case of isotropic Heisenberg models ($\Delta_x = \Delta_y = \Delta_z = \pm J$) implying all components of magnetization are conserved [9, 88]. In XXZ models ($\Delta_x = \Delta_y = J, \Delta_z = J_z \neq J$), only the z^{th} component of magnetization is conserved [8]. The above formulas are a general derivation and valid for all two-dimensional lattices and spin Hamiltonians that conserve energy and have conserved magnetizations. These agree with the previously obtained expressions in the study of various spin Hamiltonians [9, 88, 156, 217, 191].

The interaction of thermal (∇T) and magnetic field (∇B) gradients with magnetic moments are responsible for magnon mediated thermal and spin currents respectively [156]. From the fluctuation-dissipation theorem, the linear responses are related to the correlation of equilibrium fluctuations of currents which can be expressed using the Kubo formula [123] as,

$$L^{\mu,\nu}_{m,n} = \frac{1}{VT}\lim_{\tau\to\infty}\int_0^\tau dt\langle \mathcal{J}^\mu_m(0)\mathcal{J}^\nu_n(t)\rangle \tag{7.10}$$

here $m, n \in \{s, th\}$ and $\mu, \nu = \{x, y\}$ indicate the physical lattice directions and V is the volume of the system. The conductances are expressed as,

$$\sigma_{\mu\nu}(T) = \frac{1}{TL^2}\lim_{\tau\to\infty}\int_0^\tau dt\langle \mathcal{J}^\mu_s(0)\mathcal{J}^\nu_s(t)\rangle_T \tag{7.11a}$$

$$\kappa_{\mu\nu}(T) = \frac{1}{T^2L^2}\lim_{\tau\to\infty}\int_0^\tau dt\langle \mathcal{J}^\mu_{th}(0)\mathcal{J}^\nu_{th}(t)\rangle_T \tag{7.11b}$$

here $\langle ...\rangle_T$ denotes an ensemble thermal average with respect to a canonical equilibrium distribution $e^{-\beta H}/Z$ where Z is the canonical partition function and $\beta = 1/T$ is the inverse temperature.

In dealing with Hall/transverse conductivities, in addition to the Kubo contribution there is an another contribution originating from the coupling of the energy density with the pseudogravitational potential also known as energy magnetization [36]

$$\kappa_{xy} = \frac{1}{T^2L^2}\lim_{\tau\to\infty}\int_0^\tau dt\langle \mathcal{J}^x_{th}(0)\mathcal{J}^y_{th}(t)\rangle_T + \delta\kappa_{xy}, \tag{7.12}$$

where the additional term originates from the modification of energy current modification due to its circulation and is not observable in transport and hence needs to be subtracted from the total transverse contribution [135, 80],

$$\delta\kappa_{xy} = -\frac{2\sum_i \langle \vec{r}_{i,x}\mathcal{J}^y_{th}(t)\rangle}{L^2T}. \tag{7.13}$$

In this thesis we explicitly deal with *longitudnal conductivities* and leave the discussion of thermal conductivities for a future work.

7.2 Virtual spin currents

In the $JK\Gamma$ model (see eqn (7.1)), since the interaction between the spins are bond dependent implying no single component of magnetization is conserved over all the bonds, it is not possible to define an ordinary spin current (eqn (7.8)) over the entire lattice. As discussed in the previous section, conservation of components of spin magnetization is related to the equivalence of eigenvalues and in the $JK\Gamma$ Hamiltonian the eigenvalues of the interaction matrix are $(\Delta_1 = J + K, \Delta_2 = J - \Gamma, \Delta_3 = J + \Gamma)$.

Equivalence of eigenvalues results in two distinct scenarios, the $K = \pm\Gamma$ case with arbitrary value of the Heisenberg coupling (which we ignore ($J = 0$) as it does not affect the discussion resulting in the pure $K\Gamma$ model) and the $\Gamma = 0$ case which results in the pure JK model. We highlight that since energy is conserved for this model we use the conventional expression for thermal currents (eqn (7.6)) unchanged and discuss its implications in subsequent sections.

For the spin currents, instead we introduce the notion of *virtual spin currents* where we define the current as a function of the spin components conserved along each bond. Ordinary spin currents are associated with magnon-mediated transport under a magnetic field gradient [156] and the associated spin conductances are experimentally measurable quantities. The total ordinary spin current (comprising of an averaged sum over all components) can be decomposed into contributions from virtual (conserving) current (v) and non-conserving (nc) terms $\mathcal{J}_{s,tot} = \mathcal{J}_{s,v} + \mathcal{J}_{s,nc}$. Thus virtual currents reflect magnon mediated transport despite not being measurable experimentally.

In the pure JK model, the bond dependent interaction matrix $(\hat{J}^\gamma)$ has the eigenvalues $\Delta_\alpha = \Delta_\beta = J, \Delta_\gamma = J + K$ implying that S^γ is conserved along the γ bond i.e. along the z (x,y) bond

$S^z(S^x, S^y)$ is conserved. Subsequently we define the virtual current flowing through each lattice site as ,

$$\mathcal{J}^{\gamma}_{s,JK}(t) = J\sum_i \sum_{j\in\gamma(i)} (\vec{r}_i - \vec{r}_j)(\vec{S}_i \times \vec{S}_j)^{\gamma}, \tag{7.14}$$

here the three nearest neighbours in the hexagonal lattice are along the $\gamma = \{x, y, z\}$ bonds respectively. The total current (as shown in Fig. 7.1)) along the x (lattice) direction (shown by the red arrows) into a site has contributions from S^x, S^y components respectively and along the y (lattice) direction (shown by the blue arrows) has contributions from S^x, S^z respectively. These definitions define a path in the lattice space for the transport and take into account each bond exactly once.

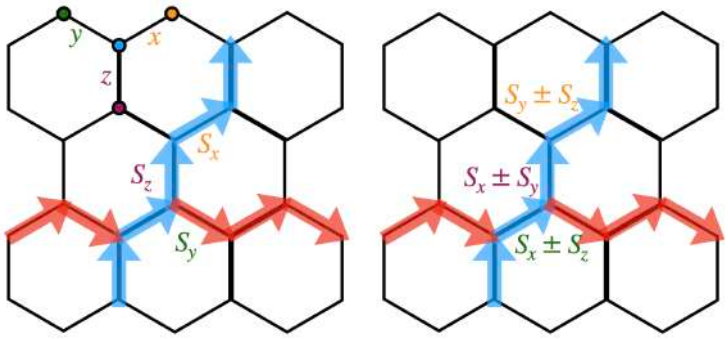

FIGURE 7.1: Hexagonal lattice with the 3 nearest neighbour bonds marked by x, y, z. The spin components conserved per bond in the JK model (left) and the $K\Gamma$ (right) is also shown. The $\pm$ corresponds to the value of K/Γ in the definition of virtual currents. The path of the current along the x-direction (shown by the red arrows) and the y-direction (shown by the blue arrows is also highlighted). The current is mediated through magnons in response to either a thermal or a magnetic gradient along the same direction as the flow of current.

In the pure $K\Gamma$ model , the interaction matrix has eigenvalues $\Delta_1 = K, \Delta_2 = \Gamma, \Delta_3 = -\Gamma$, which implies that we cannot in general define a virtual current except at special parameter points $\Gamma = 0, K = \pm\Gamma$. Since the interaction matrix is non-diagonal, to use the conventional definitions of spin currents we need to diagonalize the matrix using unitary matrices (U^{γ}) which in turn leads to a transformation of spins in order to keep the energy per bond constant expressed as,

$$h^{\gamma} = \vec{S}^T_{\gamma}\hat{J}^{\gamma}\vec{S}_{\gamma} = (\vec{S}^T_{\gamma}U^{\gamma})\hat{D}^{\gamma}([U^{\gamma}]^{\dagger}\vec{S}_{\gamma}) = \tilde{S}^T_{\gamma}\hat{D}^{\gamma}\tilde{S}_{\gamma}, \tag{7.15}$$

where the spins in the rotated frame are $\tilde{S} = U^{\dagger}\vec{S}$ and the diagonalized matrices in the rotated frame are $D = U^{\dagger}\hat{J}U$. The spins in the transformed basis are written out explicitly as,

$$\tilde{S}_x = \frac{1}{\sqrt{2}}\begin{pmatrix} \sqrt{2}S_x \\ S_y - S_z \\ S_y + S_z \end{pmatrix}, \tilde{S}_y = \frac{1}{\sqrt{2}}\begin{pmatrix} S_x - S_z \\ \sqrt{2}S_y \\ S_x + S_z \end{pmatrix},$$
$$\tilde{S}_z = \frac{1}{\sqrt{2}}\begin{pmatrix} S_x - S_y \\ S_x + S_y \\ \sqrt{2}S_z \end{pmatrix}. \tag{7.16}$$

The conservation of the γ^{th} component of spin magnetization in the rotated frame corresponds to the conservation of a trivial combination of the α, β components in the unrotated frame as determined by the unitary transformation matrix as,

$$\frac{d\tilde{S}^{\gamma}}{dt} \sim \frac{d}{dt}(S^{\alpha} \pm S^{\beta}) = 0 \tag{7.17}$$

where α, β, γ are mutually exclusive. This is also shown in Fig 7.1 where the spin components conserved along the γ bond are $S^\alpha \pm S^\beta$. This lets us subsequently define virtual spin currents at these special points $K/\Gamma = \pm 1$ through each site of the lattice as,

$$\mathcal{J}^{\gamma}_{s,K\Gamma}(t) = \Gamma \sum_i \sum_{j\in\gamma(i)} (\vec{r}_i - \vec{r}_j)[(\vec{S}_i \times \vec{S}_j)^\alpha - \frac{K}{\Gamma}(\vec{S}_i \times \vec{S}_j)^\beta]. \tag{7.18}$$

Similar to the JK case, the total current (as shown in Fig. 7.1)) along the x (lattice) direction (shown by the red arrows) into a site has contributions from $S^x \pm S^z, S^y \pm S^z$ components and along the y (lattice) direction (shown by the blue arrows) has contributions from $S^x \pm S^y, S^y \pm S^z$ respectively.

7.3 Results for the JK model

In this section we shall focus on the results of transport for the JK model. Figure 7.2 shows the renormalized longitudnal thermal conductance $\tilde{\kappa}_{\mu\mu} \equiv \kappa_{\mu\mu} T^2$ as a function of temperature at the parameter point $J = K$ deep in the antiferromagnetic phase [41, 177] for different system sizes $L \in \{24, 36, 48, 72\}$. The low-temperature transport mediated by magnons (described by linear spin wave theory (LSWT)) predicts that thermal conductivity $\kappa_{xx} \propto 1/\alpha_d$ [9, 46, 211] where α is the damping constant whose origins lie in multi-magnon scattering. The renormalized conductivity saturates to a constant value and the low temperature behaviour of conductivity (shown in the inset of Fig 7.2) is in agreement with the theoretical prediction [211, 215]. This behaviour can be qualitatively understood as the free propagation of magnons without scattering at low temperatures. However, this infinite conductivity is a purely classical feature and in the quantum regime quantum fluctuations ensures the thermal conductivity saturates to a finite value at low temperatures.

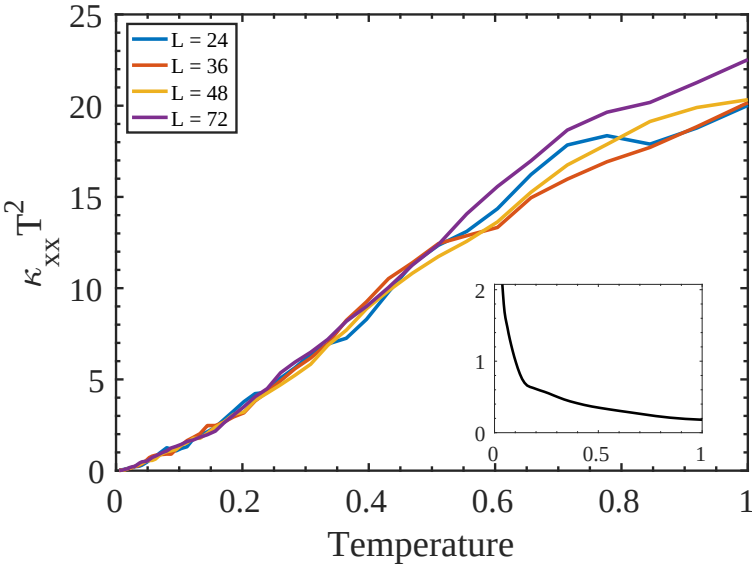

FIGURE 7.2: The renomalized thermal conductance shown for the AFM phase at the parameter point $J = K$ for various system sizes $L \in \{24, 36, 48, 72\}$. In the inset is the behaviour of the true conductivity which diverges as $T \to 0$ owing to the $1/T^2$ tail and $\kappa \sim 1/\alpha \sim 1/T^2$ where α is the magnon scattering rate. This divergence is a feature of classical spin models modelling the free propagation of magnons at low temperatures without scattering or decay but in the quantum case quantum fluctuations ensures the thermal conductivity is bounded. The thermal conductivity is featureless and does not detect the changes in spin textures with increasing temperature.

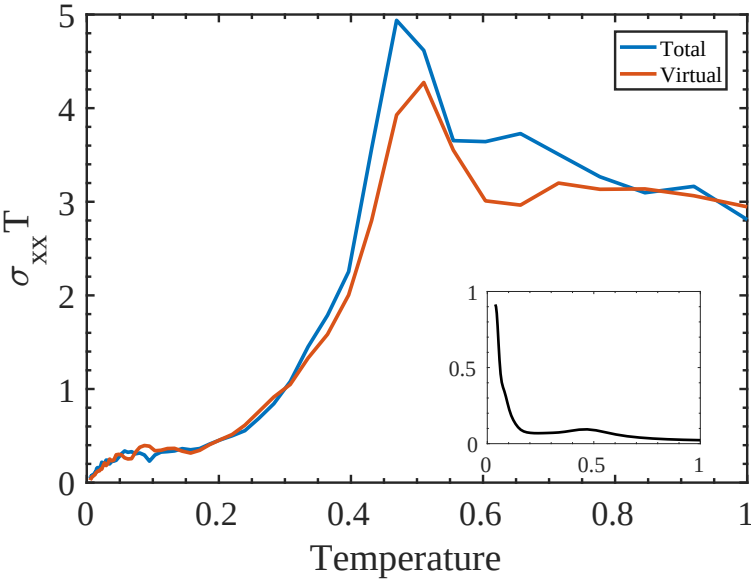

FIGURE 7.3: The renormalized spin conductivity computed from total (blue) and virtual (orange) definitions of currents is shown above deep within the AFM phase at the parameter point $J = K$. The conductance curves show a peak about $T_c \approx 0.5$ and saturates to a constant value as $T \to 0$. In the inset is the behaviour of the true conductivity which diverges as $T \to 0$ owing to the $1/T$ tail. The peak corresponds to the phase transition from a low temperature magnetic ordered state to a high temperature disordered state.The total current is also slightly larger than the virtual current which is expected since it has contributions from the virtual as well as non conserving part.

Next, we turn to the spin conductances at the parameter point $J = K$. As mentioned in section 7.1.1 in pure isotropic Heisenberg ($J = \pm 1, K = 0$) models all the components of spin are conserved and hence one could define the total longitudnal spin conductance as the averaged sum over all components as,

$$\tilde{\sigma}_{\mu\mu}(T) = \frac{1}{L^2}\frac{1}{3}\int_0^\infty dt \sum_{\alpha\in\{x,y,z\}} \langle \mathcal{J}^\alpha_{s,\mu}(0)\mathcal{J}^\alpha_{s,\mu}(t)\rangle_T, \tag{7.19}$$

where α refers to the component of spin magnetization conserved. We continue to use the same definition of total spin current at other parameter values ($K \neq 0$), though strictly speaking not all components of spin magnetization are conserved. Figure 7.3 shows the total and virtual spin conductances for the lattice size $L = 72$. We observe that both the total and virtual renormalized longitudnal spin conductances ($\tilde{\sigma}_{\mu\mu} = \sigma_{\mu\mu}T$) diverge around $T_c \approx 0.51$ showing that in contrast to thermal conductivity, spin conductance is more sensitive to changes in spin textures and can be used as a probe of phase transition form a low temperature magnetic order with a well defined magnon spectrum to a high temperature paramagnetic phase. This temperature coincides with the transition temperature T_c reported in [174] for the same parameter point.

To further understand this behaviour, we plot the extracted spin relaxation time against temperature, shown in Figure 7.4, for different lattice sizes and observe that the relaxation time diverges around $T \approx 0.5$ which coincides with the transition temperature deduced from spin conductance. The curves slightly shift towards lower temperatures upon increasing the lattice size which is just a finite size effect. In the high temperature phase the current-current correlator decays exponentially $\langle j(0)j(t)\rangle \sim \langle |j(0)|^2\rangle \exp(-t/\tau_s)$ letting us extract the spin-current relaxation time through an exponential fit. The spin-current relaxation time, which is the characteristic time between successive collisions, at long times is related to the magnon damping factor ($\tau_s \sim 1/\alpha$ [9]) which explains how multi-magnon scattering heavily restricts coherent magnon transport which

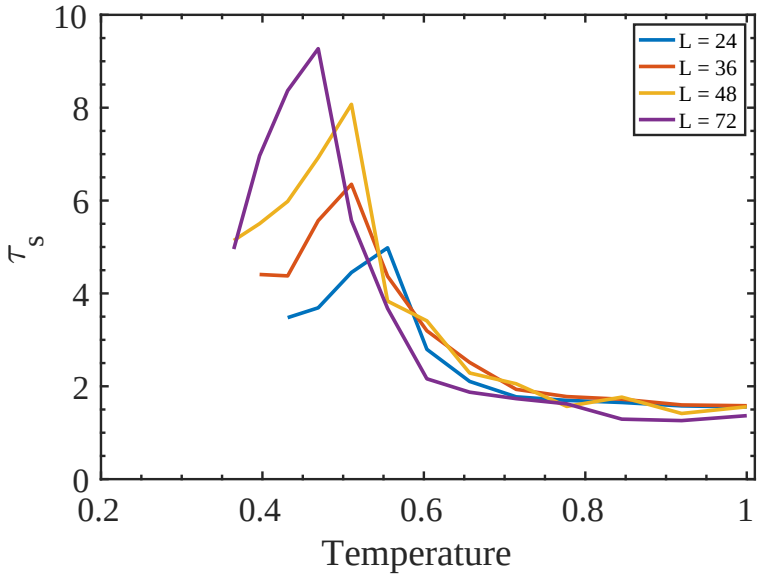

FIGURE 7.4: Relaxation time plotted against temperature. The divergence of relaxation time for virtual spin currents in the AFM phase. The exponential decay is extracted from the long tail behaviour using $\exp(-t/\tau_s)$. The temperature of divergence coincides with the temperature from the conductance curves. The current-current correlator changes behaviour from algebraic or power law decay in the ordered phase to an exponential decay in the disordered phase.

just becomes diffusive. The origin of enhancement at the short-times scale of the relaxation time towards the transition temperature is not clearly understood and maybe a combined effect of spin damping with rapid growth of spin correlation length $\xi_s \sim a \exp(\beta J)$ towards lower temperatures and other magnetic effects.

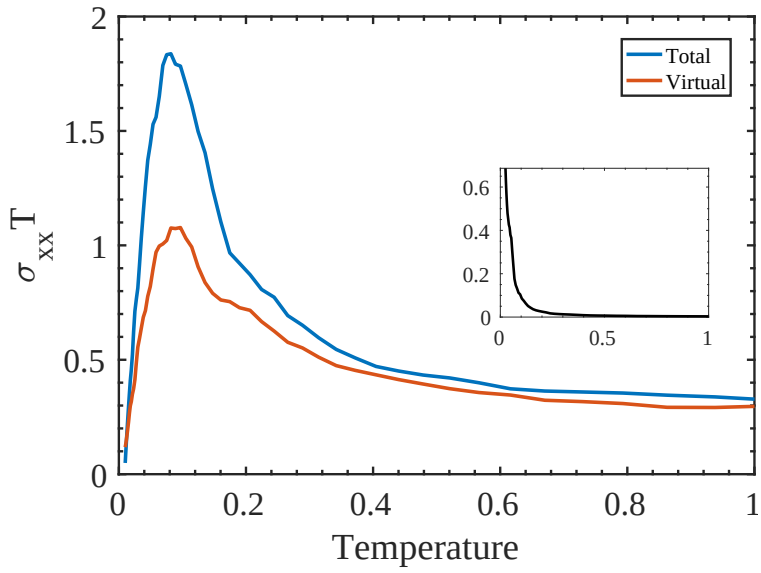

FIGURE 7.5: The virtual spin conductance plotted as a function of temperature for the zigzag phase at the parameter point $J = -K/4$. The spin conductance curve diverges at $T_c \approx 0.14$ corresponding to an order to disorder phase transition.

In Figure 7.5, the spin conductance at a different parameter point $J = -K/4$ in the zigzag phase is shown. Here the total and virtual spin conductances show a peak around $T_c \approx 0.14$ which is close to the value reported by [174]. The conductivity peak coincides with the peak in the relaxation times of the spin current (not shown here) showing that the magnon transport is highly influenced by the multi-magnon scatterings. This again emphasises that longitudinal spin

conductances could serves as probes for transition from magnetic to paramagnetic orders, which is easier to verify experimentally.

7.4 Results for the $K\Gamma$ model

We shall now discuss transport and dynamics of the $K\Gamma$ model where the bond interaction matrix is non-diagonal resulting in a modified definition of virtual spin current (see eqn (7.18)). Figure 7.7 shows the total and virtual spin conductance at the $K = \pm\Gamma$ within the vortex S_3 and the helical $S_3 \times Z_3$ phase respectively [143]. $K = \Gamma$ has a hidden $O(3)$ symmetry wherein the vortex order can be converted into a simple ferromagnet using a six sub-lattice transformation [41]. The spin conductances show a broad peak centered around $T_c \approx 0.2$ corresponding to a crossover, as opposed to the sharper peaks in the JK model corresponding to phase transitions.

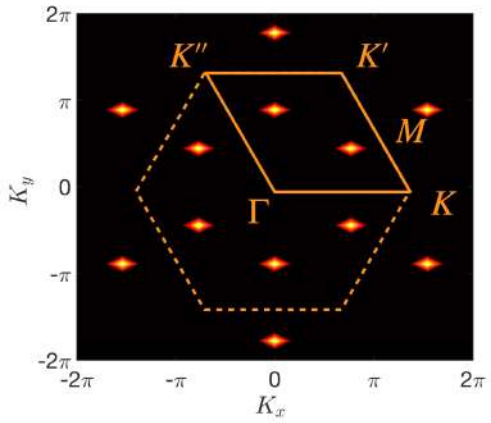

FIGURE 7.6: The static structure factor plotted for $K = -\Gamma$ at low temperature $T = 10^{-5}\sqrt{K^2+\Gamma^2}$ which has the ordering vector $\vec{Q} = 2/3\mathbf{M}$. The first Brillouin zone is indicated by the solid orange line and the high symmetry points and the path $\Gamma - K - K' - K'' - \Gamma$ along which the DSF is plotted is also shown. The length of the nearest neighbour bonds is set to unity $(a = 1)$.

At $K = -\Gamma$ there is no observable divergence and the spin conductance behaviour is rather trivial. The low temperature static structure factor (see fig 7.6) displays well defined Bragg peaks in the first Brillouin zone with ordering vectors $Q = 2/3\mathbf{M}$ suggesting that the system orders magnetically at low temperatures. The ground state was found to be a 18-site sophisticated spin helical structure [136] with 9 pairs of highly entangled double spin helices. This helical structure is highly sensitive to temperature and upon slightly increasing temperature (well below the transition temperature $T < T_c \approx 0.04$ [185]), the delicate ground state structure is completely destroyed as shown by the dynamical structure factor in Figure 7.8. The excitation spectrum is highly diffusive with broad scattering continuum over the entire magnetic bandwidth which is to be expected given the large unit cell size and the complex spin modulation pattern and multi-magnon scatterings [61]. This implies the coherent(well defined) magnon picture which is essential for spin transport dissociates upon increasing temperature and spin conductance which is related to magnon mediated transport is not a sensitive probe or conversely, the spin conductance shows that the low temperature magnetic order is not very robust against thermal fluctuations and spin transport is highly diffusive suggesting that a delicate low temperature phase smoothly melts into the high temperature disordered phase. In contrast in the AFM phase of the JK model discussed in the previous section we see that the AFM spectrum is quite robust against thermal perturbations till $T = 0.2$ before it melts at the transition temperature into a broad continuum in the paramagnetic phase and shows that the picture of coherent magnon transport is valid and spin conductance can serve as a probe to detect the change in spin textures. Thus the idea of well defined/coherent magnons is essential for the utility of spin conductance as a probe.

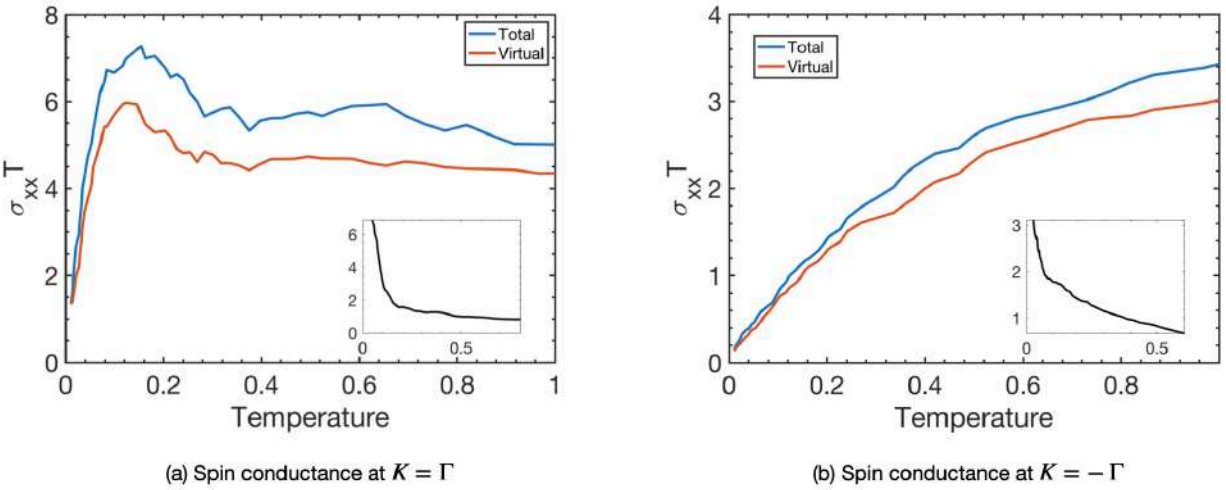

FIGURE 7.7: The virtual spin conductance is plotted as a function of temperature. At (a) $K = \Gamma$ the broad peak at $T_c \approx 0.18$ corresponds to the crossover temperature in the $K\Gamma$ model of the S_3 phase which can be reduced to a simple ferromagnet by a six-site lattice transformation. In contrast at (b) $K = -\Gamma$ the spin conductance curve shows no peak which might be explained by the decoherent magnon picture for this phase.

To understand the sophisticated low temperature magnetic order better, we study the dynamical structure factor, shown in Fig 7.9, at extremely low temperatures $T \sim 10^{-5}\sqrt{K^2+\Gamma^2}$ in order to capture the ground state and decouple all effects of thermal fluctuations and multi-magnon scatterings, along the path $\Gamma - K - K' - K'' - \Gamma$ in the first Brillouin zone shown in Fig 7.6. We further study the prominence of the spiral by analysing the dynamical response with increasing spiral (transverse spin magnetization) component or equivalently increasing Γ at three different points $K = -\sqrt{3}\Gamma, K = -\Gamma, K = -\Gamma/\sqrt{3}$ from a negligible value of $m^{\perp} \approx 10^{-4}$ for $K = -\sqrt{3}\Gamma$ to $m^{\perp} \approx 0.4$ for $K = -\Gamma/\sqrt{3}$. In addition there is a hidden symmetry transformation which makes a six-site pattern and an 18 site pattern degenerate [136]. To untangle the two effects namely the evolution of the spiral and the hidden symmetry imposed degeneracy we focus on the six-site pattern (type 1 shown in 7.9 (a),(c),(e)) and the 18 site pattern (type 2 shown in 7.9 (b),(d),(f)) separately.

Figure 7.9 (a) and (b) show clear and distinct spin wave spectrum with six spin wave modes corresponding to the six site unit cell in (a) and the hidden symmetry related degenerate 18-site order in (b) which shows lesser than 18 distinct spin wave modes suggesting some of the modes are degenerate. The spectrum is gapped and a prominent feature of type 2 is the higher intensity of the lowest frequency branches around the Γ point. The flatness of the top two high frequency bands suggests possible topological magnon [150].

Upon increasing Γ in Figure 7.9 (b) and (d) we observe that the spectrum becomes a more dispersive and bunching of spin waves into 3 bands takes place. The effect of a spiral is to modify the ordering vector from Q to $Q \pm q$ where q is related to the pitch of the spiral [106, 189]. A finite energy Gaussian envelop is always added to the spectrum to rid of numerical artifacts and mimic the finite energy resolution in experiments more closely. In systems where the pitch of the spiral is large and finite the splitting of the low frequency spin wave modes is prominent and clearly distinguishable [189] but in systems with a smaller spiral pitch the finite energy convolution leads to the merging of the closely spaced branches which appear as a broad single branch. This is consistent with our observation here, the width of the low frequency branches near the ordering vectors increase owing to the increased spiral structure of the ground state.

This trend seems to continue as we increase Γ further(see Figure 7.9 (e) and (f)). The bunching of spin waves into the three bands is more prominent here with the lower and middle bands becoming more dispersive while the high energy bands remains unaltered (compared to $K = -\Gamma$)

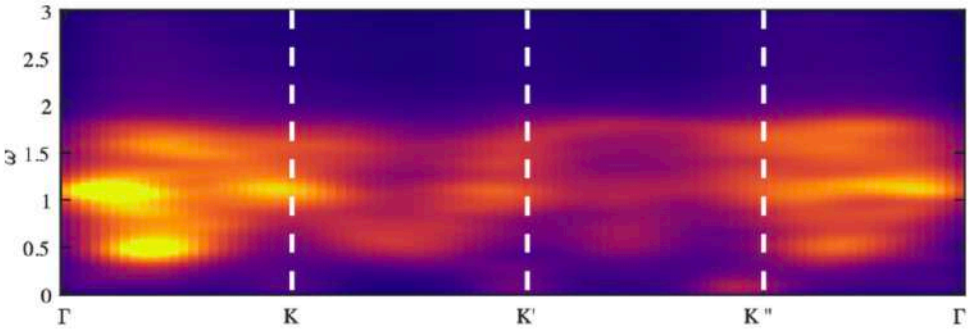

(a) DSF for spiral phase at $K = -\Gamma$ at T = 0.01

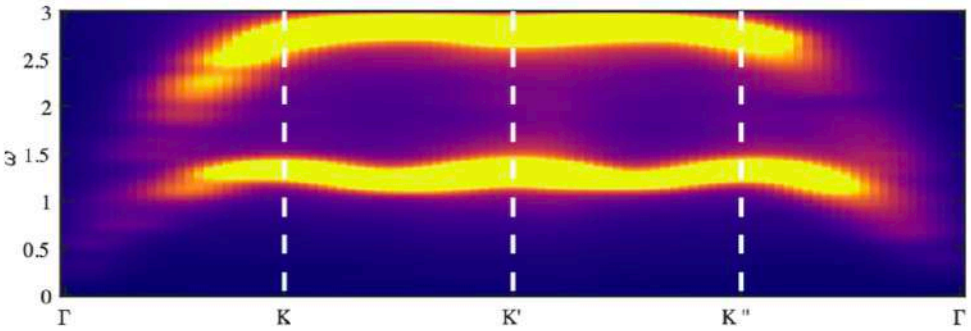

(b) DSF for AFM phase at $J = K$ at T = 0.2

FIGURE 7.8: The dynamic response for the (a) spiral phase at $T = 0.01$ and (b) AFM phase at $T = 0.2$ well below their transition temperatures is shown. The spiral spectrum disintegrates into a broad dispersive spectrum upon increasing temperature signifying that the linear magnon description is not robust to thermal fluctuations and multi-magnon scatterings play an essential role resulting in a decoherent scattering picture. The virtual spin conductance as a result is trivial. The AFM spectrum is robust against thermal perturbations till it melts at the transition temperature into a broad continuum in the paramagnetic phase and shows that the picture of coherent magnon transport is valid and spin conductance can serve as a probe to detect the change in spin textures.

showing a distinct three-mode contribution. The band gap of the spectrum is reduced which is expected as we move towards the gapless Γ spin liquid. It is however important to mention that the true ground state structure is genuinely incommensurate and while a description in terms of linear spin waves is not possible, dynamical spin spectrum show broad diffusive bands which is a result of large unit cells, spiral structure and finite energy resolution making it hard to isolate and study these highly tangled helical states in these frustrated magnets, and purports the need to complement our understanding with spin transport measurements.

7.5 Summary and Outlook

In the final chapter we studied dynamics in the $JK\Gamma$ model on the honeycomb lattice using classical spin dynamics and linear response theory.

We found that longitudinal spin conductance serves as a probe of phase transitions and is sensitive to changes in spin textures but longitudinal thermal conductance does not. However the utility of spin conductance as a probe heavily relies on having a coherent (well defined) magnon picture upto the transition temperature and if we do not have such a picture as in the case of the spiral phase spin conductance is then rather trivial. We also discovered that equivalence of

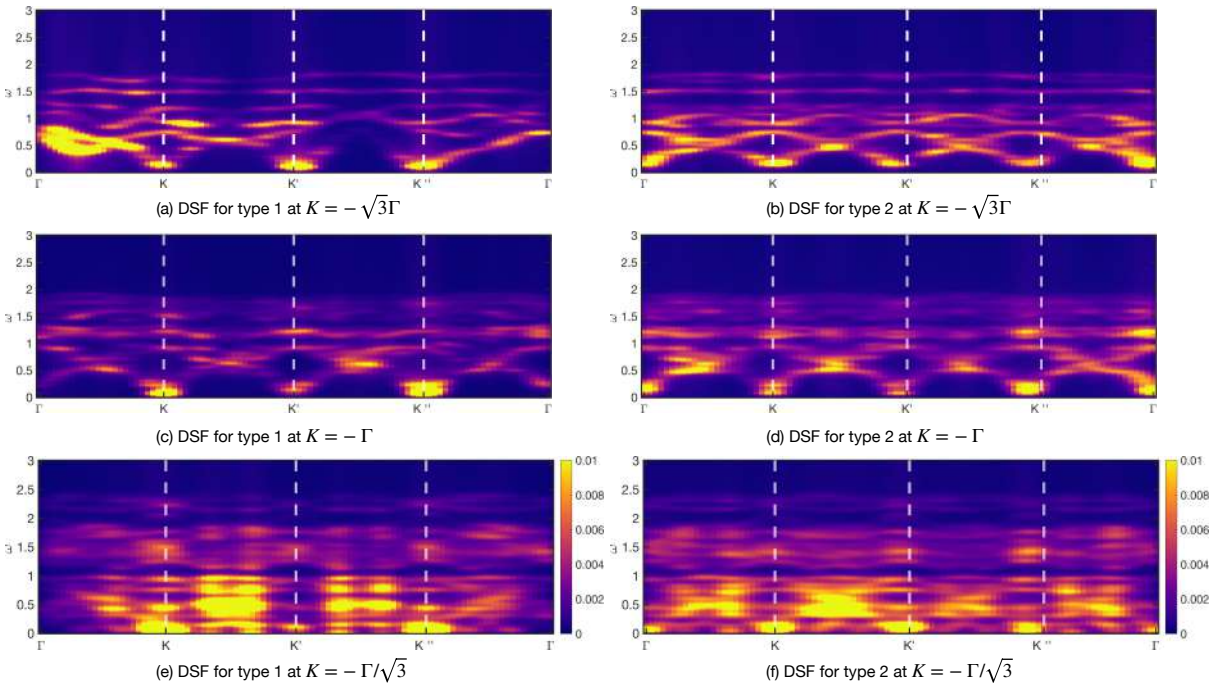

FIGURE 7.9: The dynamical response is plotted at $K = -\sqrt{3}\Gamma$, $K = -\Gamma$ and $K = -\Gamma/\sqrt{3}$ for types 1 and 2 at low temperatures $T \sim 10^{-5}\sqrt{K^2 + \Gamma^2}$. The effect of the spiral is to broaden the low frequency bands as well as bunching of the branches into bands with increasing Γ.

eigenvalues of the interaction matrix is a necessary condition for the conservation of spin magnetization and in defined the virtual current as a combination of spin components conserved along the various bonds. Virtual currents are just the conserved component of the total current and have the physical interpretation of magnon-meditated transport even though it is not directly experimentally measurable.

The dynamical structure factors for the sophisticated helical phase shows a number of interesting features such as bunching of spin waves into distinct broad dispersive bands over the magnetic bandwidth. Further the clear and distinct spin wave spectrum for small values of transverse magnetization quickly melts into blurred broad bands for larger values of transverse spin magnetization showing the effect of the spiral is to broaden and bunch bands.

We showed how longitudinal spin transport serves as a probe and can have experimental significance in the growing field of spintronics and magnonics where magnons are the main carriers. However transverse transport is a bit more subtle due to the pseudo gravitational terms one needs to consider and remains to be investigated in future works. A natural question is that if it functions to serve as a probe of phase transition like their longitudinal counterparts. Also the dynamics we carried out were classical but it is possible to incorporate semi-classical effects by assuming the spins have a Bose-Einstein distribution rather than a Boltzmann distribution at any finite temperature using coloured noise in the evolution equation. The field of spin transport in frustrated magnets unexplored with many open questions and also forms a bridge between theory and experiments and serves as a complementary tool to explore the fascinating field of frustrated magnetism.

Chapter 8

Conclusion

In this thesis, we used an *unsupervised and interpretable* machine learning framework known as Tensorial Kernel Support Vector Machine (TK-SVM) to study the $JK\Gamma$ Hamiltonian which is used to model realistic Kitaev materials. This machine learning (ML) framework was introduced in the Greitemann et al [75, 77] as a tool to classify the phase diagram in classical frustrated magnets with little to no previous knowledge of the topology of the phase diagram required. The phase segregation/classification happens in an unsupervised manner owing to the observation that the bias parameter of the decision function serves as a classifier. The phase diagram is interpreted as a grid of phase points and the weighted bias is used to determine the existence of an edge between any two vertices. This graph partitioning also known as Fiedler clustering [58] is then interpreted as the phase diagram. A major advantage of this framework is its high interpretability which lets us construct classifiers (order parameters and local constraints) from correlations between spin components to distinguish between the different phases learnt in the classification step. The implementation and interpretation of results of the machine learning framework are discussed in Chapter 2.

Quantum spin liquids (QSLs) remain elusive and the search for it experimentally continues even to this day. QSLs are characterized theoretically by exotic fractionalized excitations and other emergent phenomena which are expected to have characteristic experimental imprints but most proposed candidates magnetically order and low temperatures and their spin liquid signatures in experiments are heavily debated. The $JK\Gamma$ model was proposed to be a realistic minimalistic Hamiltonian following the seminal theoretical work of Kitaev [119] and Chaloupka et al [39, 41]. We investigated this Hamiltonian and a few other extensions motivated by experiments in subsequent chapters to uncover the rich phase diagram and complicated the phases using the machine learning framework discussed above. The main motivation of this work as mentioned earlier is two fold. First we wanted to show that TK-SVM is really successful in uncovering the topology of phase diagrams of classical frustrated magnets thus moving away from simplistic benchmarking models to realistic models thus paving the way for exploiting machine learning as a tool to study frustrated systems. Second we wanted to understand to what extent the experimental signatures and quantum results could be explained by the classical limit. We found that surprisingly many of the exotic features could be understood quite well in the classical regime thus vindicating our hypothesis.

Chapter 3 we studied the JK model which is the simplest of the proposed models for Kitaev materials and showed that we could successfully reproduce all the magnetic orders reported in literature [39]. This chapter served more as a “sanity check" to the applicability of the machine learning framework to Kitaev materials. We additionally clarified that *zigzag and stripy* orders are better described by the D_{2h}, D_2 ordering matrices respectively and also showed how we could uncover the *hidden symmetry* transformations and *subdimensional* symmetries in this ML framework.

In chapter 4 we studied the generalized $JK\Gamma$ model as well as the results of including additional secondary interactions such as Γ', J_3 on the phase diagram. These additional interactions stabilized the zigzag order thus complicating the search for a minimalistic model applicable to Kitaev materials. We discovered that our machine found a 32-site intricate magnetic order, which we christened the *nested-stripy-zigzag* which was hitherto unreported in literature and for parameters reported in literature, the Kitaev candidate $\alpha - RuCl_3$ lies at the interface of a multitude of

competing phases further corroborating our results with the experimental findings.

Chapter 5 was the last chapter where we used the ML framework to study the $K\Gamma$ model in a magnetic field. We found that the phase diagram is exceptionally rich hosting a plethora of unconventional orders and shows many common features with its quantum counterpart from field induced separation of magnetic orders to finite extension of spin liquids against perturbations. A complicated modulated phase $S_3 \times Z_3$ was found by the machine with a 18-site magnetic unit cell which could be interpreted as arising from the competition between the spin liquids. This phase is thoroughly investigated in Chapters 6, 7. We also reproduced the ground state constraints for the spin liquids by exploiting the interpretation of our ML framework and showed its consistency with those in literature. We additionally provided an alternate viewpoint where the competition or cooperation between spin liquids leads to unconventional magnetic orders.

We investigate the classical ground state of the $S_3 \times Z_3$ phase in Chapter 6 using a combination of low temperature Monte-Carlo sampling followed by spin freezing to uncover the complex spiral structure. The ground state was found to be a complicated tangle of highly structured spin double helices with a number of prominent features. In the final chapter 7 we investigated the imprint of these helical phases on dynamics and transport behaviour. To do so we introduced the concept of *virtual spin currents* and showed that spin conductance could be used as a classifier for phase transitions or cross overs with the spin conductance diverging at the transition point. This proves a valuable experimental probe and when there is a coherent magnon definition longitudinal spin conductance is a good probe. In addition we showed that the imprint of the helical structure was to broaden the spin spectrum and bunching of spin waves into broad dispersive bands also leads to trivial spin conductance behaviour.

This thesis is just a drop in the ocean of frustrated classical magnetism. There are many possible paths one might take, one could always deploy the machine learning framework to study a wide range of material-inspired model Hamiltonians and discover a plethora of unconventional phases. On the other hand, one could also ponder upon the experimental signatures or consequences of these phases on dynamics and transport and study the classical expected behaviours of experimental quantities such that one can then distinguish between truly quantum features and classical imprints in realistic experiments. This is just the start in exploration of new and exciting physics of frustrated magnetism.

Bibliography

[1] This is a similar to the mapping between the ferromagnetic and anti-ferromagnetic Heisenberg model on a bipartite lattice.

[2] Mykola Abramchuk et al. "Cu2IrO3: A New Magnetically Frustrated Honeycomb Iridate". In: *Journal of the American Chemical Society* 139.43 (Nov. 2017). Publisher: American Chemical Society, pp. 15371–15376. ISSN: 0002-7863. DOI: 10.1021/jacs.7b06911. URL: https://doi.org/10.1021/jacs.7b06911.

[3] Ian Affleck et al. "Rigorous results on valence-bond ground states in antiferromagnets". In: *Phys. Rev. Lett.* 59 (7 1987), pp. 799–802. DOI: 10.1103/PhysRevLett.59.799. URL: https://link.aps.org/doi/10.1103/PhysRevLett.59.799.

[4] Ian Affleck et al. "Valence bond ground states in isotropic quantum antiferromagnets". In: *Communications in Mathematical Physics* 115.3 (1988), pp. 477–528. DOI: 10.1007/BF01218021. URL: https://doi.org/10.1007/BF01218021.

[5] S. Agrestini et al. "Electronically highly cubic conditions for Ru in $\alpha - \mathbf{RuCl}_3$". In: *Phys. Rev. B* 96 (16 2017), p. 161107. DOI: 10.1103/PhysRevB.96.161107. URL: https://link.aps.org/doi/10.1103/PhysRevB.96.161107.

[6] P. W. Anderson. "Resonating valence bonds: A new kind of insulator?" In: *Materials Research Bulletin* 8.2 (1973), pp. 153–160. ISSN: 0025-5408. DOI: https://doi.org/10.1016/0025-5408(73)90167-0. URL: https://www.sciencedirect.com/science/article/pii/0025540873901670.

[7] V. P. Antropov, S. V. Tretyakov, and B. N. Harmon. "Spin dynamics in magnets: Quantum effects and numerical simulations (invited)". In: *Journal of Applied Physics* 81.8 (Apr. 1997), pp. 3961–3965. ISSN: 0021-8979. DOI: 10.1063/1.365023. URL: https://doi.org/10.1063/1.365023 (visited on 04/08/2023).

[8] K. Aoyama and H. Kawamura. "Spin Current as a Probe of the Vortex Topological Transition in the Classical Heisenberg Antiferromagnet on the Triangular Lattice". In: *Physical Review Letters* 124.4 (2020). DOI: 10.1103/physrevlett.124.047202. URL: https://doi.org/10.1103%2Fphysrevlett.124.047202.

[9] Kazushi Aoyama and Hikaru Kawamura. "Effects of magnetic anisotropy on spin and thermal transport in classical antiferromagnets on the square lattice". In: *Phys. Rev. B* 100 (14 2019), p. 144416. DOI: 10.1103/PhysRevB.100.144416. URL: https://link.aps.org/doi/10.1103/PhysRevB.100.144416.

[10] S. Bachus et al. *Angle-dependent thermodynamics of α-$RuCl_3$*. 2021. arXiv: 2101.07275 [cond-mat.str-el].

[11] S. Bachus et al. "Thermodynamic Perspective on Field-Induced Behavior of $\alpha-\mathrm{RuCl}_3$". In: *Phys. Rev. Lett.* 125 (9 2020), p. 097203. DOI: 10.1103/PhysRevLett.125.097203. URL: https://link.aps.org/doi/10.1103/PhysRevLett.125.097203.

[12] S.-H. Baek et al. "Evidence for a Field-Induced Quantum Spin Liquid in α-RuCl_3". In: *Phys. Rev. Lett.* 119 (3 2017), p. 037201. DOI: 10.1103/PhysRevLett.119.037201. URL: https://link.aps.org/doi/10.1103/PhysRevLett.119.037201.

[13] Leon Balents. "Spin liquids in frustrated magnets". In: *Nature* 464.7286 (Mar. 2010), pp. 199–208. ISSN: 1476-4687. DOI: 10.1038/nature08917. URL: https://doi.org/10.1038/nature08917.

[14] A. Banerjee et al. "Proximate Kitaev quantum spin liquid behaviour in a honeycomb magnet". In: *Nat. Mater.* 15 (2016), pp. 733–740. DOI: 10.1038/nmat4604.

[15] Arnab Banerjee et al. "Excitations in the field-induced quantum spin liquid state of -RuCl3". In: *npj Quantum Materials* 3.1 (Feb. 2018), p. 8. ISSN: 2397-4648. DOI: 10.1038/s41535-018-0079-2. URL: https://doi.org/10.1038/s41535-018-0079-2.

[16] Arnab Banerjee et al. "Neutron scattering in the proximate quantum spin liquid -RuCl3". In: *Science* 356.6342 (June 2017). Publisher: American Association for the Advancement of Science, pp. 1055–1059. DOI: 10.1126/science.aah6015. URL: https://doi.org/10.1126/science.aah6015 (visited on 07/26/2023).

[17] G. Baskaran, Diptiman Sen, and R. Shankar. "Spin-*S* Kitaev model: Classical ground states, order from disorder, and exact correlation functions". In: *Phys. Rev. B* 78 (11 2008), p. 115116. DOI: 10.1103/PhysRevB.78.115116. URL: https://link.aps.org/doi/10.1103/PhysRevB.78.115116.

[18] G. Bastien et al. "Pressure-induced dimerization and valence bond crystal formation in the Kitaev-Heisenberg magnet $\alpha-RuCl_3$". In: *Phys. Rev. B* 97 (24 2018), p. 241108. DOI: 10.1103/PhysRevB.97.241108. URL: https://link.aps.org/doi/10.1103/PhysRevB.97.241108.

[19] C. D. Batista, G. Ortiz, and J. E. Gubernatis. "Unveiling order behind complexity: Coexistence of ferromagnetism and Bose-Einstein condensation". In: *Phys. Rev. B* 65 (18 2002), p. 180402. DOI: 10.1103/PhysRevB.65.180402. URL: https://link.aps.org/doi/10.1103/PhysRevB.65.180402.

[20] David Bauer. *Atomistic Spin-Dynamics in Confined Magnetic Nano-Structures*. 2008.

[21] R. J. Baxter. "Colorings of a Hexagonal Lattice". In: *Journal of Mathematical Physics* 11.3 (1970), pp. 784–789. DOI: 10.1063/1.1665210. URL: https://doi.org/10.1063/1.1665210.

[22] Bernd A. Berg. *Introduction to Markov Chain Monte Carlo Simulations and their Statistical Analysis*. 2004. arXiv: cond-mat/0410490 [cond-mat.stat-mech].

[23] J. D. Bernal and R. H. Fowler. "A Theory of Water and Ionic Solution, with Particular Reference to Hydrogen and Hydroxyl Ions". In: 1.8 (Aug. 1933), pp. 515–548. DOI: 10.1063/1.1749327.

[24] Alexander J. Smola Bernhard Scholkopf. *Learning with kernels: sup- port vector machines, regularization, optimization, and beyond*. MIT press, Cambridge, MA, 2001.

[25] Sebastian Bette et al. "Solution of the heavily stacking faulted crystal structure of the honeycomb iridate H3LiIr2O6". In: *Dalton Transactions* 46.44 (2017). Publisher: The Royal Society of Chemistry, pp. 15216–15227. ISSN: 1477-9226. DOI: 10.1039/C7DT02978K. URL: http://dx.doi.org/10.1039/C7DT02978K.

[26] A. Biffin et al. "Noncoplanar and Counterrotating Incommensurate Magnetic Order Stabilized by Kitaev Interactions in $\gamma-Li_2IrO_3$". In: *Phys. Rev. Lett.* 113 (19 2014), p. 197201. DOI: 10.1103/PhysRevLett.113.197201. URL: https://link.aps.org/doi/10.1103/PhysRevLett.113.197201.

[27] Aleksey Bilogur. "Kernels and support vector machine regularization". In: (2018). URL: https://www.kaggle.com/code/residentmario/kernels-and-support-vector-machine-regularization.

[28] Annabelle Bohrdt et al. "Classifying snapshots of the doped Hubbard model with machine learning". In: *Nature Physics* 15.9 (2019), pp. 921–924. DOI: 10.1038/s41567-019-0565-x. URL: https://doi.org/10.1038/s41567-019-0565-x.

[29] LUDWIG BOLTZMANN. *Kinetic Theory*. 2003.

[30] P. W. Bridgman. "Note on the Principle of Detailed Balancing". In: *Phys. Rev.* 31 (1 1928), pp. 101–102. DOI: 10.1103/PhysRev.31.101. URL: https://link.aps.org/doi/10.1103/PhysRev.31.101.

[31] Frank R. Brown and Thomas J. Woch. "Overrelaxed heat-bath and Metropolis algorithms for accelerating pure gauge Monte Carlo calculations". In: *Phys. Rev. Lett.* 58 (23 1987), pp. 2394–2396. DOI: 10.1103/PhysRevLett.58.2394. URL: https://link.aps.org/doi/10.1103/PhysRevLett.58.2394.

[32] H. B. Cao et al. "Low-temperature crystal and magnetic structure of $\alpha - RuCl_3$". In: *Phys. Rev. B* 93 (13 2016), p. 134423. DOI: 10.1103/PhysRevB.93.134423. URL: https://link.aps.org/doi/10.1103/PhysRevB.93.134423.

[33] Luca Capriotti, Adolfo E. Trumper, and Sandro Sorella. "Long-Range N\'eel Order in the Triangular Heisenberg Model". In: *PRL* 82.19 (May 1999). Publisher: American Physical Society, pp. 3899–3902. DOI: 10.1103/PhysRevLett.82.3899. URL: https://link.aps.org/doi/10.1103/PhysRevLett.82.3899.

[34] Giuseppe Carleo and Matthias Troyer. "Solving the quantum many-body problem with artificial neural networks". In: *Science* 355.6325 (2017), pp. 602–606. ISSN: 0036-8075. DOI: 10.1126/science.aag2302. URL: http://science.sciencemag.org/content/355/6325/602.

[35] Giuseppe Carleo et al. "Machine learning and the physical sciences". In: *Rev. Mod. Phys.* 91 (4 2019), p. 045002. DOI: 10.1103/RevModPhys.91.045002. URL: https://link.aps.org/doi/10.1103/RevModPhys.91.045002.

[36] Caitlin Carnahan, Yinhan Zhang, and Di Xiao. "Thermal Hall effect of chiral spin fluctuations". In: *Phys. Rev. B* 103 (22 2021), p. 224419. DOI: 10.1103/PhysRevB.103.224419. URL: https://link.aps.org/doi/10.1103/PhysRevB.103.224419.

[37] Juan Carrasquilla. "Machine learning for quantum matter". In: *Advances in Physics: X* 5.1 (2020), p. 1797528. DOI: 10.1080/23746149.2020.1797528. URL: https://doi.org/10.1080/23746149.2020.1797528.

[38] C. Castelnovo, R. Moessner, and S. L. Sondhi. "Magnetic monopoles in spin ice". In: *Nature* 451.7174 (2008), pp. 42–45. DOI: 10.1038/nature06433. URL: https://doi.org/10.1038%2Fnature06433.

[39] J. Chaloupka and G. Khaliullin. "Hidden symmetries of the extended Kitaev-Heisenberg model: Implications for the honeycomb-lattice iridates A_2IrO_3". In: *Phys. Rev. B* 92 (2 2015), p. 024413. DOI: 10.1103/PhysRevB.92.024413. URL: https://link.aps.org/doi/10.1103/PhysRevB.92.024413.

[40] Jiri Chaloupka, George Jackeli, and Giniyat Khaliullin. "Zigzag Magnetic Order in the Iridium Oxide Na_2IrO_3". In: *Phys. Rev. Lett.* 110 (9 2013), p. 097204. DOI: 10.1103/PhysRevLett.110.097204. URL: https://link.aps.org/doi/10.1103/PhysRevLett.110.097204.

[41] Jiří Chaloupka, George Jackeli, and Giniyat Khaliullin. "Kitaev-Heisenberg Model on a Honeycomb Lattice: Possible Exotic Phases in Iridium Oxides A_2IrO_3". In: *Phys. Rev. Lett.* 105 (2 2010), p. 027204. DOI: 10.1103/PhysRevLett.105.027204. URL: https://link.aps.org/doi/10.1103/PhysRevLett.105.027204.

[42] Chih-Chung Chang and Chih-Jen Lin. "LIBSVM: A Library for Support Vector Machines". In: *ACM Trans. Intell. Syst. Technol.* 2.3 (2011). ISSN: 2157-6904. DOI: 10.1145/1961189.1961199. URL: https://doi.org/10.1145/1961189.1961199.

[43] Chih-Chung Chang and Chih-Jen Lin. "Training v-Support Vector Classifiers: Theory and Algorithms". In: *Neural Computation* 13.9 (Sept. 2001), pp. 2119–2147. ISSN: 0899-7667. DOI: 10.1162/089976601750399335. URL: https://doi.org/10.1162/089976601750399335 (visited on 04/08/2023).

[44] Xie Chen, Zheng-Cheng Gu, and Xiao-Gang Wen. "Classification of gapped symmetric phases in one-dimensional spin systems". In: *Phys. Rev. B* 83 (3 2011), p. 035107. DOI: 10.1103/PhysRevB.83.035107. URL: https://link.aps.org/doi/10.1103/PhysRevB.83.035107.

[45] Li Ern Chern et al. "Magnetic field induced competing phases in spin-orbital entangled Kitaev magnets". In: *Physical Review Research* 2.1 (2020). DOI: 10.1103/physrevresearch.2.013014. URL: https://doi.org/10.1103%2Fphysrevresearch.2.013014.

[46] A. L. Chernyshev and M. E. Zhitomirsky. "Spin waves in a triangular lattice antiferromagnet: Decays, spectrum renormalization, and singularities". In: *Phys. Rev. B* 79 (14 2009), p. 144416. DOI: 10.1103/PhysRevB.79.144416. URL: https://link.aps.org/doi/10.1103/PhysRevB.79.144416.

[47] S. K. Choi et al. "Spin Waves and Revised Crystal Structure of Honeycomb Iridate Na_2IrO_3". In: *Phys. Rev. Lett.* 108 (12 2012), p. 127204. DOI: 10.1103/PhysRevLett.108.127204. URL: https://link.aps.org/doi/10.1103/PhysRevLett.108.127204.

[48] J. Patrick Clancy et al. "Pressure-driven collapse of the relativistic electronic ground state in a honeycomb iridate". In: *npj Quantum Materials* 3.1 (Aug. 2018), p. 35. ISSN: 2397-4648. DOI: 10.1038/s41535-018-0109-0. URL: https://doi.org/10.1038/s41535-018-0109-0.

[49] R. Comin et al. "Na_2IrO_3 as a Novel Relativistic Mott Insulator with a 340-meV Gap". In: *Phys. Rev. Lett.* 109 (26 2012), p. 266406. DOI: 10.1103/PhysRevLett.109.266406. URL: https://link.aps.org/doi/10.1103/PhysRevLett.109.266406.

[50] Corinna Cortes and Vladimir Vapnik. "Support-vector networks". In: *Machine Learning* 20.3 (Sept. 1995), pp. 273–297. ISSN: 1573-0565. DOI: 10.1007/BF00994018. URL: https://doi.org/10.1007/BF00994018.

[51] Michael Creutz. "Monte Carlo study of quantized SU(2) gauge theory". In: *Phys. Rev. D* 21 (8 1980), pp. 2308–2315. DOI: 10.1103/PhysRevD.21.2308. URL: https://link.aps.org/doi/10.1103/PhysRevD.21.2308.

[52] Michael Creutz. "Overrelaxation and Monte Carlo simulation". In: *Phys. Rev. D* 36 (2 1987), pp. 515–519. DOI: 10.1103/PhysRevD.36.515. URL: https://link.aps.org/doi/10.1103/PhysRevD.36.515.

[53] Kurt Binder David Landau. *A Guide to Monte Carlo Simulations in Statistical Physics*. Cambridge University Press, Cambridge U.K. 4th edition, 2004.

[54] Dong-Ling Deng, Xiaopeng Li, and S. Das Sarma. "Quantum Entanglement in Neural Network States". In: *Phys. Rev. X* 7 (2 2017), p. 021021. DOI: 10.1103/PhysRevX.7.021021. URL: https://link.aps.org/doi/10.1103/PhysRevX.7.021021.

[55] Seung-Hwan Do et al. "Majorana fermions in the Kitaev quantum spin system -RuCl3". In: *Nature Physics* 13.11 (Nov. 2017), pp. 1079–1084. ISSN: 1745-2481. DOI: 10.1038/nphys4264. URL: https://doi.org/10.1038/nphys4264.

[56] Cora Dvorkin et al. *Machine Learning and Cosmology*. 2022. arXiv: 2203.08056 [hep-ph].

[57] Miroslav Fiedler. "A property of eigenvectors of nonnegative symmetric matrices and its application to graph theory". In: *Czechoslovak Mathematical Journal* 25.4 (1975), pp. 619–633. URL: http://eudml.org/doc/12900.

[58] Miroslav Fiedler. "Algebraic connectivity of graphs". In: *Czechoslovak Mathematical Journal* 23.2 (1973), pp. 298–305. URL: http://eudml.org/doc/12723.

[59] J. B. Fouet, P. Sindzingre, and C. Lhuillier. "An investigation of the quantum J1-J2-J3model on the honeycomb lattice". In: *The European Physical Journal B - Condensed Matter and Complex Systems* 20.2 (2001), pp. 241–254. DOI: 10.1007/s100510170273. URL: https://doi.org/10.1007/s100510170273.

[60] L. Frangou et al. "Enhanced Spin Pumping Efficiency in Antiferromagnetic IrMn Thin Films around the Magnetic Phase Transition". In: *Phys. Rev. Lett.* 116 (7 2016), p. 077203. DOI: 10.1103/PhysRevLett.116.077203. URL: https://link.aps.org/doi/10.1103/PhysRevLett.116.077203.

[61] Oliver Franke et al. "Thermal spin dynamics of Kitaev magnets: Scattering continua and magnetic field induced phases within a stochastic semiclassical approach". In: *Physical Review B* 106.17 (2022). DOI: 10.1103/physrevb.106.174428. URL: https://doi.org/10.1103%2Fphysrevb.106.174428.

[62] F. Freund et al. "Single crystal growth from separated educts and its application to lithium transition-metal oxides". In: *Scientific Reports* 6.1 (Oct. 2016), p. 35362. ISSN: 2045-2322. DOI: 10.1038/srep35362. URL: https://doi.org/10.1038/srep35362.

[63] S. Fujiyama et al. "Two-Dimensional Heisenberg Behavior of J_{eff}=1/2 Isospins in the Paramagnetic State of the Spin-Orbital Mott Insulator Sr_2IrO_4". In: *Phys. Rev. Lett.* 108 (24 2012), p. 247212. DOI: 10.1103/PhysRevLett.108.247212. URL: https://link.aps.org/doi/10.1103/PhysRevLett.108.247212.

[64] Irene S. Gabashvili. *The impact and applications of ChatGPT: a systematic review of literature reviews*. 2023. arXiv: 2305.18086 [cs.CY].

[65] S Gass et al. "Field-induced phase transitions of the Kitaev material $\alpha-RuCl_3$ probed by thermal expansion and magnetostriction". In: *arXiv preprint arXiv:2003.07081* (2020).

[66] A. K. Geim and K. S. Novoselov. "The rise of graphene". In: *Nature Materials* 6.3 (Mar. 2007), pp. 183–191. ISSN: 1476-4660. DOI: 10.1038/nmat1849. URL: https://doi.org/10.1038/nmat1849.

[67] Thomas L. Gilbert. "A phenomenological theory of damping in ferromagnetic materials". In: *IEEE Transactions on Magnetics* 40 (2004), pp. 3443–3449. URL: https://api.semanticscholar.org/CorpusID:35628797.

[68] Steven M. Girvin and Kun Yang. *Modern Condensed Matter Physics*. Cambridge: Cambridge University Press, 2019. ISBN: 978-1-107-13739-4. DOI: 10.1017/9781316480649. URL: https://www.cambridge.org/core/books/modern-condensed-matter-physics.

[69] O. Gladii et al. "Unraveling the influence of electronic and magnonic spin-current injection near the magnetic ordering transition of IrMn metallic antiferromagnets". In: *Physical Review B* 98.9 (2018). DOI: 10.1103/physrevb.98.094422. URL: https://doi.org/10.1103%2Fphysrevb.98.094422.

[70] Matthias Gohlke et al. "Dynamics of the Kitaev-Heisenberg Model". In: *Phys. Rev. Lett.* 119 (15 2017), p. 157203. DOI: 10.1103/PhysRevLett.119.157203. URL: https://link.aps.org/doi/10.1103/PhysRevLett.119.157203.

[71] Matthias Gohlke et al. "Emergence of a nematic paramagnet via quantum order-by-disorder and pseudo-Goldstone modes in Kitaev magnets". In: *arXiv preprint arXiv:2003.11876* (2020).

[72] Matthias Gohlke et al. "Quantum spin liquid signatures in Kitaev-like frustrated magnets". In: *Phys. Rev. B* 97 (7 2018), p. 075126. DOI: 10.1103/PhysRevB.97.075126. URL: https://link.aps.org/doi/10.1103/PhysRevB.97.075126.

[73] Jacob S. Gordon et al. "Theory of the field-revealed Kitaev spin liquid". In: *Nature Communications* 10.1 (2019), p. 2470. DOI: 10.1038/s41467-019-10405-8. URL: https://doi.org/10.1038/s41467-019-10405-8.

[74] Gpeyre. "Fielder Clustering". In: (2020). URL: https://commons.wikimedia.org/wiki/File:Fiedler_Vector.webm.

[75] Jonas Greitemann, Ke Liu, and Lode Pollet. "Probing hidden spin order with interpretable machine learning". In: *Phys. Rev. B* 99 (6 2019), 060404(R). DOI: 10.1103/PhysRevB.99.060404. URL: https://link.aps.org/doi/10.1103/PhysRevB.99.060404.

[76] Jonas Greitemann, Ke Liu, and Lode Pollet. "The view of TK-SVM on the phase hierarchy in the classical kagome Heisenberg antiferromagnet". In: *Journal of Physics: Condensed Matter* 33.5 (2021), p. 054002. DOI: 10.1088/1361-648x/abbe7b. URL: https://doi.org/10.1088/1361-648x/abbe7b.

[77] Jonas Greitemann et al. "Identification of emergent constraints and hidden order in frustrated magnets using tensorial kernel methods of machine learning". In: *Phys. Rev. B* 100 (17 2019), p. 174408. DOI: 10.1103/PhysRevB.100.174408. URL: https://link.aps.org/doi/10.1103/PhysRevB.100.174408.

[78] H. Gretarsson et al. "Crystal-Field Splitting and Correlation Effect on the Electronic Structure of A_2IrO_3". In: *Phys. Rev. Lett.* 110 (7 2013), p. 076402. DOI: 10.1103/PhysRevLett.110.076402. URL: https://link.aps.org/doi/10.1103/PhysRevLett.110.076402.

[79] Zheng-Cheng Gu and Xiao-Gang Wen. "Tensor-entanglement-filtering renormalization approach and symmetry-protected topological order". In: *Phys. Rev. B* 80 (15 2009), p. 155131. DOI: 10.1103/PhysRevB.80.155131. URL: https://link.aps.org/doi/10.1103/PhysRevB.80.155131.

[80] Jung Hoon Han and Hyunyong Lee. "Spin Chirality and Hall-Like Transport Phenomena of Spin Excitations". In: *Journal of the Physical Society of Japan* 86.1 (2017), p. 011007. DOI: 10.7566/jpsj.86.011007. URL: https://doi.org/10.7566%2Fjpsj.86.011007.

[81] C. L. Henley. "Power-law spin correlations in pyrochlore antiferromagnets". In: *Phys. Rev. B* 71 (1 2005), p. 014424. DOI: 10.1103/PhysRevB.71.014424. URL: https://link.aps.org/doi/10.1103/PhysRevB.71.014424.

[82] Jan Hermann, Zeno Schätzle, and Frank Noé. "Deep-neural-network solution of the electronic Schrödinger equation". In: *Nature Chemistry* 12.10 (2020), pp. 891–897. DOI: 10.1038/s41557-020-0544-y. URL: https://doi.org/10.1038/s41557-020-0544-y.

[83] V. Hermann et al. "Competition between spin-orbit coupling, magnetism, and dimerization in the honeycomb iridates: $\alpha - Li_2IrO_3$ under pressure". In: *Phys. Rev. B* 97 (2 2018), p. 020104. DOI: 10.1103/PhysRevB.97.020104. URL: https://link.aps.org/doi/10.1103/PhysRevB.97.020104.

[84] Ciarán Hickey and Simon Trebst. "Emergence of a field-driven U(1) spin liquid in the Kitaev honeycomb model". In: *Nature Communications* 10.1 (2019), p. 530. DOI: 10.1038/s41467-019-08459-9. URL: https://doi.org/10.1038/s41467-019-08459-9.

[85] Ciarán Hickey et al. "Field-Driven Gapless Spin Liquid in the Spin-1 Kitaev Honeycomb Model". In: *arXiv preprint arXiv:2001.07699* (2020).

[86] Chih-Wei Hsu and Chih-Jen Lin. "A comparison of methods for multiclass support vector machines". In: *IEEE Transactions on Neural Networks* 13.2 (2002), pp. 415–425. DOI: 10.1109/72.991427.

[87] Wen-Jun Hu et al. "Competing spin-liquid states in the spin-$\frac{1}{2}$ Heisenberg model on the triangular lattice". In: *Physical Review B* 92.14 (Oct. 2015). Publisher: American Physical Society, p. 140403. DOI: 10.1103/PhysRevB.92.140403. URL: https://link.aps.org/doi/10.1103/PhysRevB.92.140403.

[88] D. L. Huber. "Thermal Conductivity of a Heisenberg Chain*)". In: *Progress of Theoretical Physics* 39.5 (May 1968), pp. 1170–1179. ISSN: 0033-068X. DOI: 10.1143/ptp/39.5.1170. URL: https://doi.org/10.1143/ptp/39.5.1170 (visited on 04/08/2023).

[89] Koji Hukushima and Koji Nemoto. "Exchange Monte Carlo Method and Application to Spin Glass Simulations". In: *Journal of the Physical Society of Japan* 65.6 (1996), pp. 1604–1608. DOI: 10.1143/JPSJ.65.1604. URL: https://doi.org/10.1143/JPSJ.65.1604.

[90] David A. Huse and Veit Elser. "Simple Variational Wave Functions for Two-Dimensional Heisenberg Spin-\textonehalf{} Antiferromagnets". In: *Physical Review Letters* 60.24 (June 1988). Publisher: American Physical Society, pp. 2531–2534. DOI: 10.1103/PhysRevLett.60.2531. URL: https://link.aps.org/doi/10.1103/PhysRevLett.60.2531.

[91] S. Iida. "The difference between gilbert's and landau-lifshitz's equations". In: *Journal of Physics and Chemistry of Solids* 24.5 (May 1963), pp. 625–630. ISSN: 0022-3697. DOI: 10.1016/S0022-3697(63)80004-9. URL: https://www.sciencedirect.com/science/article/pii/S0022369763800049.

[92] Rusna J., D. Gotfryd, and J. Chaloupka. "Kitaev-like honeycomb magnets: Global phase behavior and emergent effective models". In: *Phys. Rev. B* 99 (6 2019), p. 064425. DOI: 10.1103/PhysRevB.99.064425. URL: https://link.aps.org/doi/10.1103/PhysRevB.99.064425.

[93] G. Jackeli and G. Khaliullin. "Mott Insulators in the Strong Spin-Orbit Coupling Limit: From Heisenberg to a Quantum Compass and Kitaev Models". In: *Phys. Rev. Lett.* 102 (1 2009), p. 017205. DOI: 10.1103/PhysRevLett.102.017205. URL: https://link.aps.org/doi/10.1103/PhysRevLett.102.017205.

[94] G. Jackeli and G. Khaliullin. "Mott Insulators in the Strong Spin-Orbit Coupling Limit: From Heisenberg to a Quantum Compass and Kitaev Models". In: *Phys. Rev. Lett.* 102 (1 2009), p. 017205. DOI: 10.1103/PhysRevLett.102.017205. URL: https://link.aps.org/doi/10.1103/PhysRevLett.102.017205.

[95] Seong-Hoon Jang et al. "Antiferromagnetic Kitaev interaction in f-electron based honeycomb magnets". In: *Phys. Rev. B* 99 (24 2019), p. 241106. DOI: 10.1103/PhysRevB.99.241106. URL: https://link.aps.org/doi/10.1103/PhysRevB.99.241106.

[96] Lukas Janssen, Eric C. Andrade, and Matthias Vojta. "Honeycomb-Lattice Heisenberg-Kitaev Model in a Magnetic Field: Spin Canting, Metamagnetism, and Vortex Crystals". In: *Phys. Rev. Lett.* 117 (27 2016), p. 277202. DOI: 10.1103/PhysRevLett.117.277202. URL: https://link.aps.org/doi/10.1103/PhysRevLett.117.277202.

[97] Lukas Janssen and Matthias Vojta. "Heisenberg-Kitaev physics in magnetic fields". In: *J. Phys.: Condens. Matter* 31.42 (2019), p. 423002. DOI: 10.1088/1361-648x/ab283e.

[98] Paul Niklas Jepsen et al. "Spin transport in a tunable Heisenberg model realized with ultracold atoms". In: *Nature* 588.7838 (2020), pp. 403–407. DOI: 10.1038/s41586-020-3033-y. URL: https://doi.org/10.1038/s41586-020-3033-y.

[99] Hong-Chen Jiang et al. "Possible proximity of the Mott insulating iridate Na_2IrO_3 to a topological phase: Phase diagram of the Heisenberg-Kitaev model in a magnetic field". In: *Phys. Rev. B* 83 (24 2011), p. 245104. DOI: 10.1103/PhysRevB.83.245104. URL: https://link.aps.org/doi/10.1103/PhysRevB.83.245104.

[100] Yi-Fan Jiang, Thomas P. Devereaux, and Hong-Chen Jiang. "Field-induced quantum spin liquid in the Kitaev-Heisenberg model and its relation to $\alpha-RuCl_3$". In: *Phys. Rev. B* 100 (16 2019), p. 165123. DOI: 10.1103/PhysRevB.100.165123. URL: https://link.aps.org/doi/10.1103/PhysRevB.100.165123.

[101] R. D. Johnson et al. "Monoclinic crystal structure of $\alpha - RuCl_3$ and the zigzag antiferromagnetic ground state". In: *Phys. Rev. B* 92 (23 2015), p. 235119. DOI: 10.1103/PhysRevB.92.235119. URL: https://link.aps.org/doi/10.1103/PhysRevB.92.235119.

[102] Y. Kasahara et al. "Majorana quantization and half-integer thermal quantum Hall effect in a Kitaev spin liquid". In: *Nature* 559.7713 (July 2018), pp. 227–231. ISSN: 1476-4687. DOI: 10.1038/s41586-018-0274-0. URL: https://doi.org/10.1038/s41586-018-0274-0.

[103] Y. Kasahara et al. "Majorana quantization and half-integer thermal quantum Hall effect in a Kitaev spin liquid". In: *Nature* 559.7713 (2018), pp. 227–231. DOI: 10.1038/s41586-018-0274-0. URL: https://doi.org/10.1038/s41586-018-0274-0.

[104] Y. Kasahara et al. "Unusual Thermal Hall Effect in a Kitaev Spin Liquid Candidate $\alpha-RuCl_3$". In: *Phys. Rev. Lett.* 120 (21 2018), p. 217205. DOI: 10.1103/PhysRevLett.120.217205. URL: https://link.aps.org/doi/10.1103/PhysRevLett.120.217205.

[105] P. W. Kasteleyn. "Dimer Statistics and Phase Transitions". In: *Journal of Mathematical Physics* 4.2 (1963), pp. 287–293. DOI: 10.1063/1.1703953. URL: https://doi.org/10.1063/1.1703953.

[106] Yasuyuki Kato, Satoru Hayami, and Yukitoshi Motome. "Spin excitation spectra in helimagnetic states: Proper-screw, cycloid, vortex-crystal, and hedgehog lattices". In: *Phys. Rev. B* 104 (22 2021), p. 224405. DOI: 10.1103/PhysRevB.104.224405. URL: https://link.aps.org/doi/10.1103/PhysRevB.104.224405.

[107] Vamshi M Katukuri et al. "Kitaev interactions between j = 1/2 moments in honeycomb Na2IrO3 are large and ferromagnetic: insights from ab initio quantum chemistry calculations". In: *New Journal of Physics* 16.1 (Jan. 2014). Publisher: IOP Publishing, p. 013056. ISSN: 1367-2630. DOI: 10.1088/1367-2630/16/1/013056. URL: https://dx.doi.org/10.1088/1367-2630/16/1/013056.

[108] Tom Kennedy and Hal Tasaki. "Hidden symmetry breaking and the Haldane phase inS=1 quantum spin chains". In: *Communications in Mathematical Physics* 147.3 (1992), pp. 431–484. DOI: 10.1007/BF02097239. URL: https://doi.org/10.1007/BF02097239.

[109] Tom Kennedy and Hal Tasaki. "Hidden Z_2Z_2 symmetry breaking in Haldane-gap antiferromagnets". In: *Phys. Rev. B* 45 (1 1992), pp. 304–307. DOI: 10.1103/PhysRevB.45.304. URL: https://link.aps.org/doi/10.1103/PhysRevB.45.304.

[110] Giniyat Khaliullin. "Orbital Order and Fluctuations in Mott Insulators". In: *Progress of Theoretical Physics Supplement* 160 (June 2005), pp. 155–202. ISSN: 0375-9687. DOI: 10.1143/PTPS.160.155. URL: https://doi.org/10.1143/PTPS.160.155.

[111] Giniyat Khaliullin and Satoshi Okamoto. "Quantum Behavior of Orbitals in Ferromagnetic Titanates: Novel Orderings and Excitations". In: *Phys. Rev. Lett.* 89 (16 2002), p. 167201. DOI: 10.1103/PhysRevLett.89.167201. URL: https://link.aps.org/doi/10.1103/PhysRevLett.89.167201.

[112] Daniel Khomskii. "Classifying multiferroics: Mechanisms and effects". In: *Physics* 2 (2009), p. 20.

[113] B. J. Kim et al. "Novel $J_{\text{eff}} = 1/2$ Mott State Induced by Relativistic Spin-Orbit Coupling in Sr_2IrO_4". In: *Phys. Rev. Lett.* 101 (7 2008), p. 076402. DOI: 10.1103/PhysRevLett.101.076402. URL: https://link.aps.org/doi/10.1103/PhysRevLett.101.076402.

[114] B. J. Kim et al. "Phase-Sensitive Observation of a Spin-Orbital Mott State in Sr2IrO4". In: *Science* 323.5919 (Mar. 2009). Publisher: American Association for the Advancement of Science, pp. 1329–1332. DOI: 10.1126/science.1167106. URL: https://doi.org/10.1126/science.1167106 (visited on 07/26/2023).

[115] Heung-Sik Kim and Hae-Young Kee. "Crystal structure and magnetism in $\alpha-RuCl_3$: An ab initio study". In: *Phys. Rev. B* 93 (15 2016), p. 155143. DOI: 10.1103/PhysRevB.93.155143. URL: https://link.aps.org/doi/10.1103/PhysRevB.93.155143.

[116] Itamar Kimchi and Yi-Zhuang You. "Kitaev-Heisenberg-J_2-J_3 model for the iridates A_2IrO_3". In: *Phys. Rev. B* 84 (18 2011), p. 180407. DOI: 10.1103/PhysRevB.84.180407. URL: https://link.aps.org/doi/10.1103/PhysRevB.84.180407.

[117] Itamar Kimchi et al. "Scaling and data collapse from local moments in frustrated disordered quantum spin systems". In: *Nature Communications* 9.1 (Oct. 2018), p. 4367. ISSN: 2041-1723. DOI: 10.1038/s41467-018-06800-2. URL: https://doi.org/10.1038/s41467-018-06800-2.

[118] T. Kimura. "Spiral Magnets as Magnetoelectrics". In: *Annual Review of Materials Research* 37.1 (2007), pp. 387–413. DOI: 10.1146/annurev.matsci.37.052506.084259. URL: https://doi.org/10.1146/annurev.matsci.37.052506.084259.

[119] Alexei Kitaev. "Anyons in an exactly solved model and beyond". In: *January Special Issue* 321.1 (Jan. 2006), pp. 2–111. ISSN: 0003-4916. DOI: 10.1016/j.aop.2005.10.005. URL: https://www.sciencedirect.com/science/article/pii/S0003491605002381.

[120] K. Kitagawa et al. "A spin–orbital-entangled quantum liquid on a honeycomb lattice". In: *Nature* 554.7692 (Feb. 2018), pp. 341–345. ISSN: 1476-4687. DOI: 10.1038/nature25482. URL: https://doi.org/10.1038/nature25482.

[121] Klos. *Magnonics and Confinement of Light in Photonic–Magnonic Crystals*. 2021.

[122] M. Krech, Alex Bunker, and D.P. Landau. "Fast spin dynamics algorithms for classical spin systems". In: *Computer Physics Communications* 111.1-3 (1998), pp. 1–13. DOI: 10.1016/s0010-4655(98)00009-5. URL: https://doi.org/10.1016%2Fs0010-4655%2898%2900009-5.

[123] Ryogo Kubo. "Statistical-Mechanical Theory of Irreversible Processes. I. General Theory and Simple Applications to Magnetic and Conduction Problems". In: *Journal of the Physical Society of Japan* 12.6 (June 1957). Publisher: The Physical Society of Japan, pp. 570–586. ISSN: 0031-9015. DOI: 10.1143/JPSJ.12.570. URL: https://doi.org/10.1143/JPSJ.12.570 (visited on 08/04/2023).

[124] Ofer Lahav. *Deep Machine Learning in Cosmology: Evolution or Revolution?* 2023. arXiv: 2302.04324 [astro-ph.CO].

[125] C. K. Lai. "Lattice gas with nearest-neighbor interaction in one dimension with arbitrary statistics". In: *Journal of Mathematical Physics* 15.10 (1974), pp. 1675–1676. DOI: 10.1063/1.1666522. URL: https://doi.org/10.1063/1.1666522.

[126] Bella Lake et al. "Quantum criticality and universal scaling of a quantum antiferromagnet". In: *Nature Materials* 4.4 (2005), pp. 329–334. DOI: 10.1038/nmat1327. URL: https://doi.org/10.1038%2Fnmat1327.

[127] P. Lampen-Kelley et al. "Anisotropic susceptibilities in the honeycomb Kitaev system $\alpha-RuCl_3$". In: *Phys. Rev. B* 98 (10 2018), p. 100403. DOI: 10.1103/PhysRevB.98.100403. URL: https://link.aps.org/doi/10.1103/PhysRevB.98.100403.

[128] P Lampen-Kelley et al. "Field-induced intermediate phase in $\alpha-RuCl_3$: Non-coplanar order, phase diagram, and proximate spin liquid". In: *arXiv preprint arXiv:1807.06192* (2018).

[129] L. Landau. "The Theory of Phase Transitions". In: *Nature* 138.3498 (Nov. 1936), pp. 840–841. ISSN: 1476-4687. DOI: 10.1038/138840a0. URL: https://doi.org/10.1038/138840a0.

[130] L. Landau and E. Lifschitz. "3 - On the theory of the dispersion of magnetic permeability in ferromagnetic bodiesReprinted from Physikalische Zeitschrift der Sowjetunion 8, Part 2, 153, 1935." In: *Perspectives in Theoretical Physics*. Ed. by L.P. PITAEVSKI. Amsterdam: Pergamon, Jan. 1992, pp. 51–65. ISBN: 978-0-08-036364-6. DOI: 10.1016/B978-0-08-036364-6.50008-9. URL: https://www.sciencedirect.com/science/article/pii/B9780080363646500089.

[131] Pontus Laurell and Satoshi Okamoto. "Dynamical and thermal magnetic properties of the Kitaev spin liquid candidate $\alpha-RuCl_3$". In: *npj Quantum Materials* 5.1 (2020), p. 2. DOI: 10.1038/s41535-019-0203-y. URL: https://doi.org/10.1038/s41535-019-0203-y.

[132] Eric Kin-Ho Lee and Yong Baek Kim. "Theory of magnetic phase diagrams in hyperhoneycomb and harmonic-honeycomb iridates". In: *Phys. Rev. B* 91 (6 2015), p. 064407. DOI: 10.1103/PhysRevB.91.064407. URL: https://link.aps.org/doi/10.1103/PhysRevB.91.064407.

[133] Eric Kin-Ho Lee, Jeffrey G. Rau, and Yong Baek Kim. "Two iridates, two models, and two approaches: A comparative study on magnetism in three-dimensional honeycomb materials". In: *Phys. Rev. B* 93 (18 2016), p. 184420. DOI: 10.1103/PhysRevB.93.184420. URL: https://link.aps.org/doi/10.1103/PhysRevB.93.184420.

[134] Hyun-Yong Lee et al. "Magnetic field induced quantum phases in a tensor network study of Kitaev magnets". In: *Nature Communications* 11.1 (2020), p. 1639. DOI: 10.1038/s41467-020-15320-x. URL: https://doi.org/10.1038/s41467-020-15320-x.

[135] Hyunyong Lee, Jung Hoon Han, and Patrick A. Lee. "Thermal Hall effect of spins in a paramagnet". In: *Physical Review B* 91.12 (2015). DOI: 10.1103/physrevb.91.125413. URL: https://doi.org/10.1103%2Fphysrevb.91.125413.

[136] Jheng-Wei Li et al. *Tangle of Spin Double Helices in the Honeycomb Kitaev-Γ Model*. 2023. arXiv: 2206.08946 [cond-mat.str-el].

[137] Yao-Dong Li et al. "Effect of spin-orbit coupling on the effective-spin correlation in $YbMgGaO_4$". In: *Phys. Rev. B* 97 (12 2018), p. 125105. DOI: 10.1103/PhysRevB.97.125105. URL: https://link.aps.org/doi/10.1103/PhysRevB.97.125105.

[138] Hai-Jun Liao et al. "Differentiable Programming Tensor Networks". In: *Phys. Rev. X* 9 (3 2019), p. 031041. DOI: 10.1103/PhysRevX.9.031041. URL: https://link.aps.org/doi/10.1103/PhysRevX.9.031041.

[139] Qinghua Liao. "Chapter Four - Enhanced sampling and free energy calculations for protein simulations". In: *Progress in Molecular Biology and Translational Science*. Ed. by Birgit Strodel and Bogdan Barz. Vol. 170. Academic Press, Jan. 2020, pp. 177–213. ISBN: 1877-1173. DOI: 10.1016/bs.pmbts.2020.01.006. URL: https://www.sciencedirect.com/science/article/pii/S187711732030017X.

[140] Lin and Ye. "Support vector machine classifiers by non-Euclidean margins". In: *AIM Sciences* (2020). URL: https://www.aimsciences.org/article/doi/10.3934/mfc.2020018.

[141] Junwei Liu et al. "Self-learning Monte Carlo method". In: *Phys. Rev. B* 95 (4 2017), p. 041101. DOI: 10.1103/PhysRevB.95.041101. URL: https://link.aps.org/doi/10.1103/PhysRevB.95.041101.

[142] Ke Liu, Jonas Greitemann, and Lode Pollet. "Learning multiple order parameters with interpretable machines". In: *Phys. Rev. B* 99 (10 2019), p. 104410. DOI: 10.1103/PhysRevB.99.104410. URL: https://link.aps.org/doi/10.1103/PhysRevB.99.104410.

[143] Ke Liu et al. "Revealing the phase diagram of Kitaev materials by machine learning: Cooperation and competition between spin liquids". In: *Phys. Rev. Research* 3 (2 2021), p. 023016. DOI: 10.1103/PhysRevResearch.3.023016. URL: https://link.aps.org/doi/10.1103/PhysRevResearch.3.023016.

[144] X. Liu et al. "Long-range magnetic ordering in Na_2IrO_3". In: *Phys. Rev. B* 83 (22 2011), p. 220403. DOI: 10.1103/PhysRevB.83.220403. URL: https://link.aps.org/doi/10.1103/PhysRevB.83.220403.

[145] W. Low. "Electronic Phenomenon: Electron Paramagnetic Resonance of Transition Ions. A. Abragam and B. Bleaney. Clarendon (Oxford University Press), New York, 1970. xvi, 912 pp., illus. $41.50. International Series of Monographs on Physics." In: *Science* 171.3976 (Mar. 1971). Publisher: American Association for the Advancement of Science, pp. 1141–1141. DOI: 10.1126/science.171.3976.1141.a. URL: https://doi.org/10.1126/science.171.3976.1141.a (visited on 07/27/2023).

[146] G. D. Mahan. *Many-Particle Physics, third edition*. Springer Science+Business Media, New York, 2000.

[147] P. A. Maksimov and A. L. Chernyshev. "Rethinking $\alpha-RuCl_3$". In: *Phys. Rev. Research* 2 (3 2020), p. 033011. DOI: 10.1103/PhysRevResearch.2.033011. URL: https://link.aps.org/doi/10.1103/PhysRevResearch.2.033011.

[148] Saptarshi Mandal and Naveen Surendran. "Exactly solvable Kitaev model in three dimensions". In: *Phys. Rev. B* 79 (2 2009), p. 024426. DOI: 10.1103/PhysRevB.79.024426. URL: https://link.aps.org/doi/10.1103/PhysRevB.79.024426.

[149] A.A. Markov. "Extension of the law of large numbers to quantities, depending on each other (1906). Reprint." eng. In: *Journal Électronique d'Histoire des Probabilités et de la Statistique [electronic only]* 2.1b (2006), Article 10, 12 p., electronic only–Article 10, 12 p., electronic only. URL: http://eudml.org/doc/128778.

[150] P. A. McClarty et al. "Topological magnons in Kitaev magnets at high fields". In: *Physical Review B* 98.6 (2018). DOI: 10.1103/physrevb.98.060404. URL: https://doi.org/10.1103%2Fphysrevb.98.060404.

[151] Pankaj Mehta et al. "A high-bias, low-variance introduction to Machine Learning for physicists". In: *Physics Reports* 810 (2019). A high-bias, low-variance introduction to Machine Learning for physicists, pp. 1 –124. ISSN: 0370-1573. DOI: https://doi.org/10.1016/j.physrep.2019.03.001. URL: http://www.sciencedirect.com/science/article/pii/S0370157319300766.

[152] Nicholas Metropolis et al. "Equation of State Calculations by Fast Computing Machines". In: *The Journal of Chemical Physics* 21.6 (Dec. 2004), pp. 1087–1092. ISSN: 0021-9606. DOI: 10.1063/1.1699114. URL: https://doi.org/10.1063/1.1699114 (visited on 04/08/2023).

[153] Carl D. Meyer. *Matrix Analysis and Applied Linear Algebra*. USA: Society for Industrial and Applied Mathematics, 2000. ISBN: 0898714540.

[154] Mjpgngras. "Wikipedia Spin Ice". In: (2013). URL: https://en.wikipedia.org/wiki/Spin_ice.

[155] K. A. Modic et al. "Robust spin correlations at high magnetic fields in the harmonic honeycomb iridates". In: *Nature Communications* 8.1 (Aug. 2017), p. 180. ISSN: 2041-1723. DOI: 10.1038/s41467-017-00264-6. URL: https://doi.org/10.1038/s41467-017-00264-6.

[156] Alexander Mook et al. "Magnon transport in noncollinear spin textures: Anisotropies and topological magnon Hall effects". In: *Phys. Rev. B* 95 (2 2017), p. 020401. DOI: 10.1103/PhysRevB.95.020401. URL: https://link.aps.org/doi/10.1103/PhysRevB.95.020401.

[157] Hidekazu Morita, Shinji Watanabe, and Masatoshi Imada. "Nonmagnetic Insulating States near the Mott Transitions on Lattices with Geometrical Frustration and Implications for $\kappa-(ET)2Cu2(CN)3$". In: *Journal of the Physical Society of Japan* 71.9 (Sept. 2002). Publisher: The Physical Society of Japan, pp. 2109–2112. ISSN: 0031-9015. DOI: 10.1143/JPSJ.71.2109. URL: https://doi.org/10.1143/JPSJ.71.2109 (visited on 07/26/2023).

[158] Maxim Mostovoy. "Ferroelectricity in Spiral Magnets". In: *Phys. Rev. Lett.* 96 (6 2006), p. 067601. DOI: 10.1103/PhysRevLett.96.067601. URL: https://link.aps.org/doi/10.1103/PhysRevLett.96.067601.

[159] Yukitoshi Motome and Joji Nasu. "Hunting Majorana Fermions in Kitaev Magnets". In: *Journal of the Physical Society of Japan* 89.1 (2020), p. 012002. DOI: 10.7566/JPSJ.89.012002. URL: https://doi.org/10.7566/JPSJ.89.012002.

[160] J. Nasu et al. "Fermionic response from fractionalization in an insulating two-dimensional magnet". In: *Nature Physics* 12.10 (Oct. 2016), pp. 912–915. ISSN: 1745-2481. DOI: 10.1038/nphys3809. URL: https://doi.org/10.1038/nphys3809.

[161] Joji Nasu, Junki Yoshitake, and Yukitoshi Motome. "Thermal Transport in the Kitaev Model". In: *Phys. Rev. Lett.* 119 (12 2017), p. 127204. DOI: 10.1103/PhysRevLett.119.127204. URL: https://link.aps.org/doi/10.1103/PhysRevLett.119.127204.

[162] Jaakko Nissinen et al. "Classification of point-group-symmetric orientational ordering tensors". In: *Phys. Rev. E* 94 (2 2016), p. 022701. DOI: 10.1103/PhysRevE.94.022701. URL: https://link.aps.org/doi/10.1103/PhysRevE.94.022701.

[163] Z. Nussinov et al. "Inference of Hidden Structures in Complex Physical Systems by Multi-scale Clustering". In: *Information Science for Materials Discovery and Design*. Ed. by Turab Lookman, Francis J. Alexander, and Krishna Rajan. Cham: Springer International Publishing, 2016, pp. 115–138. ISBN: 978-3-319-23871-5. DOI: 10.1007/978-3-319-23871-5_6. URL: https://doi.org/10.1007/978-3-319-23871-5_6.

[164] Satoshi Okamoto. "Global phase diagram of a doped Kitaev-Heisenberg model". In: *Phys. Rev. B* 87 (6 2013), p. 064508. DOI: 10.1103/PhysRevB.87.064508. URL: https://link.aps.org/doi/10.1103/PhysRevB.87.064508.

[165] Matthew J. O'Malley, Patrick M. Woodward, and Henk Verweij. "Production and isolation of pH sensing materials by carbonate melt oxidation of iridium and platinum". In: *Journal of Materials Chemistry* 22.16 (2012). Publisher: The Royal Society of Chemistry, pp. 7782–7790. ISSN: 0959-9428. DOI: 10.1039/C2JM16791C. URL: http://dx.doi.org/10.1039/C2JM16791C.

[166] Juan Osorio Iregui, Philippe Corboz, and Matthias Troyer. "Probing the stability of the spin-liquid phases in the Kitaev-Heisenberg model using tensor network algorithms". In: *Phys. Rev. B* 90 (19 2014), p. 195102. DOI: 10.1103/PhysRevB.90.195102. URL: https://link.aps.org/doi/10.1103/PhysRevB.90.195102.

[167] Linus Pauling. "The Structure and Entropy of Ice and of Other Crystals with Some Randomness of Atomic Arrangement". In: *Journal of the American Chemical Society* 57.12 (Dec. 1935). Publisher: American Chemical Society, pp. 2680–2684. ISSN: 0002-7863. DOI: 10.1021/ja01315a102. URL: https://doi.org/10.1021/ja01315a102.

[168] David Pfau et al. "Ab initio solution of the many-electron Schrödinger equation with deep neural networks". In: *Phys. Rev. Research* 2 (3 2020), p. 033429. DOI: 10.1103/PhysRevResearch.2.033429. URL: https://link.aps.org/doi/10.1103/PhysRevResearch.2.033429.

[169] K. W. Plumb et al. "$\alpha - RuCl_3$: A spin-orbit assisted Mott insulator on a honeycomb lattice". In: *Phys. Rev. B* 90 (4 2014), p. 041112. DOI: 10.1103/PhysRevB.90.041112. URL: https://link.aps.org/doi/10.1103/PhysRevB.90.041112.

[170] Frank Pollmann et al. "Symmetry protection of topological phases in one-dimensional quantum spin systems". In: *Phys. Rev. B* 85 (7 2012), p. 075125. DOI: 10.1103/PhysRevB.85.075125. URL: https://link.aps.org/doi/10.1103/PhysRevB.85.075125.

[171] A. N. Ponomaryov et al. "Nature of Magnetic Excitations in the High-Field Phase of $\alpha-RuCl_3$". In: *Phys. Rev. Lett.* 125 (3 2020), p. 037202. DOI: 10.1103/PhysRevLett.125.037202. URL: https://link.aps.org/doi/10.1103/PhysRevLett.125.037202.

[172] Pedro Ponte and Roger G. Melko. "Kernel methods for interpretable machine learning of order parameters". In: *Phys. Rev. B* 96 (20 2017), p. 205146. DOI: 10.1103/PhysRevB.96.205146. URL: https://link.aps.org/doi/10.1103/PhysRevB.96.205146.

[173] V. Popkov and G. M. Schütz. "Solution of the Lindblad equation for spin helix states". In: *Phys. Rev. E* 95 (4 2017), p. 042128. DOI: 10.1103/PhysRevE.95.042128. URL: https://link.aps.org/doi/10.1103/PhysRevE.95.042128.

[174] Craig Price and Natalia B. Perkins. "Finite-temperature phase diagram of the classical Kitaev-Heisenberg model". In: *Phys. Rev. B* 88 (2 2013), p. 024410. DOI: 10.1103/PhysRevB.88.024410. URL: https://link.aps.org/doi/10.1103/PhysRevB.88.024410.

[175] Craig C. Price and Natalia B. Perkins. "Critical Properties of the Kitaev-Heisenberg Model". In: *Phys. Rev. Lett.* 109 (18 2012), p. 187201. DOI: 10.1103/PhysRevLett.109.187201. URL: https://link.aps.org/doi/10.1103/PhysRevLett.109.187201.

[176] Kejing Ran et al. "Spin-Wave Excitations Evidencing the Kitaev Interaction in Single Crystalline $\alpha-RuCl_3$". In: *Phys. Rev. Lett.* 118 (10 2017), p. 107203. DOI: 10.1103/PhysRevLett.118.107203. URL: https://link.aps.org/doi/10.1103/PhysRevLett.118.107203.

[177] Nihal Rao, Ke Liu, and Lode Pollet. "Inferring hidden symmetries of exotic magnets from detecting explicit order parameters". In: *Physical Review E* 104.1 (2021). DOI: 10.1103/physreve.104.015311. URL: https://doi.org/10.1103%2Fphysreve.104.015311.

[178] E. Rastelli, A. Tassi, and L. Reatto. "Noncollinear magnetic order and spin wave spectrum in presence of competing exchange interactions". In: *Journal of Magnetism and Magnetic Materials* 15-18 (1980), pp. 357 –358. ISSN: 0304-8853.

[179] Jeffrey G Rau and Hae-Young Kee. "Trigonal distortion in the honeycomb iridates: Proximity of zigzag and spiral phases in Na2IrO3". In: *arXiv preprint arXiv:1408.4811* (2014).

[180] Jeffrey G. Rau, Eric Kin-Ho Lee, and Hae-Young Kee. "Generic Spin Model for the Honeycomb Iridates beyond the Kitaev Limit". In: *Phys. Rev. Lett.* 112 (7 2014), p. 077204. DOI: 10.1103/PhysRevLett.112.077204. URL: https://link.aps.org/doi/10.1103/PhysRevLett.112.077204.

[181] Jeffrey G. Rau, Eric Kin-Ho Lee, and Hae-Young Kee. "Spin-Orbit Physics Giving Rise to Novel Phases in Correlated Systems: Iridates and Related Materials". In: *Annual Review of Condensed Matter Physics* 7.1 (2016), pp. 195–221. DOI: 10.1146/annurev-conmatphys-031115-011319. URL: https://doi.org/10.1146/annurev-conmatphys-031115-011319.

[182] Ioannis Rousochatzakis and Natalia B. Perkins. "Classical Spin Liquid Instability Driven By Off-Diagonal Exchange in Strong Spin-Orbit Magnets". In: *Phys. Rev. Lett.* 118 (14 2017), p. 147204. DOI: 10.1103/PhysRevLett.118.147204. URL: https://link.aps.org/doi/10.1103/PhysRevLett.118.147204.

[183] Ioannis Rousochatzakis, Yuriy Sizyuk, and Natalia B. Perkins. "Quantum spin liquid in the semiclassical regime". In: *Nature Communications* 9.1 (Apr. 2018), p. 1575. ISSN: 2041-1723. DOI: 10.1038/s41467-018-03934-1. URL: https://doi.org/10.1038/s41467-018-03934-1.

[184] Alejandro Ruiz et al. "Correlated states in -Li2IrO3 driven by applied magnetic fields". In: *Nature Communications* 8.1 (Oct. 2017), p. 961. ISSN: 2041-1723. DOI: 10.1038/s41467-017-01071-9. URL: https://doi.org/10.1038/s41467-017-01071-9.

[185] Preetha Saha et al. "Hidden Plaquette Order in a Classical Spin Liquid Stabilized by Strong Off-Diagonal Exchange". In: *Phys. Rev. Lett.* 122 (25 2019), p. 257204. DOI: 10.1103/PhysRevLett.122.257204. URL: https://link.aps.org/doi/10.1103/PhysRevLett.122.257204.

[186] A. Sahasrabudhe et al. "High-field quantum disordered state in $\alpha - RuCl_3$: Spin flips, bound states, and multiparticle continuum". In: *Phys. Rev. B* 101 (14 2020), p. 140410. DOI: 10.1103/PhysRevB.101.140410. URL: https://link.aps.org/doi/10.1103/PhysRevB.101.140410.

[187] Luke J. Sandilands et al. "Optical probe of Heisenberg-Kitaev magnetism in $\alpha-RuCl_3$". In: *Phys. Rev. B* 94 (19 2016), p. 195156. DOI: 10.1103/PhysRevB.94.195156. URL: https://link.aps.org/doi/10.1103/PhysRevB.94.195156.

[188] Luke J. Sandilands et al. "Scattering Continuum and Possible Fractionalized Excitations in $\alpha-RuCl_3$". In: *Phys. Rev. Lett.* 114 (14 2015), p. 147201. DOI: 10.1103/PhysRevLett.114.147201. URL: https://link.aps.org/doi/10.1103/PhysRevLett.114.147201.

[189] Flaviano José dos Santos, Manuel dos Santos Dias, and Samir Lounis. "Modeling spin waves in noncollinear antiferromagnets: Spin-flop states, spin spirals, skyrmions, and antiskyrmions". In: *Physical Review B* 102.10 (2020). DOI: 10.1103/physrevb.102.104436. URL: https://doi.org/10.1103%2Fphysrevb.102.104436.

[190] Lucile Savary and Leon Balents. "Quantum Spin Liquids". en. In: *Reports on Progress in Physics* 80.1 (Jan. 2017). arXiv:1601.03742 [cond-mat], p. 016502. ISSN: 0034-4885, 1361-6633. DOI: 10.1088/0034-4885/80/1/016502. URL: http://arxiv.org/abs/1601.03742 (visited on 07/26/2023).

[191] A. V. Savin, G. P. Tsironis, and X. Zotos. "Thermal conductivity of a classical one-dimensional Heisenberg spin model". In: *Phys. Rev. B* 72 (14 2005), p. 140402. DOI: 10.1103/PhysRevB.72.140402. URL: https://link.aps.org/doi/10.1103/PhysRevB.72.140402.

[192] Bernhard Scholkopf, Christopher J. C. Burges, and Alexander J. Smola, eds. *Advances in Kernel Methods: Support Vector Learning*. Cambridge, MA, USA: MIT Press, 1999. ISBN: 0262194163.

[193] Bernhard Scholkopf et al. "New Support Vector Algorithms". In: *Neural Computation* 12.5 (May 2000), pp. 1207–1245. ISSN: 0899-7667. DOI: 10.1162/089976600300015565. URL: https://doi.org/10.1162/089976600300015565 (visited on 04/08/2023).

[194] H. J. Schulz. "Dynamics of Coupled Quantum Spin Chains". In: *Phys. Rev. Lett.* 77 (13 1996), pp. 2790–2793. DOI: 10.1103/PhysRevLett.77.2790. URL: https://link.aps.org/doi/10.1103/PhysRevLett.77.2790.

[195] J. A. Sears et al. "Magnetic order in $\alpha - RuCl_3$: A honeycomb-lattice quantum magnet with strong spin-orbit coupling". In: *Phys. Rev. B* 91 (14 2015), p. 144420. DOI: 10.1103/PhysRevB.91.144420. URL: https://link.aps.org/doi/10.1103/PhysRevB.91.144420.

[196] J. A. Sears et al. "Phase diagram of $\alpha - RuCl_3$ in an in-plane magnetic field". In: *Phys. Rev. B* 95 (18 2017), p. 180411. DOI: 10.1103/PhysRevB.95.180411. URL: https://link.aps.org/doi/10.1103/PhysRevB.95.180411.

[197] Jennifer A. Sears et al. "Ferromagnetic Kitaev interaction and the origin of large magnetic anisotropy in $\alpha-RuCl_3$". In: *Nature Physics* (2020). DOI: 10.1038/s41567-020-0874-0. URL: https://doi.org/10.1038/s41567-020-0874-0.

[198] Eran Sela et al. "Order-by-disorder and spin-orbital liquids in a distorted Heisenberg-Kitaev model". In: *Phys. Rev. B* 90 (3 2014), p. 035113. DOI: 10.1103/PhysRevB.90.035113. URL: https://link.aps.org/doi/10.1103/PhysRevB.90.035113.

[199] L. Y. Shi et al. "Field-induced magnon excitation and in-gap absorption in the Kitaev candidate $RuCl_3$". In: *Phys. Rev. B* 98 (9 2018), p. 094414. DOI: 10.1103/PhysRevB.98.094414. URL: https://link.aps.org/doi/10.1103/PhysRevB.98.094414.

[200] Yogesh Singh and P. Gegenwart. "Antiferromagnetic Mott insulating state in single crystals of the honeycomb lattice material Na_2IrO_3". In: *Phys. Rev. B* 82 (6 2010), p. 064412. DOI: 10.1103/PhysRevB.82.064412. URL: https://link.aps.org/doi/10.1103/PhysRevB.82.064412.

[201] Yogesh Singh et al. "Relevance of the Heisenberg-Kitaev Model for the Honeycomb Lattice Iridates A_2IrO_3". In: *Phys. Rev. Lett.* 108 (12 2012), p. 127203. DOI: 10.1103/PhysRevLett.108.127203. URL: https://link.aps.org/doi/10.1103/PhysRevLett.108.127203.

[202] Xue-Yang Song, Yi-Zhuang You, and Leon Balents. "Low-Energy Spin Dynamics of the Honeycomb Spin Liquid Beyond the Kitaev Limit". In: *Phys. Rev. Lett.* 117 (3 2016), p. 037209. DOI: 10.1103/PhysRevLett.117.037209. URL: https://link.aps.org/doi/10.1103/PhysRevLett.117.037209.

[203] M. Songvilay et al. "Kitaev interactions in the Co honeycomb antiferromagnets $Na_3Co_2SbO_6$ and $Na_2Co_2TeO_6$". In: *Phys. Rev. B* 102 (22 2020), p. 224429. DOI: 10.1103/PhysRevB.102.224429. URL: https://link.aps.org/doi/10.1103/PhysRevB.102.224429.

[204] Lieven Vandenberghe Stephen Boyd. *Convex Optimization*. Cambridge University Press, Cambridge, U.K., 2004.

[205] Bill Sutherland. "Model for a multicomponent quantum system". In: *Phys. Rev. B* 12 (9 1975), pp. 3795–3805. DOI: 10.1103/PhysRevB.12.3795. URL: https://link.aps.org/doi/10.1103/PhysRevB.12.3795.

[206] Jenő Sólyom. *Fundamentals of the Physics of Solids*. Springer Berlin, Heidelberg, 2007.

[207] Mathieu Taillefumier et al. "Competing Spin Liquids and Hidden Spin-Nematic Order in Spin Ice with Frustrated Transverse Exchange". In: *Phys. Rev. X* 7 (4 2017), p. 041057. DOI: 10.1103/PhysRevX.7.041057. URL: https://link.aps.org/doi/10.1103/PhysRevX.7.041057.

[208] Hidenori Takagi et al. "Concept and realization of Kitaev quantum spin liquids". In: *Nat. Rev. Phys.* 1.4 (2019), pp. 264–280. DOI: 10.1038/s42254-019-0038-2. URL: https://doi.org/10.1038/s42254-019-0038-2.

[209] T. Takayama et al. "Hyperhoneycomb Iridate $\beta-Li_2IrO_3$ as a Platform for Kitaev Magnetism". In: *Phys. Rev. Lett.* 114 (7 2015), p. 077202. DOI: 10.1103/PhysRevLett.114.077202. URL: https://link.aps.org/doi/10.1103/PhysRevLett.114.077202.

[210] T. Takayama et al. "Pressure-induced collapse of the spin-orbital Mott state in the hyperhoneycomb iridate". In: *Physical Review B* 99.12 (2019). DOI: 10.1103/physrevb.99.125127. URL: https://doi.org/10.1103%2Fphysrevb.99.125127.

[211] Gen Tatara. "Thermal vector potential theory of magnon-driven magnetization dynamics". In: *Phys. Rev. B* 92 (6 2015), p. 064405. DOI: 10.1103/PhysRevB.92.064405. URL: https://link.aps.org/doi/10.1103/PhysRevB.92.064405.

[212] V. Todorova et al. "On AgRhO2, and the new quaternary delafossites AgLi1/3M2/3O2, syntheses and analyses of real structures". In: *Journal of Solid State Chemistry* 184.5 (May 2011), pp. 1112–1119. ISSN: 0022-4596. DOI: 10.1016/j.jssc.2011.03.014. URL: https://www.sciencedirect.com/science/article/pii/S0022459611001113.

[213] Yoshinori Tokura and Shinichiro Seki. "Multiferroics with Spiral Spin Orders". In: *Advanced Materials* 22.14 (2010), pp. 1554–1565. DOI: https://doi.org/10.1002/adma.200901961. URL: https://onlinelibrary.wiley.com/doi/abs/10.1002/adma.200901961.

[214] Simon Trebst and Ciarán Hickey. "Kitaev materials". In: *Physics Reports* 950 (2022), pp. 1–37. ISSN: 0370-1573. DOI: https://doi.org/10.1016/j.physrep.2021.11.003. URL: https://www.sciencedirect.com/science/article/pii/S0370157321004051.

[215] Stéphane Ty and Bertrand I Halperin. "Damping of spin waves in a two-dimensional Heisenberg antiferromagnet at low temperatures". In: *Physical Review B* 42.4 (1990), p. 2096.

[216] GV Uimin. "One-dimensional problem for S= 1 with modified antiferromagnetic Hamiltonian". In: *JETPL* 12 (1970), p. 225.

[217] . "Spin and thermal conductivity in a classical disordered spin chain". In: *Phys. Rev. B* 92 (13 2015), p. 134305. DOI: 10.1103/PhysRevB.92.134305. URL: https://link.aps.org/doi/10.1103/PhysRevB.92.134305.

[218] L. S. I. Veiga et al. "Pressure tuning of bond-directional exchange interactions and magnetic frustration in the hyperhoneycomb iridate $\beta - Li_2IrO_3$". In: *Phys. Rev. B* 96 (14 2017), p. 140402. DOI: 10.1103/PhysRevB.96.140402. URL: https://link.aps.org/doi/10.1103/PhysRevB.96.140402.

[219] Viciu, L. and Huang, Q. and Morosan, E. and Zandbergen, H. W. and Greenbaum, N. I. and McQueen, T. and Cava, R. J. "Structure and basic magnetic properties of the honeycomb lattice compounds Na $_2$Co $_2$TeO $_6$ and Na $_3$Co $_2$SbO $_6$". In: *Journal of Solid State Chemistry France* 180.3 (Mar. 2007), pp. 1060–1067. DOI: 10.1016/j.jssc.2007.01.002.

[220] Tom Vieijra et al. "Restricted Boltzmann Machines for Quantum States with Non-Abelian or Anyonic Symmetries". In: *Phys. Rev. Lett.* 124 (9 2020), p. 097201. DOI: 10.1103/PhysRevLett.124.097201. URL: https://link.aps.org/doi/10.1103/PhysRevLett.124.097201.

[221] M. P. Walser et al. "Direct mapping of the formation of a persistent spin helix". In: *Nature Physics* 8.10 (2012), pp. 757–762. DOI: 10.1038/nphys2383. URL: https://doi.org/10.1038/nphys2383.

[222] Jiucai Wang, B. Normand, and Zheng-Xin Liu. "One Proximate Kitaev Spin Liquid in the $K - J - \Gamma$ Model on the Honeycomb Lattice". In: *Phys. Rev. Lett.* 123 (19 2019), p. 197201. DOI: 10.1103/PhysRevLett.123.197201. URL: https://link.aps.org/doi/10.1103/PhysRevLett.123.197201.

[223] Wei Wang et al. "Theoretical investigation of magnetic dynamics in $\alpha-RuCl_3$". In: *Phys. Rev. B* 96 (11 2017), p. 115103. DOI: 10.1103/PhysRevB.96.115103. URL: https://link.aps.org/doi/10.1103/PhysRevB.96.115103.

[224] Steven R. White and A. L. Chernyshev. "Neél Order in Square and Triangular Lattice Heisenberg Models". In: *Phys. Rev. Lett.* 99 (12 2007), p. 127004. DOI: 10.1103/PhysRevLett.99.127004. URL: https://link.aps.org/doi/10.1103/PhysRevLett.99.127004.

[225] S. C. Williams et al. "Incommensurate counterrotating magnetic order stabilized by Kitaev interactions in the layered honeycomb $\alpha-Li_2IrO_3$". In: *Phys. Rev. B* 93 (19 2016), p. 195158. DOI: 10.1103/PhysRevB.93.195158. URL: https://link.aps.org/doi/10.1103/PhysRevB.93.195158.

[226] Stephen M. Winter et al. "Breakdown of magnons in a strongly spin-orbital coupled magnet". In: *Nature Communications* 8.1 (2017), p. 1152. DOI: 10.1038/s41467-017-01177-0. URL: https://doi.org/10.1038/s41467-017-01177-0.

[227] Stephen M. Winter et al. "Challenges in design of Kitaev materials: Magnetic interactions from competing energy scales". In: *Phys. Rev. B* 93 (21 2016), p. 214431. DOI: 10.1103/PhysRevB.93.214431. URL: https://link.aps.org/doi/10.1103/PhysRevB.93.214431.

[228] Stephen M Winter et al. "Models and materials for generalized Kitaev magnetism". In: *Journal of Physics: Condensed Matter* 29.49 (2017), p. 493002. DOI: 10.1088/1361-648x/aa8cf5. URL: https://doi.org/10.1088%2F1361-648x%2Faa8cf5.

[229] William Witczak-Krempa et al. "Correlated Quantum Phenomena in the Strong Spin-Orbit Regime". In: *Annual Review of Condensed Matter Physics* 5.1 (Mar. 2014). Publisher: Annual Reviews, pp. 57–82. ISSN: 1947-5454. DOI: 10.1146/annurev-conmatphys-020911-125138. URL: https://doi.org/10.1146/annurev-conmatphys-020911-125138 (visited on 07/26/2023).

[230] Ulli Wolff. "Collective Monte Carlo Updating for Spin Systems". In: *Phys. Rev. Lett.* 62 (4 1989), pp. 361–364. DOI: 10.1103/PhysRevLett.62.361. URL: https://link.aps.org/doi/10.1103/PhysRevLett.62.361.

[231] F. Y. Wu. "DIMERS ON TWO-DIMENSIONAL LATTICES". In: *International Journal of Modern Physics B* 20.32 (2006), pp. 5357–5371. DOI: 10.1142/S0217979206036478. URL: https://doi.org/10.1142/S0217979206036478.

[232] Y Miyatake et al. "On the implementation of the 'heat bath' algorithms for Monte Carlo simulations of classical Heisenberg spin systems". In: *Journal of Physics C: Solid State Physics* 19.14 (May 1986), p. 2539. ISSN: 0022-3719. DOI: 10.1088/0022-3719/19/14/020. URL: https://dx.doi.org/10.1088/0022-3719/19/14/020.

[233] Ravi Yadav et al. "Kitaev exchange and field-induced quantum spin-liquid states in honeycomb -RuCl3". In: *Scientific Reports* 6.1 (Nov. 2016), p. 37925. ISSN: 2045-2322. DOI: 10.1038/srep37925. URL: https://doi.org/10.1038/srep37925.

[234] Ravi Yadav et al. "Large off-diagonal exchange couplings and spin liquid states in C_3-symmetric iridates". In: *Phys. Rev. B* 100 (14 2019), p. 144422. DOI: 10.1103/PhysRevB.100.144422. URL: https://link.aps.org/doi/10.1103/PhysRevB.100.144422.

[235] Ravi Yadav et al. "Strong Effect of Hydrogen Order on Magnetic Kitaev Interactions in $H_3LiIr_2O_6$". In: *Phys. Rev. Lett.* 121 (19 2018), p. 197203. DOI: 10.1103/PhysRevLett.121.197203. URL: https://link.aps.org/doi/10.1103/PhysRevLett.121.197203.

[236] Youhei Yamaji et al. "First-Principles Study of the Honeycomb-Lattice Iridates Na_2IrO_3 in the Presence of Strong Spin-Orbit Interaction and Electron Correlations". In: *Phys. Rev. Lett.* 113 (10 2014), p. 107201. DOI: 10.1103/PhysRevLett.113.107201. URL: https://link.aps.org/doi/10.1103/PhysRevLett.113.107201.

[237] Simeng Yan, David A. Huse, and Steven R. White. "Spin Liquid Ground State of the $S=1/2$ Kagome Heisenberg Model". en. In: *Science* 332.6034 (June 2011). arXiv:1011.6114 [cond-mat, physics:quant-ph], pp. 1173–1176. ISSN: 0036-8075, 1095-9203. DOI: 10.1126/science.1201080. URL: http://arxiv.org/abs/1011.6114 (visited on 07/26/2023).

[238] Feng Ye et al. "Direct evidence of a zigzag spin-chain structure in the honeycomb lattice: A neutron and x-ray diffraction investigation of single-crystal Na_2IrO_3". In: *Phys. Rev. B* 85 (18 2012), p. 180403. DOI: 10.1103/PhysRevB.85.180403. URL: https://link.aps.org/doi/10.1103/PhysRevB.85.180403.

[239] J. M. Yeomans and Joseph Rudnick. "Statistical Mechanics of Phase Transitions". In: *Physics Today* 46.7 (July 1993), pp. 80–80. ISSN: 0031-9228. DOI: 10.1063/1.2808979. URL: https://doi.org/10.1063/1.2808979 (visited on 04/08/2023).

[240] T Yokoi et al. "Half-integer quantized anomalous thermal Hall effect in the Kitaev material $\alpha-RuCl_3$". In: *arXiv preprint arXiv:2001.01899* (2020).

[241] Junki Yoshitake, Joji Nasu, and Yukitoshi Motome. "Fractional Spin Fluctuations as a Precursor of Quantum Spin Liquids: Majorana Dynamical Mean-Field Study for the Kitaev Model". In: *Phys. Rev. Lett.* 117 (15 2016), p. 157203. DOI: 10.1103/PhysRevLett.117.157203. URL: https://link.aps.org/doi/10.1103/PhysRevLett.117.157203.

[242] Wei Zhang et al. "Parallel distributed processing model with local space-invariant interconnections and its optical architecture". In: *Applied Optics* 29.32 (Nov. 1990). Publisher: Optica Publishing Group, pp. 4790–4797. DOI: 10.1364/AO.29.004790. URL: https://opg.optica.org/ao/abstract.cfm?URI=ao-29-32-4790.

[243] Yi Zhang et al. "Machine learning in electronic-quantum-matter imaging experiments". In: *Nature* 570.7762 (2019), pp. 484–490. DOI: 10.1038/s41586-019-1319-8. URL: https://doi.org/10.1038/s41586-019-1319-8.

[244] Bowen Zhao, Phillip Weinberg, and Anders W. Sandvik. "Symmetry-enhanced discontinuous phase transition in a two-dimensional quantum magnet". In: *Nature Physics* 15.7 (2019), pp. 678–682. DOI: 10.1038/s41567-019-0484-x. URL: https://doi.org/10.1038/s41567-019-0484-x.

[245] Jiacheng Zheng et al. "Gapless Spin Excitations in the Field-Induced Quantum Spin Liquid Phase of $\alpha-RuCl_3$". In: *Phys. Rev. Lett.* 119 (22 2017), p. 227208. DOI: 10.1103/PhysRevLett.119.227208. URL: https://link.aps.org/doi/10.1103/PhysRevLett.119.227208.

[246] Weihong Zheng et al. "Excitation spectra of the spin-$\frac{1}{2}$ triangular-lattice Heisenberg antiferromagnet". In: *Phys. Rev. B* 74 (22 2006), p. 224420. DOI: 10.1103/PhysRevB.74.224420. URL: https://link.aps.org/doi/10.1103/PhysRevB.74.224420.

[247] M. E. Zhitomirsky. "Octupolar ordering of classical kagome antiferromagnets in two and three dimensions". In: *Phys. Rev. B* 78 (9 2008), p. 094423. DOI: 10.1103/PhysRevB.78.094423. URL: https://link.aps.org/doi/10.1103/PhysRevB.78.094423.

[248] Zheng Zhu, Zheng-Yu Weng, and DN Sheng. "Magnetic Field Induced Spin Liquids in $S = 1$ Kitaev Honeycomb Model". In: *arXiv preprint arXiv:2001.05054* (2020).

[249] Zheng Zhu et al. "Robust non-Abelian spin liquid and a possible intermediate phase in the antiferromagnetic Kitaev model with magnetic field". In: *Phys. Rev. B* 97 (24 2018), p. 241110. DOI: 10.1103/PhysRevB.97.241110. URL: https://link.aps.org/doi/10.1103/PhysRevB.97.241110.

[250] Zhenyue Zhu and Steven R. White. "Spin liquid phase of the $S = 1/2$ Heisenberg model on the triangular lattice". In: *Physical Review B* 92.4 (July 2015). Publisher: American Physical Society, p. 041105. DOI: 10.1103/PhysRevB.92.041105. URL: https://link.aps.org/doi/10.1103/PhysRevB.92.041105.